

Université du Québec
Institut National de la Recherche Scientifique
Centre Eau Terre Environnement

**TEMPORAL AND SPATIAL EVOLUTION OF THE MIXED
LAYER IN THE SOUTHERN BEAUFORT SEA AND THE
AMUNDSEN GULF**

Par

Somayeh Nahavandian Esfahani

Thèse présentée pour l'obtention du grade de
Philosophiae doctor, (Ph.D.)
en sciences de l'eau

Jury d'évaluation

Examineur externe	Dr. Brad deYoung, Professor Department of Physics and Physical Oceanography Memorial University
Examineur externe	Dr. Richard E. Thomson, Research Scientist Institute of Ocean Sciences Fisheries and Oceans Canada
Examineur interne	Dr. Yves Secretan, Professor Institut National de la Recherche Scientifique Centre Eau Terre Environnement
Codirecteur de recherche	Dr. Louis Prieur, Directeur de recherche émérite Laboratoire d'Océanographie de Villefranche Directeur de recherche, CNRS, Villefranche sur mer
Directeur de recherche	Dr. Yves Gratton, Professor Institut National de la Recherche Scientifique Centre Eau Terre Environnement

RÉSUMÉ

La couche mélangée, la couche de surface océanique dotée de propriétés physiques constantes en raison du mélange, joue un rôle important dans les études biologiques et de contaminants. La présente thèse se veut une tentative d'améliorer notre connaissance de l'océan Arctique à travers une étude des caractéristiques des couches mélangées dans le sud de la mer de Beaufort et dans le golfe d'Amundsen. La profondeur de la couche mélangée a été estimée à l'aide de cinq méthodes différentes et nous avons constaté que la plus appropriée pour notre région d'étude est une version modifiée de l'algorithme de Holte et Talley (2009). Notre étude est basée sur de nombreuses séries de données récentes et uniques recueillies dans le sud de la mer de Beaufort au cours des hivers 2003-2004 et 2007-2008, ainsi que pendant les étés et les automnes de 2002, 2003, 2004, 2005, 2006, 2007, 2008 et 2009. Sa grande particularité est que nous présentons pour la première fois une analyse de deux années complètes de données obtenues en 2003-2004 et 2007-2008: ce sont les premières données hivernales recueillies dans la région.

L'évolution temporelle et la répartition spatiale des profondeurs de la couche mélangée ont été étudiées dans quatre sous-régions, subdivisées à nouveau en eaux côtières (*inshore*, profondeur < 200 m) et hauturières (*offshore*, profondeur > 200 m). Il a été démontré que la couche mélangée est généralement plus profonde dans les zones *offshore* au cours de l'automne, en hiver et au printemps tandis qu'en été, elle est comparable dans les deux zones *inshore* et *offshore*. La profondeur de la couche mélangée était significativement plus profonde en 2007-2008 par rapport à toutes les autres années en raison d'un upwelling intense observé à l'automne 2007. Les différences entre les hivers de 2004 et 2008 sont également dues aux différentes couvertures de glace dans les régions à l'étude: la banquise côtière (landfast ice) en 2003-2004 versus la banquise de mer (drift ice) en 2007-2008. En outre, la profondeur de la couche mélangée est moindre au cours de l'été et, par la suite, elle s'approfondit progressivement jusqu'à ce qu'elle atteigne son épaisseur maximale en avril. L'étude de fonctions de distribution de probabilité ont montré que la distribution est la plupart du temps de type "bosse" (hump), ce qui signifie qu'il n'y avait qu'une seule gamme de profondeur préférée de la couche mélangée pour chaque région et saison.

L'originalité de cette thèse réside dans l'approche que nous avons utilisée pour étudier l'évolution de la couche mélangée à partir d'une station fixe dans la baie de Franklin, dans le golfe d'Amundsen. Nous avons analysé le bilan de masse de la couche mélangée entre décembre 2003 et juin 2004 sur la base de l'approche de budget de chaleur d'Emery (1976), adaptée par Prieur et al. (2010). La seule hypothèse nécessaire est qu'il n'y a pas advection latérale non divergente. La beauté de cette approche est qu'elle ne nécessite que des profils verticaux de densité, obtenus à partir de plate-forme fixe ou de profileurs dérivants. Cette méthode nous permet également de comprendre, pour la première fois, l'effet important de l'advection verticale à la base de la couche mélangée. Cette méthode nous permet aussi de produire une estimation des taux de croissance de la glace de surface. L'analyse de quatre mois de concentrations de *Chla* au-dessous de la glace a montré que la floraison printanière commence juste après que la couche mélangée ait atteint sa plus grande épaisseur au printemps et produit ses concentrations maximales environ un mois plus tard.

ABSTRACT

The mixed layer, which is the oceanic surface layer with constant physical properties due to mixing, plays an important role in contaminant and biological studies. This thesis is an attempt to further enhance our knowledge of the Arctic Ocean through a study of the characteristics of the mixed layer in southern Beaufort Sea and Amundsen Gulf.

The Mixed Layer Depth was estimated using five different methods and it was found that the most appropriate one for our study region was a modified version of the Holte and Talley (2009) algorithm. Our study is based on numerous recent, unique data sets gathered in southern Beaufort Sea during the winters of 2003-2004 and 2007-2008, as well as during the summers and falls of 2002, 2003, 2004, 2005, 2006, 2007, 2008 and 2009. Its unique feature is the two complete years of data obtained during 2003-2004 and 2007-2008.

The temporal evolution and the spatial distribution of the Mixed Layer Depths was studied in four subregions, further subdivided into inshore (depths < 200 m) and offshore (depths > 200 m) subregions. It was shown that the Mixed Layer Depth was generally deeper offshore during the fall, winter and spring, while in summer they are comparable in both regions. The Mixed Layer Depth was significantly deeper during 2007-2008 compared to all the other years due to a strong upwelling event in the fall of 2007. Differences between the winters of 2004 and 2008 are also due to the different ice covers in the study regions: landfast ice in 2003-2004 versus drifting ice floes in 2007-2008. Furthermore, the Mixed Layer Depths were the shallowest during the summer and afterwards they gradually deepened until they reached their maximum thickness in April. Probability distribution functions showed that the distribution are mostly of the one “hump” variety, meaning that there was a single, preferred Mixed Layer Depth range for each region and season.

The originality of this thesis lies in the approach we used to study the mixed layer evolution at a fixed station in Franklin Bay, Amundsen Gulf. We analyzed the mass budget of the mixed layer between December 2003 and June 2004, based on the heat

budget approach of Emery (1976) and modified by Prieur et al. (2010). The only assumption needed was that there was no non-divergent lateral advection. The beauty of the approach is that it needs only vertical density profiles, from moored or drifting instruments. This method also enables us to include the important effect of the vertical advection at the base of the mixed layer and produces an estimate of the surface ice growth rates. The analysis of four months of under ice *Chl a* concentrations has shown that blooming starts just after the mixed layer has attained its largest thickness in the spring, and reaches its maximum concentrations about one month later.

ACKNOWLEDGMENTS

I would first like to thank my supervisor, Prof. Yves Gratton who introduced me to the world of oceanography. I am also grateful to my cosupervisor, Dr. Louis Prieur for his great ideas and valuable comments during my research. Without their support and encouragement this thesis would not have been possible. I would also like to thank the members of my PhD thesis committee, Profs. Brad deYoung, Richard E. Thomson and Yves Secretan for their advice, ideas and valuable comments. I also wish to thank Profs. Isabelle Laurion from INRS and Sally MacIntyre from University of California, Santa Barbara for their support and ideas during my PhD mini-project and Profs. Michel Gosselin from ISMER and Tim Papakyriakou from the University of Manitoba for sharing their data.

I would also like to thank the members of our research group for their contributions, especially, I am grateful to Caroline Sévigny, Véronique Lago and Jessy Barrette. The support of the university staffs, particularly, Jean-Daniel Bourgault and Suzanne Dussaut is also gratefully acknowledged.

Last but not least, I wish to express my sincere gratitude to my motherland and my family, particularly, my parents who have been always an endless source of inspiration, love and wisdom throughout my life, either beside me or from afar. Finally, I am deeply indebted to my husband for his constant and unconditional love, support and encouragement.

CONTENTS

RÉSUMÉ	iii
ABSTRACT	v
ACKNOWLEDGMENTS	vii
CONTENTS	viii
LIST OF FIGURES	xii
LIST OF TABLES	xxiii
LIST OF SYMBOLS	xxv
Liste des figures citées	xxxix
Liste des tableaux cités	xxxv
0 SYNTHÈSE EN FRANÇAIS	xxxvii
0.1 Introduction	xxxvii
0.1.1 Motivation	xxxvii
0.1.2 Objectifs	xxxviii
0.2 Région d'étude et données disponibles	xxxix
0.2.1 L'Arctique Canadien	xxxix
0.2.2 La mer de Beaufort et le golfe Amundsen	xl
0.2.3 Les données disponibles	xli
0.3 Méthodes d'estimation de la profondeur de la couche mélangée	xlii
0.3.1 Méthodes d'estimation de la <i>MLD</i>	xliii
0.3.2 Évaluation des méthodes	xliv
0.4 Évolution temporelle et distribution spatiale de la profondeur de la couche mélangée	xlvi
0.4.1 Variations spatiales	xlvi
0.4.2 Évolution temporelle de la <i>MLD</i>	xlviii

0.5	Les flux océaniques sous la glace et leurs impacts sur la profondeur de la couche mélangée	li
0.5.1	Les flux océaniques pendant CASES (2003-2004) et les variations de la <i>MLD</i>	li
0.5.2	Comparaison entre le flux de la flottabilité calculé avec les méthodes NS et LP	liii
0.5.3	Observations atmosphériques, de la glace et de la neige en relation avec la variation de la <i>MLD</i>	liii
0.5.4	Corrélation croisée entre les flux océaniques et la <i>MLD</i> pour différentes stations	liii
0.5.5	Modélisation de la <i>MLD</i> en utilisant une méthode de régression linéaire et multiple	liv
0.5.6	Estimation de l'épaisseur de la glace et la <i>MLD</i>	liv
0.5.7	Floraison et la <i>MLD</i>	liv
0.6	Conclusions	lv
1	INTRODUCTION	1
1.1	Motivation	1
1.2	The Mixed Layer	2
1.2.1	Definition of the Mixed Layer	2
1.2.2	The Mixed Layer in different regions	3
1.3	Objectives	7
1.4	Structure of the thesis	8
2	STUDY REGION AND AVAILABLE DATA	9
2.1	The Arctic Ocean and Canadian Archipelago	9
2.1.1	Circulation, vertical structure and ice in the Arctic	9
2.1.2	Beaufort Sea and Amundsen Gulf	14
2.2	Available data	19
2.2.1	CASES (2002, 2003 and 2004)	19
2.2.2	ArcticNet 2005 and 2006	20
2.2.3	CFL 2007 and 2008	21
2.2.4	Malina (2009)	24
2.3	Summary	24
3	METHODS TO ESTIMATE THE MIXED LAYER DEPTH	25
3.1	Introduction	25
3.2	Density in the Arctic	25
3.3	<i>MLD</i> estimation methods	28
3.3.1	Threshold method	28
3.3.2	TF and TFL methods	29

3.3.3	HT and HTN methods	32
3.3.4	Other methods	34
3.4	Assessment of the methods	36
3.4.1	Visual inspection of the profiles	36
3.4.2	Statistical evaluation	39
3.4.3	In situ validation	41
3.5	Summary	44
4	TEMPORAL EVOLUTION AND SPATIAL DISTRIBUTION OF THE MIXED LAYER DEPTH	47
4.1	Introduction	47
4.2	Methodology	48
4.2.1	Difficulties and approaches	48
4.2.2	Statistical definitions	48
4.2.3	Available data in the subregions	53
4.3	Spatial distribution of the <i>MLD</i>	54
4.3.1	Inshore and offshore	56
4.3.2	Spatial variations of the <i>MLD</i> between the subregions	62
4.3.3	Evolution of the <i>MLD</i> in Transects	67
4.4	Temporal evolution of the <i>MLD</i>	70
4.4.1	Seasonal evolution of the <i>MLD</i> during the CASES (2003-2004) and CFL (2007-2008)	70
4.4.2	Interannual evolution of the <i>MLD</i>	83
4.5	Summary	90
5	UNDER ICE OCEANIC FLUXES AND THEIR IMPACTS ON THE MIXED LAYER DEPTH	93
5.1	Introduction	93
5.2	Methodology	94
5.2.1	Oceanic and atmospheric flux estimations	94
5.2.2	Ice thickness estimation using the fluxes	106
5.2.3	Cross-correlations function	108
5.2.4	Data	108
5.3	Results and discussion	110
5.3.1	Ocean fluxes during CASES (2003-2004) and <i>MLD</i> variations	110
5.3.2	Comparison between buoyancy flux calculated with the NS and the LP methods	121
5.3.3	Atmospheric flux, oceanic flux and the <i>MLD</i>	123
5.3.4	Cross-correlation between ocean fluxes and the <i>MLD</i> at different stations	126
5.3.5	Modeling the <i>MLD</i> using a linear and multiple regression method	130

5.3.6	Ice thickness estimation and the <i>MLD</i>	133
5.3.7	Blooming and the <i>MLD</i>	135
5.3.8	Two unusual cases	137
5.4	Summary	139
6	SUMMARY AND CONCLUSIONS	142
	REFERENCES	155
	APPENDICES	156
	Appendix A	156
	Appendix B	160
	Appendix C	164

LIST OF FIGURES

2.1	The Canadian Arctic Archipelago and Greenland.	10
2.2	Pathways of the Pacific (blue lines) and Atlantic (red lines) waters in the Arctic Ocean. Modified after McLaughlin et al. (1996)	11
2.3	Schematic T-S diagram presenting a schematic vertical structure of the water column in the Southeast Beaufort Sea: the Polar Mixed layer (PML), the Bering Sea Summer Water (BSSW), the Bering Sea Winter Water (BSWW), the Arctic Thermocline (ATh), the Atlantic Layer (AL) and the Canada Deep Basin Water (CBDW).The depths are approximative. Modified after Gratton et al. (2012) . The black line is Temperature-Salinity diagram sampled during the Arctic Internal Wave Experiment. The color circles are from ArcticNet-Geotraces cast 0903034.	12
2.4	Map of the study area showing the different locations quoted in the text.	13
2.5	Circulation of the water on the Mackenzie Shelf: The surface anti-cyclonic Beaufort Gyre (solid black lines), the deep cyclonic Beaufort Undercurrent (blue arrows), the surface cyclonic coastal current (dashed line) and the Mackenzie River (white).	15
2.6	Wind forcing (blue arrow) and vertical water transport (downward: the circles with crosses and upward: the circles with points).	16
2.7	Rosette and CTD on the CCGS Amundsen.	20
2.8	Sampling stations in 2002, 2003 and 2004 during CASES. The location of the fixed station (between December 2003 and 30 May 2004) is identified by a red star.	21
2.9	Location of the sampling stations during ArcticNet 2005 and 2006.	22
2.10	Location of the sampling stations in 2007-2008 during the CFL program.	22
2.11	Location of the sampling stations in 2009 during the Malina program.	23
3.1	Temperature-Salinity ($T - S$) diagram showing the density minus 1000 (σ_t) isolines in kg m^{-3} . The dashed line is the freezing temperature as a function of temperature and salinity. Note that the smaller figure at the bottom right shows the density isolines for the temperature between -2 and 30°C.	26

3.2	Monthly values (in 2003-2004) of R at different depths illustrating the temperature and salinity effects on density. Values of $R < 1$ indicate that salinity effects are dominant.	27
3.3	Example of MLD estimation with the threshold method using profile 076 from leg 0801 (sampled on 13 January 2008). The blue, red and green squares are for thresholds of 0.03, 0.04 and 0.05 kg m^{-3} respectively. In this case a larger threshold value would be needed.	28
3.4	Potential density time series for the months of January and February 2004 at the CASES winter station. Only two months are shown to make the graphs more legible. The thick red lines are the MLD density estimated with the threshold method using 0.03 kg m^{-3} (panel a), 0.04 kg m^{-3} (panel b) and 0.05 kg m^{-3} (panel c). The blue line is the density at 10 m. The green and black lines are the densities at $MLD+3$ m and $MLD+10$ m. The reason behind the choice of the last two will become obvious in chapter 5.	30
3.5	Example of MLD estimations with the TF and TFL methods for two profiles: (a) cast 075 from leg 0402 (CASES) and (b) cast 124 from leg 0801 (CFL), two winter profiles.	32
3.6	Example of MLD estimation with the HTN method using profile 080 from leg 0801. The red line is the final MLD	33
3.7	Three methods to estimate the MLD are compared using profile 076 from leg 0801. (a) The TH method is used in the left panel, (b) the TF method in the central panel and (c) the HTN method in the right panel. The red lines highlight the final MLD estimated by the HTN method.	34
3.8	Comparison between methods: each + represents a MLD estimation. Panels (a), (b) and (c) compare the TF, TFL and HTN methods to the TH method (0.05 kg m^{-3}). Panel (d) compares the TFL and TF; panel (e) compares the HTN and TF and panel (f) compares the HTN and TFL. An error upper limit of 0.05 is used for the TF and TFL methods. The diagonal red line is the 1:1 fit.	37
3.9	Comparison of the $MLDs$ obtained by visual inspection of the profiles with the $MLDs$ estimated by the four other automatic methods. The yellow diagonal line is the 1:1 fit.	38
3.10	Potential density time series at 5 m (blue lines), at the MLD (red lines), at $MLD+3$ m (green lines) and $MLD+10$ m (black lines) in the fall of 2003 during leg 0304. The $MLDs$ are calculated using the TH method (threshold of 0.05 kg m^{-3}) (panel a), the TF method (panel b), the TFL method (panel c) and the HTN method (panel d).	42

3.11	Potential density time series at 10 m (blue lines), at the <i>MLD</i> (red lines), at <i>MLD</i> +3 m (green lines) and <i>MLD</i> +10 m (black lines) in the winter of 2004 during leg 0401. The <i>MLDs</i> are calculated using the TH method (threshold of 0.05 kg m^{-3}) (panel a), the TF method (panel b), the TFL method (panel c) and the HTN method (panel d). The magenta ellipses highlight the periods for which our method fails; they are discussed in the text.	43
3.12	Potential density time series at 10 m (blue lines), at the <i>MLD</i> (red lines), at <i>MLD</i> +3 m (green lines) and <i>MLD</i> +10 m (black lines) in the winter of 2008 during leg 0801. The <i>MLDs</i> are calculated using the TH method (threshold of 0.05 kg m^{-3}) (panel a), the TF method (panel b), the TFL method (panel c) and the HTN method (panel d).	45
4.1	(a) Locations of the sampling stations as a function of time during CASES leg 0202. (b) <i>MLDs</i> at the same locations based on the HTN method. The <i>MLDs</i> are in meters.	49
4.2	Four subregions considered in this study: Beaufort, Mouth, Amundsen and Franklin.	50
4.3	Gaussian distribution of a hypothetical data set with different values of the standard deviations.	51
4.4	Salinity at 5 m in the fall of 2003 (during leg 0304; left) and in the fall of 2007 (during leg 0706; right). The estimation was performed using ordinary Kriging. The symbols correspond to the locations of <i>MLDs</i> deeper than their surroundings along the salinity front in 2007: <i>MLD</i> > 60 m (triangle), 45 m (square), 45 m (ellipse) and 35 m (star).	55
4.5	Inshore-offshore salinity section (km 0 is inside the Mackenzie River) that shows a pool of fresher water isolated from the main Mackenzie discharge by an upwelling event. The stations were visited between 22 September and 14 October 2002. The estimation was performed using ordinary Kriging. Modified after Garneau et al. (2006)	55
4.6	Monthly mean values of the inshore (blue) and offshore (red) <i>MLDs</i> regardless of the subregion during CASES (2003-2004). The dashed lines are the 95% confidence intervals on the mean value of the <i>MLD</i> . Number of the observation in each month is shown in Table 4.3.	57
4.7	Probability density functions for the <i>MLDs</i> inshore and offshore areas during CASES (2003-2004) in (a) October, (b) November, (c) June and (d) July.	57
4.8	Monthly mean values of the inshore (blue) and offshore (red) <i>MLDs</i> during the CFL (2007-2008). The dash lines are the 95% confidence intervals on the mean value of the <i>MLD</i> . Number of the observation in each month is shown in Table 4.4.	59

4.9	Probability density functions of the inshore and offshore <i>MLDs</i> during the CFL (2007-2008). (a) October, (b) March, (c) April, (d) May, (e) June and (f) July.	59
4.10	Mean values of the inshore (blue) and offshore (red) <i>MLDs</i> regardless of the subregion during (a) Fall 2002 (CASES), (b) Summer 2005 (ArcticNet), (c) Fall 2006 (ArcticNet) and (d) Summer 2009 (Malina). The dash lines are uncertainty limits with 95% confidence intervals on the mean inshore <i>MLD</i> (blue solid line) and offshore (red solid line).	61
4.11	Probability density functions of <i>MLD</i> inshore and offshore areas during (a) Fall 2002 (CASES), (b) Summer 2005 (ArcticNet), (c) Fall 2006 (ArcticNet) and (d) Summer 2009 (Malina).	61
4.12	Mean values of the inshore (blue) and offshore (red) <i>MLDs</i> within the subregions during (a) Fall 2002 in the BF, (b) Fall 2003 in the BF, (c) Fall 2007 in the M, (d) Spring 2004 in the M, (e) Spring 2008 in the AM, (f) Summer 2008 in the M, (g) Summer 2008 in the BF and (h) Summer 2009 in the BF. The dash lines are uncertainty limits with 95% confidence intervals on the mean inshore <i>MLD</i> (blue solid line) and offshore (red solid line).	64
4.13	Probability density functions of <i>MLDs</i> inshore and offshore areas within the subregions during (a) Fall 2002 in the Beaufort subregion, (b) Fall 2003 in the Beaufort subregion, (c) Fall 2003 in the Mouth subregion, (d) Spring 2004 in the Mouth subregion, (e) Spring 2008 in the Amundsen subregion, (f) Summer 2008 in the Mouth subregion, (g) Summer 2008 in the Beaufort subregion and (h) Summer 2009 in the Beaufort subregion.	64
4.14	Probability density functions of offshore <i>MLDs</i> in different subregions in (a) Fall 2003, (b) Spring 2004, (c) Fall 2007, (d) Spring 2008, (e) Summer 2008 and (f) Summer 2009.	65
4.15	(a) and (b) Locations of the sampling stations as a function of time along transects Tr3 and TrAM during fall 2002 (leg 0202). (c) Temperature contours with salinity isolines (white lines) and the <i>MLD</i> (black lines) along Tr3 (from south to North) and along TrAM (from East to West). Distances are from the coast.	68
4.16	(a), (b), (c) and (d) Locations of the sampling stations as a function of time along transects Tr1, Tr2, Tr3 and TrAM during fall 2003 (leg 0304). (e) Temperature contours with salinity isolines (white lines) and the <i>MLD</i> (black lines) along Tr1 (from South to North), Tr2 (from South to North), Tr3 (from South to North) and TrAM (from East to West). The sampling is done during leg 0304 in fall 2003.	69

- 4.17 Seasonal variations of the *MLD* in different subregions during 2003-2004 (CASES); (a) Amundsen, (b) Mouth and (c) Franklin subregions. The mean values and their variability are presented on the left side and the PDF on the right side. The mean values for each season (solid lines) with their 95% confidence intervals (dashed lines) are presented with the time evolution (color coded) of the estimated *MLDs*. The right-hand figures are the PDFs for the corresponding seasons. The number of intervals in each PDF panel is selected according to the available observations. For example, in the Franklin in the summer we have the least number of intervals because the number of samples is small (13). 71
- 4.18 (a), (b), (c) Locations of the sampling stations as a function of time in the Amundsen region during fall, spring and summer 2003-2004, respectively. The color of the circles identifies the sampling date. 72
- 4.19 Contours of the temperature in the Amundsen subregion with salinity isolines (white lines) during three different seasons in 2003-2004. (a) Fall, (b) spring and (c) summer. The black broken lines are the *MLDs*. The Sampling Sequences (STS) axis (in days) start at zero in each panel. Note that density contours follow salinity contours. 73
- 4.20 (a), (b), (c) Locations of the sampling stations as functions of time in the Mouth region during fall, spring and summer 2003-2004, respectively. The color of the circles identifies the sampling date. 74
- 4.21 Contours of the temperature with salinity isolines (white lines) in the Mouth region during different seasons in 2003-2004. (a) Fall, (b) spring and (c) summer. The black broken lines are the *MLDs*. The Sampling Sequences (STS) axis (in days) starts at zero in each panel. 75
- 4.22 (a), (b), (c) and (d) Locations of the sampling stations as functions of time in the Franklin subregion during fall, winter, spring and summer of 2003-2004, respectively. The color of the circles identifies the sampling date. 76
- 4.23 Contours of the temperature with salinity isolines (white lines) in the Franklin subregion during different seasons of 2003-2004. (a) Fall, (b) winter, (c) spring and (d) summer. The black broken lines are the *MLDs*. The Sampling Sequences (STS) axis (in days) starts at zero in each panel. 77
- 4.24 Seasonal variations of the *MLD* in the Amundsen and Mouth subregions during 2007-2008 (CFL). (a) Amundsen and (b) Mouth. The mean values and their variability are presented on the left side and the seasonal PDF on the right side. The mean values for each season (solid lines) with their 95% confidence intervals (dashed lines) are presented with the seasonal evolution (color coded) of the estimated *MLDs*. The number of intervals in each case is selected with respect to the available number of data. . . 78

4.25	(a), (b), (c) and (d) Locations of the sampling stations as a function of time in the Amundsen subregion during fall, winter, spring and summer 2007-2008, respectively. The color of circles represents the sampling dates.	79
4.26	Contours of the temperature with salinity isolines (white lines) in the Amundsen subregion during different seasons of 2007-2008. (a) Fall, (b) Winter, (c) Spring and (d) Summer. The black broken lines are the <i>MLDs</i> . The Sampling Sequences (STS) axis (in days) starts at zero in each panel.	80
4.27	(a), (b), (c) and (d) Locations of the sampling stations as functions of time in the Mouth subregion during fall, winter, spring and summer 2007-2008, respectively. The color of the circles identify the sampling dates.	81
4.28	Contours of the temperature with salinity isolines (white lines) for the Mouth subregion, during different seasons of 2007-2008. (a) Fall, (b) winter, (c) spring and (d) summer. The black broken lines are the <i>MLDs</i> . The Sampling Sequences (STS) axis starts at zero in each panel.	82
4.29	<i>MLDs</i> during fall 2002, all of 2003-2004 and 2007-2008, summer 2005, fall 2006 and summer 2009.	83
4.30	Monthly mean values of the <i>MLD</i> during 2003-2004 (green) and 2007-2008 (red). The dashed lines are the 95% confidence interval on the mean value of the <i>MLD</i> . Upward triangles in green and red are the monthly minimum <i>MLDs</i> and downward triangles in green and red are the monthly maximum <i>MLDs</i> .	84
4.31	Interannual variations of the <i>MLDs</i> in summer and fall. The diagrams on the left-hand side present color coded, <i>MLD</i> seasonal distribution. The mean values for each season (solid lines) with their 95% confidence intervals (dashed lines) are also presented. The panels on the right-hand side present the corresponding PDFs. (a) Fall, (b) Summer.	86
4.32	Interannual variations of the <i>MLD</i> in different subregions. The mean values for each season (solid lines) with their 95% confidence intervals (dashed lines) are also presented.	88
4.33	Contours of the temperature with salinity isolines (white lines) in the Amundsen subregion during different years. (a) 2002, (b) 2003, (c) 2006 and (d) 2007. The black broken lines are the <i>MLDs</i> .	89
5.1	Visual presentation of the method showing how the reference depth ($-hc$) is chosen. C_{pres} is the residual mass content in a density profile; $J_b(t1)$ and $J_b(t2)$ are the temporal variation of the buoyancy in the time interval between $t1$ and $t2$. At the bottom, the density profiles at time $t1$, ($\rho(z, t1)$) and $t2$, ($\rho(z, t2)$) are shown. Modified after Prieur et al. (2010) .	101
5.2	Locations and names of the stations where the ocean fluxes are calculated.	110

- 5.3 Contours of density at the fixed station. The white lines are the vertical positions with time of the density of the different reference depths $\sigma_{\theta hc}^{t=1}$. The black numbers are the depths of each reference at the beginning of the sampling period. The black line is the *MLD*. 111
- 5.4 Temporal variation of the cumulative buoyancy flux ($CumJ_b$) for different reference depths: $hc = -45$ m (blue), $hc = -50$ m (red), $hc = -55$ m (green), $hc = -60$ m (black) and $hc = -65$ m (brown stars). The black rectangles highlight the events discussed in the text. 112
- 5.5 Temporal variation of (a) the vertical velocity based on density $w_\rho = -\left(\frac{\partial \rho}{\partial t}\right)_{-hc} / \left(\frac{\partial \rho}{\partial z}\right)_{-hc}$ (b) the vertical velocity based on salinity $w_s = -\left(\frac{\partial S}{\partial t}\right)_{-hc} / \left(\frac{\partial S}{\partial z}\right)_{-hc}$ and (c) the vertical velocity based on temperature $w_\theta = -\left(\frac{\partial \theta}{\partial t}\right)_{-hc} / \left(\frac{\partial \theta}{\partial z}\right)_{-hc}$ at the fixed station in the Franklin Bay. The reference depth, hc , is -50 m. Note the change of scale for the temperature-based vertical velocities. These velocities vary from zero (often) to values two orders of magnitude larger than the velocities calculated from the density or the salinity fields. 114
- 5.6 Upper panel: water density at different depths (10, 15, 20 m and hc) and mean value of the density between the water surface and $hc = -50$ m. The two other panels present the salinity and temperature corresponding to the density in the first panel. 115
- 5.7 (a), (b) and (c) are the contours of density, salinity and temperature at the fixed station. The white lines are the density, salinity and temperature isolines at the reference depth ($hc = -50$ m) at the beginning of the period. The black line is the *MLD*. White ellipses are the special cases that will be discussed in the text. 116
- 5.8 The first three panels present the temporal variations of $CumJ_b$, C_ρ , C_{pres} , between the surface and $-hc$. The lower panel presents the temporal variation of the *MLD* at the fixed station in the Franklin Bay. The dashed lines show the trends of each curve. 117

- 5.9 Temporal variation of (a) the cumulative values of the different terms contributing to the density flux. The blue line shows the cumulative value of $dC_{\rho_{res}}/dt$, the red line the cumulative value of the vertical advection term $w_{\rho}(\langle\rho\rangle - \rho_{-hc})$, the green line the cumulative value of $(hc\frac{d\rho_{-hc}}{dt})$ and the black line is cumulative value of the mass flux at the surface. (b) The cumulative values of the salinity flux components. The blue line shows the cumulative value of $(dC_{S_{res}}/dt)$, the red line the cumulative value of the vertical advection $w_s(\langle S\rangle - S_{-hc})$, the green line the cumulative value of $(hc\frac{dS_{-hc}}{dt})$ and the black line the cumulative value of the salinity flux at the water surface (J_s). (c) The cumulative values of the different heat flux terms. The blue line shows the cumulative value of dH_{res}/dt , the red line cumulative value of the vertical advection term $\frac{w_{\theta}}{hc}(H_{strg} - hc\rho C_{\rho}\theta_{-hc})$, the green line the cumulative value of $(hc\rho C_{\rho}\frac{d\theta_{-hc}}{dt})$ and the black line cumulative value of the heat flux at the water surface. The dashed lines represent the tendency of each variable. 119
- 5.10 (a) Cumulative value of the heat and salinity flux contributions to the surface buoyancy flux based on the NS formulation and the LP method. The blue line is $CumJ_{bT}$, the red line $CumJ_{bS}$ and the green line $(CumJ_{bT} + CumJ_{bS})$ for the NS formulation. For the LP method, the dash-dotted blue line is $CumJ_{bT}$, the dash-dotted red line is $CumJ_{bS}$, the dash-dotted green line is $CumJ_{bT} + CumJ_{bS}$ and the dash-dotted black line is $CumJ_b$. The lower panel presents the temporal evolution of the MLD 122
- 5.11 In the upper panel, the blue line shows the in-situ total atmospheric flux calculated using sensible the heat flux in green, the latent heat flux in red, the short wave radiation in cyan, the incoming and outgoing long wave radiation in yellow and magenta, respectively. In the lower panel, the blue line is the cumulative value of dH_{res}/dt , the red line is the cumulative value of the vertical advection term $Cum(Adv_{Hhc}) = \frac{w_{\theta}}{hc}(H_{strg} - hc\rho C_{\rho}\theta_{-hc})$, the green line is the cumulative value of $(hc\rho C_{\rho}d\theta_{-hc}/dt)$ and the black line is cumulative value of the heat flux under the ice ($CumQ$) between the surface water and depth of $-hc$ (hear $hc = 50$ m). Black dashed lines represent the tendency of each variable. 124
- 5.12 Atmospheric fluxes with their tendency before and after 26 March (day 87, shown by vertical black line), blue line shows atmospheric in-situ total flux calculated using the sensible heat flux (in green), the latent heat flux (in red) and the short wave radiation (in cyan). Long wave heat ingoing and outgoing are respectively in yellow and magenta. . . . 125

- 5.13 (a) Surface air temperature. (b) Snow temperature at different depths (5, 20, 35, 50 and 60 mm). (c) Ice temperature at different depths (100, 80, 70, 60, 50, 30, 20, 15, 10, 5 and 1 cm). (d) The Mixed Layer Depth. The vertical black line identifies the position of 26 March 2004 (day 87). 127
- 5.14 Cross-correlation between the *MLD* and different terms: $Cum(dC_{pres}/dt)$ in blue, $CumJ_b$ in red, $Cum(Adv_{\rho hc})$ in green and $Cum(hc d\rho_{-hc}/dt)$ in cyan. The number of lags is 60 and the cross-correlations for the lags are shown with circles, squares, diamonds and stars for $Cum(dC_{pres}/dt)$, $CumJ_b$, $Cum(Adv_{\rho hc})$ and $Cum(hc d\rho_{-hc}/dt)$, respectively. The dashed black lines are the confidence limits. Vertical black line shows maximum cross-correlation values of cross-correlation coefficients between the *MLD* and $Cum(dC_{pres}/dt)$ and $CumJ_b$ (around 21th day). 128
- 5.15 Observed *MLDs* vs. Modeled (linear regression) *MLDs* using the cumulative value of each term. The blue circles are the *MLDs* modeled using the value of $CumJ_b$ 21 days prior to *MLDs* observation as an explanatory variable. The red circles are the modeled *MLDs* using $Cum(dC_{pres}/dt)$; the green circles are the modeled *MLDs* using $Cum(Adv_{\rho hc})$; the cyan circles are the modeled *MLDs* using $Cum(hc d\rho_{-hc}/dt)$ 131
- 5.16 Observed *MLDs* vs. Modeled (multiple linear regression) *MLDs*. Blue circles are the modeled *MLDs* using the sum of $Cum(dC_{pres}/dt)$, $Cum(Adv_{\rho hc})$ and $Cum(hc d\rho_{-hc}/dt)$; the red circles are the modeled *MLDs* using the sum of $CumJ_b$ (with a delay of minus 21 days), $Cum(dC_{pres}/dt)$, $Cum(Adv_{\rho hc})$ and $Cum(hc d\rho_{-hc}/dt)$ 132
- 5.17 Upper panel: salt mass content; middle panel: salt flux using the time variation of the salt mass content; lower panel: ice growth velocity calculated by the [Cox and Weeks \(1988\)](#) method. 134
- 5.18 Upper panel: comparison between the estimated ice thickness using the [Cox and Weeks \(1988\)](#) method and observed values from the literature. Lower panel: corresponding *MLD*. 134
- 5.19 Temporal variation of (a) the PAR, (b) the air temperature, (c) the surface water salinity, (d) the ice thickness, (e) the chlorophyll a (*Chl a*) concentration and (f) the *MLD* at the CASES fixed station. 136
- 5.20 Temporal variation of the (a) chlorophyll a (*Chl a*) concentrations, (b) ice thickness and (c) *MLD* at the CFL stations listed in Table 5.1. . . . 137
- 5.21 Upper panel: wind speed ($m s^{-1}$) and direction in southern Amundsen Gulf; north is upwards. The wind data are from the NARR reanalysis. Bottom panel: density contours at the CASES fixed station. 138

5.22	Temporal variation of (a) the cumulative value of $Cum(dC_{pres}/dt)$, $Cum(hc d\rho_{-hc}/dt)$, $Cum(Adv_{\rho_{hc}})$ and $CumJ_m$. (b) Temporal variation of $CumJ_b$ and (c) of the MLD at the drift station 2008-19D during CFL. The dashed line in each panel is the linear tendency of each curve.	139
5.23	(a), (b) and (c) are the contours of density, salinity and temperature, respectively, at the drift station 2008-19D during CFL. The white lines are the density, salinity and temperature of the reference depth ($hc = -57$ m) and the black line in each panel is the MLD for the same period.	140
5.24	Cross-correlation at drift station 2008-19D between the MLD and $Cum(dC_{pres}/dt)$ in blue, $CumJ_b$ in red, $Cum(Adv_{\rho_{hc}})$ in green and $Cum(hc d\rho_{-hc}/dt)$ in cyan. The number of lags is 15 and the cross-correlations for the lags are shown with circles, squares, diamonds and stars respectively for $Cum(dC_{pres}/dt)$, $CumJ_b$, $Cum(Adv_{\rho_{hc}})$ and $Cum(hc d\rho_{-hc}/dt)$. The dashed black lines are the confidence limits.	140
A.1	Temporal variation of $CumJ_b$, $Cum(dC_{pres}/dt)$, $Cum(Adv_{\rho_{hc}})$ and $Cum(hc d\rho_{hc}/dt)$ and the MLD at stations 5D, 7D, 12D, 14D, 17D and 26D during CFL (2007-2008). The dashed line in each subplot shows the linear tendency of each curve.	157
A.2	Temporal variation of $CumJ_b$, $Cum(dC_{pres}/dt)$, $Cum(Adv_{\rho_{hc}})$ and $Cum(hc d\rho_{hc}/dt)$ and the MLD at stations 27D, 29D, 33D, 41D, 43D and F2 during CFL (2007-2008). The dashed line in each subplot shows the linear tendency of each curve.	158
A.3	Temporal variation of $CumJ_b$, $Cum(dC_{pres}/dt)$, $Cum(Adv_{\rho_{hc}})$ and $Cum(hc d\rho_{hc}/dt)$ and the MLD at stations F3, F7 and 235 during CFL (2007-2008) and Malina (2009). The dashed line in each subplot shows the linear tendency of each curve.	159
B.1	Contours of density, salinity and temperature at stations 5D, 7D, 12D, 14D, 17D and 26D. The white lines are the density, salinity and temperature isolines at the reference depth. The black lines are the MLD . . .	161
B.2	Contours of density, salinity and temperature at stations 27D, 29D, 33D, 41D, 43D and F2. The white lines are the density, salinity and temperature isolines at the reference depth. The black lines are the MLD . . .	162
B.3	Contours of density, salinity and temperature at stations F3, F7 and 235. The white lines are the density, salinity and temperature isolines at the reference depth. The black lines are the MLD	163

- C.1 Cross-correlation, at stations 5D, 7D, 12D, 14D, 17D and 26D, between MLD and $Cum(dC_{pres}/dt)$ in blue, $CumJ_b$ in red, $Cum(Adv_{\rho_{hc}})$ in green and $Cum(hcd\rho_{hc}/dt)$ in cyan. The cross correlations for the lags are shown with circles, squares, diamonds and stars respectively for $Cum(dC_{pres}/dt)$, $CumJ_b$, $Cum(Adv_{\rho_{hc}})$ and $Cum(hcd\rho_{hc}/dt)$. The dashed black lines are confidence limit. 165
- C.2 Cross-correlation, at stations 27D, 29D, 33D, 41D, 43D and F2, between MLD and $Cum(dC_{pres}/dt)$ in blue, $CumJ_b$ in red, $Cum(Adv_{\rho_{hc}})$ in green and $Cum(hcd\rho_{hc}/dt)$ in cyan. The cross correlations for the lags are shown with circles, squares, diamonds and stars respectively for $Cum(dC_{pres}/dt)$, $CumJ_b$, $Cum(Adv_{\rho_{hc}})$ and $Cum(hcd\rho_{hc}/dt)$. The dashed black lines are confidence limit. 166
- C.3 Cross-correlation, at stations F3, F7 and 235, between MLD and $Cum(dC_{pres}/dt)$ in blue, $CumJ_b$ in red, $Cum(Adv_{\rho_{hc}})$ in green and $Cum(hcd\rho_{hc}/dt)$ in cyan. The cross correlations for the lags are shown with circles, squares, diamonds and stars respectively for $Cum(dC_{pres}/dt)$, $CumJ_b$, $Cum(Adv_{\rho_{hc}})$ and $Cum(hcd\rho_{hc}/dt)$. The dashed black lines are confidence limit. 167

LIST OF TABLES

3.1	Statistical fit indicators between the <i>MLDs</i> obtained by visual inspection and by the TH, TF, TFL and HTN methods. The threshold used in the TH is 0.05 kg m^{-3} , and the error norm in the TFL is 0.05. The yellow boxes indicate the best statistical while the green boxes highlight the second best fits.	40
4.1	Tabulated values of t as a function of N , the number of observations (Coleman and Steele, 1999).	52
4.2	The number of individual MLD estimates available for different years for each subregion. Y, BM, In, Off stand for Year, Bathymetry, Inshore and Offshore, respectively. W, Sp, Su and F stand for Winter, Spring, Summer and Fall.	54
4.3	Student t -test comparisons between inshore and offshore <i>MLDs</i> during CASES (2003-2004). N_1 and N_2 are the number of inshore and offshore observations. T- t and C- t are the tabulated t and calculated t values using equation 4.7. The results of the t -test are either Significant (Sig.) or Non-Significant (No Sig.). Mean inshore and Mean offshore are the confidence intervals on the monthly mean.	56
4.4	Student t -test comparisons between inshore and offshore <i>MLDs</i> during CFL (2007-2008). N_1 and N_2 are the number of inshore and offshore observations. T- t and C- t are the tabulated t and calculated t values using equation 4.7. The results of the t -test are either Significant (Sig.) or Non-Significant (No Sig.). Mean inshore and Mean offshore are the confidence intervals on the monthly mean.	58
4.5	Student t -test comparisons between inshore and offshore <i>MLDs</i> during fall 2002 (CASES), late summer 2005 (ArcticNet), fall 2006 (ArcticNet) and summer 2009 (Malina). N_1 and N_2 are the number of inshore and offshore observations. T- t and C- t are the tabulated t and calculated t values using equation 4.7. The results of the t -test are either Significant (Sig.) or Non-Significant (No Sig.). Mean inshore and Mean offshore are the confidence intervals on the monthly mean <i>MLD</i>	60

4.6	Student t -test comparisons between inshore and offshore MLD s in the different sub-regions. N is the number of realizations. $T-t$ and $C-t$ are the tabulated t and calculated t values using equation 4.7. The results of the t -test are either Significant (Sig.) or Non-Significant (No Sig.).	63
4.7	Comparison between offshore MLD s from different years and seasons. See Figure 4.2 for the definition of the regions.	66
4.8	Student t -tests comparisons between monthly averaged MLD s during 2003-2004 (CASES) and 2007-2008 (CFL). N_1 and N_2 are the number of monthly CTDs during CASES and CFL, respectively. $T-t$ and $C-t$ are the tabulated t and calculated t values. The results of the t -test are either Significant (Sig.) or Non-Significant (No Sig.). Mean CASES and Mean CFL are the 95% confidence intervals on the monthly mean value of the MLD	85
5.1	Characteristics of the stations where the ocean fluxes are calculated. Ship's drift is the distance covered by the ship during a sampling period.	109
5.2	The trend of the MLD and of the different terms in equation 5.22, $CumJ_b$, $Cum(dC_{pres}/dt)$, $Cum(Adv_{\rho_{hc}})$ and $Cum(hcd\rho_{hc}/dt)$, at each station. D, A and NS are used to qualify the trends and mean "Descending", "Ascending" and "Not Significant", respectively. A "Not Significant" trend means that the variation of the parameter during the sampling period is less than 5%.	120
5.3	Cross correlation between the MLD and the terms in equation 5.22, $CumJ_b$, $Cum(dC_{pres}/dt)$, $Cum(Adv_{\rho_{hc}})$ and $Cum(hcd\rho_{hc}/dt)$, at each station. The blue and red boxes indicate respectively that the parameter is positively (negatively) correlated with the MLD with delay (D+ and D-). The green and yellow boxes highlight respectively that the parameter is positively (negatively) correlated with the MLD simultaneously (S+ and S-). NS means that correlation is not significant.	129

LIST OF SYMBOLS

Abbreviation

AL	Atlantic Layer
AO	Arctic Oscillation
ATH	Arctic Thermocline
BSSW	Bering Sea Summer Water
BSWW	Bering Sea Winter Water
CAA	Canadian Arctic Archipelago
CASES	Canadian Arctic Shelf Exchange Study
CBDW	Canada Basin Deep Water
CCGS	Canadian Coast Guard Ship
CDF	Cumulative Distribution Function
CFL	Circumpolar Flaw Lead Study
CTD	Conductivity, Temperature, Depth
Cum	Cumulative value
DA	Dipole Anomaly
ECSW	Eastern Chukchi Summer Water
ENSO	El Niño-Southern Oscillation
FWC	Freshwater Content
GD	Gradient density method
GOTM	General Ocean Turbulence Model
HA	Hour Angle

HC	Heat Content
HT	Holte-Taley method
HTN	Holte-Taley method modified by the author (Nahavandian)
In	Inshore
LE	Latent heat
LP	Prieur et al. (2010)
LW	Longwave radiation
MAE	Mean Absolute Error
MD	Deepest minimum density method
ML	Mixed Layer
MLD	Mixed Layer Depth
MLDC	Calculated <i>MLD</i>
MLDV	<i>MLD</i> obtained from visual inspection
NaN	Not a Number
NAO	North Atlantic Oscillation
NARR	North American Regional Reanalysis
NSIDC	National Snow and Ice Data Center
Off	Offshore
PAR	Photosynthetically Active Radiation
PDF	Probability Density Function
PDIFF	Peak differences
PDO	Pacific Decadal Oscillation
PML	Polar Mixed Layer
POMME	Programme Océan Multidisciplinaire Méso Echelle
Prob	Probability

PYCN	Pycnocline fit method
RAE	Relative Absolute Error
RES	Residual
RMSE	Root Mean Square Error
RSqr	Pearson product moment correlation coefficient
SHEBA	Surface Heat Budget of the Arctic Ocean
SMC	Salt mass content
SST	Sea Surface Temperature
STS	Sampling Time Sequence
SW	Shortwave radiation
TDS	Trans-polar Drift Stream
TF	Thomson-Fine method
TFL	Modified version of TF method
TH	Threshold method
Tr	Transect
VI	Visual Inspection method
WCSW	Western Chukchi Summer Water

Greek letters

α	Thermal expansion coefficient of water
β	Salinity contraction coefficient
δ	Solar declination
ρ	Density
ρ_s	Reference density
σ	Standard deviation
σ	Stefan-Boltzmann constant

σ_t	Density based on T
σ_θ	Potential density based on potential temperature
θ	Potential temperature
φ	Latitude

Roman letters

A	Surface Area
c	Cloud cover fraction
C_E	Transfer coefficient for latent heat
C_H	Transfer coefficient for sensible heat
c_p	Specific heat of water
C_s	Salt content
C_ρ	Mass content
C_θ	Temperature content
C_{xy}	Cross-covariance
D	Depth of mixed layer
da	Element of surface A
E	Evaporation rate
e	Vapor pressure
F_{salt}	Salt flux
g	Standard gravity
H	Sensible heat
h	Ice thickness
H_{strg}	Upper ocean heat storage
hc	Reference depth
J_b	Buoyancy flux

J_m	Mass flux
J_s	Salt flux imposed by the atmosphere
k_{eff}	Effective distribution coefficient
L_v	Latent heat of vaporization
N	Buoyancy frequency
P	Pressure
P_r	Precipitation rate
Q	Heat
Q_0	Incoming radiation for cloudless skies
q_s	Surface specific humidity
q_{10m}	10 meter specific humidity
R	Density dependency indicator, equation 3.1
R_{xy}	Cross-correlation function
S	Salinity
S_c	Solar constant
T	Temperature
t	time
T_a	Air temperature
T_d	Dew point temperature
T_{sfc}	Sea surface temperature
u	Eastward velocity
V	Growth rate of ice thickness
v	Northward velocity
V_{wg}	Geostrophic wind speed
w	Upward velocity

x	Eastward coordinate
y	Northward coordinate
Z	Zenith angle
z	Upward coordinate

Special symbols

$\langle \rangle$	Ensemble average
$\nabla \bullet$	Divergence
\vec{n}	Normal unit directed outward
\vec{V}	Velocity vector
x'	Fluctuating part of x

LISTE DES FIGURES CITÉES DANS LA SYNTHÈSE EN FRANÇAIS

Les numéros des figures sont ceux du texte anglais: les figures ne sont pas reproduites dans la synthèse en français.

2.1	Archipel arctique canadien et Groenland	10
2.2	Circulation des eaux Pacifiques (lignes bleues) et Atlantiques (lignes rouges) de l'océan Arctique. Modifié d'après McLaughlin et al. (1996)	11
2.3	Diagramme T-S présentant la structure verticale de la colonne d'eau dans le Sud de la mer de Beaufort: <i>the Polar Mixed layer</i> (PML), <i>the Bering Sea Summer Water</i> (BSSW), <i>the Bering Sea Winter Water</i> (BSWW), <i>the Arctic Thermocline</i> (ATH), <i>the Atlantic Layer</i> (AL) et <i>the Canada Deep Basin Water</i> (CBDW). Modifié d'après (Gratton et al., 2012). La ligne noire est le diagramme de température-salinité échantillonné au cours de l' <i>Arctic Internal Wave Experiment</i> . Les cercles colorés sont de ArcticNet-Geotraces cast 0903034.	12
2.4	Carte de la région d'étude montrant les différentes positions citées dans le texte.	13
2.5	Circulation de l'eau sur le plateau du Mackenzie: La surface anti-cyclonique de Gyre de Beaufort (lignes noires pleines), le courant cyclonique profond du <i>Beaufort Undercurrent</i> (flèches bleues), le courant cyclonique de surface côtière (ligne en pointillés) et le fleuve Mackenzie (blanc).	15
2.7	Rosette et CTD à bord du NGCC Amundsen.	20
3.8	Comparaison entre les méthodes: chaque + représente une <i>MLD</i> estimée. Panneaux (a), (b) et (c) comparent les méthodes TF, TFL et HTN avec la méthode TH (0.05 kg m^{-3}). Panneau (d) compare la TFL et TF; panneau (e) compare la HTN et TF et le panneau (f) compare la HTN et TFL. Une limite supérieure d'erreur de 0.05 est utilisé pour les méthodes TF et TFL.	37

3.10	Séries chronologiques de densité à 5 m (lignes bleues), à la <i>MLD</i> (lignes rouges), à la <i>MLD</i> +3 m (lignes vertes) et la <i>MLD</i> +10 m (lignes noires) à l'automne 2003, lors de leg 0304. Les <i>MLDs</i> sont calculées en utilisant la méthode TH (seuil de 0.05 kg m^{-3}) (panneau a), la méthode de TF (panneau b), la méthode TFL (panneau c) et la méthode de HTN (panneau d).	42
4.2	Quatre sous-régions considérées dans cette étude: Beaufort, Mouth, Amundsen et Franklin.	50
4.6	Les valeurs moyennes mensuelles de <i>MLDs</i> de <i>Inshore</i> (bleu) et <i>Offshore</i> (rouge) indépendamment de la sous-région pendant CASES (2003-2004). Les traits en pointillés représentent les intervalles de confiance à 95%.	57
4.7	Les fonctions de densité de probabilité (PDF) de la <i>MLD</i> de <i>Inshore</i> et <i>Offshore</i> pendant CASES (2003-2004) en (a), octobre (b) novembre, (c) juin et (d) juillet.	57
4.14	Les fonctions de densité de probabilité (PDF) de la <i>MLD</i> de <i>Offshore</i> dans les différentes sous-régions en (a) automne 2003, (b) printemps 2004, (c) automne 2007, (d) printemps 2008, (e) été 2008 et (f) été 2009.	65
4.15	(a), (b) La distribution temporelle des stations le long des transects Tr3 et TrAM au cours de l'automne 2002 (leg 0202). (c) Les contours de température avec isolignes de salinité (lignes blanches) et la <i>MLD</i> (lignes noires) le long Tr3 (du sud au nord) et le long de TrAM (d'est en ouest). Les distance sont calculées à partir de la côte.	68
4.16	(a), (b), (c) and (d) La distribution temporelle des stations le long des transects Tr1, Tr2, Tr3 and TrAM au cours de l'automne 2003 (leg 0304). (e) Les contours de température avec isolignes de salinité (lignes blanches) et la <i>MLD</i> (lignes noires) le long Tr1 (du sud au nord), Tr2 (du sud au nord), Tr3 (du sud au nord) and TrAM (d'est en ouest). L'échantillonnage se fait au cours du leg 0304 à l'automne 2003.	69
4.17	Les variations saisonnières de la <i>MLD</i> dans différentes sous-régions au cours de 2003-2004 (CASES); (a) Amundsen, (b) Mouth et (c) Franklin. Les valeurs moyennes et leur variabilité sont présentés sur le côté gauche et les PDFs sur le côté droit. Les valeurs moyennes pour chaque saison (lignes continues) avec leurs intervalles de confiance à 95% (lignes pointillées) sont présentées selon leur évolution dans le temps (code couleur) de la <i>MLDs</i> estimées. Le nombre d'intervalles dans chaque panneau de PDF est choisi en fonction des observations disponibles. Par exemple, dans Franklin pendant l'été on a le plus petit nombre d'intervalles, car le nombre d'échantillons est faible (13).	71

4.23	Contours de la température avec isolignes de salinité (lignes blanches) dans la sous-région Franklin pendant les différentes saisons de 2003 à 2004. (a) automne, (b) hiver, (c) printemps (d) été. Les lignes noires sont les <i>MLDs</i> . L'axe de séquences d'échantillonnage (STS) commence à zéro dans chaque panneau.	77
4.30	Les valeurs moyennes mensuelles de la <i>MLD</i> en 2003-2004 (vert) et 2007-2008 (rouge). Les lignes pointillées sont l'intervalle de confiance à 95%. Triangles vers haut en vert et rouge sont les minimums mensuels de la <i>MLD</i> et les triangles vers bas en vert et rouge sont les maximums mensuels de la <i>MLD</i>	84
4.31	Les variations interannuelles de la <i>MLD</i> en été et à l'automne. Les diagrammes sur le côté gauche présentent la distribution saisonnière de la <i>MLD</i> . Les valeurs moyennes pour chaque saison (lignes pleines) avec leurs intervalles de confiance à 95% (lignes pointillées) sont également présentés. Les panneaux sur le côté droit présentent les PDFs correspondantes. (a) automne, (b) été.	86
5.6	Panneau du haut: la densité de l'eau à différentes profondeurs (10, 15, 20 m et <i>hc</i>) et la valeur moyenne de la densité entre la surface et $hc = -50$ m. Les deux autres panneaux présentent la salinité et la température correspondant à la densité du premier panneau.	115
5.8	Les trois premiers panneaux présentent les variations temporelles de $CumJ_b$, C_ρ , C_{pres} , entre la surface et $-hc$. Le panneau du bas présente la variation temporelle de la <i>MLD</i> à la station fixe dans la baie Franklin. Les lignes pointillées indiquent les tendances de chaque courbe.	117
5.13	(a) La température de l'air en surface. (b) La température de la neige à des profondeurs différentes (5, 20, 35, 50 et 60 mm). (c) La température de la glace à des profondeurs différentes (100, 80, 70, 60, 50, 30, 20, 15, 10, 5 et 1 cm). (d) La profondeur de la couche mélangée. La ligne noire verticale identifie la position du 26 mars 2004 (jour 87).	127
5.14	Corrélation croisée entre la <i>MLD</i> et différents termes: $Cum(dC_{pres}/dt)$ en bleu, $CumJ_b$ en rouge, $Cum(Adv_{\rho_{hc}})$ en vert et $Cum(hc d\rho_{-hc}/dt)$ en cyan. Le nombre de retards est de 60 et les corrélations croisées pour chaque retard sont présentés avec le cercle, carré, diamant et étoile pour $Cum(dC_{pres}/dt)$, $CumJ_b$, $Cum(Adv_{\rho_{hc}})$ et $Cum(hc d\rho_{-hc}/dt)$, respectivement. Les lignes noires pointillées sont les limites de confiance.	128
5.18	Panneau supérieur: comparaison entre l'épaisseur de la glace estimée en utilisant la méthode de Cox and Weeks (1988) et les valeurs observées. Panneau inférieur: correspondant la <i>MLD</i>	135

- 5.19 La variation temporelle de (a) la PAR, (b) la température de l'air, (c) la salinité de l'eau de surface, (d) l'épaisseur de la glace, (e) la concentration de chlorophylle (*Chl a*) et (f) la *MLD* à la station fixe de CASES. . . . 136

LISTE DES TABLEAUX CITÉS DANS LA SYNTHÈSE EN FRANÇAIS

Les numéros des tableaux sont ceux du texte anglais: les tableaux ne sont pas reproduits dans la synthèse en français.

3.1	Indicateurs d'ajustement statistique entre les <i>MLDs</i> obtenus par l'inspection visuelle et par les méthodes TH, TF, TFL et HTN. Le seuil utilisé dans le TH est de 0.05 kg m^{-3} , et la norme d'erreur dans le TFL est de 0.05. Les cases en jaunes indiquent les meilleurs ajustements statistiques. Les boîtes vertes mettent en évidence les indicateurs lorsque la méthode de HTN termine en seconde place.	41
4.2	Estimations disponibles de la <i>MLD</i> au cours des différentes années dans chaque sous-région. Y, BM, In, Off représentent l'année, la bathymétrie, <i>Inshore</i> et <i>Offshore</i> , respectivement. W, Sp, Su et F représentent hiver, printemps, été et automne.	53
4.3	<i>t</i> -test de Student entre les <i>MLDs</i> de <i>Inshore</i> et <i>offshore</i> pendant CASES (2003-2004). N_1 et N_2 sont le nombre d'observations de <i>Inshore</i> et <i>offshore</i> . $T-t$ et $C-t$ sont les valeurs tabulées et calculées de <i>t</i> en utilisant l'équation 4.7. Les résultats de la <i>t</i> -test sont soit significatifs (Sig.) ou non significatifs (No Sig.). <i>Mean Inshore</i> et <i>offshore</i> sont les intervalles de confiance autour de la moyenne mensuelle.	56
4.7	Comparaison entre la <i>MLD</i> de <i>Offshore</i> entre différentes années et différentes saisons. Voir la figure 4.2 pour la définition des régions.	65
4.8	<i>t</i> -test de Student entre les valeurs moyennes mensuelles de <i>MLDs</i> pendant CASES (2003-2004) et CFL (2007-2008). N_1 et N_2 sont le nombre de CTDs mensuelles au cours de CASES et CFL, respectivement. $T-t$ et $C-t$ sont les valeurs tabulées et calculées de <i>t</i> en utilisant l'équation 4.7. Les résultats de la <i>t</i> -test sont soit significatifs (Sig.) ou non significatifs (No Sig.). <i>Means</i> sont les intervalles de confiance autour de la moyenne mensuelle.	84
5.1	Caractéristiques des stations où les flux océaniques sont calculés. <i>Ship's drift</i> est la distance parcourue par le navire pendant une période d'échantillonnage.	108

- 5.2 La tendance de la MLD et des différents termes de l'équation 5.22, $CumJ_b$, $Cum(dC_{pres}/dt)$, $Cum(Adv_{\rho_{hc}})$ et $Cum(hcd\rho_{hc}/dt)$, à chaque station. D, A et NS sont utilisés pour qualifier les tendances et signifient "Descending", "Ascending" et "Not Significant", respectivement. La tendance "Not Significant" signifie que la variation du paramètre au cours de la période d'échantillonnage est inférieure à 5%. 120

CHAPTER 0

SYNTHÈSE EN FRANÇAIS

0.1 Introduction

0.1.1 Motivation

L'océan Arctique joue un rôle important dans le climat mondial: c'est la région où le réchauffement climatique est le plus prononcé. Les observations confirment que l'océan Arctique et ses mers secondaires se réchauffent déjà et que la superficie de la couche chaude de fond de l'Atlantique a augmenté ([Serreze et al., 2000](#)). Les effets de l'Arctique sur le climat mondial impliquent les échanges atmosphère-glace-océan et leurs effets sur la circulation thermohaline globale ([Aagaard and Carmack, 1994](#)). La distribution de la glace de mer (tant en superficie qu'en épaisseur) a diminué au cours des dernières décennies: le minimum absolu de la banquise de l'Arctique a été observé en août 2012 (NSIDC, 19 Septembre 2012), après les précédents minima de 2005 et 2007 ([Wang et al., 2009](#)). Ceci est particulièrement apparent dans l'archipel arctique canadien et dans la partie sud de la mer de Beaufort ([Barber and Hanesiak, 2004](#)). L'étendue de la couverture de glace a diminué au taux d'environ 11% par décennie entre 1979 et 2007 ([Polyakov et al., 2012](#)) et la moyenne minimale d'étendue de la glace en 2007-2008 a montré une diminution d'environ 37% par rapport à la climatologie des glaces de la période 1980-1999 ([Wang and Overland, 2009](#)). Selon [Comiso \(2006\)](#), cette tendance se poursuivra à l'avenir avec une augmentation de température de l'eau et du taux de fonte de la glace pérenne. Différents facteurs tels que la température, le vent, les vagues, les courants et le forçage atmosphérique influencent le couvert de glace de l'Arctique ([Comiso et al., 2008](#)) et, à son tour, les caractéristiques de l'eau de la couche de surface de l'océan polaire. La perte de la glace arctique conduit à une plus grande exposition de l'océan au rayonnement solaire et aux vents qui affectent directement la surface de l'océan. La couche mélangée qui est le principal objet de cette thèse est la couche d'interface océanique entre l'atmosphère et l'océan profond.

La couche mélangée est une couche de surface océanique dans laquelle la salinité, la densité ou la température sont quasi uniformes en raison de forts mélanges initiés par l'échange air-mer tels que le flux de chaleur et la force du vent. L'épaisseur de la couche mélangée (ci-après *MLD*) joue un rôle très important dans le changement climatique, car elle agit comme une interface entre l'atmosphère et l'océan profond. La profondeur de la couche mélangée a un rôle important dans le transfert de la chaleur, de la masse et de quantité de mouvement entre l'atmosphère et l'océan (Schneider and Müller, 1990). La productivité biologique est souvent contrôlée par la *MLD* et l'intensité du mélange turbulent au sein de la couche mélangée. Elle contrôle également l'entraînement des éléments nutritifs provenant des couches plus profondes (Liu, 2009).

0.1.2 Objectifs

L'objectif de cette thèse est d'améliorer notre compréhension de la couche mélangée dans le sud de la mer de Beaufort et le golfe d'Amundsen. Le sud de la mer de Beaufort, et en particulier le golfe d'Amundsen, ont été moins étudiés en raison de la rareté des données. Grâce aux récents programmes CASES (Canadian Arctic Shelf Exchange Study: 2001-2006), CFL (Circumpolar Flaw Lead Study: 2006-2011), ArcticNet (2004-2018) et Malina (2009-2013), nous possédons désormais un vaste ensemble de données uniques et précieuses pour nous aider à mieux comprendre les différents processus physiques dans l'Arctique, en particulier dans le golfe d'Amundsen. Pour atteindre cet objectif, je vais me concentrer sur l'évolution temporelle et la distribution spatiale de la profondeur de la couche mélangée dans ces régions. L'objectif général sera atteint à travers quatre objectifs spécifiques.

- Évaluer les différentes méthodes d'estimation de la *MLD* et sélectionner la plus appropriée pour cette région d'étude;
- Étudier la distribution spatiale de la *MLD* en divisant la région d'étude en sous-régions;
- Analyser l'évolution temporelle de la *MLD*, c'est à dire l'évolution mensuelle, saisonnière et interannuelle;
- Enquêter sur les relations entre les flux atmosphériques et océaniques et l'évolution de la *MLD* ainsi que l'épaisseur de la glace.

0.2 Région d'étude et données disponibles

0.2.1 L'Arctique Canadien

L'océan Arctique est un océan presque fermé avec une superficie de plus 14 000 000 km². Il est bordé par l'océan Pacifique et le détroit de Béring, par l'océan Atlantique et le détroit de Fram et la mer de Barents et par l'archipel canadien. L'archipel arctique canadien couvre une grande partie du plateau continental polaire de l'Amérique du Nord. Il est bordé à l'ouest par la mer de Beaufort, à l'est par la baie de Baffin, le Groenland et le détroit de Davis, au sud par la baie d'Hudson et la partie continentale du Canada et au nord par l'océan Arctique (voir la figure 2.1). Comme le montre la figure 2.1, l'archipel canadien comprend de grandes et de petites îles. L'eau est fournie à l'océan Arctique à partir de trois sources différentes: l'océan Atlantique, l'océan Pacifique et les rivières (Jones et al., 1998). La circulation de l'eau Atlantique est complexe et il y a une trace importante de son flux dans tous les bassins de l'Arctique (Nansen, Amundsen, Makarov et les bassins canadiens) (McLaughlin et al., 1996). La majorité de l'eau Atlantique entre par le détroit de Fram et rencontre les eaux de surface de l'Arctique moins denses. Ensuite, les eaux coulent jusqu'à la couche intermédiaire de l'océan Arctique, appelée couche Atlantique, et produisent une épaisse couche située à une profondeur d'environ 300 à 500 m. De l'autre côté, les eaux Pacifique pénètrent dans l'océan Arctique par le détroit de Béring. Les eaux du Pacifique sont plus présentes dans le bassin canadien tel qu'illustré à la figure 2.2 (Aagaard, 1981, McLaughlin et al., 1996, Jones et al., 1998). Selon McLaughlin et al. (1996), les intrusions d'eau du Pacifique dans l'ouest du bassin canadien affectent le mélange dans cette région de l'archipel et modifient la stabilité de la colonne d'eau.

La colonne d'eau dans le sud-est de la mer de Beaufort peut être divisée en quatre couches distinctes. La figure 2.3 présente un diagramme température et salinité (diagramme TS) échantillonné au cours de l'Arctic Internal Wave Experiment (Levine et al. (1986); la ligne noire) et montre les différentes masses d'eau dans la mer de Beaufort. Elle présente également la structure de la densité au large des côtes de la rivière Mackenzie (cercles de couleur), dans la région d'étude. La première couche est la couche mélangée polaire (PML) avec une épaisseur typique de moins de 50 m, d'une salinité inférieure à 31 et des températures variables (voir la figure 2.3). Dans l'Arctique, les eaux de ruissellement continental et la fonte des glaces diminuent la salinité dans la couche de surface. Une salinité inférieure en surface conduit à une augmentation de la stratification et inhibe le mélange avec les couches inférieures, tandis que le rejet du sel en raison du gel en hiver augmente la convection verticale et génère davantage de mélange (Aagaard et al., 1981). La deuxième couche est une couche halocline froide qui se situe

entre 50 et 250 m, avec $T < 1^\circ\text{C}$ et $31 < S < 34.4$ (Carmack et al., 1989, McLaughlin et al., 2004). L'halocline est aussi un indicateur de la pycnocline, puisque la densité dans cette région est déterminée en majorité par la salinité. L'importance de cette halocline froide est qu'elle isole l'eau de surface couverte par la glace de l'eau plus chaude du fond et empêche l'échange de chaleur entre ces couches, empêchant ainsi la fonte des glaces (Aagaard et al., 1981, Rudels et al., 1996). L'halocline est principalement formée par les eaux du Pacifique et peut être subdivisée en trois sous-couches comme le montre la figure 2.3. La partie supérieure de l'halocline arctique se compose des eaux estivales du Pacifique qui forment un maximum local de température située entre 50 à 100 m, et correspondant à $31 < S < 32$. Cette couche est la Bering Sea Summer Water (BSSW, voir figure 2.3) et est caractérisée par une augmentation de concentration en oxygène dissous et une diminution de concentration en nutriment (Jones et al., 1998). La couche halocline intermédiaire est située à des profondeurs comprises entre 100 et 200 m avec une température minimale entre -1.5 et -1.25°C et une salinité d'environ 33.1 (voir la figure 2.5). La concentration en oxygène dissous diminue dans cette couche bien qu'elle soit riche en nutriments, car les eaux proviennent des mers de Béring et de Chukchi en hiver lorsque la production biologique y est très faible. En dessous de la BSSW, la couche Thermocline Arctique (ATh) forme la partie inférieure de la couche halocline. La température augmente fortement dans cette couche, qui est une transition vers la couche Atlantique (AL). La troisième couche est la couche Atlantique (AL illustrée à la figure 2.3) qui se trouve à des profondeurs supérieures à 250 m, avec $T > 0^\circ\text{C}$ et $S > 34$ (Rudels et al., 1994, Carmack and Kulikov, 1998). La température s'inverse dans cette couche, ce qui entraîne une diminution de la température avec la profondeur (Carmack and Kulikov, 1998). Enfin, la quatrième et dernière couche au fond de la mer de Beaufort est la Canada Basin Deep Water (CBDW). Cette couche est relativement homogène avec des températures négatives et une salinité $S \approx 34.9$ (Carmack and Kulikov, 1998).

0.2.2 La mer de Beaufort et le golfe Amundsen

La mer de Beaufort est bordée par une ligne entre Pointe Barrow en Alaska et à l'ouest les îles de la reine Elizabeth dans l'ouest de l'archipel canadien (voir la figure 2.1 et la figure 2.2). Sa superficie est d'environ 450 000 km². La mer de Beaufort est influencée au sud par le fleuve Mackenzie, la quatrième plus grande rivière se déchargeant dans l'océan Arctique (Yunker and Macdonald, 1995) et la plus grande dans l'Arctique de l'Ouest. Dans la mer de Beaufort, au large du plateau du Mackenzie, le mouvement de la glace et de l'eau de surface sont régis par la gyre anti-cyclonique de Beaufort qui a pour effet d'accumuler d'importantes quantités d'eau douce dans la couche de surface du bassin canadien (Newton et al., 2006). Sous la surface, le mouvement de l'eau est inversée

(cyclonique) et est connu sous le nom de Beaufort Undercurrent. La gyre de Beaufort et le Beaufort Undercurrent sont présentés à la figure 2.5. La circulation dans notre région d'étude est assez complexe et semble fortement influencée par des paramètres externes, tels que la circulation atmosphérique et l'écoulement des rivières (Newton et al., 2006). Les échanges entre les eaux profondes et superficielles se déroulent sous l'influence de l'atmosphère qui produisent des événements de remontée d'eau appelés upwelling ou de descente des eaux appelées downwelling. Les vents d'ouest le long de la côte poussent l'eau de surface vers le bas (downwelling) et transporte l'eau douce vers le golfe Amundsen. Les vents d'est le long des côtes du sud de la mer de Beaufort et poussent les eaux de surface loin du plateau du Mackenzie et attirent ainsi les eaux plus profondes à la surface (upwelling) (Williams and Carmack, 2008).

Le golfe d'Amundsen est situé au sud-est de la mer de Beaufort (figure 2.4). Les limites du golfe d'Amundsen sont l'île Banks au nord, l'île Victoria à l'est et les côtes des Territoires du Nord-Ouest au sud (voir les figures 2.1 et 2.4). Le golfe d'Amundsen est l'une des deux extrémités occidentales navigables du passage du Nord-Ouest, qui pourrait avoir une importance croissante en tant que voie de navigation dans l'avenir en raison des changements climatiques (Peterson et al., 2008).

0.2.3 Les données disponibles

Les données utilisées dans cette étude proviennent de quatre projets de recherche de grande envergure entre 2002 et 2009. Ces projets sont le Canadian Arctic Shelf Exchange Study (CASES, 2002-2006), ArcticNet (2004-2018), Circumpolar Flaw Lead System study (CFL, de 2006 à 2011) et Malina (2008-2013). L'instrument d'échantillonnage très utilisé en océanographie est le Conductivity Temperature Depth ou CTD. La rosette-CTD (voir la figure 2.7) comprend un capteur CTD SeaBird-9Plus fixé à la base d'un cadre circulaire qui accueille 24 bouteilles Niskin. L'appareil mesure simultanément la température (T), la conductivité (C) et la pression hydrostatique (p).

CASES La première expédition a été réalisée à bord du navire de la Garde Côtière Canadienne NGCC Pierre Radisson entre septembre et octobre 2002 (138 profils de CTD). La deuxième partie du programme a été réalisée entre septembre 2003 et août 2004 à bord du NGCC Amundsen (836 profils de CTD). Au cours de cette expédition, le navire est demeuré en station fixe (70°02.71 N et 126°18.06 W) dans la baie de Franklin du 9 décembre 2003 au 30 mai 2004. C'était la première fois qu'un brise-glace de recherche hivernait dans le golfe d'Amundsen.

ArcticNet Les données du golfe d’Amundsen et de la mer de Beaufort ont été échantillonnées en 2005 (leg 0501), entre le 1er et le 14 septembre 2005 (63 profils de CTD), en 2006 (leg 0603) entre le 30 septembre et le 19 octobre (73 profils de CTD).

CFL L’échantillonnage au cours du programme Circumpolar Flaw Lead System (CFL) dans la mer de Beaufort et le golfe d’Amundsen a été mené entre septembre 2007 et août 2008 (1023 profils de CTD). C’était la première fois qu’un brise-glace de recherche restait mobile pendant l’hiver dans le chenal de séparation circumpolaire (Circumpolar Flaw Lead) de la mer de Beaufort et du golfe d’Amundsen. Le seul autre navire qui passa l’hiver dans l’Arctique fut le NGCC Des Groseilliers qui dériva avec le pack central de glace durant l’hiver 1998, lors du projet American SHEBA (Surface Heat Budget of the Arctic Ocean) (Macdonald et al., 2002). L’échantillonnage pendant CFL a été démarré en mode de transect dans les sites d’eau libre dans le golfe d’Amundsen et le sud de la mer de Beaufort, du 18 octobre 2007 au 27 novembre 2007. Les stations d’échantillonnage de l’hiver 2007-2008 sont de trois types: les stations dérivantes (drift stations), les stations de banquise côtière (landfast ice stations) et les stations en eau libre.

Malina Une vaste étude dans le bassin du Mackenzie et le sud de la mer de Beaufort (leg 0902) a été réalisée en juillet et août 2009 (211 profils CTD) à bord du NGCC Amundsen au large du fleuve Mackenzie, entre le golfe d’Amundsen et le canyon Mackenzie.

0.3 Méthodes d’estimation de la profondeur de la couche mélangée

Dans cette étude, quatre méthodes différentes utilisées pour estimer la profondeur de la couche mélangée sont évaluées et comparées en utilisant diverses techniques statistiques et d’observation. Les méthodes pour l’estimation de la *MLD* sont la méthode du seuil (Schneider and Müller, 1990), la méthode Thomson-Fine (TF) (Thomson and Fine, 2003), une version modifiée de la méthode de TF (TFL) et la méthode Holte-Talley (HT) (Holte and Talley, 2009) modifié par l’auteur (HTN). Enfin, les résultats issus de ces méthodes sont comparés et la méthode la plus appropriée pour notre région est choisie pour être utilisée dans le reste de la thèse.

0.3.1 Méthodes d'estimation de la *MLD*

Méthode de seuil La méthode de seuil (TH) est la méthode la plus commune pour estimer la *MLD*. Cette méthode peut être utilisée en considérant les profils de température, de salinité et de densité avec différentes valeurs de seuil. Selon cette méthode, la *MLD* est la profondeur à laquelle la température ou la différence de densité dépasse une quantité prédéfinie (appelée seuil) par rapport à la valeur de référence de surface (Schneider and Müller, 1990, Kara et al., 2000). Bien que l'idée de base soit la même, les valeurs seuils utilisées pour les calculs de la *MLD* sont différentes d'une région à l'autre. Kara et al. (2000) et de Boyer Montégut et al. (2004) ont examiné de nombreux profils pour déterminer les critères de seuil optimal pour calculer la *MLD*. de Boyer Montégut et al. (2004) ont suggéré les valeurs seuils de température et de densité pour l'océan global de $0.2\text{ }^{\circ}\text{C}$ et 0.03 kg m^{-3} respectivement. L'essai de trois valeurs de seuil différentes (0.03 , 0.04 et 0.05 kg m^{-3}) a démontré que, dans de nombreux cas, une valeur de seuil plus élevée est parfois nécessaire pour estimer la *MLD* dans notre région d'étude.

Méthodes TF et TFL Thomson and Fine (2003) ont utilisé l'algorithme de "split and merge" développé par Pavlidis and Horowitz (1974) pour calculer les *MLDs*. L'algorithme définit un certain nombre de segments linéaires pour un profil de données telles que la densité. Ensuite, le profil est reproduit en définissant les emplacements d'un groupe de points de rupture au milieu de ces segments. Les points de rupture localisent l'endroit où la pente du profil change. A chaque étape, la différence entre le profil d'origine et les segments ajustés est calculée. Tant que cette différence demeure supérieure à un seuil donné, le segment se divise en deux segments linéaires de longueur égale. La même longueur signifie que chaque segment doit contenir le même nombre de points. Deux segments peuvent fusionner dans un nouveau segment dès que ce nouveau segment respecte la norme d'erreur. Sur la base de cette technique, la *MLD* est définie comme étant la profondeur de la jonction des deux premiers segments.

En raison de la variabilité dans les profils de densité, les *MLDs* estimées en utilisant la méthode de TF différaient parfois beaucoup de la *MLD* estimée visuellement. Pour améliorer l'estimation de la *MLD* avec la méthode de TF, quelques modifications ont été proposées par Lago (2006) (rapport non publié, INRS). Les modifications de la méthode de TF ont été ajoutées principalement à l'algorithme de division de segment. Afin de minimiser les effets de fluctuations des profils de densité, un filtre à moyenne mobile est appliquée sur les données d'origine avant qu'elles ne soient traitées. De plus, au lieu de diviser un segment en deux parties égales et de déplacer les points de jonction afin de réduire l'erreur, la méthode TFL définit les points de jonction là où le gradient dans

les données est le plus grand. En outre, la division d'un profil avec la méthode TFL commence à partir du fond tandis que dans le procédé de TF, l'analyse des segments commence à partir de la surface. De plus, quatre conditions sont également imposées afin d'éviter de sélectionner des points critiques parasites.

Les méthodes HT et HTN Holte and Talley (2009) ont calculé les *MLDs* avec des méthodes différentes, y compris le seuil, la méthode du gradient et la méthode de la pycnocline en utilisant des profils de densité, de température et de salinité. Dans cette méthode, des algorithmes différents sont utilisés pour l'été et l'hiver dans les océans Pacifique et Atlantique Sud (Holte and Talley, 2009). HT détermine la *MLD* en utilisant différentes méthodes en fonction de la spécificité de chaque profil. Une approche multi-méthodes similaire à celle HT est adoptée par l'auteur (méthode HTN) pour la région d'étude. Dans le procédé de HTN seulement les profils de densité sont utilisés et le même algorithme est utilisé pour l'été et l'hiver. L'algorithme calcule quatre *MLDs* possibles en utilisant le minimum de densité le plus profonde (MD), la méthode de seuil (TH), la méthode de gradient de densité (GD) et la méthode de la pycnocline (PYCN). Les modifications apportées à la méthode sont décrites en détail dans la section 3.3.3 de la thèse.

0.3.2 Évaluation des méthodes

Trois approches sont utilisées pour évaluer les méthodes d'estimation de la *MLD* utilisées dans notre étude (TH, TF, TFL et HTN) et choisir la plus appropriée pour le reste de l'étude. Les approches sont basées sur une inspection visuelle, l'analyse statistique et la validation in situ.

En observation visuelle, chaque profil de densité est soigneusement examiné afin de déterminer la valeur de la *MLD*. Le but est de chercher un changement brutal qui rend le profil de densité plus uniforme au-dessus de la pycnocline. L'inspection visuelle fournit une base pour l'estimation de la *MLD* et est utilisée pour comparer les résultats provenant d'autres procédés. Les *MLDs* estimées par les différentes méthodes sont tracées l'une en fonction l'autre sur la figure 3.8. Il faut noter que la méthode TF et en particulier la méthode TFL surestiment parfois les *MLDs*. La comparaison entre les *MLDs* calculées par la méthode de seuil (valeur de seuil de 0.05 kg m^{-3}) et la méthode de TF montre que ces deux méthodes sont généralement comparables car les *MLDs* sont concentrées autour de la ligne rouge 1:1 (figure 3.8a). Comme il est montré sur les figure 3.8b et c, la méthode du seuil sous-estime les *MLDs* par rapport aux méthodes TFL et HTN. Les figures 3.8c et d montrent que la méthode du seuil et les méthodes

de TF sous-estiment généralement la *MLD* en comparaison avec les méthodes TFL et HTN.

Afin d'évaluer la cohérence entre les différentes méthodes d'estimation de la *MLD* plusieurs statistiques (Dawson et al., 2007) sont utilisées. Ce sont les différences entre les maximums (PDIFF, équation 3.5), l'erreur absolue moyenne (MAE, l'équation 3.6), l'erreur quadratique moyenne (RMSE, l'équation 3.7), l'erreur absolue relative (RAE, l'équation 3.8), et le coefficient de corrélation de Pearson (RSqr, l'équation 3.9).

Le tableau 3.1 présente les résultats des tests statistiques. La méthode HTN est clairement la plus statistiquement cohérente. Elle fonctionne bien dans tous les aspects. Les cases surlignées jaunes dans le tableau 3.1 montrent que, basé sur la moyenne, le minimum, les statistiques MAE, RMSE, RAE et RSqr, la méthode de HTN calcule des *MLDs* plus semblables à celles des inspections visuelles, par rapport aux autres méthodes. En outre, les cases surlignées en vert dans le tableau 3.1 indiquent que sur la base des statistiques Max et PDIFF, la méthode TFL estime le meilleure *MLD* mais que la méthode de HTN termine en second. Pour résumer, la comparaison entre les *MLDs* identifiées visuellement et calculées révèle que la méthode HTN est le plus compatible avec les observations.

La figure 3.10 montre que la densité en surface (5 m) et la densité de la *MLD* obtenue en utilisant toutes les méthodes sont très similaires. Par contre la densité en surface et la densité de $MLD_{TH}+3$ m et $MLD_{TH}+10$ m sont différentes. Pour ce cas particulier, la figure 3.10b montre que la densité à la surface, MLD_{TF} et $MLD_{TF}+3$ m sont très similaires les unes aux autres. Il en ressort que la méthode de TF sous-estime la *MLD* plus que n'importe quelle autre méthode. Cette figure montre également que, bien que les écarts entre les lignes de densité dérivées de la méthode du seuil sont un peu plus grands que les écarts obtenus par la méthode TF. La méthode du seuil sous-estime également la *MLD*. Les figures 3.10c et d montrent que les estimations TFL et HTN sont plus proches de la valeur réelle puisque la densité à la surface (5 m) et la *MLD* coïncident alors que les lignes de densité de la *MLD*, $MLD+3$ m et $MLD+10$ m ne coïncident pas.

Bien que les valeurs de la *MLD* sont correctement estimées par les deux méthodes TFL et HTN, un examen attentif de ces deux panneaux montre que la méthode de HTN présente un peu plus d'écarts entre la densité de la *MLD* et $MLD+3$ m.

0.4 Évolution temporelle et distribution spatiale de la profondeur de la couche mélangée

Les variations spatiales (par régions) et temporelles (interannuelles, saisonnières et mensuelles) de la couche mélangée dans le sud de la mer de Beaufort et le golfe d'Amundsen sont étudiées dans ce chapitre. Tous les *MLDs* dans ce chapitre sont estimées en utilisant la méthode HTN. La région d'étude sera divisée en quatre sous-régions distinctes (figure 4.2) pour étudier de manière plus adéquate les variations spatiales et temporelles. Notez que des données ne sont pas toujours disponibles chaque année pour la même sous-région. Afin d'évaluer le rôle possible de la profondeur de l'eau sur les variations de la *MLD*, chaque sous-région est divisée de nouveau en *inshore* (profondeurs inférieures à 200 m) et *offshore* (profondeurs supérieures à 200 m). Les variations saisonnières, interannuelles et spatiales de la *MLD* sont ensuite étudiées dans chaque sous-région. La distribution spatiale de la *MLD* est étudiée au cours des différentes années et saisons. Tout d'abord les valeurs de la *MLD* sont comparées dans chacune des quatre sous-régions, ainsi que dans les régions *inshore* et *offshore*. Le nombre de données disponibles chaque année, la saison et la sous-région sont présentés dans le tableau 4.2.

0.4.1 Variations spatiales

Inshore-Offshore À titre d'exemple, la comparaison entre les *MLDs* dans les régions *inshore* et *offshore* est réalisée pour les données de CASES (2003-2004). Des tests de Student sont effectués entre les *MLDs* moyennes *inshore* et *offshore* pendant les quatre mois pour lesquels des données sont disponibles dans les deux régions. Comme le montre le tableau 4.3, les valeurs de t calculées ($C - t$) sont supérieures aux valeurs de t tabulées ($T - t$), sauf en novembre et juillet où ils sont proches les uns des autres. Cela signifie que, pendant les quatre mois, les valeurs moyennes des *MLDs* *inshore* et *offshore* sont significativement différentes. La faible différence entre $C - t$ et $T - t$ dans le tableau 4.3 en juillet indique que les valeurs moyennes des *MLDs* sont proches les uns des autres, mais significativement différentes. Ceci est cohérent avec la figure 4.6 où les valeurs moyennes des *MLDs* dans *inshore* et *offshore* pour novembre et juillet sont plus proches les uns des autres, mais statistiquement différentes. La figure 4.7 montre que les fonctions de densité de probabilité (PDF) de la *MLD* pendant le programme CASES sont compatibles avec les valeurs moyennes (figure 4.6). La PDF donne les informations supplémentaire sur la distribution de la *MLD* qui nous aide de mieux interpréter la variation spatiale et temporelle de la *MLD*. En octobre, novembre et juin des *MLDs* plus profondes sont plus fréquentes dans la région *inshore*. En juillet, les

plus fréquentes *MLDs* dans *inshore* et *offshore* sont environ 5 m ce qui est cohérent avec le fait que la fonte des glaces va produire des *MLDs* plus minces.

Les variations spatiales de la *MLD* entre les sous-régions Le but de cette section est d'analyser la variation spatiale des *MLDs* entre les sous-régions pour la même période d'échantillonnage. Le tableau 4.7 présente toutes les données disponibles avec un nombre suffisant de réalisations (au moins 14) pour cette analyse. En dehors du printemps 2008, les valeurs moyennes des *MLDs* sont raisonnablement comparables dans toutes les régions, pour la même saison. Au printemps 2008 (cas 4 dans le tableau 4.7), la valeur moyenne des *MLDs* est significativement plus grande dans la région Amundsen que dans la région Franklin. Les PDFs (figure 4.14d) montrent que les *MLDs* les plus grandes (40-50 m) sont plus fréquentes dans le golfe d'Amundsen tandis que dans la baie de Franklin les *MLDs* de 15-25 m sont plus fréquentes. À l'automne 2003 (cas 1 dans le tableau 4.7), contrairement aux valeurs moyennes, les PDFs des *MLDs* dans les sous-régions montrent que les *MLDs* ne sont pas tout à fait semblables (voir la figure 4.14a). La *MLD* la plus fréquente dans la région Mouth (figure 4.14a) est la plus grande (20 m), tandis que dans la baie de Franklin, elle est la plus petite (10 m). Dans les régions Beaufort et Amundsen les *MLDs* les plus fréquentes sont d'environ 15 m et sont comparables. La figure 4.14b montre que, au printemps 2004 (cas 2 dans le tableau 4.7), bien que les *MLDs* les plus fréquentes sont d'environ 15 m dans l'Amundsen, les PDFs dans les régions Franklin et Mouth montrent que les *MLDs* les plus fréquentes sont d'environ 25 m et 40 m, respectivement. Bien que les PDFs à l'automne 2007 et l'été 2008 (figure 4.14c et e) montrent que les distributions de la *MLD* sont presque comparables dans toutes les sous-régions, avec un pic autour de 20 m à l'automne 2007 et de 5 m à l'été 2008, des *MLDs* profondes sont également fréquentes dans Amundsen et Mouth (voir le second pic sur la droite dans les lignes bleues et vertes des figures 4.14c et e). Les PDFs à l'été 2009 (figure 4.14f) montrent que, dans la sous-région de Beaufort, les *MLDs* avec des valeurs comprises entre 5-10 m sont plus fréquentes tandis que dans la région Mouth les *MLDs* les plus fréquentes sont l'ordre de 10-15 m. Les résultats présentés dans cette étude sur la base de l'analyse des valeurs moyennes et des PDFs démontrent clairement qu'analyser uniquement les valeurs moyennes n'est pas suffisant pour comparer les *MLDs* de différentes régions. Bien que les valeurs moyennes soient comparables, les courbes PDF révèlent des disparités importantes entre les sous-régions.

Distribution des *MLDs* le long des transects La distribution des *MLDs* est comparée au cours des mêmes années, mais le long de trois différents transects. La *MLD* et l'évolution des paramètres physiques sont analysés pendant le leg 0202, à l'automne 2002, le long de deux transects: Tr3 (au large du fleuve Mackenzie) et TrAM (d'est en

ouest) (voir la figure 4.15), ainsi qu'à l'automne 2003, lors du long de quatre transects pendant le leg 0304: Tr1 (du Cap Parry à l'île de Banks), Tr2 (du cap Bathurst à l'île de Banks), TR3 et TrAM (figure 4.16). La figure 4.15 illustre le fait que, à l'automne 2002, dans les régions côtières les eaux de surface (Tr3) sont plus chaudes et plus stratifiées que les eaux hauturières (*offshore*) et la *MLD* est donc moins profonde dans les régions côtières qu'hauturières. Dans le golfe d'Amundsen l'eau de surface est plus stratifiée dans l'est et il n'y a pas de couche mélangée pour les 20 premiers km, mais quand nous nous dirigeons vers l'ouest la couche mélangée apparaît. Comme il est clair dans la figure 4.15c, sous la couche mélangée dans l'halocline, l'eau est plus chaude par rapport aux couches supérieure et inférieure (NSTM (Jackson et al., 2010) ou sTM (Sévigny, 2013) alors que nous n'observons pas une telle couche le long du transect Tr3 dans la mer de Beaufort.

La figure 4.16 montre la variation de la *MLD* et des propriétés physiques de l'automne 2003 le long des quatre transects: Tr1, TR2, TR3 et TrAM. Cette figure montre que près des côtes les isolignes de salinité sont généralement plus proches les unes des autres ce qui indique une forte stratification et une *MLD* moins profonde. Le long du transect Tr3, en passant de la côte au large, l'eau de surface devient plus froide et moins stratifiée et la *MLD* devient plus profonde. Cette figure montre également que Tr1 et Tr2 sont généralement comparables en termes de la *MLD*, la température de surface et de la salinité. Juste en dessous de la couche mélangée une couche relativement plus chaude est observée le long de Tr1, Tr2 et TrAM tandis que cette couche ne se retrouve pas le long de Tr3.

0.4.2 Évolution temporelle de la *MLD*

Grâce aux deux longues séries de données des années 2003-2004 (CASES) et 2007-2008 (CFL), nous sommes en mesure d'étudier l'évolution saisonnière ainsi que l'évolution interannuelle dans chaque sous-région.

Évolution saisonnière de la *MLD* À titre d'exemple de l'évolution saisonnière de la *MLD*, nous comparons les *MLDs* entre l'automne, l'hiver, le printemps et l'été dans la baie Franklin pendant le programme CASES (2003-2004). La figure 4.17c montre que la *MLD* moyenne est la plus profonde au printemps et la plus faible en été dans la sous-région Franklin. La *MLD* en hiver est plus profonde qu'à l'automne, mais moins profonde que celle du printemps. La PDF en été dans cette sous-région possède un pic à 5 m. Dans la région Franklin, la PDF à l'automne, l'hiver et le printemps possèdent des pics à 10 m, 15-20 m et 5 m, respectivement. Ces valeurs démontrent également que

les *MLDs* profondes sont plus fréquentes au printemps par rapport aux autres saisons.

La figure 4.23 montre que la *MLD* augmente progressivement à l'automne jusqu'à ce qu'elle atteigne sa valeur maximale le 10 décembre, avant de diminuer progressivement. Le comportement de la *MLD* à la fin de l'automne et au début de l'hiver peut être due à un upwelling près de la lisière de la glace (ice-edge upwelling) causé par les vents favorables de l'est (figure 4.23b). L'effet d'un upwelling à la lisière de la glace sur la colonne d'eau est indiqué à la figure 4.23b par une ellipse rouge. En hiver, la température de la couche superficielle est plus faible et la *MLD* est généralement plus profonde qu'à l'automne. Après l'upwelling à la lisière de la glace, la *MLD* augmente et atteint 34 m en STS 99 (7 Février) (Sampling Time Sequence: séquence d'échantillonnage en jours; chaque séquence débute au temps $t=0$) puis elle diminue jusqu'à 14 m à la fin de février. La *MLD* augmente ensuite jusqu'à la fin mars. Bien que la température de la couche de surface au printemps soit légèrement plus élevée qu'à l'hiver, la salinité est également plus élevée en raison du rejet de sel relié à la formation de glace. La *MLD* commence à diminuer à la fin du mois de mai lorsque la température de la couche de surface augmente en raison de la pénétration de la radiation solaire. Les tourbillons anticycloniques, le 30 avril et le 16 mai, comme le suggère Barrette (2012), font diminuer la *MLD* comme la montre la figure 4.23c (ellipses rouges). Tout au cours du printemps et pour la plus grande partie de l'hiver, la couche mélangée est associée à l'isoline 31 de la salinité. En été, même avec un petit nombre d'observations, nous observons que la couche de surface est chaude et complètement stratifié, ce qui rend la *MLD* plus mince.

Évolution interannuelle de la *MLD* La comparaison interannuelle des *MLDs* est réalisée en utilisant les données de 2002, 2003-2004, 2005, 2006, 2007-2008 et 2009. Les valeurs moyennes mensuelles de la *MLD* pour 2003-2004 et 2007-2008, indépendamment de la région, sont comparées graphiquement sur la figure 4.30. Comme il est évident dans cette figure, la *MLD* s'approfondit en hiver et atteint sa valeur maximale au printemps tandis que la plus faible valeur observée l'a été pendant 2003-2004 (CASES) et 2007-2008 (CFL). Les valeurs moyennes de la *MLD* sont évidemment plus profondes au cours de CFL qu'au cours de CASES en dehors de juin et juillet où leur différence est très petite. La moyenne de la *MLD* est de 70% plus grande lors de CFL que lors de CASES avec plus que 100% d'écart en février. Dans les deux cas, la *MLD* approfondit d'octobre à avril, puis devient moins profonde. La valeur moyenne maximale de la *MLD* dans les deux ensembles de données est observée en avril et le minimum est en juillet et août. La valeur maximale de la *MLD* pendant CFL est beaucoup plus élevée que pendant CASES la plupart du temps, à l'exception de juin, juillet et août. En juin et août le maximum de la *MLD* est plus grand pendant CASES que CFL, et en juillet les *MLDs* maximales sont presque les mêmes dans les deux cas. Les valeurs minimales sont

toujours semblables, sauf en mars. Comme il est évident sur la figure 4.30, les intervalles de confiance à 95% des moyennes mensuelles ne se chevauchent pas. Cela signifie que les valeurs moyennes mensuelles de la *MLD* sont significativement différentes entre CASES et CFL, ce qui est cohérent avec les résultats mensuels des tests de Student présentés dans le tableau 4.8.

En outre, une comparaison interannuelle au cours de l'automne est réalisée entre les années 2002, 2003, 2006 et 2007 (lorsque des observations suffisantes sont disponibles). Comme le montre la figure 4.31, les moyennes à l'automne 2007 sont les plus élevées par rapport aux autres années. La PDF (à droite) montre également une augmentation significative en 2007, tandis que la PDF et les valeurs moyennes de la *MLD* des autres années sont très similaires. Cette augmentation notable de la *MLD* est due à un upwelling comme il a été rapporté par Tremblay et al. (2011). Selon Williams and Carmack (2008) les effets des mouvements de marée et d'un vent favorable peuvent conduire à un upwelling dans la région du Cap Bathurst. L'influence de l'upwelling est généralement limitée à quelques kilomètres du Cap Bathurst comme observé sur de nombreuses images satellites (Gratton et al., 2012). Néanmoins, à l'automne 2007, les effets du upwelling peuvent être observés plus de 200 km au nord du cap Bathurst. La signature du upwelling a également été observée le printemps suivant (Tremblay et al., 2011). Les forts vents d'est soufflant parallèlement à la côte à l'automne 2007 sont responsables de l'événement et ont aussi retardé la formation de la glace de près de six semaines.

La comparaison entre la *MLD* de étés 2004, 2005, 2008 et 2009 montre que les valeurs moyennes au cours des étés 2004, 2008 et 2009 sont généralement comparables alors que la valeur moyenne de la *MLD* en 2005 est légèrement plus grande que les autres années (figure 4.31). La PDF en été montre également un léger décalage vers des valeurs plus élevées en 2005, alors que dans les autres années, les PDFs sont très similaires. Les grandes *MLDs* à l'été 2005 pourraient être dues à la période d'échantillonnage (soit 2 à septembre et 14 septembre) qui est près de l'automne. Rappelons qu'en fin d'été et début d'automne, la *MLD* devient souvent plus profonde en raison du démarrage de la période de refroidissement, et de l'augmentation de la vitesse du vent et du nombre de tempêtes.

0.5 Les flux océaniques sous la glace et leurs impacts sur la profondeur de la couche mélangée

La relation entre les flux océaniques sous la glace et les variations de la *MLD* sont examinés dans une couche entre la surface et une profondeur de référence (*hc*) pendant les hivers 2004 et 2008. Cette profondeur de référence est choisie en fonction des deux conditions suivantes: (1) *hc* doit toujours être plus profonde que la valeur maximale de la *MLD* au cours de la période d'échantillonnage à la station désirée. (2) La valeur maximale de la densité dans la couche de mélange doit toujours être inférieure à la densité initiale à *hc*. Une méthode mise au point par [Prieur et al. \(2010\)](#) (ci-après LP) est utilisée pour calculer les flux océaniques (de masse et de flottabilité) en utilisant le bilan de masse de la couche mélangée. Ce type d'approche a été introduite par [Emery \(1976\)](#) qui a estimé le bilan de chaleur de la couche mélangée dans le Pacifique. Notre approche est cependant la seule qui tienne compte de l'advection verticale.

Le flux de flottabilité est calculé en tenant compte des contributions de l'apport de chaleur et d'eau douce tel que décrit dans [Gill \(1982\)](#). Les équations que nous utilisons sont cependant celles qui ont été adaptées par [Nerheim and Stigebrandt \(2006\)](#) (formulation NS) pour calculer le flux de flottabilité entre la surface et la *MLD*. Dans la formulation NS l'advection verticale n'est pas prise en compte.

Le calcul du flux de chaleur atmosphérique total a été effectué en utilisant les données atmosphériques in situ dans la baie de Franklin au cours du programme CASES sur la base de la formulation de [Parkinson and Washington \(1979\)](#). La méthode utilisée pour l'estimation du taux croissance de la glace est celle de [Cox and Weeks \(1988\)](#) à partir des profils CTD.

0.5.1 Les flux océaniques pendant CASES (2003-2004) et les variations de la *MLD*

Cette partie de l'étude est surtout basée sur les données recueillies pendant la station fixe du programme CASES pendant laquelle, en plus du grand nombre de profils CTD échantillonnés (deux fois par jour), les flux atmosphériques et l'épaisseur de la glace ont aussi été mesurés. Par souci de cohérence, pour les autres stations mentionnées au tableau 5.1, la profondeur de référence a également été choisie 7 m au-dessous de la valeur maximale de la *MLD* à chaque station.

Les valeurs cumulées de différents paramètres sont calculées comme $CumJ_b$ (la

valeur cumulée de flux de flottabilité utilisant l'équation 5.30), $CumJ_m$ (le terme I dans l'équation 5.22 est la valeur cumulée du flux de masse utilisant les équations 5.19 et 5.30), C_{pres} (contenu résiduel en masse de la couche mélangée calculé en utilisant l'équation 5.21), $Cum(Adv_{\rho_{hc}})$ (la valeur cumulée de l'advection verticale, le terme II dans l'équation 5.22), $Cum(hc d\rho/dt)$ (la valeur cumulée de la variation temporelle de densité à la profondeur de référence, le terme III dans l'équation 5.22). L'équation 5.22 est reproduite ci-dessous:

$$dC_{pres}/dt = \overbrace{+J_b(\rho_s/g)}^I + \overbrace{w_{-hc}(\rho_{-hc} - \langle\rho\rangle)}^{II} + \overbrace{hc \times d\rho_{-hc}/dt}^{III} \quad (5.22)$$

Comme le montre les figures 5.6 et 5.8a, lorsque $CumJ_b$ augmente (diminue), C_{pres} augmente (diminue) et en outre, la différence de densité entre la surface et la profondeur de référence augmente (diminue). Comme mentionné précédemment, la valeur cumulée du flux de flottabilité ou du flux de masse ($CumJ_b$ ou $CumJ_m$) sous la glace est un indicateur de l'influence atmosphérique au-dessous de la glace. Le flux de flottabilité est affecté par des échanges de chaleur et de salinité (équation 5.5), ce qui signifie que lorsque l'eau se réchauffe ou que la salinité diminue en raison de la fonte des glaces, le flux de flottabilité devient positif, tandis que le refroidissement de l'eau et l'augmentation de la salinité mènent à un flux de flottabilité négatif. Par conséquent, l'évolution du flux de flottabilité peut être utilisée pour estimer les variations des flux atmosphériques. La MLD s'approfondit généralement au cours de la période d'échantillonnage, même si elle ne suit pas exactement la variation de $CumJ_b$. La MLD s'approfondit jusqu'au 2 avril, puis devient moins profonde entre les 2 et 19 avril. Cependant, $CumJ_b$ montre en général une tendance à la baisse jusqu'à la fin de la période d'échantillonnage.

Le tableau 5.2 montre les tendances de la MLD , $CumJ_b$, $Cum(dC_{pres}/dt)$, $Cum(Adv_{\rho_{hc}})$ et $Cum(hc d\rho_{-hc}/dt)$ pour les stations étudiées. Comme le montre ce tableau, MLD et $CumJ_b$ ont des tendances similaires dans 70% des cas. De même, 77% des $MLDs$ ont des tendances similaires à $Cum(dC_{pres}/dt)$ comme on s'y attendait. La MLD et $Cum(Adv_{\rho_{hc}})$ affichent des tendances inverses pour 70% du temps, alors que la MLD et $Cum(hc d\rho_{-hc}/dt)$ étaient semblables 67% du temps. Des tendances similaires entre la MLD et $CumJ_b$, comme mentionné précédemment, confirme que $CumJ_b$ diminue (augmente) et la MLD augment (diminue) pendant des périodes de refroidissement (réchauffement). Les valeurs de la variation temporelle de la MLD , de $Cum(dC_{pres}/dt)$, de $Cum(Adv_{\rho_{hc}})$ et de $Cum(hc d\rho_{-hc}/dt)$ aux différentes stations sont énumérées dans le tableau 5.2.

0.5.2 Comparaison entre le flux de la flottabilité calculé avec les méthodes NS et LP

La différence entre le flux de flottabilité obtenue par la formulation NS et la méthode de LP est probablement dû à l'advection verticale qui est prise en compte dans la méthode de LP, mais n'est pas présente dans la formulation NS.

0.5.3 Observations atmosphériques, de la glace et de la neige en relation avec la variation de la *MLD*

Les figures 5.13a, b et c montrent la température de l'air à la surface ainsi que les températures de neige et de glace à différentes profondeurs entre le 22 janvier et le 23 mai. Les tendances descendante et ascendante de la température dans la glace et la neige sont semblables à celles de la température de l'air en surface. Comme le montre la figure 5.13, du début de l'échantillonnage jusqu'au 8 mars, la *MLD* s'approfondit alors que les températures de l'air à la surface, de la neige et de la glace diminuent. Cependant, les températures commencent à augmenter progressivement après ce moment alors que la *MLD* continue de s'approfondir jusqu'au 2 avril. Par conséquent, il semble que ces températures influent sur la *MLD* à retardement et non pas immédiatement à cause de propriétés d'isolation de la glace et de la neige.

0.5.4 Corrélation croisée entre les flux océaniques et la *MLD* pour différentes stations

La fonction de corrélation croisée calculée entre la *MLD* et chacun terme de l'équation 5.22 pour un décalage (lag) est présentée à la figure 5.14. Les valeurs maximales des coefficients de corrélation croisée entre la *MLD* et $Cum(dC_{pres}/dt)$ et la *MLD* et $CumJ_b$ sont respectivement de 0.36 et de 0.4, mais avec 21 jours de retard. Ces facteurs influent sur la *MLD* à retardement et non pas immédiatement. Comme le montre la figure 5.14, $Cum(Adv_{\rho_{hc}})$ et $Cum(hc d\rho_{-hc}/dt)$ sont corrélés avec la *MLD* sans délai avec des coefficients de corrélation de -0.63 et 0.57 respectivement. La corrélation négative entre la *MLD* et $Cum(Adv_{\rho_{hc}})$ (terme II dans l'équation 5.22) démontre que ce terme a un effet inverse sur la *MLD*. En d'autres mots, quand $Cum(Adv_{\rho_{hc}})$ diminue (augmente) ou est à la baisse (à la hausse), la *MLD* augmente (diminue).

0.5.5 Modélisation de la *MLD* en utilisant une méthode de régression linéaire et multiple

Les résultats de la régression linéaire et multiple suggèrent que la combinaison de $Cum(Adv_{\rho_{hc}})$ modifié, $Cum(hc d\rho_{-hc}/dt)$ et $Cum(dC_{pres}/dt)$ et les données antérieures de $CumJb$ (avant le 20e jour) donne la meilleure estimation de la *MLD* par rapport aux autres combinaisons de paramètres ($R^2 = 0.644$). Il convient de noter que ces résultats sont en accord avec ceux qui émanent de l'étude des corrélations croisées confirmant le lien entre la *MLD* et le flux de flottabilité de surface et les mouvements à la base de la couche de surface.

0.5.6 Estimation de l'épaisseur de la glace et la *MLD*

La figure 5.18a montre l'épaisseur de la glace observée et estimée à partir des mesures des profils CTD. La figure indique clairement que les valeurs de l'épaisseur de glace estimées par le méthode de Cox and Weeks (1988) sont très proches des valeurs d'épaisseur de glace mesurées. Étant donné que la mesure de l'épaisseur de glace est complexe, ces résultats démontrent qu'il est possible de calculer l'épaisseur de la glace sur la base de mesures CTD uniquement.

0.5.7 Floraison et la *MLD*

Au début de mars, l'augmentation du rayonnement (PAR sur la figure 5.19a) permet au phytoplancton de se développer de plus en plus, ce qui est rendu évident par l'augmentation de la concentration de *Chl a* sous la glace de mer. Au début de l'échantillonnage (fin février) la concentration de *Chl a* sous la glace de mer à la station fixe était très faible (0.015 mg m^{-2}) pendant qu'avant la période de floraison, qui est définie par une augmentation rapide de la concentration de *Chl a* (du 3 avril au 23 mai), la concentration était inférieure à 2.035 mg m^{-2} , comme signalé par la figure 5.19e. La concentration de *Chl a* sous la glace de mer a commencé à augmenter au début d'avril avec l'augmentation saisonnière de la température de l'air (figure 5.19b). Ensuite, elle a atteint son maximum de 27.82 mg m^{-2} le 23 mai. Après cette date, la concentration de *Chl a* diminuée jusqu'à ce qu'elle atteigne près de zéro le 21 juin, qui coïncide avec le début de la fonte de la glace (figure 5.19d et e). Comme le montre la figure 5.19f, la *MLD* s'approfondit à partir du début de la période d'échantillonnage jusqu'à ce qu'elle atteigne son maximum 43 m le 2 avril, après quoi elle continue à diminuer malgré de légères fluctuations. Cette date correspond au début de la floraison planctonique et

peut donc être associée au début de la pénétration de la radiation solaire dans l’océan. Il est à noter qu’il n’y a pas eu d’échantillonnage CTD à la station fixe en juin. Comme le montre la figure 5.19d et f, le premier maximum local de la concentration de *Chla* est apparu le 3 mai, environ un mois après la valeur maximale de la *MLD* (le 2 avril), et 20 jours plus tard, nous avons assisté à la valeur maximale de *Chla*, soit le 23 mai.

0.6 Conclusions

Le profil de densité potentiel a été utilisé pour calculer les *MLDs* et cinq procédés différents ont été testés: (1) la méthode du seuil (TH), (2) la méthode de Thomson et Fine (2003) (TF), (3) une modification de la méthode de Thomson et Fine (TFL), (4) une modification de la méthode de Holte et Talley (2009) (HTN) et (5) la méthode d’inspection visuelle (VI). Il a été constaté que la version modifiée de la méthode de Holte et Talley (HTN) est la méthode la plus appropriée pour notre région et, possiblement, pour l’Arctique.

La région d’étude a été divisée en quatre sous-régions: Amundsen (AM), Mouth (M), Beaufort (BF) et Franklin (F). Chaque sous-région a été sub-divisée en zones côtières (profondeur < 200 m) et zones hauturières (profondeur > 200 m). La comparaison entre *MLD* côtières et hauturières révèle que les *MLDs* hauturières étaient plus profondes que les *MLDs* côtières en automne, en hiver et au printemps. Pendant l’été, les *MLDs* côtières et hauturières étaient comparables. Le résultat de la comparaison entre les sous-régions a montré que les *MLDs* étaient généralement comparables si les comparaisons sont effectuées dans la même sous-région et pendant la même saison. Cependant, les grandes *MLDs* ont été plus souvent observées dans les sous-régions Amundsen et Mouth. Les analyses saisonnières ont démontré que dans toutes les sous-régions, les *MLDs* moyennes ainsi que les *MLDs* les plus fréquentes commencent à s’approfondir en fin d’été et continuent à s’approfondir jusqu’à ce qu’ils atteignent leur maximum au printemps. Les comparaisons interannuelles de la *MLD* entre CASES (2003-2004) et CFL (2007-2008) ont montré qu’elles sont très différentes en automne, en hiver et au printemps alors qu’en été, elles étaient comparables. La comparaison mensuelle entre ces deux séries d’un an a démontré que toutes les *MLDs* étaient significativement plus profondes pendant CFL, sauf pour les mois de juin et juillet. La valeur moyenne la plus profonde de la *MLD* a été observée en avril dans les deux séries. La comparaison interannuelle, sans tenir compte des sous-régions, entre les automnes de 2002, 2003, 2006 et 2007 a montré que les *MLDs* étaient significativement plus élevés à l’automne 2007 que pendant toutes les autres années, et que les *MLDs* les plus fréquentes étaient toujours les plus élevées. L’analyse des *MLDs* au cours des étés 2004, 2005, 2008 et

2009 a révélé que les *MLDs* étaient comparables pendant l'été. Les *MLDs* profondes en 2007-2008 étaient reliées à l'upwelling qui a eu lieu à l'automne 2007 et dont les effets sont restés observables jusqu'au printemps suivant. En outre, au cours de CFL, l'échantillonnage a été effectué à partir de la glace dérivante dans le flaw lead où la glace gèle continuellement et la convection, en raison de rejet de sel, provoque l'augmentation des *MLDs*. Enfin, la plupart des fonctions de distribution de probabilités étaient d'un type à une «bosse» montrant une gamme unique de profondeur *MLD* pour chaque région. Ces résultats démontrent l'analyse des valeurs moyennes ne suffit pas pour comparer les *MLDs* entre différentes régions: il faut aussi comparer les fonctions de densité de probabilités.

Nous avons analysé le bilan de masse de la couche mélangée entre décembre 2003 et juin 2004 sur la base de l'approche du budget de chaleur d'Emery (1976), modifiée par Prieur et al. (2010). La seule hypothèse nécessaire était qu'il n'y a pas d'advection latérale non divergente. La beauté de cette approche est qu'elle ne nécessite que des profils verticaux de densité à partir d'instruments de mouillage ou de profileurs dérivants. La comparaison entre les flux de flottabilité cumulatifs ($CumJ_b$) a montré que les effets de l'advection verticale sur le flux de flottabilité sont importants. Les analyses ont aussi démontré que les flux de flottabilité cumulés sous la glace ($CumJ_b$) sont également un excellent indicateur du temps nécessaire à la couche mélangée pour intégrer les flux de surface. De plus l'advection verticale sous la couche de surface a une relation inverse et simultanée avec les variations de la *MLD*. En outre, les résultats de la régression multiple simple suggèrent que la combinaison de termes $Cum(Adv_{\rho_{hc}})$, $Cum(hc d\rho_{-hc}/dt)$ et $Cum(dC_{pres}/dt)$ et les données antérieures de $CumJ_b$ (avec un délai de 21 jours) donne la meilleure estimation de la *MLD* en comparaison avec toute autre combinaison de paramètres. En outre, cette méthode peut être utilisée pour estimer le taux de croissance de l'épaisseur de la glace. Elle n'a besoin que d'une valeur initiale de l'épaisseur de la glace. Enfin, l'analyse des concentrations de *Chl a* sous la glace a démontré que la floraison a commencé immédiatement après que la *MLD* ait atteint son maximum (MLD_{max}). Pendant CASES, les concentrations de $Chl a_{max}$ ont commencé à apparaître environ un mois après que la MLD_{max} . La date de début de la floraison a été utilisée comme un indicateur révélant le moment où la lumière a commencé à pénétrer au travers de la glace, et nous ont donc indiqué le moment où la chaleur a commencé à atteindre la couche de surface. Cela explique pourquoi la *MLD* et l'épaisseur de la glace ont continué d'augmenter même après que le réchauffement de l'atmosphère ait débuté. Finalement, nous pensons que l'approche LP peut être utilisée même dans certains cas d'advection horizontale, s'il est possible d'identifier des événements comme les tourbillons et les upwellings car il serait alors possible de post-corriger le modèle en conséquence.

CHAPTER 1

INTRODUCTION

1.1 Motivation

The Arctic Ocean plays an important role in the global climate: it is the region where climate change is expected to be most pronounced. Observations confirm that the Arctic Ocean and its marginal seas are already warming and the areal extent of the bottom Atlantic warm layer has increased (Serreze et al., 2000). The effects of the Arctic on the global climate involve the surface atmosphere-ice-ocean exchanges and consequently the global thermohaline circulation (Aagaard and Carmack, 1994). The total sea ice distribution (areal and thickness) in the Arctic Ocean has declined over the past several decades: the absolute minimum Arctic ice pack extent was observed in August 2012 (NSIDC September 19, 2012), after previous minimums in 2005 and 2007 (Wang et al., 2009). This decline in ice extent is especially apparent in the Canadian Archipelago and the Southern Beaufort Sea (Barber and Hanesiak, 2004). The extent of ice cover decreased at the rate of approximately 11% per decade between 1979 and 2007 (Polyakov et al., 2012), however, the average minimum sea ice extent in 2007-2008 showed an approximate 37% decrease compared with sea ice climatology between 1980 and 1999 (Wang and Overland, 2009). According to Comiso (2006), this trend will continue in the future together with an increase in water temperature and the rate of melting of perennial ice. Different factors such as temperature, wind, waves, currents and atmospheric forcing influence the Arctic sea ice cover (Comiso et al., 2008) and, in turn, the water characteristics of the polar ocean surface layer. Loss of Arctic ice cover leads to more exposure of the ocean to solar radiation and winds which affects the ocean surface directly. The mixed layer which is the major subject of this thesis is an oceanic interface surface layer between the atmosphere and the Deep Ocean (this will be explained in more detail in section 1.2).

In this thesis, I focus on the seasonal variations in the polar mixed layer since I

have access to a unique time series of two winters of temperature and salinity profiles. I propose a method to follow the evolution of the mixed layer and of the ice cover, using only temperature and salinity data. This approach is presented in Chapter 5 and was motivated by a study by Emery (1976) in which he describes the evolution of the mixed layer in the northeastern Pacific by looking at its heat budget. I use a similar approach based on the mass budget of the mixed layer.

1.2 The Mixed Layer

1.2.1 Definition of the Mixed Layer

The mixed layer is an oceanic surface layer in which the salinity, density, and temperature are almost uniform due to the high mixing initiated by the air-sea exchange such as heat flux and wind stress. The depth of the mixed layer (hereafter *MLD*) is mainly controlled by kinetic and potential energies (Kraus and Turner, 1967). Kinetic energy has a destabilizing effect and can be created and added to the mixed layer (ML) by wind, currents, convection, etc. On the other hand potential energy has a stabilizing effect which can be added by freshwater and incoming heat fluxes (Sarkar, 2007). The range of *MLD* variations is large as it can be changed from a few centimeters, in completely stratified waters, to thousands of meters (about 1500 m in the Labrador Sea major convection areas).

The *MLD* plays a very important role in climate change because it acts as an interface between the atmosphere and deeper ocean. The depth of the mixed layer has an important role in transferring heat, mass and momentum between the atmosphere and the ocean (Schneider and Müller, 1990). On the other hand the strength of the stratification under the mixed layer limits its influence on deeper layers (Schneider and Müller, 1990). Biological productivity is often controlled by the thickness of the mixed layer and the strength of turbulent mixing within the mixed layer. The *MLD* also regulates the entrainment of nutrients from the deeper layers (Liu, 2009). For example, the *MLD* has a very important impact on the dynamics of phytoplankton among all of the possible physical factors (Lavigne et al., 2013). The *MLD* impacts phytoplankton by controlling light and nutrient availability (Philips et al., 1997). The effects of *MLD* variations on biology can differ from one region to another. In regions where light is abundant, deepening of the ML can bring more nutrients to the euphotic layer and can result in increased biological production. The euphotic layer is the layer where light is sufficient to sustain photosynthesis. In regions where light is limited deepening of the ML may result in increased nutrient movement to the surface layer

however, phytoplankton may be carried out of the euphotic region, causing a decrease in biological production.

1.2.2 The Mixed Layer in different regions

The mid-latitude oceans' mixed layer has been already widely studied because of its important role in air-sea interactions (Schneider and Müller, 1990, Kara et al., 2000, Alexander et al., 2001). In this section we briefly review some studies on the mixed layer across the world's oceans and the methods used to calculate them.

Northeast Pacific Ocean In recent years several studies have been conducted on the *MLD* in the northeast Pacific Ocean. According to Freeland et al. (1997) between 1977-88 and 1960-76, mid winter *MLD* has declined markedly. Also the results of Jackson (2006)'s research revealed that the winter *MLD* has had a shoaling trend over the past 50 years in the center of Gulf of Alaska, reaching its shallowest value in the winters of 2002-2003 and 2003-2004. Thomson and Fine (2009) calculated *MLDs* from a simple diagnostic (Niiler, 1977) and bulk (Gaspar, 1988) model and also observations (between August 1956–December 1980) that revealed that over the past 52 years contrary to the winter *MLD* the summer *MLD* had no significant trend in the central northeast Pacific. According to Polovina et al. (1995), in the subtropical gyre the *MLD* has been deepening during the same 50 year period. Polovina et al. (1995) used temperature profiles, Freeland et al. (1997) used salinity profiles and Jackson (2006) used the 1-D GOTM (General Ocean Turbulence Model) model to calculate the *MLD*. The results of modeling the *MLD* with different atmospheric forcing, performed by Jackson et al. (2006), show that the sensitivity of the *MLD* to climate change is not uniform and it can be affected simultaneously by the ENSO (El Niño-Southern Oscillation), the PDO (Pacific Decadal Oscillation) and advection. Note that ENSO is the index indicative of a cyclic warming and cooling of the surface of the central and eastern Pacific ocean and the index of PDO is the EOF of monthly sea surface temperature anomalies of the North Pacific. Jackson et al. (2006) showed that although the *MLD* is most sensitive to the PDO phase change since wind has the most impact on the *MLD*. The PDO is an index which is detected as warm or cool surface waters in the Pacific Ocean. The west pacific cools down and part of the eastern ocean becomes warm respectively during the positive phase while the opposite pattern occurs during the negative phase. ENSO is a important coupled ocean-atmosphere event which causes interannually global climate variability. ENSO driven pattern alters wind, surface temperature, humidity and cloud cover over the North Pacific and affect the freshwater fluxes, surface heat momentum, sea surface temperature, salinity and *MLD* anomalies. This result also confirms the

results of [Large and Crawford \(1995\)](#) who showed that wind stress has the greatest effect on deepening of the *MLD* in the northeast Pacific Ocean. Some studies propose that the Pacific Decadal Oscillation is a main factor of *MLD* variations in the northeast Pacific Ocean ([Polovina et al., 1995](#), [Cummins and Lagerloef, 2002](#)). The PDO is a mode of inter-decadal climate variability which impacts the sea surface temperature (SST), wind strength and direction, and sea level pressure. Some studies have found that PDO-induced climate changes are responsible for 70–90% of *MLD* variability over the past 50 years since it is correlated with the depth of the pycnocline ([Cummins and Lagerloef, 2002](#)). [Lagerloef \(1995\)](#) showed that wind stress plays an important role in altering the strength of Ekman pumping which impacts the pycnocline and consequently the *MLD*. On the other hand [Whitney and Welch \(2002\)](#) showed that El Niño-Southern Oscillation (ENSO) events are responsible for the shoaling of the *MLD*. [Whitney and Welch \(2002\)](#) calculated the *MLD* using temperature profiles.

Gulf of Alaska A study in the Gulf of Alaska carried out by [Sarkar et al. \(2005\)](#) between 1997 and 2004, demonstrated that the deepest *MLDs* on the shelf occurred in late winter and early spring (March/April) due to low temperatures, freshwater inputs and also storms events during this time of year. As expected, they found that the shallowest *MLD* occurred in the summer caused by freshwater from ice melt starting in late spring. The *MLD* starts deepening again in the fall because of cold temperatures and fall storms. The inter-annual variability of the *MLD* from 1997 to 2004 could be due to different reasons such as El-Niño or La-Niña events, horizontal advection and several anticyclonic eddies passing through the offshore area. Note that El-Niño is an index which is characterized by unusually warm temperature while La-Niña by unusually cold temperature of the equatorial Pacific. [Sarkar et al. \(2005\)](#) show a shoaling trend in the offshore area and a deepening trend in the inshore area. It should be noted that the method of *MLD* calculation was the split and merge method ([Thomson and Fine, 2003](#)) which is discussed in chapter 3.

Atlantic Ocean As a part of the study in the Canary Basin in the North Atlantic Ocean carried out between June and November 1993 by [Caniaux and Planton \(1998\)](#), the *MLD* variation was investigated. The *MLDs* were calculated based on temperature profiles. This study showed that in the northern part of the basin the *MLD* was shallower than in the south and deepened to 54 m in November. This was due to a period of large meteorological variability which leads to *MLD* deepening ([Caniaux and Planton, 1998](#)). Based on the measurements a net decrease of the sea surface temperature (SST) of approximately 2.5 °C was observed over 30 days while over 22 days the mixed layer temperature decreased about 1.5 °C as the *MLD* decreased. As part of the Programme

Océan Multidisciplinaire Méso Echelle (POMME) in the northeast Atlantic between October 2000 and September 2001, [Paci et al. \(2005\)](#) modeled mixed layer evolution during the restratification period of POMME experiment (between February and May 2001) and compared the modeled *MLD* with estimated one based on potential density profile. They found that the mean value of the *MLD* increased from February until 1 March when it reached its maximum value of 180 m because of the cooling period. From 1 March to 10 April, the mean value of the *MLD* decreased rapidly as the oceanic response to air-sea flux warming. They observed a deeper *MLD* in the north part of their study region (up to about 400 m) than in the south part (less than 50 m). Moreover, the authors found that the *MLD*, SST and vertical velocities had filament-shaped structures located at fronts between mesoscale eddies.

Antarctic A seasonal and inter-annual study on variations of the *MLD* between 1991 and 2001 in the Antarctic region by [Chaigneau et al. \(2004\)](#) showed that during winter the *MLD* (about 150 m) is associated with the halocline while during summer the *MLD* (around 40 – 60 m) is associated with the thermocline. The decrease of the wind and stronger upwelling near the Antarctic Divergence leads to a shallower *MLD* in the South Antarctic Zone (AZ-S). The region of rapid transition between the Continental Water Boundary to the south and the Polar Front to the north is called the Antarctic Divergence. The authors found that the *MLD* was primarily affected by the surface wind as well as the surface heat flux. In this study the *MLD* was calculated based on the summer temperature profile, the winter salinity profile and the temperature and salinity near the Antarctic Divergence because both play an equal role in this region.

Gulf of Maine According to [Christensen and Pringle \(2012\)](#), the *MLD* shoaled through the winter in the coastal and eastern regions of the Gulf of Maine. In this study the *MLD* was calculated using a potential density. The results showed that the shallow *MLD* was primarily due to the salinity and was mainly controlled by advection. Decreasing trend of salinity and increasing trend of temperature during stratification period, which leads to *MLD* shoaling, were due to advection.

Labrador Sea The study by [Pickart et al. \(2002\)](#) in the Labrador Sea during convective mixing from February-March 1997, showed that the deepest *MLDs* were observed at about 1500 m in the central region of the study area while near the coast of Greenland the *MLD* was less than 100 m. Convective mixing is the vertical movement of water and its properties is because of density differences in the water. The cold air temperatures and strong westerly winds during the sampling period led to overturning

to about 1500 m which led to very deep *MLDs*. During this study the *MLDs* were calculated using temperature, salinity and potential density profiles. Convection is also observed in our region but it rarely reaches the bottom as the stratification is very strong, except in shallow areas.

Irminger Sea [Våge et al. \(2008\)](#) studied the impact of the Greenland tip jet on the mixed layer in the Irminger Sea during winter demonstrating that the wintertime *MLD* in the spring of 2003 reached 400 m and 300 m in the spring of 2004. The Greenland tip jet is the strong and intermittent wind caused by atmospheric forcing over the southern Irminger Sea ([Pickart et al., 2003](#)). The authors showed that both of these winters were mildly impacted by a low North Atlantic Oscillation (NAO) index. The deeper *MLD* during the winter of 2003 was due to the higher number of tip jet events created by currents produced by storms near southern Greenland. The *MLDs* were calculated using the method presented by [Pickart et al. \(2002\)](#) based on temperature, salinity and potential density.

Arctic A study in the Arctic central Canada Basin was done on the mixed layer properties during the summers of 2004 and 2009 by [Toole et al. \(2010\)](#). The *MLDs* were calculated based on temperature and salinity profiles. Their results showed that the average *MLD* in summer was commonly less than 12 m while in winter it rarely exceeded 40 m. Their observations revealed that the salinity of the central Canada Basin is low (average about 28). Using a 1-D ocean mixed layer model they found that the very strong density stratification at the base of the ML inhibits deepening of the surface layer in the Canada Basin. The presence of this strong density stratification limits transfer of the deep ocean heat flux to the surface which could influence the sea ice cover.

Global Ocean An analysis of the *MLD* variability in the global ocean between 1960-2007 was performed by [Liu \(2009\)](#). In this study the potential density profiles were used to calculate the *MLDs*. The results revealed that the maximum value of the *MLD* in the tropical Pacific exceeded 75 m in the central basin while in the east it decreased to less than 40 m. In the western equatorial Atlantic the *MLD*, based on temperature profile, was deeper than 75 m. In the Northern Pacific and Atlantic the *MLD* reached its maximum by the end of February or the beginning of March. The highest spatial and temporal variability of the *MLD* was found in the subtropics and mid-latitudes of the western half of the Pacific Ocean. The highest variability in the Atlantic Ocean occurred during the winter and spring in the subtropics and mid-latitudes. The annual

average value of the *MLD* in the eastern Pacific deepened by 10 m during the El Niño and the correlation between the *MLD* and SST was positive, while in the western Pacific and the eastern Indian Ocean the *MLD* decreased in depth by 10 – 15 m. Over the past 48 years the *MLD* has deepened in the central North Pacific and North Atlantic Ocean. This deepening trend in the North Pacific is due to the increasing trend in the PDO Index and in the North Atlantic, because of the positive trend in the NAO Index (Liu, 2009).

1.3 Objectives

The objective of the present thesis is to further enhance our understanding of the mixed layer in the Southern Beaufort Sea and Amundsen Gulf. The Arctic region plays a vital role in world heat balance and climate change and it is thus very important to understand what is occurring physically in different regions of the Arctic Ocean. The Southern Beaufort Sea and especially the Amundsen Gulf have been less studied due to the scarcity of data. Thanks to the recent research programs such as CASES (2001-2006), CFL (2006-2011), ArcticNet (2004-2018) and Malina (2009-2013), we now have vast, unique and invaluable datasets to help us improve our understanding of the different physical processes in the Arctic, especially in the Amundsen Gulf where no significant study had been performed before these programs. To reach this objective, I will focus on the temporal and spatial evolution of the mixed layer depth in these regions. The general objective will be reached through four specific objectives.

- Assess different methods of *MLD* estimation and select the most appropriate one for this study region;
- Study the spatial distribution of the *MLD* by dividing the region of study into subregions;
- Analyze the temporal evolution of the *MLD*, i.e. monthly, seasonal and interannual evolution of the *MLD*;
- Investigate the relations between the atmospheric and oceanic fluxes as well as ice thickness and the *MLD* evolution.

1.4 Structure of the thesis

The thesis is organized in five chapters. The first chapter contains the motivation, Mixed Layer definition and the objectives of the study. The second chapter presents the study region and the different data sets used in this study. The third chapter introduces the four different methods used to calculate *MLDs*. This chapter also describes the statistical tools used to select the most adequate method for the study region. The fourth chapter consists of two main parts describing the spatial distribution and temporal evolution of the *MLD* in the region. The fifth chapter details the impacts of the oceanic and atmospheric fluxes as well as vertical motions at the base of the surface layer on the *MLD*. It also investigates techniques of ice thickness calculations based on oceanic data and studies the relationship between ice thickness and the *MLD* evolution. The main results are summarized in the conclusion.

CHAPTER 2

STUDY REGION AND AVAILABLE DATA

2.1 The Arctic Ocean and Canadian Archipelago

The Arctic Ocean is an almost closed ocean with an area over 14,000,000 km². It communicates with the Pacific Ocean via the Bering Strait, with the Atlantic Ocean via the Fram Strait and Barents Sea and with the Canadian Archipelago (see Figure 2.1 and 2.2). The Canadian Arctic Archipelago covers a large portion of the Polar Continental Shelf of North America, bordered to the West by the Beaufort Sea, to the east by Baffin Bay, Greenland and the Davis Strait, the south by Hudson Bay and the Canadian mainland and to the north by the Arctic Ocean (see Figure 2.1). As shown in Figure 2.1, the Canadian Archipelago includes both large and small islands. Approximately 70% of the water in the Canadian Archipelago does not exceed 500 m in depth. The region experiences extremes of solar radiation: relatively high in summer, but limited in winter. The climate of the area close to the center and east of the archipelago is affected by the mountainous islands of Ellesmere, Devon and Baffin (Ingram et al., 2002). The Canadian Arctic Archipelago is also characterized by a blanket of sea-ice which varies throughout the year.

2.1.1 Circulation, vertical structure and ice in the Arctic

Water is supplied to the Arctic Ocean from three different sources: the Atlantic Ocean, the Pacific Ocean and rivers (Jones et al., 1998). These sources of water have their own physicochemical (i.e. salinity, temperature, nutrient concentrations) properties which make it possible to identify the origin of water masses in the region (Carmack et al., 1989). The distribution of the Atlantic and Pacific waters reflects the circulation of the surface waters. The circulation of Atlantic water is complex and there is an important trace of its flow in all Arctic basins (Nansen, Amundsen, Makarov and the Canadian

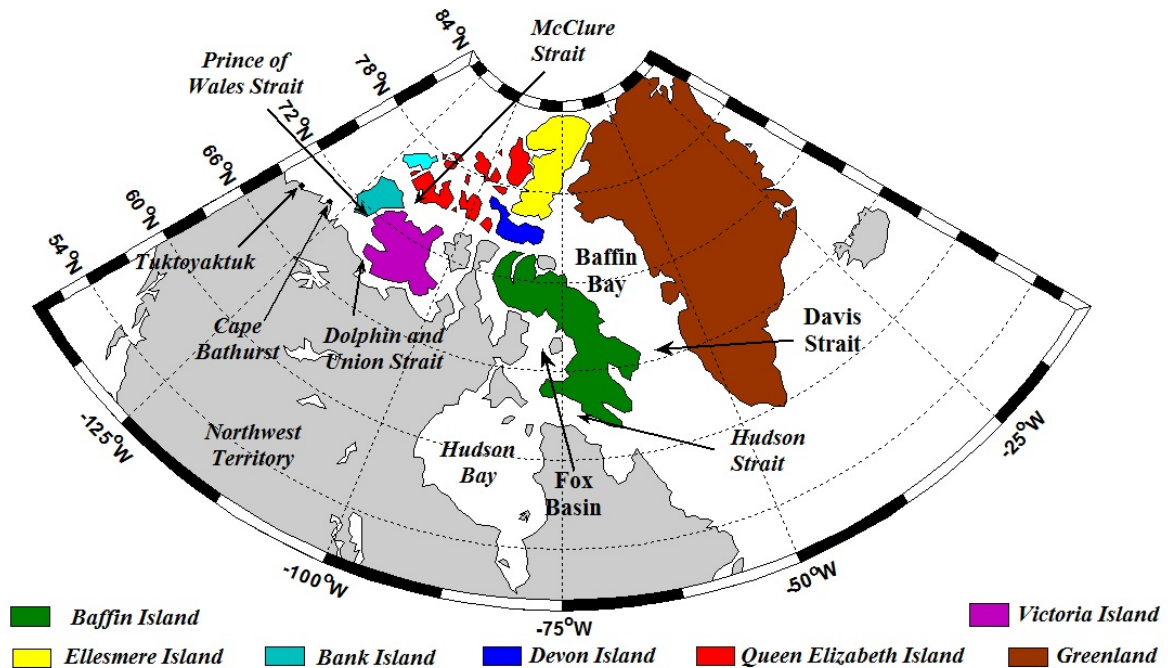


Figure 2.1: The Canadian Arctic Archipelago and Greenland.

Basins) (McLaughlin et al., 1996). The majority of the Atlantic water enters through the Fram Strait and meets the less dense Arctic surface waters. Then, the Atlantic water sinks to the intermediate layer of the Arctic Ocean known as the Atlantic layer and produces a thick layer located at a depth of approximately 300 to 500 m. A smaller portion of the Atlantic water entering the Barents Sea spreads over the Siberian plateau and is mixed with fresh water coming from Russian rivers (mainly the Yenisei, Ob and Lena) and then flows over these shallow shelves. In the fall it is cooled and enriched by salt due to ice formation (Rudels et al., 2000). According to Shimada et al. (2001), the Western Chukchi Summer Water (WCSW) with $S > 32$, is the summer shelf water which enters the Arctic Basin via the Chukchi Sea. The Eastern Chukchi Summer Water (ECSW) with $31 < S < 32$ and non-uniform spatial temperature comes from the Eastern Chukchi Sea and corresponds to the Alaskan Coastal Water (Coachman et al., 1975, Shimada et al., 2001). On the other side, the Pacific waters enter the Arctic Ocean through the Bering Strait. The Pacific waters are more significant in the Canadian Basin as it is shown in Figure 2.2 (Aagaard, 1981, McLaughlin et al., 1996, Jones et al., 1998). According to McLaughlin et al. (1996), the Pacific water intrusions in the western Canadian basin affect mixing in this region of the archipelago and modifies the stability of the water column. The characteristics of the Pacific water are seasonally modified in the Chukchi Sea (Figure 2.2) by ice formation, melting and heat exchange which produce different varieties of water masses (Shimada et al., 2001, Pickart, 2004), including the Bering Sea water masses. This seasonally modified water is generally divided into Bering Sea Winter Water (BSWW) and Bering Sea Summer

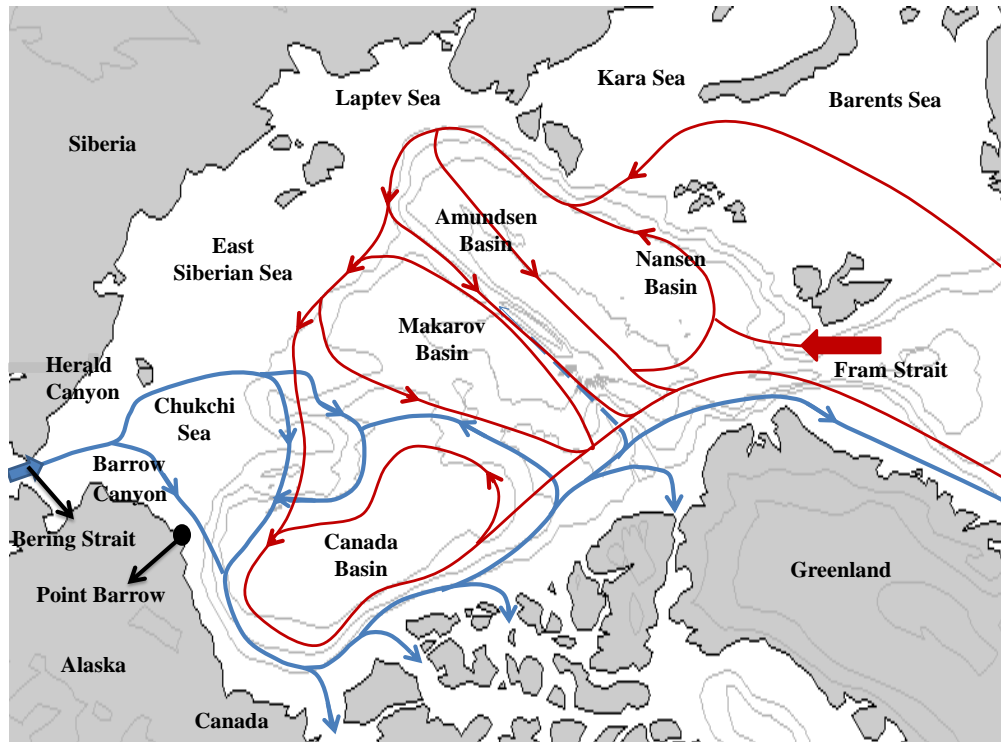


Figure 2.2: Pathways of the Pacific (blue lines) and Atlantic (red lines) waters in the Arctic Ocean. Modified after [McLaughlin et al. \(1996\)](#).

Water (BSSW) ([Ekwurzel et al., 2001](#)). During summer, the BSSW water layer is transported eastward by the Alaskan Coastal jet and penetrates into the Beaufort Sea through the Barrow Canyon (Figure 2.2) and then finally reaches the Canadian Arctic Archipelago (CAA). A branch of Pacific water passes through Herald Canyon situated in the west of the Chukchi Sea and then turns into the Beaufort Sea as shown in Figure 2.2. In winter, the western branch of Pacific water takes a northern direction after crossing the Bering Strait and is transformed in the Chukchi Sea by mixing with the fresh water from Russian rivers and ice formation. Because of their different routes and different source water characteristics, these waters preserve some of their original properties which enables the identification of their Pacific origin throughout the year ([Jones et al., 1998](#)). These differences in physical and also chemical properties between the Atlantic and Pacific waters can be used to determine their circulation paths and their relative contribution to the Arctic Ocean.

Vertical density structure The water column in the southeastern Beaufort Sea can be divided into four distinct layers. The black line in Figure 2.3 presents a Temperature-Salinity diagram (T-S diagram) sampled during the Arctic Internal Wave Experiment ([Levine et al. \(1986\)](#); black line) that shows different water layers in the middle of

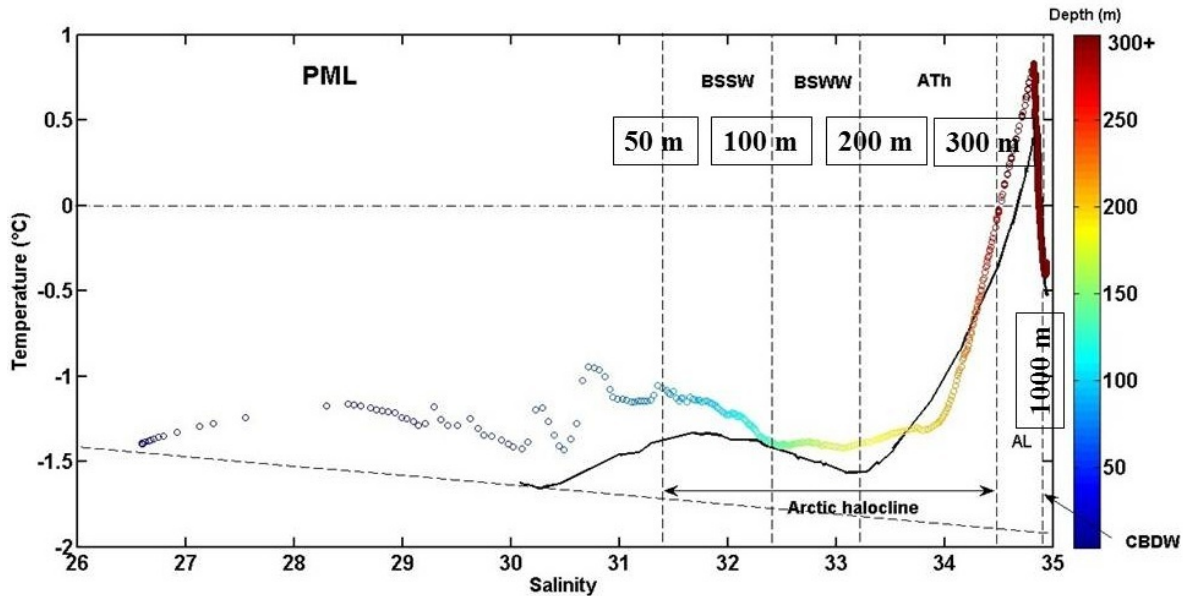


Figure 2.3: Schematic T-S diagram presenting a schematic vertical structure of the water column in the Southeast Beaufort Sea: the Polar Mixed layer (PML), the Bering Sea Summer Water (BSSW), the Bering Sea Winter Water (BSWW), the Arctic Thermocline (ATH), the Atlantic Layer (AL) and the Canada Deep Basin Water (CBDW). The depths are approximative. Modified after [Gratton et al. \(2012\)](#). The black line is Temperature-Salinity diagram sampled during the Arctic Internal Wave Experiment. The color circles are from ArcticNet-Geotraces cast 0903034.

Beaufort Sea. This figure also presents the density structure offshore of the Mackenzie River (color circles), within the study region.

The first layer is the Polar Mixed Layer (PML) with a typical thickness less than 50 m with salinity less than 31 and variable temperatures (see Figure 2.3). In the Arctic, the continental runoff and ice melting reduce the salinity in the surface layer. Lower salinity at the surface leads to an increase in stratification and inhibits mixing with the lower layers, whereas salt rejection due to the freezing in winter increases convection and generates more mixing ([Aagaard et al., 1981](#)). In general, this surface layer is subjected to seasonal influences that modify its physical characteristics. The combination of these phenomena is crucial for the formation of the surface layers of the Arctic basins ([Aagaard et al., 1981](#), [Carmack and Kulikov, 1998](#)).

The second layer is a cold halocline layer which is found between 50 and 250 m, with $\theta < 1^\circ\text{C}$ and $31 < S < 34.4$ ([Carmack et al., 1989](#), [McLaughlin et al., 2004](#)). The halocline is also indicative of the pycnocline, since the density is determined dominantly by the salinity. The importance of this cold halocline is that it isolates the surface ice covered water from the deep warmer water and inhibits the heat exchange between these

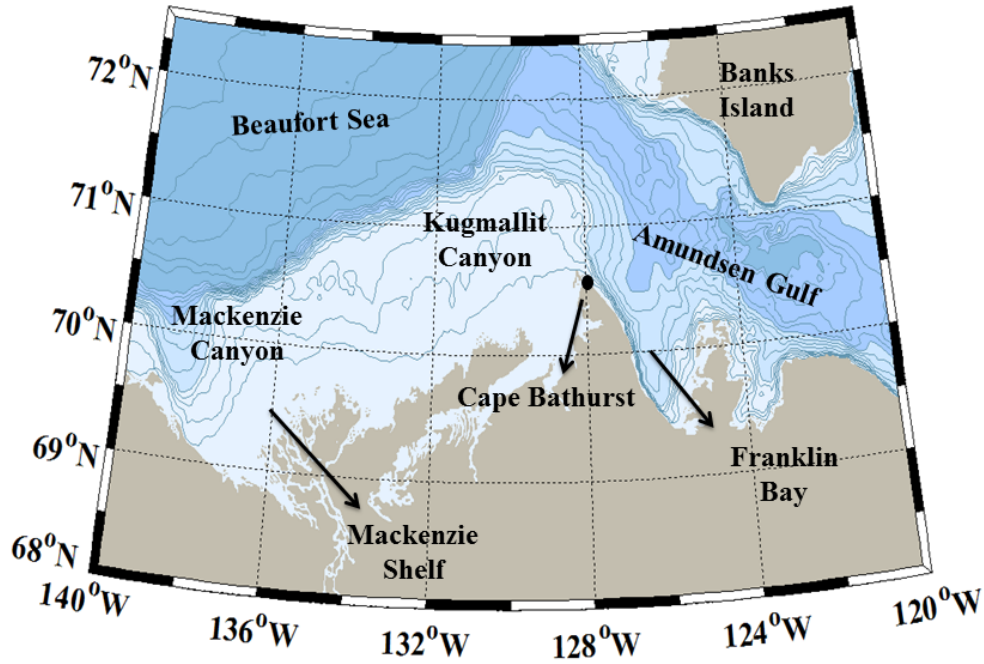


Figure 2.4: Map of the study area showing the different locations quoted in the text.

layers preventing ice melting (Aagaard et al., 1981, Rudels et al., 1996). The cold halocline is principally formed by Pacific waters and can be subdivided into three sub-layers as shown in Figure 2.3. The upper part of the Arctic halocline is composed of the summer Pacific waters that form a local temperature maximum located between 50-100 m, and corresponding with $31 < S < 32$. This layer is the BSSW (see Figure 2.3) with higher dissolved oxygen concentrations and lower nutrient concentrations (Jones et al., 1998). The intermediate halocline layer is located between 100 and 200 m and contains a temperature minimum ($-1.5 < \theta < -1.25^\circ\text{C}$) with a salinity of approximately 33.1 due to the BSWW waters (see Figure 2.3). The dissolved oxygen concentration decreases in this layer but it is rich in nutrients because the waters originate in the Bering and Chukchi Seas in winter when biological production is very low. Under the BSWW the Arctic Thermocline layer (ATh) forms the lower part of the halocline layer. The temperature increases sharply in this layer which is a transition to the Atlantic layer (AL).

The third layer is the Atlantic layer (AL shown in Figure 2.3) that underlays the Arctic halocline and is found at depths below 250 m, with $T > 0^\circ\text{C}$ and $S > 34$ (Rudels et al., 1994, Carmack and Kulikov, 1998). The temperature reverses in this layer, resulting in a decrease in the temperature with increasing depth (Carmack and Kulikov, 1998).

Finally, the fourth and last layer at the bottom of the Beaufort Sea is the Canada

Basin Deep Water (CBDW). This layer is relatively homogeneous with negative temperatures $\theta < 0^\circ\text{C}$ and a salinity $S \approx 34.9$ (Carmack and Kulikov, 1998).

2.1.2 Beaufort Sea and Amundsen Gulf

The Beaufort Sea is bordered by a line from Point Barrow in Alaska to the west of the Queen Elisabeth Islands in the western Canadian Archipelago (see Figure 2.2) has an area of about 450,000 km². The Southern Beaufort Sea is influenced by the Mackenzie River, the fourth largest river discharging into the Arctic Ocean (Yunker and Macdonald, 1995) and the largest in the Western Arctic. The waters on the Mackenzie Shelf (Figure 2.4) are affected by river flow, air temperatures, wind, current, coastal currents and vary seasonally (Macdonald, 2000). The Mackenzie flows into the Arctic Ocean through a vast delta and is a site of ecological importance for large colonies of birds, fish and marine mammals (Carmack and Macdonald, 2002).

In the Beaufort Sea, off the Mackenzie Shelf, the motion of ice and surface water is governed by the anti-cyclonic Beaufort Gyre which has the effect of accumulating important volumes of freshwater in the Canadian Basin surface layer (Newton et al., 2006). Under the surface, the water motion is reverse (cyclonic) and is known as the “Beaufort undercurrent”. The Beaufort Gyre and Beaufort undercurrent are shown in Figure 2.5. To the north, the Beaufort Gyre is bordered by the eastern Siberian current that traverses the Arctic flowing to the Greenland Sea through the Fram Strait. This transpolar current exports the ice out of the Arctic through the Fram Strait. The surface waters leave the Arctic mainly through the Fram Strait and follow along the Greenland and Iceland coasts where they play an important role in the deep convection formed in this region that feeds the global thermohaline circulation (Jones et al., 1998). Part of the surface water traverses the CAA where it largely determines the oceanic conditions in Baffin Bay and the Labrador Sea. The origin of these two outflows is different. The waters that leave the Arctic through the Fram Strait originate from the Atlantic (McLaughlin et al., 2004) while the waters that traverse the CAA originate, in large part, from the Pacific (Jones et al., 1998).

The circulation in our study region is strongly affected by external parameters, such as atmospheric circulation and river flows (Newton et al., 2006). This circulation can be divided into two types: the surface circulation, which is particularly important for the ice cover dynamics and the deep circulation. The exchanges between deep and superficial waters take place under the atmospheric influences known as upwelling or downwelling which are due to the indirect effect of wind. The westerly winds along

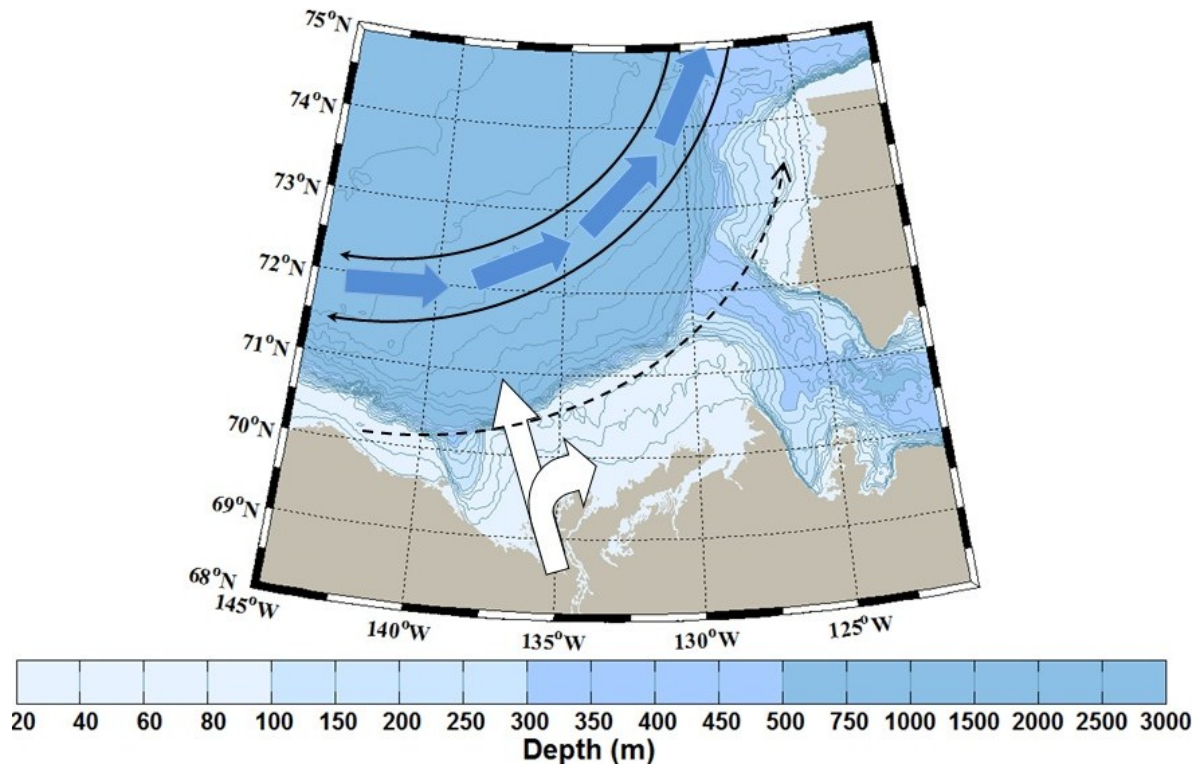


Figure 2.5: Circulation of the water on the Mackenzie Shelf: The surface anti-cyclonic Beaufort Gyre (solid black lines), the deep cyclonic Beaufort Undercurrent (blue arrows), the surface cyclonic coastal current (dashed line) and the Mackenzie River (white).

the coast push the surface water down (downwelling) and transport the freshwater to the Amundsen Gulf. The easterly winds along the southern Beaufort Sea coasts draw deeper waters to the shelf surface (upwelling) and push the surface waters away from the Mackenzie shelf (see Figure 2.6) (Williams and Carmack, 2008).

Wind-driven upwelling along the continental shelf of the Beaufort Sea in the late summer and also early fall downwelling could play important roles in the development of turbulence. According to Lukovich and Barber (2006), upwelling and downwelling are also responsible for the variability of the ice concentration in the region. The southern Beaufort Sea shelf is transected by two major submarine canyons, the wide Mackenzie Canyon and the narrow Kugmallit Canyon. In these Canyons the potential for upwelling is high (Carmack and Kulikov, 1998) (see Figure 2.4).

The Amundsen Gulf is located southeast of the Beaufort Sea (Figure 2.4). The boundaries of the Amundsen Gulf are Banks Island to the north, Victoria Island to the east and the coasts of the Northwest Territories to the south (see Figures 2.1 and 2.4). It stretches over 400 km in longitude and 150 km between Banks Island and Cape Bathurst, where it connects with the Beaufort Sea. The Amundsen Gulf is one of

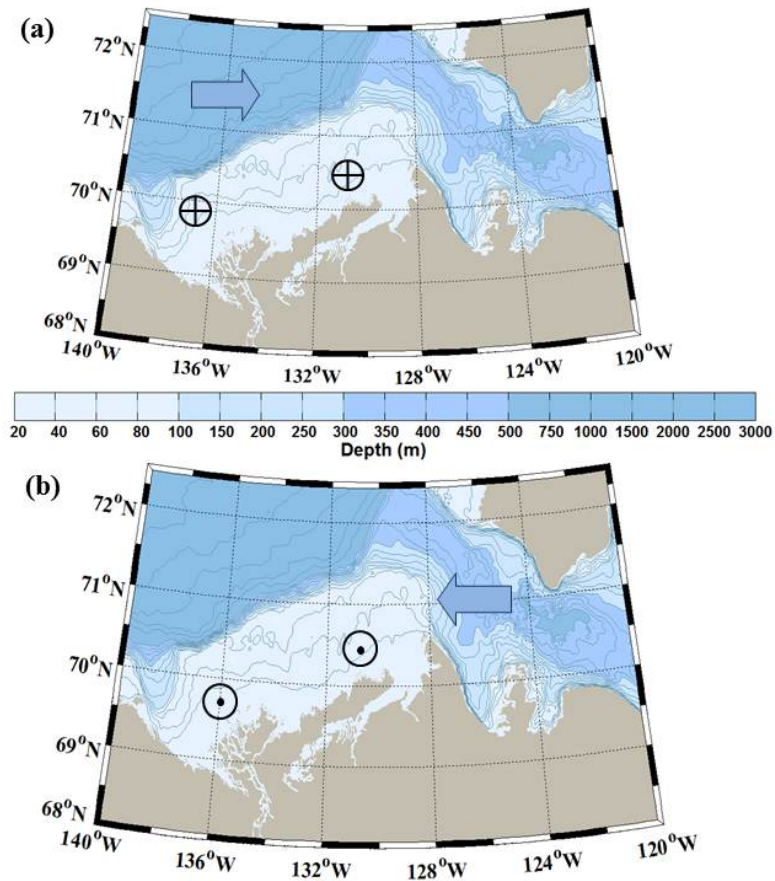


Figure 2.6: Wind forcing (blue arrow) and vertical water transport (downward: the circles with crosses and upward: the circles with points).

two possible western endpoints of the Northwest Passage, which may have an increasing importance as a shipping route in the future because of climate changes (Peterson et al., 2008). The Amundsen Gulf contains one of the largest polynyas in the Arctic, known as the Cape Bathurst Polynya. This polynya is one of the largest habitat for birds and mammals (see below).

Ice Ice cover variations as well as climate changes in the Arctic are affected not only by the atmospheric circulation patterns, but also by the circulation of Arctic surface waters. Air temperature plays an important role in sea-ice freezing and melting. Hence, the ice cover changes seasonally in the Canadian Beaufort Shelf region as it is described by Carmack and Macdonald (2002). At the end of winter when freezing days stop accumulating (end of April) four different regions are identified based on the characteristics of the ice cover.

- i. **Landfast ice** The landfast ice is sea ice that has frozen along the coasts. The maximum thickness that landfast in the Arctic is 2 m (Galley, 2009, Wadhams, 2000).
- ii. **Stamukhi** Convergence of ice causes the formation of stamukhi or inverted dams of broken ice that may occasionally reach the bottom. Near the coast, the stamukhi impounds the flow of fresh upper water of the Mackenzie and underlying brackish sea water and forms a seasonal lake known as Lake Herlinveaux (Carmack and Macdonald, 2002). In the ice breakup season, the combination of relatively warm water increases the melting of sea ice and forces the opening of stamukhi which in turn releases water from Lake Herlinveaux (Carmack and Macdonald, 2002).
- iii. **Polynya** Beyond the stamukhi there is a flaw polynya or an occasionally open water area throughout the winter period. Polynyas are areas partially or completely free of ice in ice-covered regions. This lead is usually generated when the Arctic ice pack moves away from the coast, pushed by the winds. Generally, the polynyas are formed by two different mechanisms. Firstly, in a “latent heat” polynya, ice may form within a region and be continually removed by wind and/or currents. The latent heat of ice melting provides balance to the heat loss and maintains the open water. Secondly, in a “sensible heat” polynya, relatively warm water may enter the region and prevent ice formation (Smith et al., 1990). In the polynya, the salt rejection at the water surface due to ice formation creates convective mixing. The third largest polynya in area in the Arctic is located in the Amundsen Gulf and is known as the Cape Bathurst polynya. There is high inter-annual variability in ice dynamics in Cape Bathurst polynya as well as its

duration and extent of opening. Satellite observations show that the ice dynamics in this region is mostly controlled by easterly winds (Fett et al., 1994). Owing to storm and wind events, large flaw leads form near Cape Bathurst and off the west coast of Banks Island (Arrigo and VanDijken, 2004).

- iv. **Arctic packs** Finally, seaward of the flaw lead, there are the drifting first-year and multiyear polar packs that move freely on the ocean surface.

Seasonal ice cover in the region Ice breakup in the Mackenzie River starts in the upstream region of the river in late April and continues progressively downstream to the delta until around the end of May. The river discharge increases progressively in the second half of spring and reaches its peak between mid-May and June which leads to flooding in the estuary. The accumulation of freshwater river runoff creates increased pressure and attempts to force its way into the ocean. During this period of the year, high turbidity and warm geysers exiting through the holes and cracks in the ice are frequent in the Mackenzie area. In late July and early August, the shelf may still be covered by ice, while by the end of September the shelf is ice free. The landfast ice vanishes and the heat from solar radiation warms the river water resulting in additional ice melt. The Mackenzie River continues to pour large amounts of freshwater into the ocean and forms a plume of low salinity and high turbidity water. The plume from the river imposes a strong stratification of surface layers in the top 5 to 10 meters. This stratification during the summer is produced not only by the runoff but also by the melting of surface sea ice. In the absence of wind, the outflow of the Mackenzie River tends to turn eastwards because of the Coriolis force and flows along the Tuktoyaktuk Peninsula and entering into the Amundsen Gulf (shown in Figure 2.6). The ice reaches its minimum value in mid-September. At this time the freshwater due to ice melting and runoff is found all over the Canadian Shelf. Freezing begins a few weeks later. Storms during summer and early fall mix the surface water and during winter, when the sea is ice-covered, wind effects are diminished while density-driven flows due to brine release dominate (Melling and Lewis, 1982).

Tidal currents are not a major source of mixing energy in the Arctic (Kowalik and Proshutinsky, 1994). The tidal currents on the Canadian Shelf as in the other Arctic Seas are generally weak, except in the area surrounding the shelf break north of Cape Bathurst where the strong tidal currents are a source of mixing (Williams and Carmack, 2008).

2.2 Available data

The data used in this study originate from four large research projects between 2002 and 2009 in the Arctic waters. They include the Canadian Arctic Shelf Exchange Study (CASES, 2002-2006), ArcticNet (2004-2018), the Circumpolar Flaw Lead system study (CFL, 2006-2011) and Malina (2008-2013).

The CTD-Rosette is a sampling instrument that is very often used in oceanography because it combines water sampling and properties profiling. The Rosette includes a SeaBird 911 plus CTD (Conductivity, Temperature and Depth) profiler attached at the base of a circular frame that accommodates 24 Niskin bottles (see Figure 2.7). This instrument measures simultaneously the temperature (T), conductivity (C) and the hydrostatic pressure (p). Salinity (S) is calculated from electrical conductivity and temperature. The frequency of sampling of this instrument is 24 Hz and its descent rate is approximately 1 m s^{-1} . Data validation was carried out by Pascal Guillot of the groupe interinstitutionnel de recherche océanographique du Québec (Québec-Océan), following the standards of UNESCO. A SBE-43 CTD sensor is also attached to measure the dissolved oxygen concentrations. The processing steps include calibration of coefficients, data conversion to physical units, alignment correction and extraction of bad data. During winter, the Rosette is deployed from the ship's moonpool which is an opening in the ship's hull. The moon pool can be opened when the ship is stationary to allow the deployment of sampling instruments during the winter.

CTD casts are labeled according to specific rules whereby the cast identification is a concatenation of three parts. Assuming a cast with the name of $xyyzzz$, the first part (xx) indicates the year of sampling, the second part (yy) is a sequential Québec-Océan cruise number, and the third part (zzz) is the sequential cast number. It should be noted that the combination of year and sequential cast number (xyy) gives the leg number. For example 0803001 shows that this measurement has been done in 2008, in the third cruise in that year, and is the first cast of the leg (0803).

2.2.1 CASES (2002, 2003 and 2004)

The CASES program was a multidisciplinary international program aimed at studying the ecosystems of the Mackenzie Shelf and Amundsen Gulf (see Figure 2.8). The particularity of CASES is that it included a large community of scientists in all fields of Arctic oceanography (physical oceanography, meteorology, glaciology, biogeochemistry, polar biology, etc.), giving them the opportunity to work together and share a vast amount



Figure 2.7: Rosette and CTD on the CCGS Amundsen.

of data. Two different expeditions were carried out during the CASES program. The first expedition was carried out on board the Canadian Coast Guard Ship (CCGS) Pierre Radisson between September and October 2002 (138 CTD casts). The second part of the program was carried out between September 2003 and August 2004 aboard the CCGS Amundsen (836 CTD casts). During this expedition the ship remained at a fixed station ($70^{\circ}02.71$ N and $126^{\circ}18.06$ W) in Franklin Bay (see Figure 2.8) between 9 December and 30 May. It was the first time a research icebreaker remained for such a long time in the Amundsen Gulf.

2.2.2 ArcticNet 2005 and 2006

ArcticNet is a Network Center of Excellence in Canada (2004-2018) that brings together more than 145 scientists in different fields of study who collaborate to study the impacts of climate change in the coastal Canadian Arctic. The ArcticNet data used in this study were obtained during the summer of 2005 and fall of 2006. The data in the Amundsen Gulf and Beaufort Sea were sampled in 2005 (leg 0501), between September 1st and 14th of 2005 (63 casts), in 2006 (leg 0603) between the 30th of September and the 19th October of 2006 (73 casts). The map of the sampling locations during ArcticNet in 2005 and 2006 is shown in Figure 2.9. Since the sampling in the fall of 2007 (leg

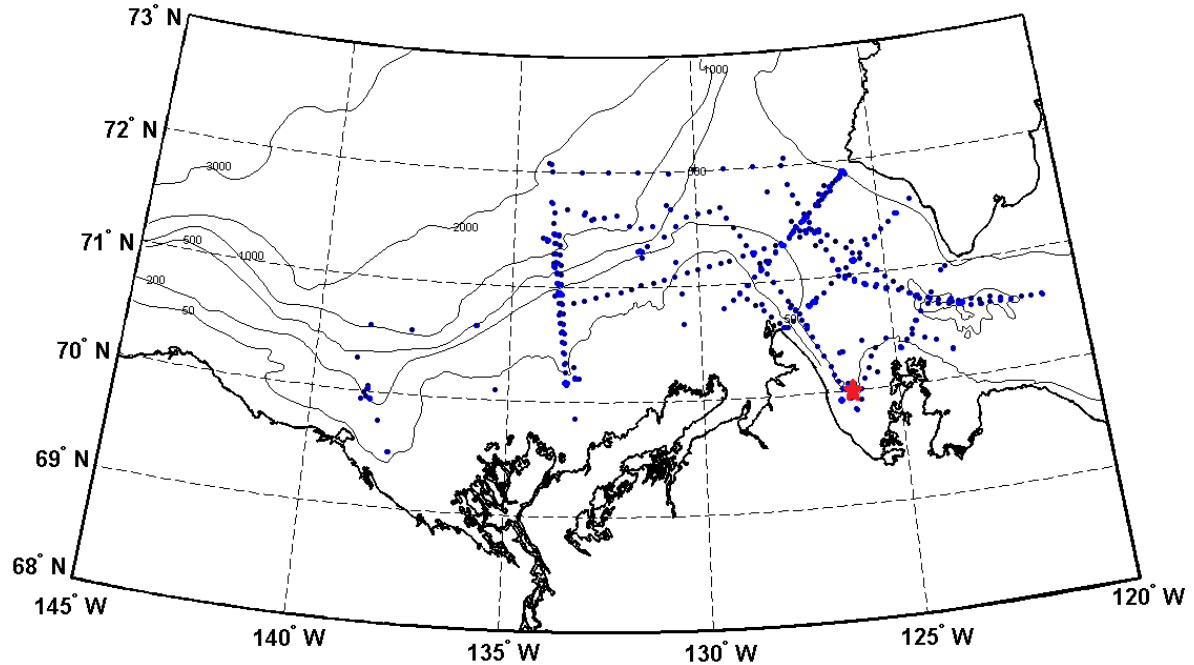


Figure 2.8: Sampling stations in 2002, 2003 and 2004 during CASES. The location of the fixed station (between December 2003 and 30 May 2004) is identified by a red star.

0706) between the 28th of September and the 18th of October was carried out jointly by ArcticNet and CFL, the sampling in leg 0706 is shown in Figure 2.10 with the other legs of the CFL program.

2.2.3 CFL 2007 and 2008

The Circumpolar Flaw Lead is a permanent characteristic of the central Arctic that is formed when the central mobile ice pack moves away from coastal fast ice. This flaw lead which is circumpolar, begins forming in the fall and during the winter is covered by thin ice that exists throughout the winter.

The Circumpolar Flaw Lead (CFL) project involved large numbers of ocean and atmosphere specialists with observations and modeling backgrounds. The sampling in the Beaufort Sea and Amundsen Gulf was done between September 2007 and August 2008 (1023 casts). This program was conducted on the Mackenzie Shelf and in the Amundsen Gulf to examine the impacts of climate change on the nature of the flaw lead. Furthermore, the effect of these changes on the marine ecosystem, contaminant transport, carbon fluxes, and the exchange of greenhouse gases across the air-sea interface was studied. The program focused on the oceanic and atmospheric forcing of the ice cover in these regions in order to describe how these physical processes impact biology

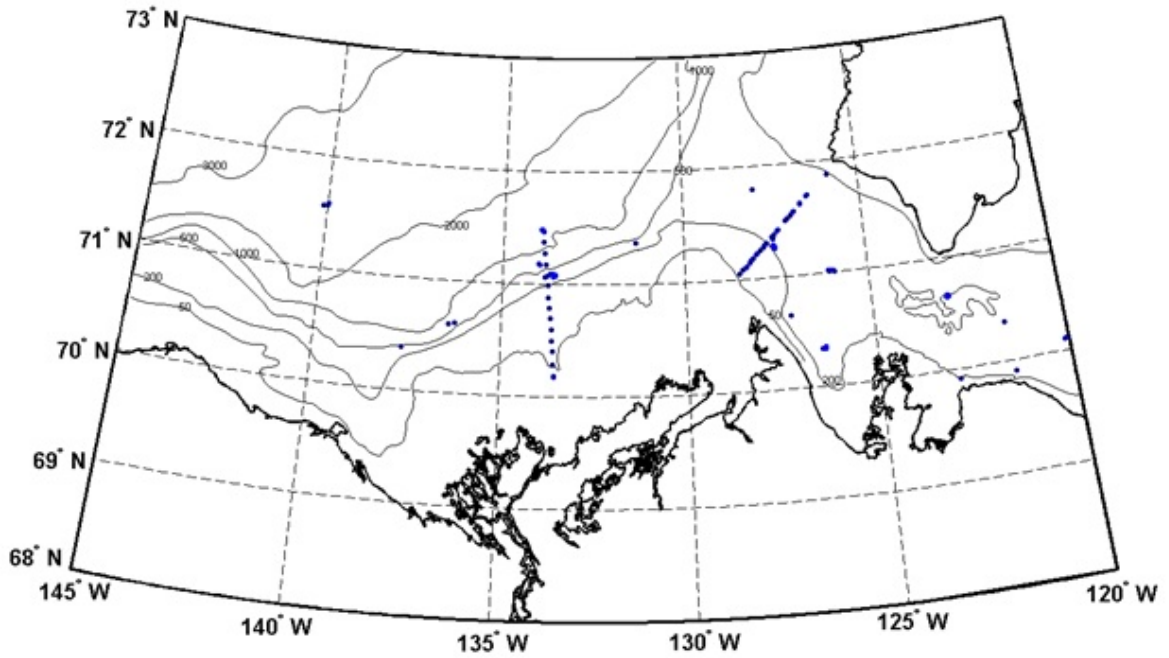


Figure 2.9: Location of the sampling stations during ArcticNet 2005 and 2006.

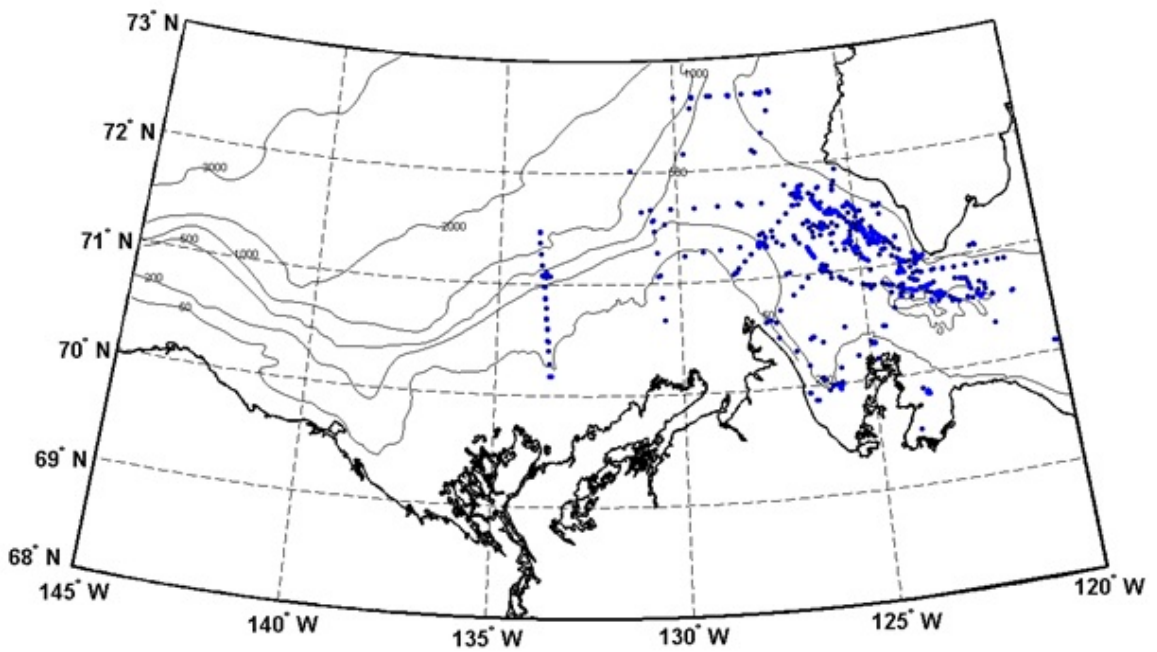


Figure 2.10: Location of the sampling stations in 2007-2008 during the CFL program.

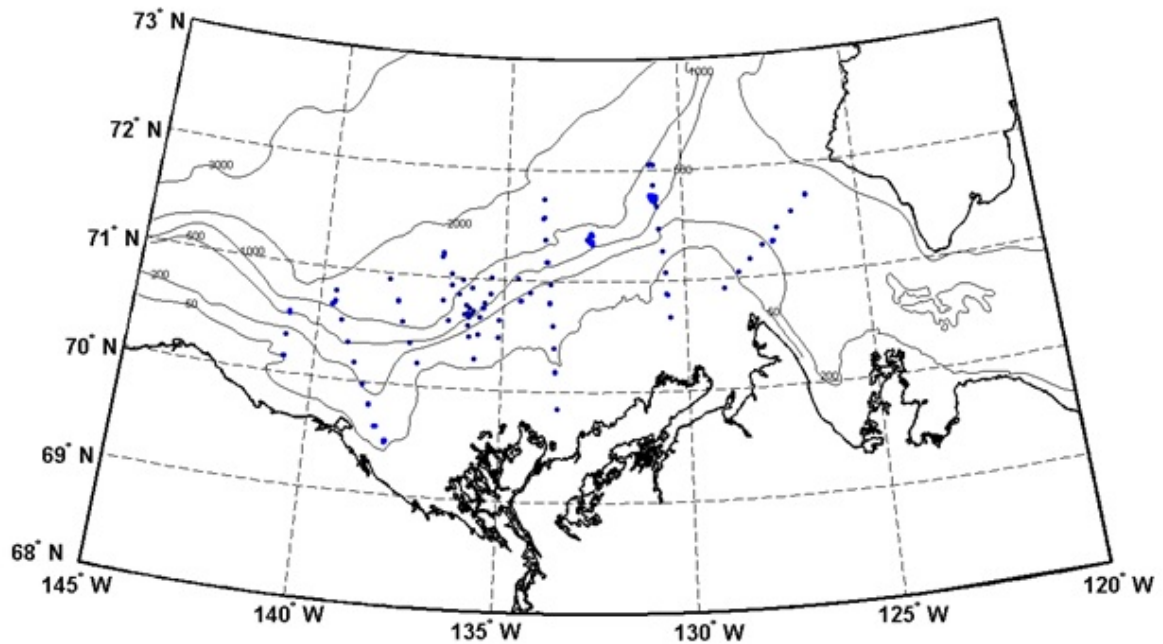


Figure 2.11: Location of the sampling stations in 2009 during the Malina program.

within the Arctic. This was the first time a research icebreaker stayed mobile during a winter in the circumpolar flow lead of the Beaufort Sea and Amundsen Gulf. The only other ship which overwintered in the Arctic was the CCGS Des Groseilliers which drifted with the central ice pack in the winter of 1998 during the American SHEBA (Surface Heat Budget of the Arctic Ocean) (Macdonald et al., 2002).

Sampling during CFL started in “transect mode” in open-water sites in the Amundsen Gulf and the southern Beaufort Sea from 18 October 2007 up to 27 November 2007. The winter sampling stations were of three types: drift stations, landfast ice stations and open-water stations. In Drift stations, the ship enter the ice and drifted with large ice floes. The “drift mode” included 44 stations, visited between 28 November 2007 and 31 May 2008 in the northern Amundsen Gulf and south of Banks Island. The ship spent approximately 4-5 days in each drift site with the maximum duration of 30 successive days on the same ice pack (Station D19). The fast ice sampling sites between May and June were mostly visited in the ice melt season. The majority of landfast stations were located on the south of the Amundsen Gulf between Franklin Bay and Darnley Bay (see Figures 2.10 and 5.3). Some landfast ice sampling was also done in Prince of Wales Strait. There were 17 fast ice stations with an average sampling time of 3.5 days. The longest station lasted 10 days. Open-water sampling then continued until the August 7. A map of the sampling stations during the CFL is shown in Figure 2.10.

2.2.4 Malina (2009)

An ice free ocean leads to an increase in absorbed solar radiation, permafrost thawing, and growing river runoff which is responsible for more organic carbon export to the ocean and results in an increase in atmospheric CO₂. To determine and monitor the balance of these processes, an extensive study in the Mackenzie River / Beaufort Sea system was conducted in July and August 2009 aboard the CCGS Amundsen (leg 0902). Figure 2.11 shows the summer of 2009 sampling stations (186 casts) during Malina.

2.3 Summary

In this study, I will focus mostly on the data from two full years of sampling: CASES 2003-2004 and CFL 2007-2008. This large data base provides a unique opportunity to study the temporal (seasonal and inter-annual) and spatial evolution of the mixed layer in the southern Beaufort Sea and Amundsen Gulf. It should be noted that with the exception of SHEBA there is no other winter data set for the Canadian Beaufort Sea. Moreover, the CASES and CFL are the only two twelve month data sets. The different sampling situations during these two years give us a chance to study the effect of ice cover on the mixed layer variations.

CHAPTER 3

METHODS TO ESTIMATE THE MIXED LAYER DEPTH

3.1 Introduction

In the present chapter four different methods to estimate the mixed layer depth are assessed and compared using various statistical and observational techniques. Three issues are addressed in this chapter. Firstly, I explain why density profiles are used for *MLD* computations in the present thesis. Secondly, I describe four different methods for the estimation of *MLDs* namely, the threshold method (Schneider and Müller, 1990), Thomson-Fine (TF) method (Thomson and Fine, 2003), a modified version of the TF method (TFL) and, the Holte-Taley (HT) method (Holte and Talley, 2009) modified by the author (HTN). Finally, the results emerging from these methods are compared and I select the most appropriate method to be used in the rest of the thesis.

It should be kept in mind that the estimation of the *MLD* is not always straightforward and uncertainties may exist because of the complexity of the mixed layer processes. For example, although the physical parameters are relatively uniform within the ML, there are always slight variations which may complicate computerized *MLD* calculations. However, the present chapter is an attempt to clarify the difficulties associated with *MLD* estimation in the Arctic and to present a way to best overcome the complexities of this region.

3.2 Density in the Arctic

Density varies with temperature, salinity and pressure. The relationship between density, temperature and salinity is illustrated in the temperature-salinity ($T-S$) diagram presented in Figure 3.1. Density (ρ) increases with salinity and pressure and decreases

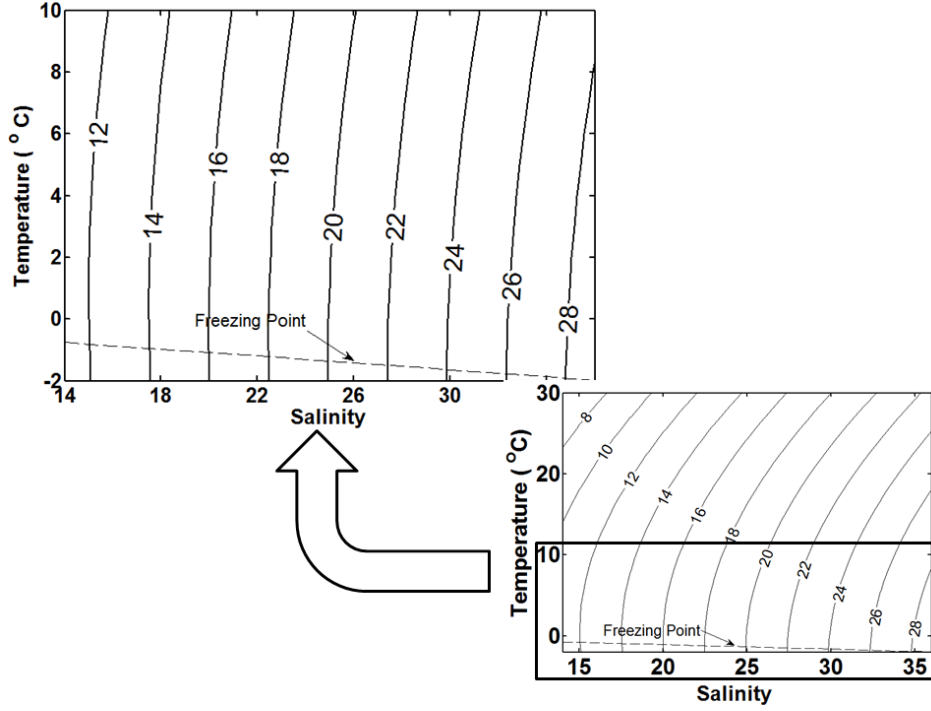


Figure 3.1: Temperature-Salinity ($T - S$) diagram showing the density minus 1000 (σ_t) isolines in kg m^{-3} . The dashed line is the freezing temperature as a function of temperature and salinity. Note that the smaller figure at the bottom right shows the density isolines for the temperature between -2 and 30°C .

with increasing temperature. Figure 3.1 also shows that the relation between density and both temperature and salinity is nonlinear. In the Arctic, where the temperature is low, the density is dominated by the salinity. For temperatures lower than 10°C (Arctic) and especially for $T < 0^\circ\text{C}$ (Arctic winter) the density isolines are parallel to the temperature axis. Even though one can assume that the salinity has a dominant role on density in our region of study, the effects of temperature and salinity on density are analyzed here in more details to make sure that this assumption is also valid for warmer periods of the year.

The effect of salinity and temperature on density can be examined using equation 3.1 (Sarkar, 2007), where T_{mean} , T_{max} , T_{min} and S_{mean} , S_{max} , S_{min} are respectively the monthly mean, maximum and minimum values of temperature and salinity at six depths. In this equation, R represents the ratio of density variation due to the temperature variation (between its minimum T_{min} and maximum T_{max} values) when the salinity is constant (S_{mean}) to the density variation due to the salinity variation (between its minimum S_{min} and maximum S_{max} values) when the temperature is constant (T_{mean}).

$$R = \frac{\rho(T_{min}, S_{mean}) - \rho(T_{max}, S_{mean})}{\rho(T_{mean}, S_{max}) - \rho(T_{mean}, S_{min})} \quad (3.1)$$

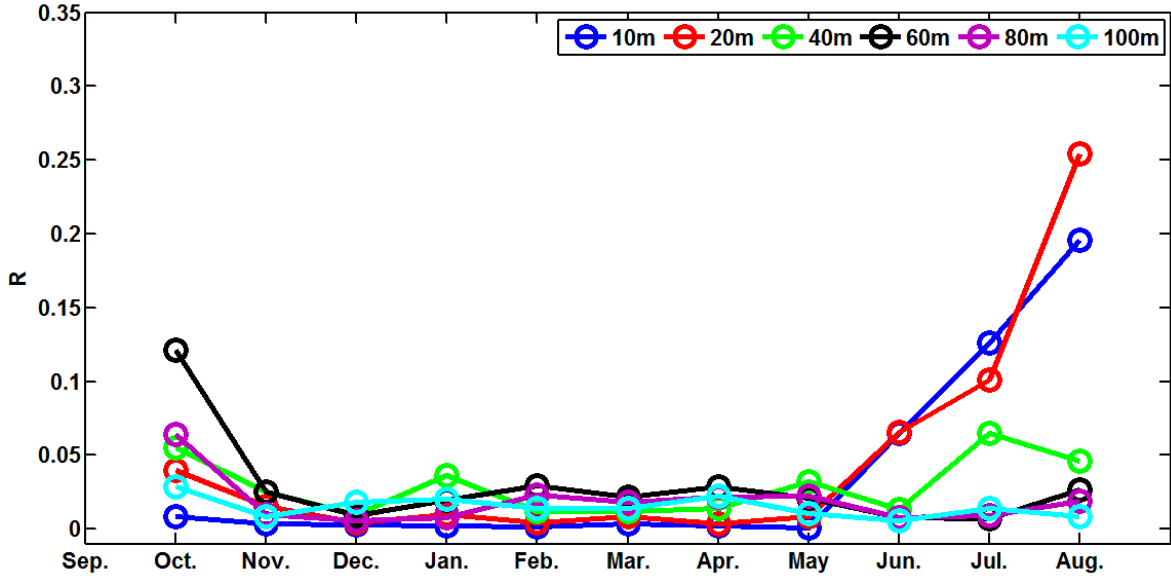


Figure 3.2: Monthly values (in 2003-2004) of R at different depths illustrating the temperature and salinity effects on density. Values of $R < 1$ indicate that salinity effects are dominant.

In other words, $R > 1$ and $R < 1$ respectively show that temperature and salinity play dominant roles in the density determination. Figure 3.2 presents R values at different depths calculated for CASES data.

As shown in Figure 3.2 the monthly R at different depths is always less than one which means that the density is more sensitive to the salinity in this region, as was expected. R is very small and near to zero due to the high value of its denominator which shows the very dominant effect of salinity between November and May. As previously noted, in cold and salty water, the density is more sensitive to the salinity than temperature. The fact that R is near zero at depths of 10-20 m from December to May confirms that the salinity is dominated over temperature for density determination. Although the value of R is larger between June and October (see Figure 3.2), this value is still much lower than 1 which shows the dominant role of salinity in density determination in warmer periods of the year.

The density is a very important property of sea water since, for example, a small variation in density due to cooling or heating can lead to strong currents. Moreover, the stability of the water column is related to the density at each depth. Since the variation of density in the ocean is entirely in the last two digits (in the range between 1000 and 1028 kg m⁻³), it is simpler to use $\sigma_t = \rho(S, T, P) - 1000$ instead of ρ (Pond and Pickard, 1983). In order to eliminate the adiabatic heating and cooling effect it is more appropriate to use potential temperature (θ) instead of in situ temperature (T).

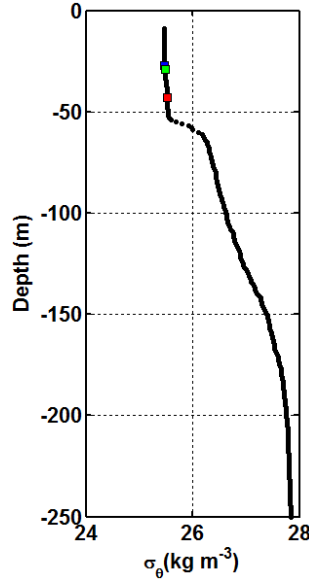


Figure 3.3: Example of *MLD* estimation with the threshold method using profile 076 from leg 0801 (sampled on 13 January 2008). The blue, red and green squares are for thresholds of 0.03, 0.04 and 0.05 kg m⁻³ respectively. In this case a larger threshold value would be needed.

It is worth mentioning that there is not generally a large difference between θ and T in the surface layer especially at depths less than 100 m. The calculated density using potential temperature is called potential density $\sigma_\theta = \rho(S, \theta, 0) - 1000 \text{ kg m}^{-3}$ which is used in this study in order to calculate the *MLD*.

3.3 *MLD* estimation methods

In this section four methods to calculate the *MLD* are presented. In section 3.3.4 some other methods used in other studies are briefly discussed.

3.3.1 Threshold method

The threshold method (TH) is the simplest method for estimating *MLDs*. This method can be used based on temperature, salinity and density profiles with different threshold values. According to this method the *MLD* is the depth at which the temperature or potential density difference exceeds a predefined amount (called the threshold) with respect to the surface reference value (Schneider and Müller, 1990, Kara et al., 2000). Although the basic idea is the same the threshold values used for *MLD* calculations

are different from one region to another. Kara et al. (2000), de Boyer Montégut et al. (2004) examined numerous profiles to find the optimal threshold criteria to calculate the *MLD*. de Boyer Montégut et al. (2004) suggested the threshold values of temperature and density for the global ocean as 0.2°C and 0.03 kg m^{-3} respectively. Chaigneau et al. (2004) calculated the *MLD* based on a density profile using a threshold value of 0.02 kg m^{-3} while Christensen and Pringle (2012) and Toole et al. (2010) calculated the *MLD* using the threshold method based on a density profile with a threshold value of 0.01 kg m^{-3} . Levitus (1982) used a threshold value of 0.5°C in order to calculate the *MLDs*. In the present study different threshold values ranging between 0.01 and 0.05 kg m^{-3} are used. Figure 3.3 shows an example of the threshold method with values of 0.03 , 0.04 and 0.05 kg m^{-3} , larger thresholds leading to unreasonably high *MLDs*. As shown in this figure, even for the largest value (0.05 kg m^{-3}) the *MLD* is sometimes underestimated with these thresholds in our study region.

Figure 3.4 shows the density at different depths, i.e. at 10 m below the surface, *MLD*, *MLD*+ 3 m and *MLD*+ 10 m during the winter when the *MLD* is calculated using threshold method with the threshold values of 0.03 , 0.04 and 0.05 kg m^{-3} . The depth of 10 m was considered to be the surface since the shallowest depth of sampling in the winter was 10 m . As shown in this figure, the density at a depth of 10 m almost entirely coincides with the density at the *MLD* for all threshold values. This is consistent with the fact that the density is constant at the *MLD*. The density at *MLD*+ 3 m is also very similar to the density at *MLD*, for the most part. This means that the *MLDs* are underestimated by these threshold values. The analysis of numerous density profiles show that a single-value threshold may not be capable of estimating the *MLD* in the present study region.

3.3.2 TF and TFL methods

Thomson and Fine (2003) used the “split and merge” algorithm of Pavlidis and Horowitz (1974) in order to compute the *MLDs*. The algorithm fits a number of linear segments to a data profile such as the density profile. Then the curve is reproduced by defining the locations of a set of break points with the minimum number of segments, while the difference between the observed and fitted curves becomes smaller than a pre-defined error norm. The predefined error norm is the root-mean-square difference between observed and fitted curves for a given cast. The break points locate where the slope of the profile changes. At each step the difference between the original profile and the approximated fitted segments is verified and once this difference becomes larger than a given threshold the segment gets split into two linear equal-length segments. The same length means that each segment must contain the same number of points. Two

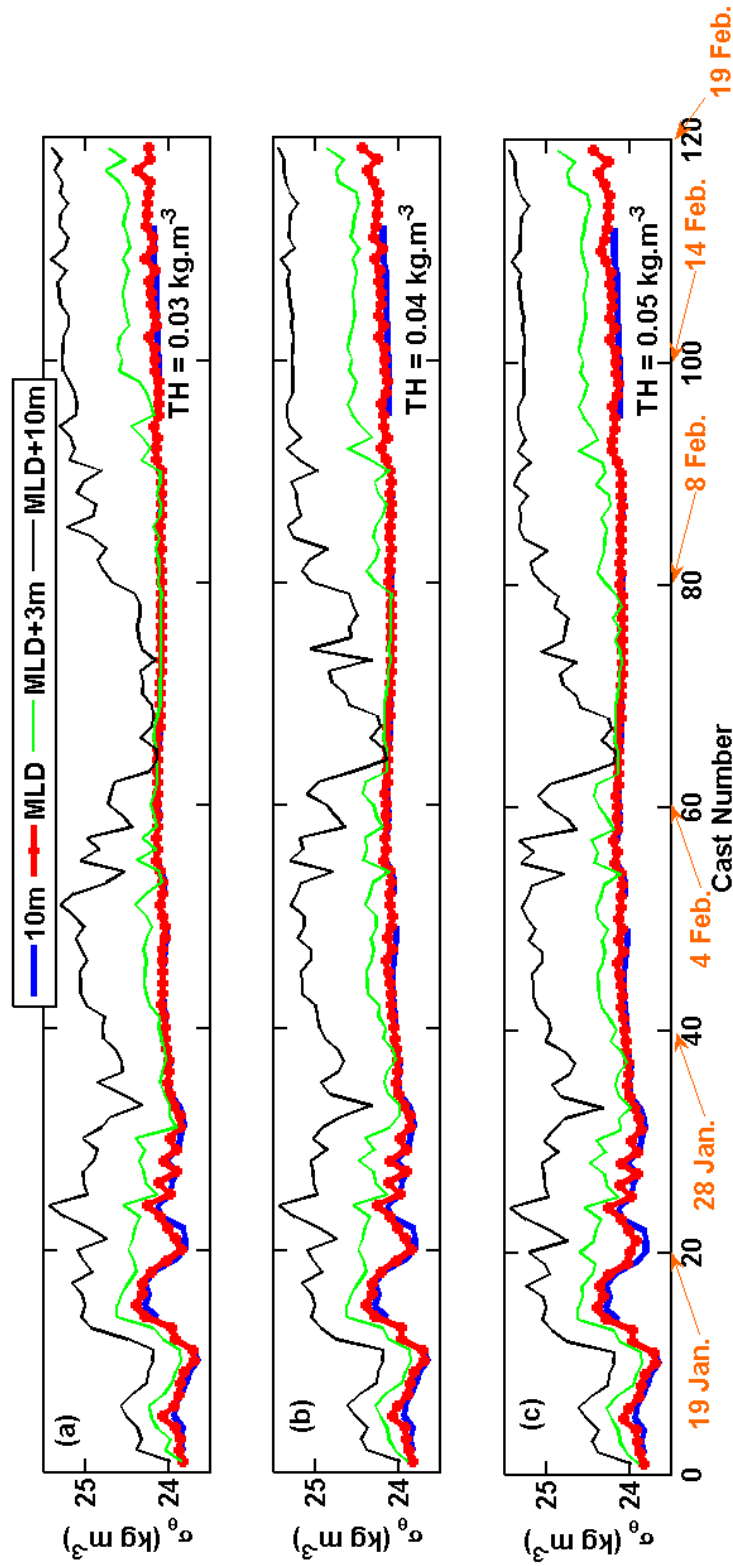


Figure 3.4: Potential density time series for the months of January and February 2004 at the CASES winter station. Only two months are shown to make the graphs more legible. The thick red lines are the *MLD* density estimated with the threshold method using 0.03 kg m^{-3} (panel a), 0.04 kg m^{-3} (panel b) and 0.05 kg m^{-3} (panel c). The blue line is the density at 10 m. The green and black lines are the densities at *MLD*+3 m and *MLD*+10 m. The reason behind the choice of the last two will become obvious in chapter 5.

segments may merge in to a new one as soon as the new segment respects the error norm. Based on this technique, the *MLD* is defined as the depth of the junction of the first two segments.

Because of some fluctuations in the density profiles, the estimated *MLDs* using the TF differed from the visually estimated *MLD*. In some instances when a profile has no real critical point, the TF algorithm detects some and conversely in a profile with several critical points the algorithm may fail to detect all of them. To improve the *MLD* estimation with the TF method, some modifications have been proposed by Véronique Lago (2006) (unpublished report, INRS). Modifications in the TF method were mainly added to the segment splitting algorithm. In order to minimize the effects of the fluctuations in the density profiles, a weighted moving average filter is applied to the original data before it is processed. Then, instead of splitting a segment into two equal segments and moving the junction points to reduce the error, the TFL method sets the junction points where the gradient in the data is the largest. Furthermore, the splitting of a profile with the TFL method starts from the bottom while in the TF method the analysis of the segments starts from the surface. In addition, four conditions are also imposed to avoid selecting spurious critical points. The conditions are the following.

- i. The gradient at a splitting point should be more than a chosen error norm (0.05). This prevents the algorithm from splitting a segment that could turn out to be the *MLD*. Figure 3.5a shows that this condition in the TFL method may occasionally help to better estimate the *MLD*. A set of error norms between 0.01 and 0.05 have been tested and finally a threshold of 0.05 has been selected for the rest of the study.
- ii. The second condition prevents splitting of a segment if the next segment has no significant gradient. This condition avoids choosing the *MLD* inside a region with no important gradient due to occasional small and arbitrary fluctuations in the profile. Figure 3.5b shows that the TF method estimates the *MLD* inside a region with no significant gradient.
- iii. The third condition prevents splitting the curve where the gradient in a new segment is significantly similar to the previous one. This condition ensures that the segment will not be divided without showing significant changes.
- iv. Another condition is imposed in the merging step such that the segments are merged together if their gradients are sufficiently close. In the present thesis, the *MLD* is calculated by both the TF and TFL methods with error norms of 0.01, 0.02, 0.03, 0.04 and 0.05 kg m⁻³.

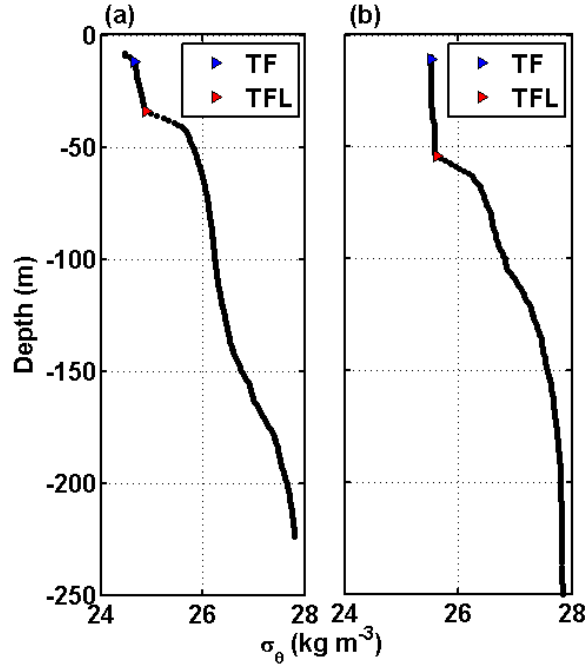


Figure 3.5: Example of *MLD* estimations with the TF and TFL methods for two profiles: (a) cast 075 from leg 0402 (CASES) and (b) cast 124 from leg 0801 (CFL), two winter profiles.

3.3.3 HT and HTN methods

Holte and Talley (2009) calculated possible *MLDs* with different methods including the threshold, gradient and pycnocline methods using density, temperature and salinity profiles. The method of Holte and Taley (HT) selects the final *MLD* with respect to certain conditions. In this method, two different algorithms are used for summer and winter in the South Pacific and Atlantic oceans (Holte and Talley, 2009). The HT technique determined the *MLD* using different methods based on the particularity of each profile.

A similar multi-method approach as HT is adopted by the author (HTN method) for the present region of study. In the HTN method only density profiles are used and the same algorithm is used during summer and winter. The algorithm calculates four possible *MLD* using the deepest minimum density (MD), threshold method, gradient density method (GD) and pycnocline fit method (PYCN).

The HTN approach can be summarized as follows:

- i. The algorithm initially calculates the deepest level at which the density is mini-

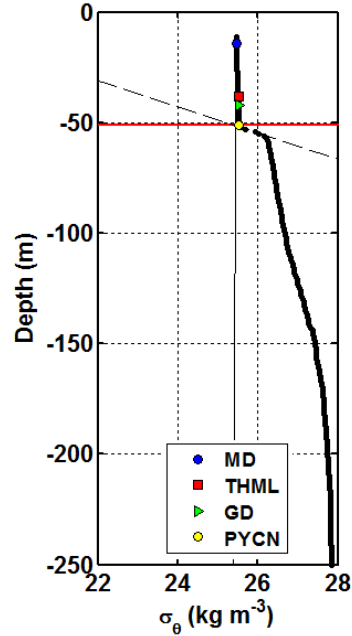


Figure 3.6: Example of *MLD* estimation with the HTN method using profile 080 from leg 0801. The red line is the final *MLD*.

- mum (MD) and places the *MLD* equal to the MD (blue circle in Figure 3.6).
- ii. It then uses the threshold method with a threshold of 0.05 kg m^{-3} to find the *MLD*. The *MLD* obtained in this step is called the TH. The algorithm then chooses the *MLD* equal to TH, if TH depth is larger than MD and difference between the density in TH and surface is less than 0.4 kg m^{-3} (red square in Figure 3.6).
 - iii. In the next step, the algorithm calculates the *MLD* using the gradient method (GD). Starting from the surface, the algorithm chooses the first depth at which the potential density gradient ($d\sigma_\theta/dz$) is larger than 0.05 kg m^{-4} . The algorithm then chooses the *MLD* equal to the GD if the GD is larger than the TH and the difference between the density in the GD and surface is less than 0.4 kg m^{-3} (green right triangle in Figure 3.6). Since for most of the profiles the surface data are not available, the reference surface for the *MLD* estimations is assumed to be the minimum depth, shallower than 10 m, where data are available.
 - iv. In the last step the *MLD* is calculated using the pycnocline method (PYCN). In this step, an algorithm fits a straight line to the mixed layer of the potential density profile. For each fit line, the error value is calculated by summing the square of the difference between the fit and the profile. Then the algorithm chooses the deepest depth with allowable error (less than 10^{-10}) and extends the mixed layer fit to the depth of the profile. The center of the pycnocline is also the location of the largest gradient in the profile. Then a straight line is fit to the seasonal

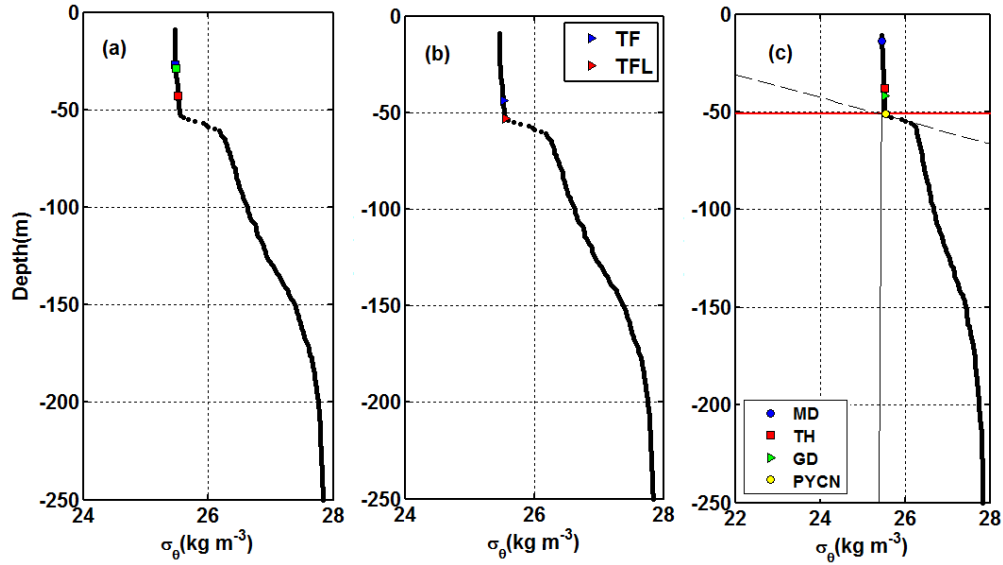


Figure 3.7: Three methods to estimate the *MLD* are compared using profile 076 from leg 0801. (a) The TH method is used in the left panel, (b) the TF method in the central panel and (c) the HTN method in the right panel. The red lines highlight the final *MLD* estimated by the HTN method.

pycnocline. Finally one set of possible *MLD* values is calculated by finding the intersection points between the mixed layer and the pycnocline fit (PYCN). If the lines do not intersect, the *MLD* is set to zero. In this step of the algorithm, the *MLD* value is set to the PYCN if its value is larger than the chosen *MLD* from the previous step and the difference between the potential density in the PYCN and surface is larger than 0.4 kg m^{-3} (yellow circle in Figure 3.6). The reader is referred to Holte and Talley (2009) for more details on this technique.

As an example, Figure 3.7 shows a comparison between different methods for the same profile. In this example, the HTN and TFL methods present very similar results. In summary, the HTN method provides an efficient and precise technique to estimate the *MLD* in this region of study. In the following sections, through some statistical and visual analyses the strength of this technique is demonstrated.

3.3.4 Other methods

Other *MLD* calculation methods have been used in other studies: they are presented in this section. Note that these methods are not used in this thesis because as it will be explained later they do not estimate the *MLD* as well as methods applied in this study.

Polovina method Due to unavailability of salinity data, Polovina et al. (1995) used the temperature profile in order to calculate the *MLD* in the central and northern Pacific Ocean. They developed two algorithms to define the *MLD* as a depth at which the comparison between the vertical temperature gradient and the deeper water gradients is small. The first algorithm required at least four data points in less than 50 m. The *MLD* is the depth at which the gradient of the profile is smaller than a defined least square criterion. The second algorithm is based on the temperature gradient profile. In this algorithm the temperature profile is interpolated using a cubic spline and then the gradient profile of the interpolated temperature is calculated. The estimated *MLD* is where the gradient profile is larger than 0.1 ($^{\circ}\text{C}/\text{m}$). The first algorithm is the primary algorithm and is the less sensitive one. If the conditions of the first algorithm fail then the second algorithm is used.

Pickart method The method of *MLD* calculation by Pickart et al. (2002) was done in two steps. Firstly the approximate extent of the ML was visually estimated based on the potential density profile. Then the mean and standard deviation of the density in the visually approximated *MLD* was calculated and overlaid on the original density profile. In the second step the *MLD* was determined as the depth where the original profile transected one of the standard deviation overlaid lines.

Step-function least squares regression method Freeland et al. (1997) used a two-segment least squares approach in order to calculate the *MLD* in the northeast Pacific Ocean. They used a least-squares-fit of a constant potential density $\sigma_{\theta 1}$ between a near-surface depth (z_a) and the estimated *MLD* (D) and another least-squares-fit of a constant potential density $\sigma_{\theta 2}$ between the estimated *MLD* and an arbitrary depth below the depth of seasonal mixing, ($z_b = 200-500$). Note that the method is insensitive to the reference depth (z_b). The steplike potential density can be written as:

$$f(z) = \begin{cases} \sigma_{\theta 1} & z_a < z < D \\ \sigma_{\theta 2} & D < z < z_b \end{cases} \quad (3.2)$$

A least squares approximation to $f(z)$ requires to minimize the following integral:

$$\Phi = \int_{z_a}^D [\sigma_{\theta}(z) - \sigma_{\theta 1}]^2 dz + \int_D^{z_b} [\sigma_{\theta}(z) - \sigma_{\theta 2}]^2 dz \quad (3.3)$$

Minimizing this integral leads to three equations for $\sigma_{\theta 1}$, $\sigma_{\theta 2}$ and D which can be solved numerically (Thomson and Fine, 2003).

Integral method This is a simple method used for *MLD* calculation by Price et al. (1986) in which the *MLD* (D) is obtained by equation 3.4 in which $N_b^2(z) = -\frac{g}{\rho_0} \frac{d\rho}{dz}$ is the buoyancy frequency, g is the acceleration of gravity, ρ_0 is a reference density, z_a and z_b are as in equation 3.2.

$$D = \frac{\int_0^{z_b} z N_b^2(z) dz}{\int_0^{z_b} N_b^2(z) dz} = \frac{\int_{z_a}^{z_b} (\sigma_{\theta b} - \sigma_{\theta}) dz}{\sigma_{\theta b} - \sigma_{\theta a}} \quad (3.4)$$

According to Thomson and Fine (2003) step-function and integral methods estimate more pycnocline depth rather than the *MLD*.

3.4 Assessment of the methods

Three approaches are employed in this section to assess the methods used in this study (TH, TF, TFL and HTN) and to choose the most appropriate one for the rest of the study. The approaches are based on visual inspection, statistical analysis and in situ validation.

3.4.1 Visual inspection of the profiles

Because of the fluctuations and discontinuities in density profiles, there exist scenarios where some methods fail to give an acceptable estimation of the *MLD*. In visual inspection, each density profile is carefully examined for determining the value of the *MLDs* in order to avoid having extreme *MLDs* (much smaller or larger than real *MLDs*). The purpose is to look for an abrupt change which makes the density profile no longer uniform above the pycnocline. The visual inspection provides a non-computational basis for the estimation of the *MLD* and is used to validate the results emerging from other methods.

In order to compare the *MLD* calculated by one method with another, the *MLDs* are plotted against each other (see Figure 3.8). The *MLDs* of 2218 casts calculated with four different methods are shown in this figure. A large number of points around the red line show that the *MLDs* estimated by both methods are similar to each other. Large numbers of points away from the red line demonstrate that one method is more biased than another.

It should be noted that the TF and especially the TFL methods occasionally overes-

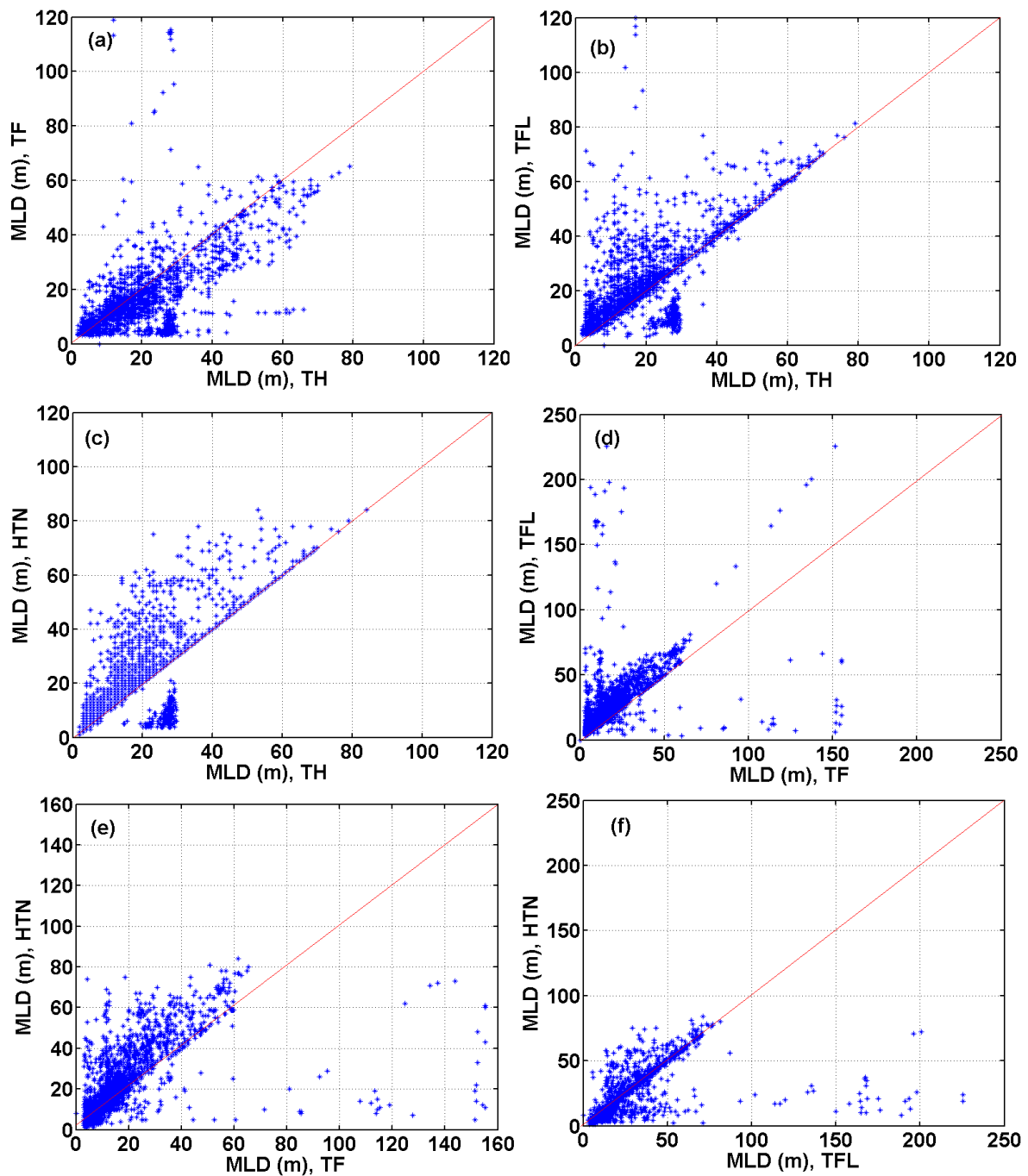


Figure 3.8: Comparison between methods: each + represents a *MLD* estimation. Panels (a), (b) and (c) compare the TF, TFL and HTN methods to the TH method (0.05 kg m^{-3}). Panel (d) compares the TFL and TF; panel (e) compares the HTN and TF and panel (f) compares the HTN and TFL. An error upper limit of 0.05 is used for the TF and TFL methods. The diagonal red line is the 1:1 fit.

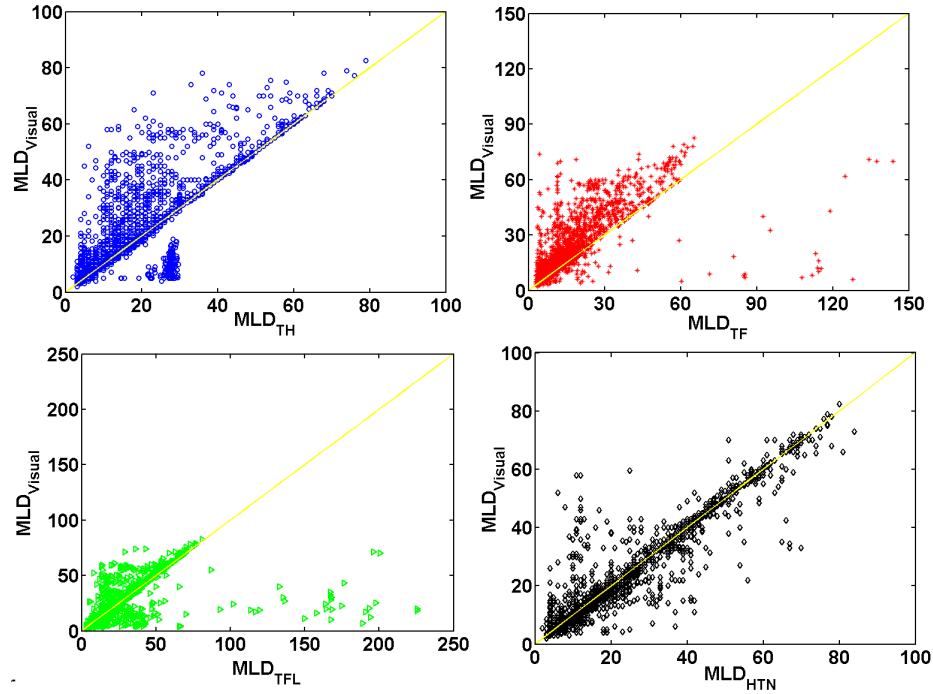


Figure 3.9: Comparison of the $MLDs$ obtained by visual inspection of the profiles with the $MLDs$ estimated by the four other automatic methods. The yellow diagonal line is the 1:1 fit.

estimate the $MLDs$. Of 2218 CTD casts analyzed in this study, the TF and TFL methods produced 24 and 30 MLD values larger than 100 m, respectively. These large values are eliminated in Figure 3.8a, b, c and e, when the $MLDs$ are larger than 120 m. The comparison between $MLDs$ calculated by the threshold method (threshold value of 0.05 kg m^{-3}) and the TF method shows that these two methods are generally comparable because the $MLDs$ are concentrated around the red line (Figure 3.8a). As shown in Figure 3.8b and c, the threshold method underestimates the $MLDs$ compared with the TFL and HTN methods. Figure 3.8c and d show that generally the threshold and TF methods underestimate the MLD in comparison with the TFL and HTN methods.

I present in Figure 3.9 a comparison between the visual method and all four other methods. As demonstrated in this figure, the Threshold and TF methods generally underestimate the $MLDs$ compared with the visually estimated $MLDs$. The $MLDs$ estimated from HTN (black diamonds) method are more concentrated around the 1:1 line, implying that this method calculates the most similar $MLDs$ to our visual estimations, compared to the other methods

3.4.2 Statistical evaluation

Neglecting the MLDs larger than 110 m using TF and TFL methods some statistical parameters are calculated between different MLD estimation methods and the visual MLDs. The statistical parameters are the peak differences (*PDIFF*, equation 3.5), the mean absolute error (*MAE*, equation 3.6), the root mean square error (*RMSE*, equation 3.7), the relative absolute error (*RAE*, equation 3.8), and the Pearson product moment correlation coefficient (*RSqr*, equation 3.9). These five statistics are chosen among several proposed in Dawson et al. (2007) because they are the most common statistics used in previous studies and also because they provide an effective means for the comparison between the *MLDs* obtained from our different methods and the visual inspection. Here I compare the four estimation methods (the *MLDCs* in the equations) to the observations (visual inspection: *MLDV*).

The *PDIFF* (equation 3.5) simply compares the maximum values of two estimation methods. It does not represent overall agreement, only the relationship between the largest values in each data set. It is also useful to evaluate whether or not the methods are able to produce the same range as the visual inspection. A perfect fit would produce a *PDIFF* of zero. The *MAE* (equation 3.6) is the metric representing the overall agreement between methods and visual inspection. The best fit would produce the smallest *MAE*. The *RMSE* (equation 3.7) assesses the cumulative deviations between methods and visual inspections. The *RAE* (equation 3.8) is the ratio of the total relative error between methods and visual inspections to differences between the visual inspection and their mean values. The lower the ratio, the better the fit will be. Finally, the *RSqr* (equation 3.9) also known as the Pearson product moment correlation coefficient, is a correlation coefficient between the desired method and the visual inspection. It compares the ratio of the combined dispersion to the total dispersion of the calculated and visual series. “It describes the proportion of the total statistical variance in the modeled time series that can be explained by the model” (Dawson et al., 2007). The *RSqr* varies between 0 (poor model) and 1 (perfect fit).

$$PDIFF = \max(MLDV) - \max(MLDC) \quad (3.5)$$

$$MAE = \frac{1}{n} \sum_{i=1}^n (MLDV - MLDC) \quad (3.6)$$

Table 3.1: Statistical fit indicators between the *MLDs* obtained by visual inspection and by the TH, TF, TFL and HTN methods. The threshold used in the TH is 0.05 kg m^{-3} , and the error norm in the TFL is 0.05. The yellow boxes indicate the best statistical while the green boxes highlight the second best fits.

Stat	TH (0.05)	TF (0.05)	TFL (0.05)	HTN	Visual
<i>Mean</i>	20.7	17.2	24.2	24.2	24.2
<i>Min</i>	2	3	3	2	2
<i>Max</i>	79	95	93	84	82
<i>PDIFF</i>	-3	13	11	2	
<i>MAE</i>	6.6	8.1	3.9	2.8	
<i>RMSE</i>	11.1	12.6	8.7	6.1	
<i>RAE</i>	0.5	0.6	0.3	0.2	
<i>RSqr</i>	0.6	0.6	0.7	0.9	

$$RMSE = \sqrt{\frac{\sum_{i=1}^n (MLDV - MLDC)^2}{n}} \quad (3.7)$$

$$RAE = \frac{\sum_{i=1}^n |MLDV - MLDC|}{\sum_{i=1}^n |MLDV - \overline{MLDV}|} \quad (3.8)$$

$$RSqr = \left[\frac{\sum_{i=1}^n (MLDV - \overline{MLDV})(MLDC - \overline{MLDC})}{\sum_{i=1}^n (MLDV - \overline{MLDV})^2 \sum_{i=1}^n (MLDC - \overline{MLDC})^2} \right]^2 \quad (3.9)$$

Table 3.1 summarizes the results of the statistical tests. The HTN method is clearly the most statistically consistent one. It performs well in all aspects. The yellow boxes highlighted in Table 3.1 show that based on all the parameters, the HTN method calculates the most similar *MLDs* to the visual inspections, compared to the other methods. Additionally, the green highlights in Table 3.1 indicate that based on the *Min*, *MAE*, *RMSE*, *RAE* and *RSqr* statistics the TFL method estimates the best second *MLDs*. It worth mentioning that based on statistics both TFL and HTN estimate the *MLDs* close to the visual *MLDs* but the HTN method is the most consistent one with the observations. In addition, it should be noted that for the statistical comparison we neglected very large *MLDs* estimated by the TFL method which confirms that the HTN method is the most appropriate method for the *MLD* computation.

3.4.3 In situ validation

A last validation will be performed using two density time series: a fall time series and a winter time series. The winter data was obtained through a moon pool and the first valid observation was set at 10 m because heat contamination from the CCGS Amundsen’s hull (7 m draft). For the rest of the year, the first data point is usually at 1 m, except in bad weather when it is at 5 m and, only rarely, at 10 m. The sensitivity of the four automatic *MLD* calculation methods is examined by plotting the *MLD* density (thick red lines), the density at the *MLD*+3 m (green lines), the density at *MLD*+10 m (black lines), and the density at 5 m (blue lines) for the fall time series. This is shown in Figure 3.10 for leg 0304 (15 October to 25 November 2003), in Figure 3.11 for leg 0401 (7 January to 17 February 2004), and in Figure 3.12 for leg 0801 (1 February to 13 March 2008). The best overall fit is for the method for which the *MLDs* (red lines) and the surface density (blue lines) almost merge (uniform surface layer). At the same time, the most consistent estimations are for methods for which the *MLD*+3 m (green lines) and the *MLD*+10 m are systematically above the *MLDs* (red lines), showing that these densities are found below the mixed layer in the pycnocline region.

Figure 3.10 shows the density at the surface (5 m) and the *MLD* using all the methods are very similar and by increasing the depth to $MLD_{TH}+3$ m and $MLD_{TH}+10$ m the density increases. For this specific case, Figure 3.10b shows that the density at the surface, MLD_{TF} and $MLD_{TF}+3$ m are very similar to each other, this reveals that the TF method underestimates the *MLD* more than any other technique. This figure also shows that although the difference between the density lines derived from the threshold method are slightly greater than the TF method, the threshold method also underestimates the *MLD*. Figures 3.10c and d show that the TFL and HTN estimates of the *MLD* are closer to the real value since the density at the surface (5 m) and the *MLD* coincide while the density lines of the *MLD*, *MLD*+3 m and *MLD*+10 m do not. Although the *MLD* values are correctly estimated by both the TFL and HTN methods, a close look at these two panels shows that the HTN method presents slightly more gaps between the density at the *MLD* and *MLD*+3 m. Moreover, the blank regions (missing *MLD* estimates) in Figure 3.10c indicate very large *MLDs* estimated by the TFL method, while this is not the case with the HTN method (Figure 3.10d).

A similar example is shown in Figure 3.11 using data collected during the winter of 2004. The *MLDs* are again calculated using the same methods. As shown in Figure 3.11a and b, the density at the surface (10 m) and the *MLD* (using the TH and TF methods) coincide as is expected. On the other hand the line of density at *MLD*+3 m (shown in Figure 3.11 as $MLD_{TH}+3$ m and $MLD_{TF}+3$ m) is very close to the line of density at the *MLD* (shown in Figure 3.11 as TH and TF). This shows that the TH

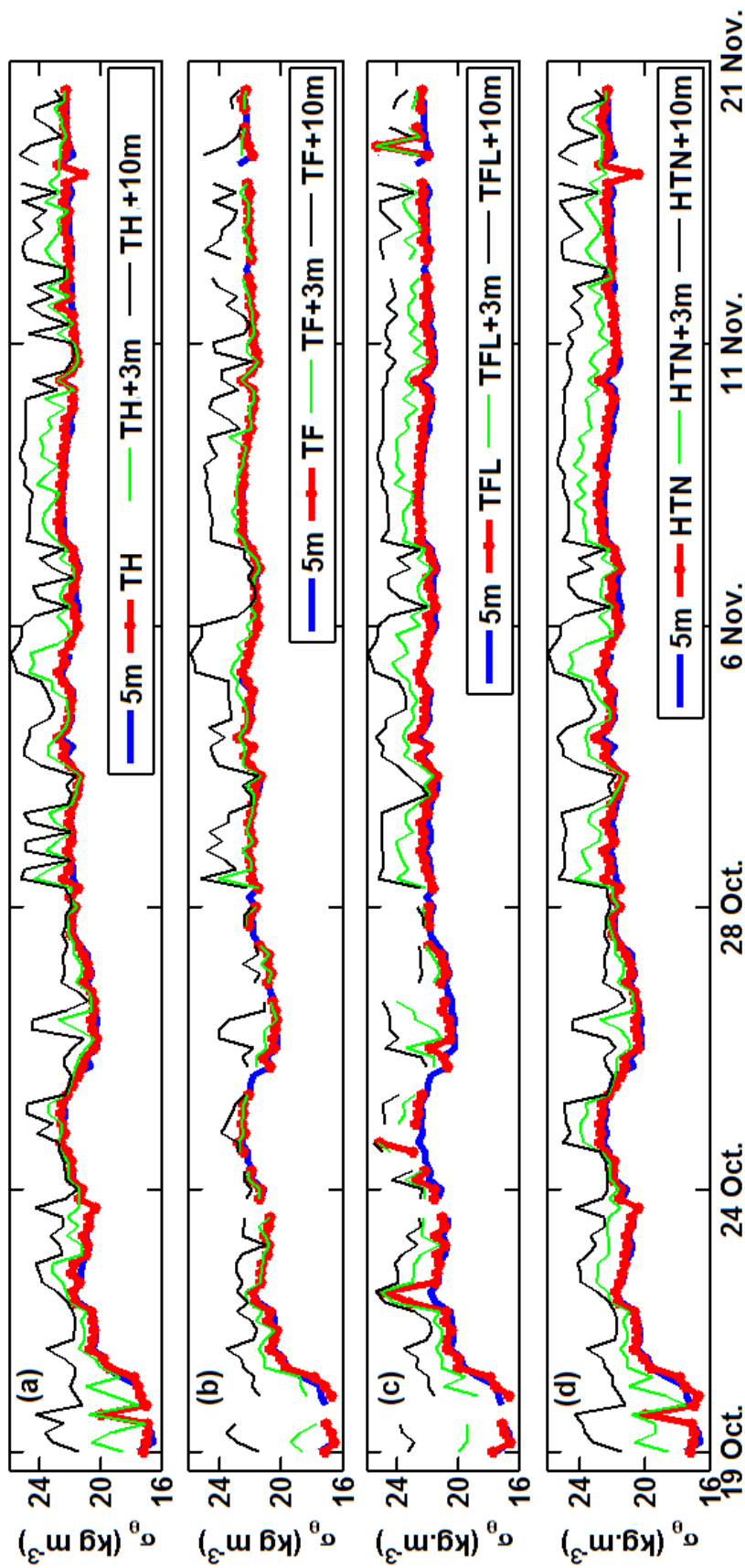


Figure 3.10: Potential density time series at 5 m (blue lines), at the MLD (red lines), at $MLD+3$ m (green lines) and $MLD+10$ m (black lines) in the fall of 2003 during leg 0304. The $MLDs$ are calculated using the TH method (threshold of 0.05 kg m^{-3}) (panel a), the TF method (panel b), the TFL method (panel c) and the HTN method (panel d).

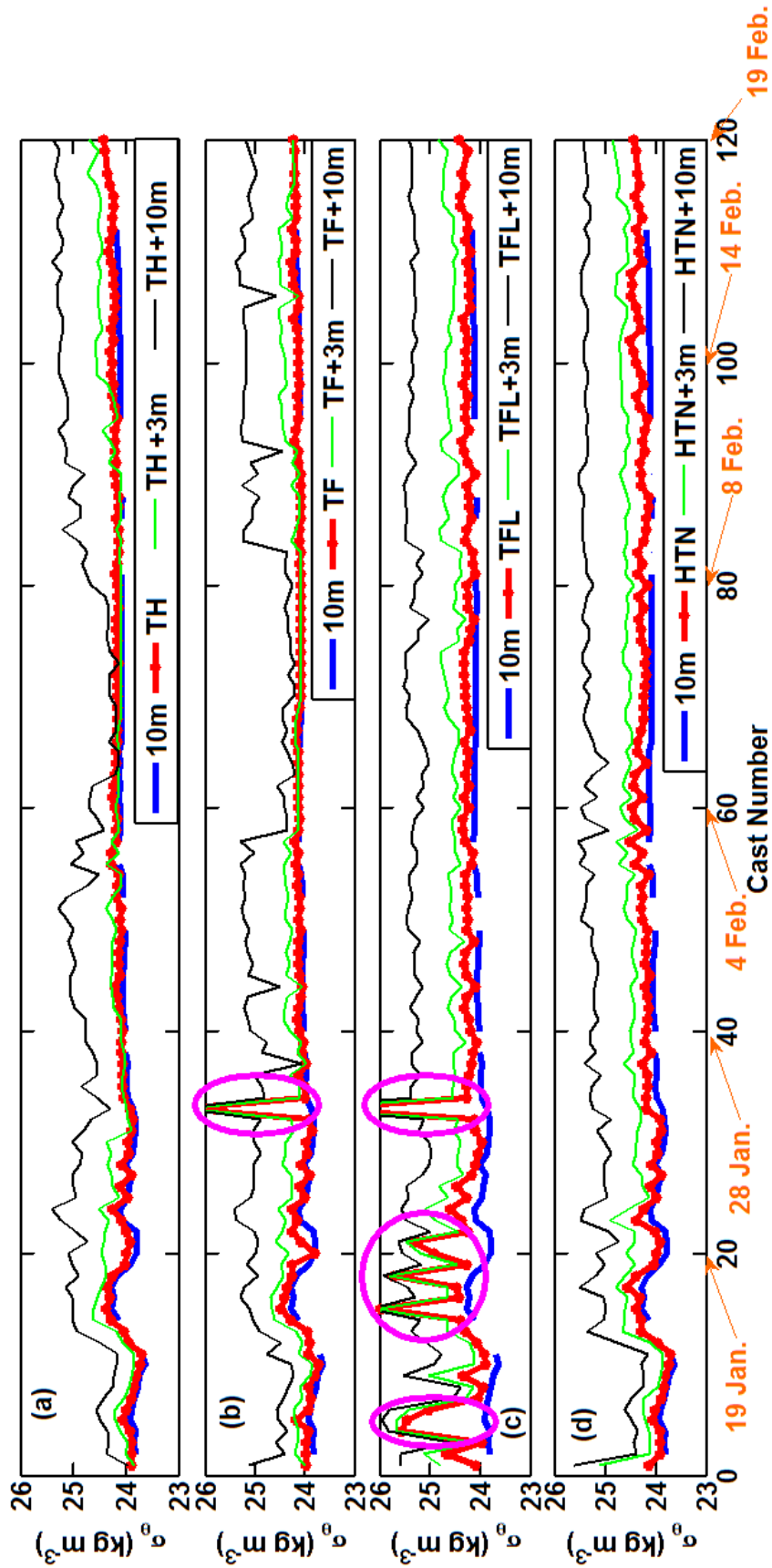


Figure 3.11: Potential density time series at 10 m (blue lines), at the $MLD+3$ m (green lines) and $MLD+10$ m (black lines) in the winter of 2004 during leg 0401. The $MLDs$ are calculated using the TH method (threshold of 0.05 kg m^{-3}) (panel a), the TF method (panel b), the TFL method (panel c) and the HTN method (panel d). The magenta ellipses highlight the periods for which our method fails; they are discussed in the text.

and TF methods underestimate the MLD because it is expected that the densities at the MLD and $MLD+3$ m are completely different. This difference is larger when the $MLDs$ are calculated using the TFL and HTN methods but the TFL method occasionally overestimates the MLD as shown in the figure with magenta ellipses. The large difference between densities at the surface (10 m) and the MLD and also the similarity of density lines at the MLD , $MLD+3$ m and $MLD+10$ m demonstrates that the TF and TFL methods occasionally position $MLDs$ very deep in the pycnocline.

Figure 3.12 shows the densities at different depths (i.e. at 10 m, MLD , $MLD+3$ m and $MLD+10$ m) as a function of time while the $MLDs$ are calculated using the TH, TF, TFL and HTN methods during the winter of 2008. As shown in Figure 3.12a and b, the densities at 10 m and at the MLD , calculated using the TH and TF methods, are very similar. On the other hand, as shown in Figure 3.12c the densities at $MLD_{TH} + 3$ m and $MLD_{TF} + 3$ m are also similar to the density at 10 m and the MLD especially for the TF method (MLD_{TF}). It shows that the TH and TF methods underestimate the MLD because the density at $MLD+3$ m is inside the mixed layer. The densities at 10 m and MLD_{TFL} are very similar while the density line at $MLD_{TFL} + 3$ m is further from the density line at MLD_{TFL} . This demonstrates that the $MLDs$ estimated using the TFL method are more similar to the real MLD than those derived from the TH and TF methods. The densities at the surface and MLD_{HTN} are not as similar as the other methods, moreover, the density lines at $MLD_{HTN}+3$ m and $MLD_{HTN}+10$ m are located in the pycnocline and they are further from the density line at MLD_{HTN} contrary to the other methods especially TH and TF. This demonstrates that even though the density at the surface (10 m) and MLD_{HTN} are slightly different, the distance between the density lines of MLD_{HTN} , $MLD_{HTN} + 3$ m and $MLD_{HTN} + 10$ m shows that the MLD calculated by the HTN method more accurately predicts the actual value than the other methods.

3.5 Summary

Five methods of estimating the Mixed Layer Depth were investigated: (1) the threshold method (TH), (2) the Thomson and Fine (2003) method (TF), (3) a modification of the Thomson and fine method (TFL), (4) a modification of the Holte and Talley (2009) method (HTN) and (5) the visual inspection method (VI). The version of Holte and Talley modified in this thesis is the most statistically consistent method. It is also the one that best represents a vertically uniform mixed layer. This method will be used in the remainder of the thesis. In chapter 5, I will estimate the fluxes entering the mixed layer from below: the HTN is the method that minimizes the error in these flux

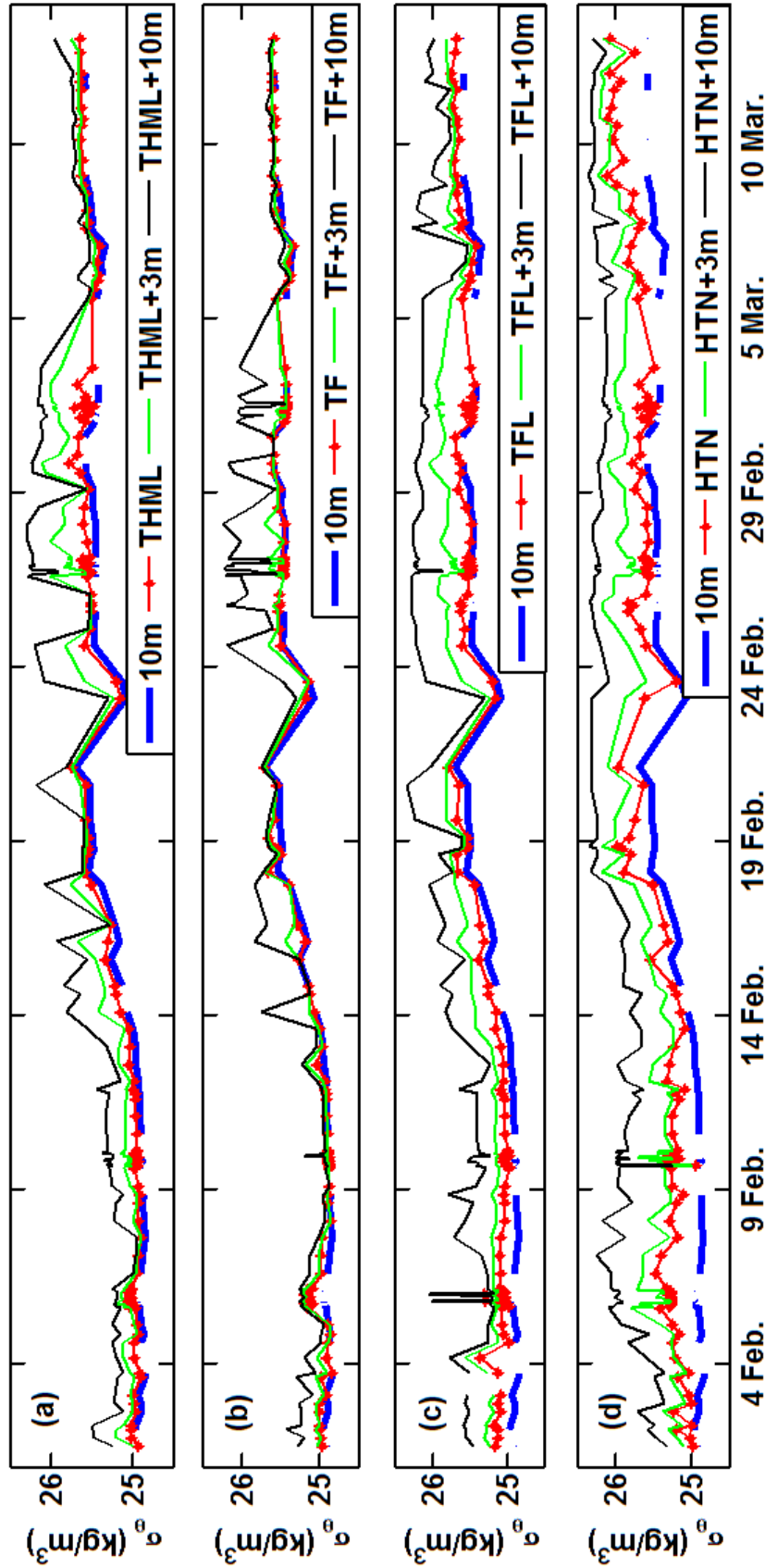


Figure 3.12: Potential density time series at 10 m (blue lines), at the MLD (red lines), at the $MLD+3$ m (green lines) and $MLD+10$ m (black lines) in the winter of 2008 during leg 0801. The $MLDs$ are calculated using the TH method (threshold of 0.05 kg m^{-3}) (panel a), the TF method (panel b), the TFL method (panel c) and the HTN method (panel d).

calculations.

CHAPTER 4

TEMPORAL EVOLUTION AND SPATIAL DISTRIBUTION OF THE MIXED LAYER DEPTH

4.1 Introduction

The temporal and spatial variability of the *MLD* is directly related to many processes such as surface atmospheric forcing, horizontal advection, internal waves, tidal mixing, etc. Each forcing has its own temporal and spatial scales: *MLDs* vary diurnally, seasonally and interannually (de Boyer Montégut et al., 2004). In this chapter, I will discuss the spatial (by regions) and temporal (interannually, monthly and seasonally) variability of the ML in the southern Beaufort Sea and the Amundsen Gulf thanks to the available data that includes two complete years of observations during CASES (2003-2004) and CFL (2007-2008), as well as the seasonal observations (summer and fall) during 2002, 2005, 2006 and 2009 as described in section 2.2. All the *MLDs* in this chapter are estimated using the HTN method as explained in the previous chapter.

The study region will be divided into four separate subregions in order to explore more adequately the spatial and temporal variations. Note that data are not always available every year for the same region. In order to separate the respective roles of inshore versus offshore physical processes, the region will be further divided into inshore (depths shallower than 200 m) and offshore (depths greater than 200 m). This division is made because it is expected that, in addition to continental slope dynamics or freshwater discharge effects, ice type differences between inshore and offshore areas affect the *MLD*. The seasonal, interannual and spatial variations of *MLD* are then studied in each subregion with respect to the bathymetry.

4.2 Methodology

4.2.1 Difficulties and approaches

The observations available in our region of study provide a unique and invaluable source of information for the analysis of mixed layer in the Arctic. However, the database is incomplete because the data collection in this region is very costly and challenging. In general, one of the major challenges in the analysis of oceanographic data is that the data are not synoptic and a sufficient number of samples are never available at the same time. In our study region, despite having two year-long datasets for 2003-2004 and 2007-2008, the observations were not spatially and temporally captured in the same manner in each year. For example, we have two time series of winter observations but they were not obtained at the same exact location. Thus when we perform interannual comparisons, it should be kept in mind that spatial effects may also play important role.

As a first example, the locations of the sampling stations as a function of time as well as *MLD* evolution at these stations during leg 0202 of CASES (observations from the fall of 2002), are shown in Figure 4.1. For instance, the *MLDs* in Franklin Bay vary significantly although the sampling was done on two successive days. In general, this figure shows that the variations in the *MLDs* are irregular both in time and in space. To overcome these difficulties, the analysis is performed in two main parts. The first part deals with the spatial distribution of the *MLD*. In order to study the spatial distribution of the *MLD*, different approaches are employed. First of all, the region of study is divided into four subregions presented in Figure 4.2. The spatial variations of *MLD* are then studied in these subregions as well as in the inshore and offshore regions. In the second part of this chapter, the variations of *MLD* are analyzed temporally. The seasonal, interannual and monthly variations of the *MLD* are discussed when sufficient observations are available. This classification will allow us to use a statistical approach to describe the *MLD* variability.

4.2.2 Statistical definitions

Uncertainty interval An uncertainty is associated with the mean value of a set of estimated *MLDs* like any other measured parameters. It is important to know the level of the uncertainty in order to be able to properly interpret any average results emerging from the present study. The experimental variability is more often associated with a

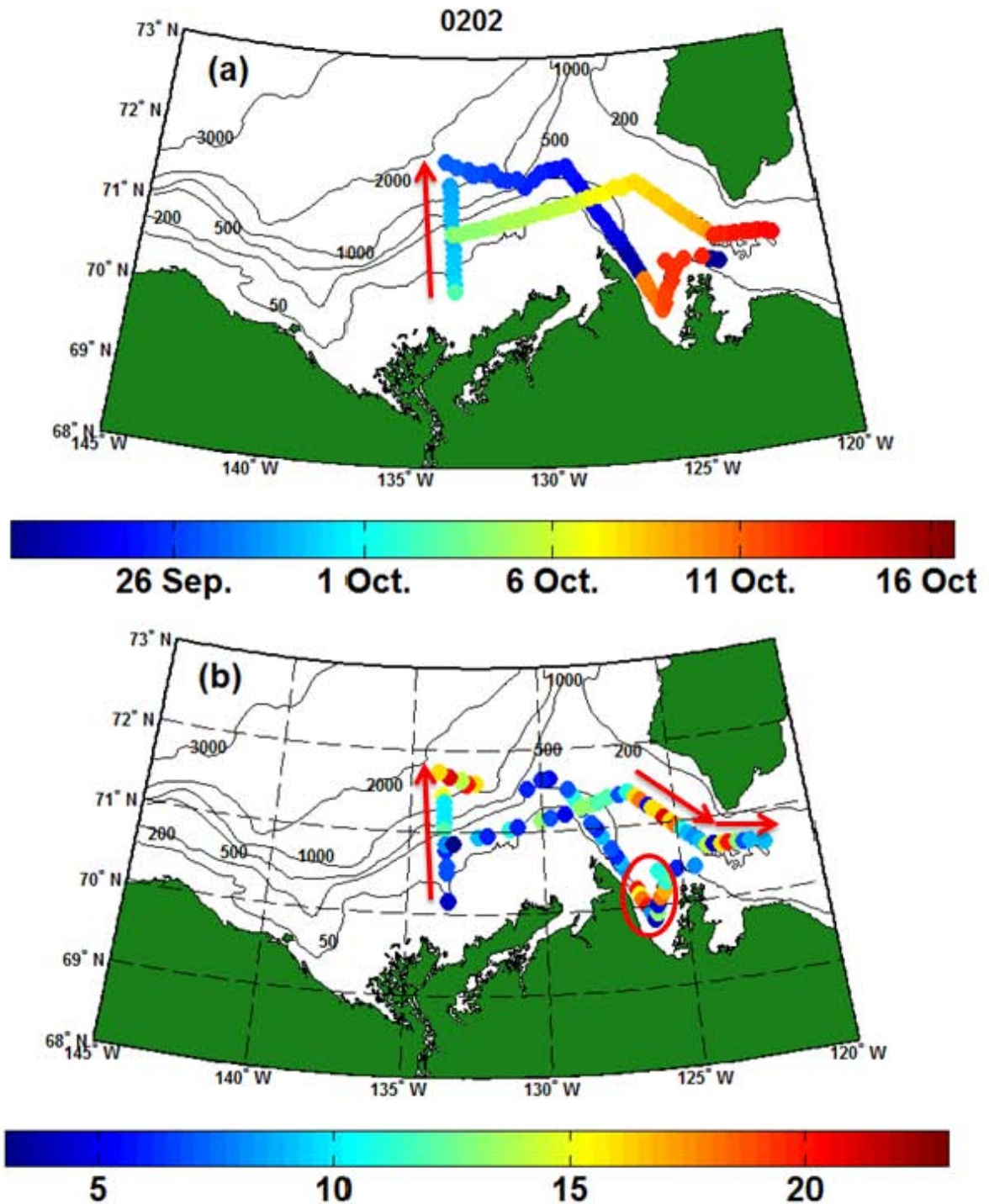


Figure 4.1: (a) Locations of the sampling stations as a function of time during CASES leg 0202. (b) *MLDs* at the same locations based on the HTN method. The *MLDs* are in meters.

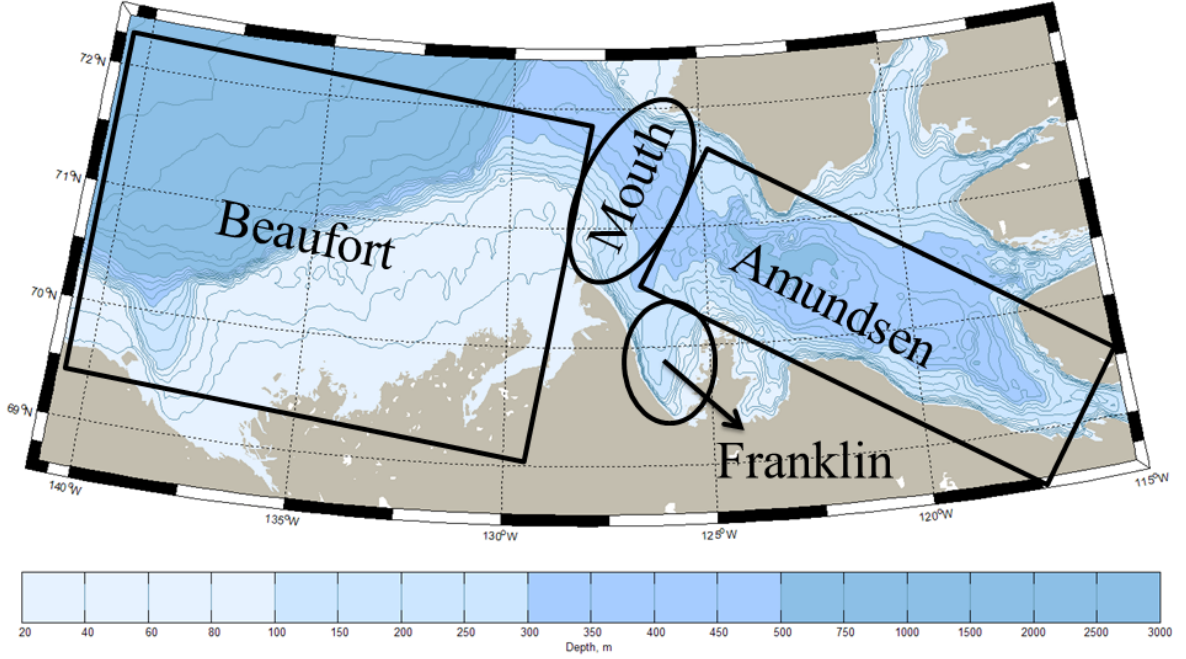


Figure 4.2: Four subregions considered in this study: Beaufort, Mouth, Amundsen and Franklin.

Gaussian distribution than any other distribution (Coleman and Steele, 1999). In this study I presume that the data are Gaussian even if they are not, in order to calculate the confidence interval on the mean of each data set in a systematic manner.

The equation of the Gaussian distribution can be written as:

$$f(X) = \frac{1}{\sigma\sqrt{2\pi}} e^{-(X-\bar{X})^2/2\sigma^2} \quad (4.1)$$

where $f(X)$ is the probability that a single measurement or a calculated parameter based on a measurement of X (here the MLD) lies between X and $X + dX$ while \bar{X} is the mean value of distribution is defined as:

$$\bar{X} = \frac{1}{N} \sum_{i=1}^N X_i \quad (4.2)$$

and σ is the standard deviation of distribution defined as:

$$\sigma = \left[\frac{1}{N-1} \sum_{i=1}^N (X_i - \bar{X})^2 \right]^{1/2} \quad (4.3)$$

The variance is simply the square of the standard deviation. A plot of equation 4.1 with $\bar{X} = 0$ and different standard deviations is shown in Figure 4.3. As the value of standard deviation increases, the range of X distribution also increases such that the area under the curve of Gaussian distribution of data is equal to one $\int_{-\infty}^{+\infty} f(X) dX = 1$.

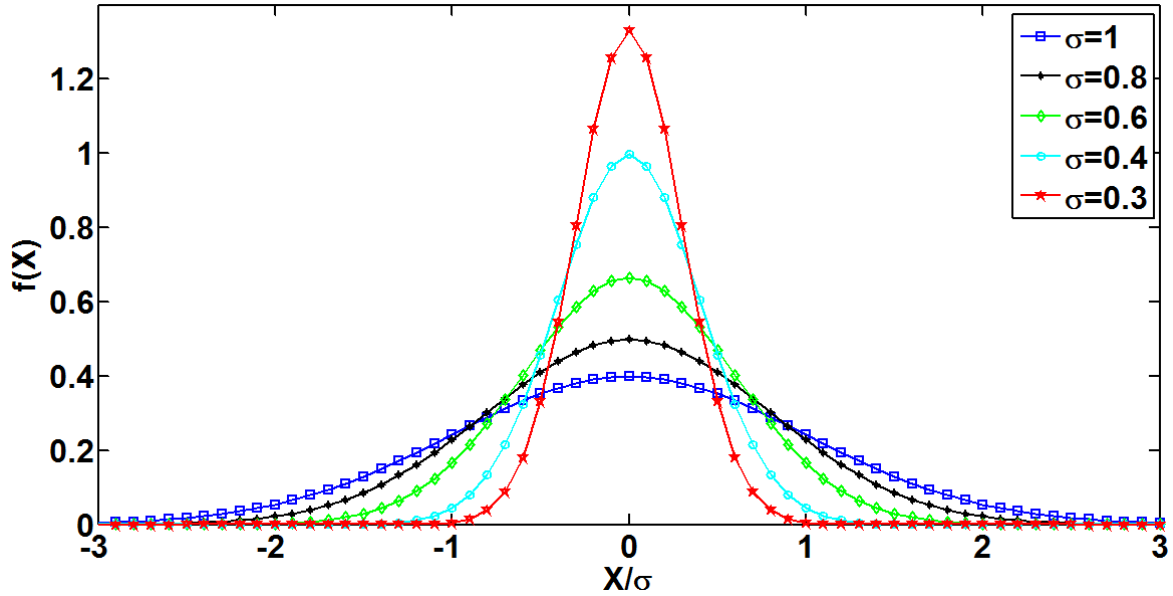


Figure 4.3: Gaussian distribution of a hypothetical data set with different values of the standard deviations.

Suppose that we want to determine the probability that a Gaussian population falls within a certain range around the mean value of data ($\pm\Delta X$) expressed as follows:

$$Prob(\Delta X) = \int_{\bar{X}-\Delta X}^{\bar{X}+\Delta X} \frac{1}{\sigma\sqrt{2\pi}} e^{-(X-\bar{X})^2/2\sigma^2} dX \quad (4.4)$$

In order to simplify equation 4.4, we can write: $t = (X - \bar{X})/\sigma$ which is tabulated. Then the equation 4.4 can be rewritten as follows where $t_1 = \Delta X/\sigma$.

$$Prob(t_1) = \frac{1}{\sqrt{2\pi}} \int_{-t_1}^{t_1} e^{-t^2/2} dt \quad (4.5)$$

In this study the 95% confidence interval of a Gaussian distribution is used in order to calculate uncertainties (Coleman and Steele, 1999). We define the 95% confidence limit for a sample with N number of data from a Gaussian distribution as:

$$P_{\bar{X}} = \frac{t\sigma}{\sqrt{N}} \quad (4.6)$$

where t values are given in Table 4.1.

Student t -test To compare two series of data having possibly unequal variances, a modified Student's t -test can be used. This test assumes that the random variable is normally distributed. Unfortunately, this is not always the case. This test compares the two mean values with respect to the standard deviation of the difference between

Table 4.1: Tabulated values of t as a function of N , the number of observations (Coleman and Steele, 1999).

N	5	8	11	14	17	20	25	30	40	60	120	∞
$t(95\%)$	2.571	2.306	2.201	2.145	2.11	2.086	2.06	2.042	2.021	2	1.98	1.96

the means. The student's t -test tells us if the mean values of two series are equal or significantly different. In order to do this test, the t parameter is calculated using the following equation.

$$t = \frac{\overline{X}_1 - \overline{X}_2}{\sqrt{\frac{S_1^2}{N_1} + \frac{S_2^2}{N_2}}} \quad (4.7)$$

If $\overline{X}_2 > \overline{X}_1$ the numerator becomes $\overline{X}_2 - \overline{X}_1$. In this equation, \overline{X}_i , S_i^2 and N_i^2 are the arithmetic mean, sample variance and size of i^{th} series of data. The term in the denominator is the variance of the difference between the two means. Then the t -table is consulted for $(N_1 + N_2 - 2)$ degrees of freedom and the required level of probability ($p = 0.05$). Next, we compare the tabulated t value with t value calculated using equation 4.7. If the calculated t is larger than the tabulated one, it indicates that the means of these two series of data are significantly different at the $p = 0.05$ level. In other words there is a 95% chance that mean values be significantly different.

Probability density function The probability distributions of the $MLDs$ are also analyzed in this study. These probability distributions give us information about the frequency of occurrence of the $MLDs$ over discrete intervals. In order to be able to compare different periods or regions with different characteristics (e.g. number of realization), the histograms are normalized by the number of data points in each discrete interval to insure that the area under will be one. These normalized histograms are in fact probability density function (PDF). Note that the PDF can be also obtained using the histogram of cumulative distribution function (CDF). The CDF or $P(x)$ is the probability that MLD can be found at a value equal or less than x . The PDF value is never negative and the area under the PDF curve is always equal to 1 (i.e. $\sum_0^{x_n} p(x_i) \cdot \Delta x_i = 1$); where x_n is defined value which must be larger than maximum value of MLD). The CDF goes towards zero ($P(x) \rightarrow 0$) as $x \rightarrow 0$ and goes toward one ($P(x) \rightarrow 1$) as $x_i \rightarrow x_n$. In this study the discrete intervals are the same for all the probability density function ($\Delta x_i = 5$ m).

Kriging Kriging, a method of interpolation as well as extrapolation, is used for our spatial data. An oceanographic application of Kriging, called the Gauss-Markov estima-

tion method, is presented by [Denman and Freeland \(1985\)](#). This technique is a BLUE (Best Linear Unbiased Estimator) and allows extrapolating outside the measurement grid, while providing a spatial assessment of the error associated with the estimation. Kriging is based on the idea that the value of a variable at an unknown point is sum of known values of its neighbors weighted by their correlation as a function of their distances. Estimation of unknown values of the random variable Z at a location of x_p using known values observed x_i is given by

$$Z(x_p) = \sum_{i=1}^N w_i \cdot Z(x_i) \quad (4.8)$$

One necessary condition for using Kriging is that mean and variance of Z are stationary. This means that they do not depend on the position of the points, only on the distance between the points. We use ordinary Kriging because the mean of the random variables are unknown. The Kriging uses semi-variograms (half of the variogram) to determine the weights in equation 4.8 (see [Journel and Huijbregts \(1978\)](#) and [Deutsch and Journel \(1992\)](#)). The semi-variogram is calculated using equation 4.9.

$$\gamma(h) = \frac{1}{2n(h)} \sum_{i=1}^{n(h)} (Z(x_i) - Z(y_i))^2 \quad (4.9)$$

for the $n(h)$ points located at a distance $h = |x_i - y_i|$ apart. The next step is to adjust an analytical function or model to the points of semi-variogram using least squares. This step is the most delicate part of Kriging because the shape of the model will influence the estimation process. The two types of most commonly used models are the exponential and Gaussian models which are used in the present study. It was found that the exponential model fits our observations better. The equation of the exponential model is the following.

$$\gamma(h) = c(1 - e^{-h/a}) + c_0 \quad (4.10)$$

where a denotes the distance at which the value of semi-variogram reaches a sill or plateau. The sill is the upper bound of the semi-variogram curve ($\gamma = c_0 + c$) and ($\gamma = c_0$) is the nugget effect, the value of $\gamma(0)$. For the exponential model used in this study $c_0 = 0$, i.e. $\lim_{h \rightarrow 0} \gamma(h) = c_0 = 0$.

4.2.3 Available data in the subregions

As mentioned earlier, the region of study is divided into four subregions (see [Figure 4.2](#)). The number of available data in each year, season and subregion is presented in [Table 4.2](#).

Table 4.2: The number of individual MLD estimates available for different years for each subregion. Y, BM, In, Off stand for Year, Bathymetry, Inshore and Offshore, respectively. W, Sp, Su and F stand for Winter, Spring, Summer and Fall.

Y	BM	Amundsen				Beaufort				Mouth				Franklin			
		W	Sp	Su	F	W	Sp	Su	F	W	Sp	Su	F	W	Sp	Su	F
2002	In				6				18				14				9
	Off				17				19				11				7
2003	In								14				16				10
	Off				39				20				40				21
2004	In		8								25	7					
	Off		39	19							16	8		196	152	8	
2005	In											10					
	Off			10				10				11				16	
2006	In								9				12				
	Off				17				12				6				7
2007	In				6				15				8				6
	Off				100				11				42				
2008	In		76	9				16				22			38		
	Off	260	123	29				29		27		19					
2009	In							30				7					
	Off							90				20					

4.3 Spatial distribution of the *MLD*

In this section the spatial distribution of the *MLD* is studied during different years and seasons. First of all the *MLD* values are compared in each of the four subregions, as well as inshore and offshore. As it is shown in Table 4.2, the minimum number of data in the subregions is 6 and the maximum number is 260. In order to compare inshore and offshore areas we need data in both regions : only regions with at least 14 data points are considered. As mentioned at the beginning of the chapter, *MLDs* may vary along a single sampling transect. This is illustrated in Figure 4.4 and Figure 4.5. These variations are due to different wind events as well as to the freshwater and seasonal ice distributions that vary even within each region.

Upwelling events are frequent in the region (Williams and Carmack, 2008, Tremblay et al., 2011). Minimum length scale of the coastal upwelling at Cape Bathurst is about 25 km (Williams and Carmack, 2008). According to Mundy et al. (2009) length scale of ice-edge upwelling is less than 10 km. The event of the fall of 2007 was the strongest event observed in the region since we began to sample, and its effects were felt as late as the spring of 2008 (Tremblay et al., 2011). The low salinity circle near the

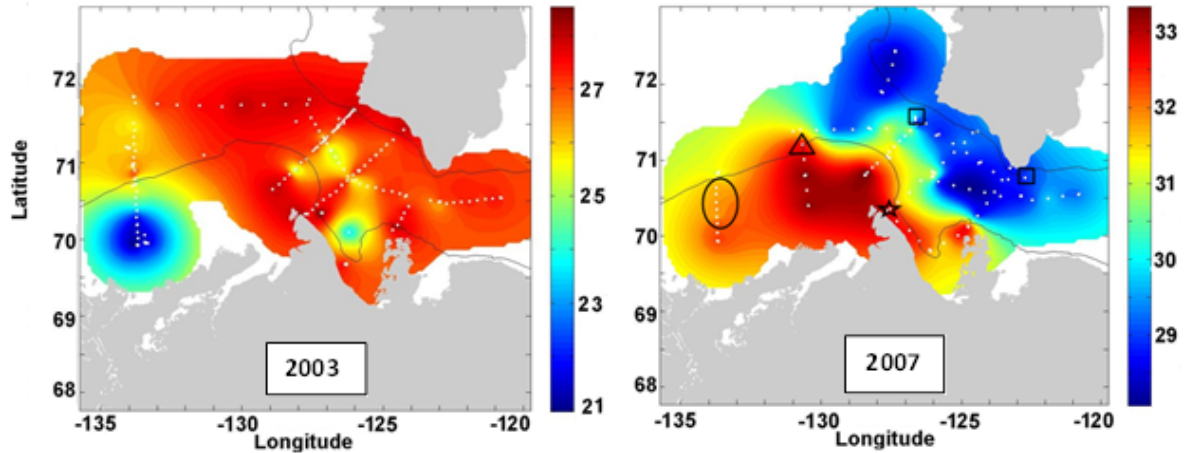


Figure 4.4: Salinity at 5 m in the fall of 2003 (during leg 0304; left) and in the fall of 2007 (during leg 0706; right). The estimation was performed using ordinary Kriging. The symbols correspond to the locations of *MLD*s deeper than their surroundings along the salinity front in 2007: *MLD* > 60 m (triangle), 45 m (square), 45 m (ellipse) and 35 m (star).

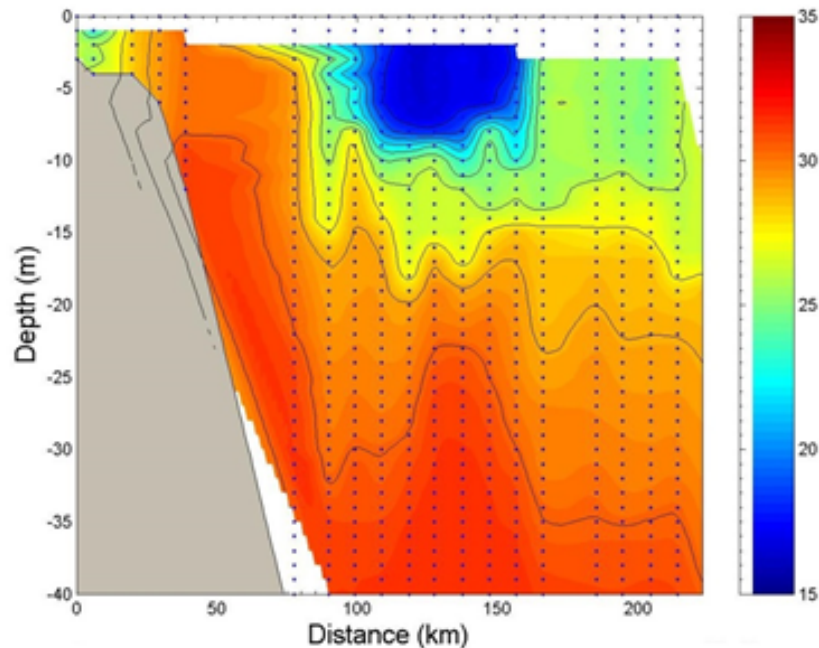


Figure 4.5: Inshore-offshore salinity section (km 0 is inside the Mackenzie River) that shows a pool of fresher water isolated from the main Mackenzie discharge by an upwelling event. The stations were visited between 22 September and 14 October 2002. The estimation was performed using ordinary Kriging. Modified after [Garneau et al. \(2006\)](#).

Table 4.3: Student t -test comparisons between inshore and offshore MLD s during CASES (2003-2004). N_1 and N_2 are the number of inshore and offshore observations. $T-t$ and $C-t$ are the tabulated t and calculated t values using equation 4.7. The results of the t -test are either Significant (Sig.) or Non-Significant (No Sig.). Mean inshore and Mean offshore are the confidence intervals on the monthly mean.

Month	Oct.	Nov.	Jun.	Jul.
N_1	17	28	34	20
N_2	63	51	64	36
$T-t$	1.99	1.99	1.98	2
$C-t$	4.77	2.3	3.93	2.03
Student t -test	Sig.	Sig.	Sig.	Sig.
Mean MLD (In)	6.2-6.7	14-15.4	14.8-17.2	5.6-6
Mean MLD (Off)	13-13.8	17.2-18	25-27	7.7-8.4

Mackenzie mouth in 2003 (Figure 4.4, left panel) is not an interpolation glitch. The same type of event was also observed in 2002. Fresher water from the Mackenzie River can accumulate in a restricted region and can even be observed offshore, isolated by an upwelling event (Figure 4.5). Strong ice-edge upwelling events were also observed in the region and especially in June 2008 (Mundy et al., 2009). These events may also generate temporary frontal zones. The impact of frontogenesis on the mixing process in 2003-2004 was studied by Sévigny (2013). She found many fronts in the local upwelling regions (coastal and ice-edge) where mixing was larger than the surroundings by as much as a factor of five.

4.3.1 Inshore and offshore

4.3.1.1 Regardless of the subregions

CASES (2003-2004) Student t -tests are carried out between the inshore and offshore mean MLD s during CASES for four months for which data are available in both regions. As shown in Table 4.3 the calculated t values ($C-t$) are larger than tabulated t value ($T-t$) except in November and July when they are close to each other. This means that in all four months, the mean value of the MLD s inshore and offshore are significantly different. The small difference between $C-t$ and $T-t$ in Table 4.3 in July means that the mean values of the MLD are close to each other, but significantly different. This is consistent with Figure 4.6 where the inshore and offshore mean values for November and July are closer to each other, but statistically different.

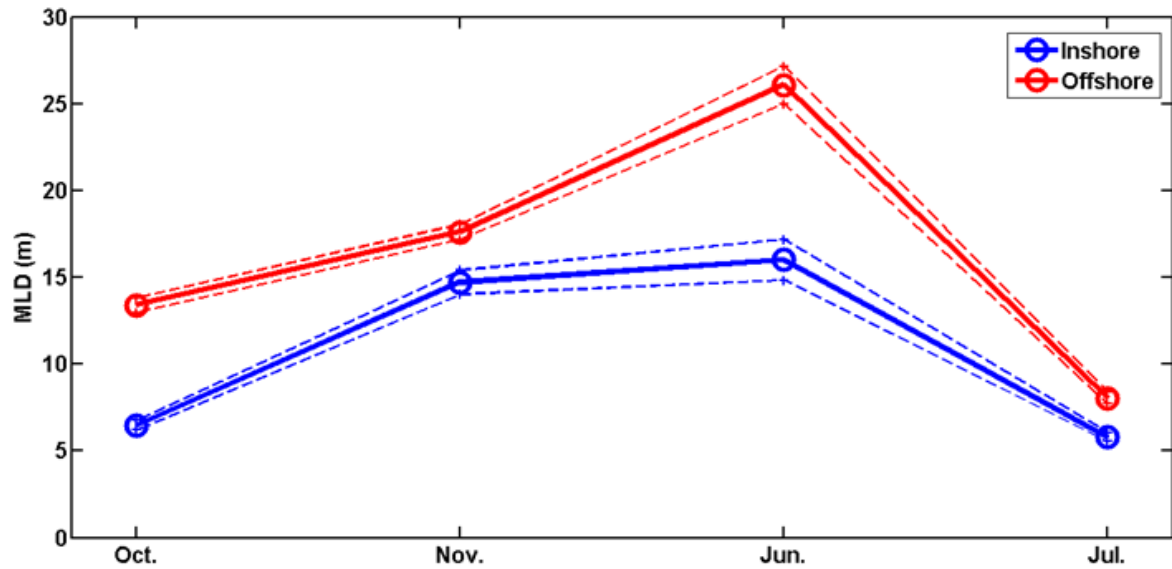


Figure 4.6: Monthly mean values of the inshore (blue) and offshore (red) *MLDs* regardless of the subregion during CASES (2003-2004). The dashed lines are the 95% confidence intervals on the mean value of the *MLD*. Number of the observation in each month is shown in Table 4.3.

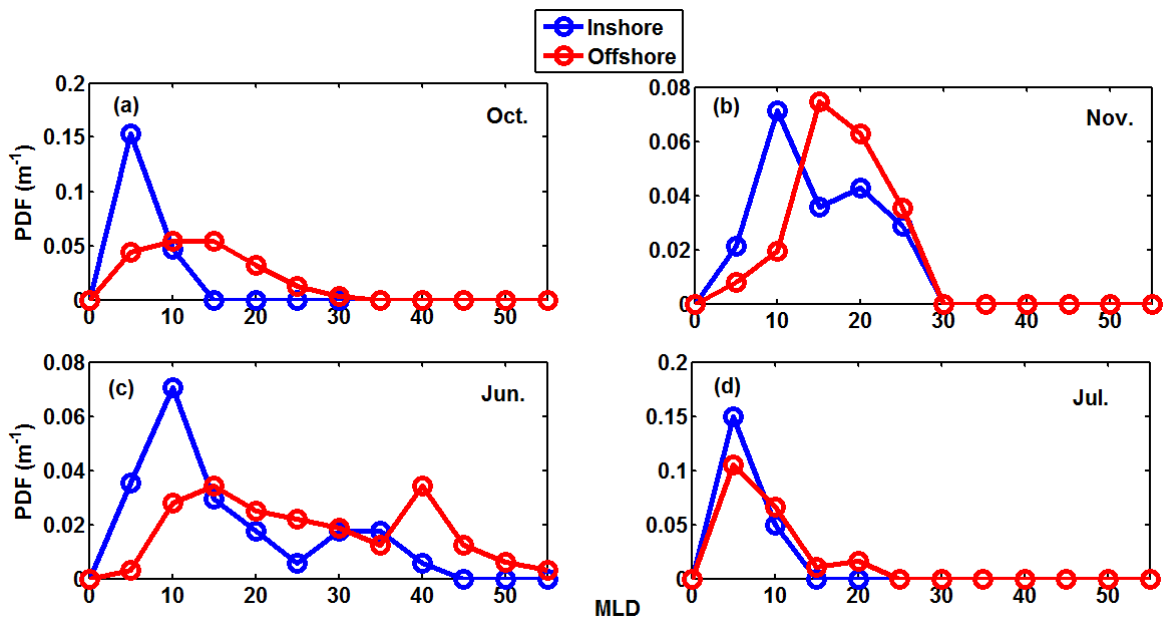


Figure 4.7: Probability density functions for the *MLDs* inshore and offshore areas during CASES (2003-2004) in (a) October, (b) November, (c) June and (d) July.

Table 4.4: Student t -test comparisons between inshore and offshore $MLDs$ during CFL (2007-2008). N_1 and N_2 are the number of inshore and offshore observations. $T-t$ and $C-t$ are the tabulated t and calculated t values using equation 4.7. The results of the t -test are either Significant (Sig.) or Non-Significant (No Sig.). Mean inshore and Mean offshore are the confidence intervals on the monthly mean.

Month	Oct.	Mar.	Apr.	May	Jun.	Jul.
N_1	29	49	22	40	71	34
N_2	48	54	80	55	21	94
$T-t$	1.99	1.99	1.99	1.99	1.99	1.98
$C-t$	4.88	2.69	12.02	2.68	1.51	1.91
Student t -test	Sig.	Sig.	Sig.	Sig.	No sig.	No sig.
Mean MLD (In)	30-33.5	41.7-42.8	31.7-34.7	36.2-40	17-19.6	7-8
Mean MLD (Off)	18.5-19.5	45.4-47.4	58.5-60	47.2-52.4	14-17	8.9-9.6

Figure 4.7 shows that probability density functions (PDF) for the $MLDs$ during the CASES are consistent with the mean values (Figure 4.6). In October, November and June deeper $MLDs$ are more frequent offshore. In July the most frequent $MLDs$ in both inshore and offshore are about 5 m which is consistent with the fact that ice melting will produce thinner $MLDs$.

CFL (2007-2008) Table 4.4 presents student's t -test results between inshore and offshore $MLDs$ during CFL for the six months when observations are available in both regions. As shown in Table 4.4, $C-t$ values are larger than $T-t$ in October, March, April and May which means that mean value of inshore and offshore $MLDs$ are significantly different in these months. On the other hand the $C-t$ values are smaller than $T-t$ values in June and July which means that mean value of inshore and offshore $MLDs$ are not significantly different. The largest difference between $C-t$ and $T-t$ values is in April.

Figure 4.8 shows that in March, April and May the mean values of MLD are larger offshore than inshore while in October the mean value is larger inshore than offshore. This is different than in 2003-2004 when the $MLDs$ were always larger offshore. The confidence intervals overlap in June and July. Figure 4.9 shows the probability density function (PDF) of the inshore and offshore $MLDs$ for the same months. The PDFs are very different from month to month and the only month when the inshore and offshore distributions are remotely similar was found in 2003-2004 in the month of July when smaller $MLDs$ are observed.

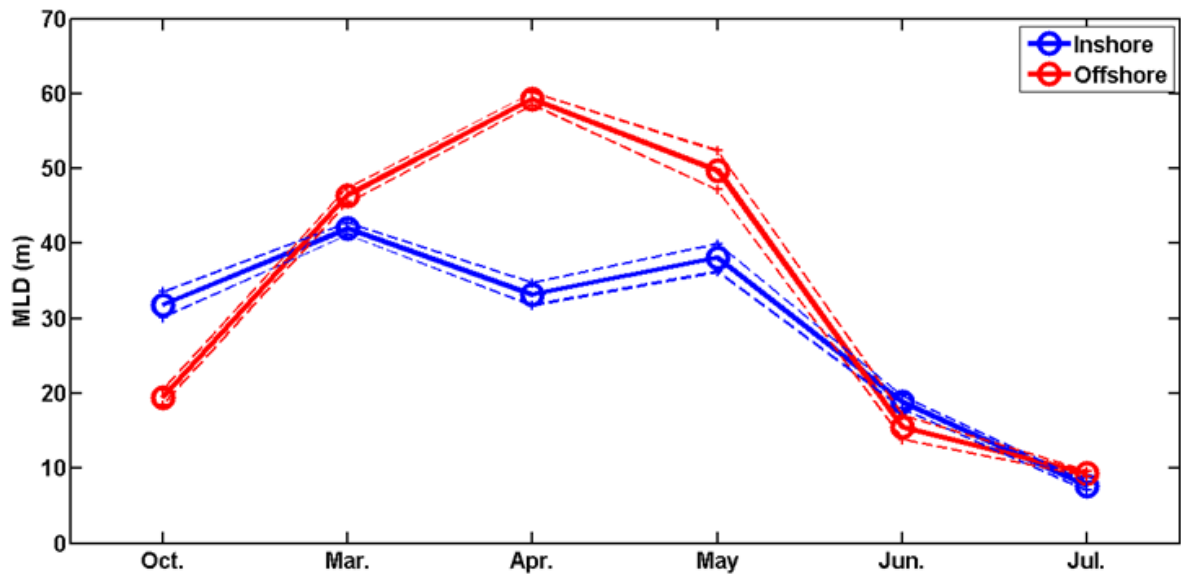


Figure 4.8: Monthly mean values of the inshore (blue) and offshore (red) *MLDs* during the CFL (2007-2008). The dash lines are the 95% confidence intervals on the mean value of the *MLD*. Number of the observation in each month is shown in Table 4.4.

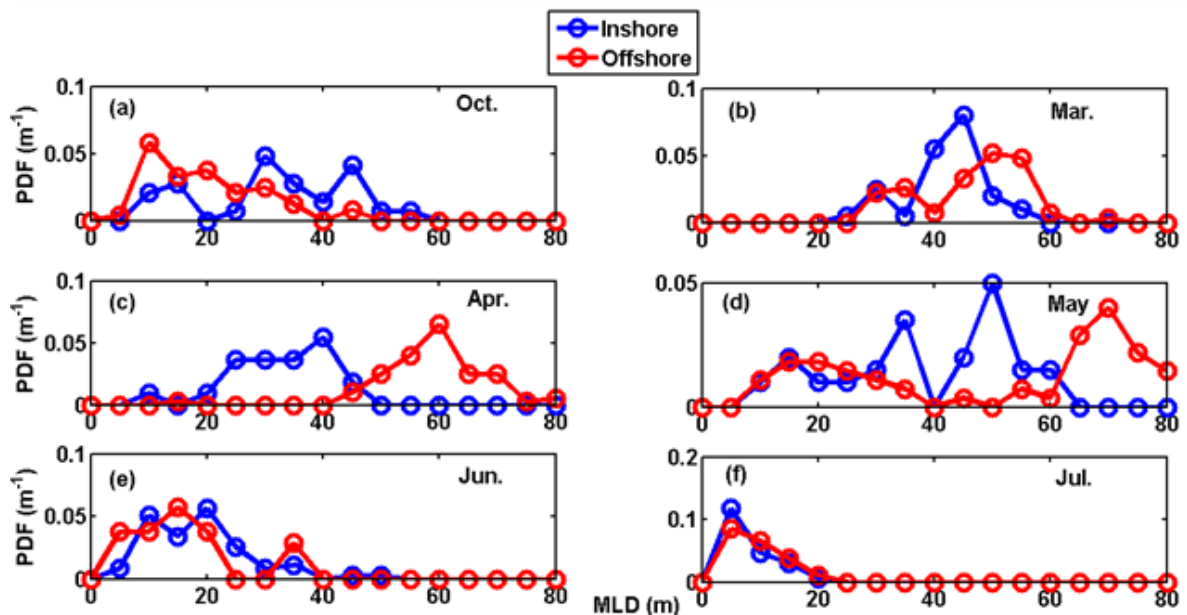


Figure 4.9: Probability density functions of the inshore and offshore *MLDs* during the CFL (2007-2008). (a) October, (b) March, (c) April, (d) May, (e) June and (f) July.

Table 4.5: Student t -test comparisons between inshore and offshore $MLDs$ during fall 2002 (CASES), late summer 2005 (ArcticNet), fall 2006 (ArcticNet) and summer 2009 (Malina). N_1 and N_2 are the number of inshore and offshore observations. $T-t$ and $C-t$ are the tabulated t and calculated t values using equation 4.7. The results of the t -test are either Significant (Sig.) or Non-Significant (No Sig.). Mean inshore and Mean offshore are the confidence intervals on the monthly mean MLD .

Month	Fall 2002	Summer 2005	Fall 2006	Summer 2009
N_1	46	12	21	37
N_2	55	47	42	110
$T-t$	1.99	2	2	1.98
$C-t$	3.59	1.19	1.17	1.93
Student t -test	Sig.	No Sig.	No Sig.	No Sig.
Mean MLD (In)	7.9-10.3	8-12.8	8.2-14	7-9.2
Mean MLD (Off)	11-13.8	10.7-12.8	11.2-14.6	8.5-9.8

CASES (2002), ArcticNet (2005 and 2006), Malina (2009) The comparison between inshore and offshore $MLDs$ is done using student t -test (Table 4.5) (Figure 4.10) and PDF (Figure 4.11) for the series of observations in fall 2002 (CASES), fall 2006 (ArcticNet), late summer 2005 (ArcticNet) and summer 2009 (Malina). The results of the student t -test in Table 4.5 show that in fall 2002, the $C-t$ value is larger than the $T-t$ value: the mean values of fall 2002 are therefore significantly different. As also shown in Figure 4.10, there is no overlap between the confidence intervals. This figure gives an idea of the distribution of the observations around the means. In summer 2005, fall 2006 and summer 2009, $C-t$ values are smaller than $T-t$ value: the inshore and offshore mean $MLDs$ are therefore comparable. The overlaps between confidence intervals in summer 2005, fall 2006 and summer 2009 confirms the results of student t -test presented in Table 4.5.

The probability density functions are shown in Figure 4.11 and they confirm the results of student t -test shown in Table 4.5 as well as the mean values comparison in Figure 4.10. Figure 4.11 shows that the most frequent $MLDs$ in fall 2002 offshore area are larger than inshore area, about 10-15 m and 5 m respectively. In summer 2005 and summer 2009, they are comparable while in fall 2006 the most frequent $MLDs$ are slightly larger.

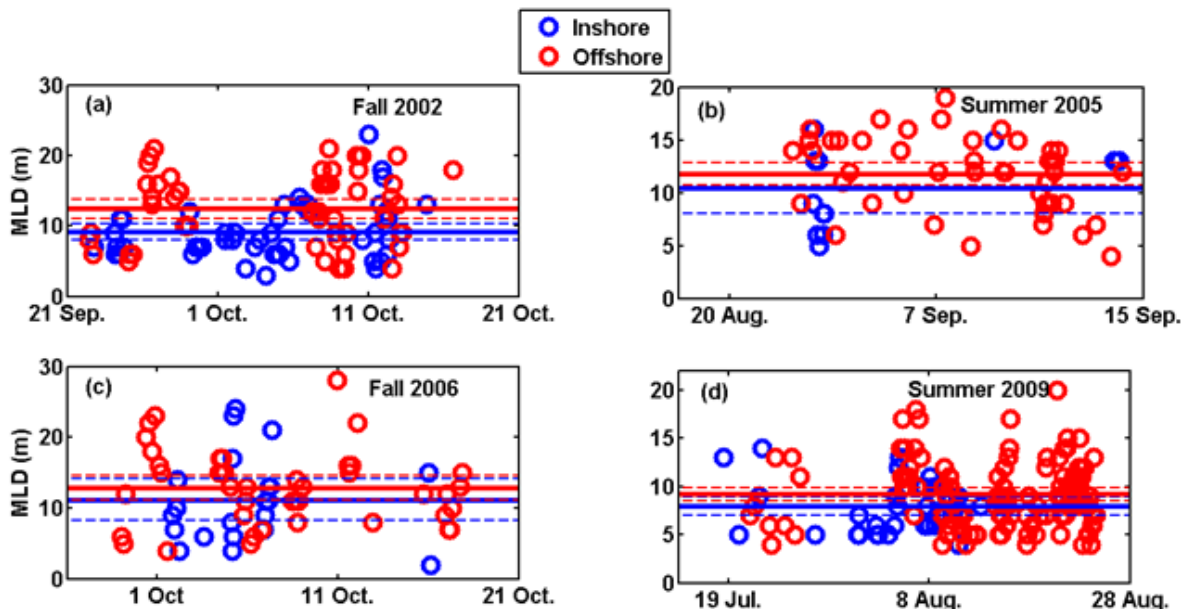


Figure 4.10: Mean values of the inshore (blue) and offshore (red) MLD s regardless of the subregion during (a) Fall 2002 (CASES), (b) Summer 2005 (ArcticNet), (c) Fall 2006 (ArcticNet) and (d) Summer 2009 (Malina). The dash lines are uncertainty limits with 95% confidence intervals on the mean inshore MLD (blue solid line) and offshore (red solid line).

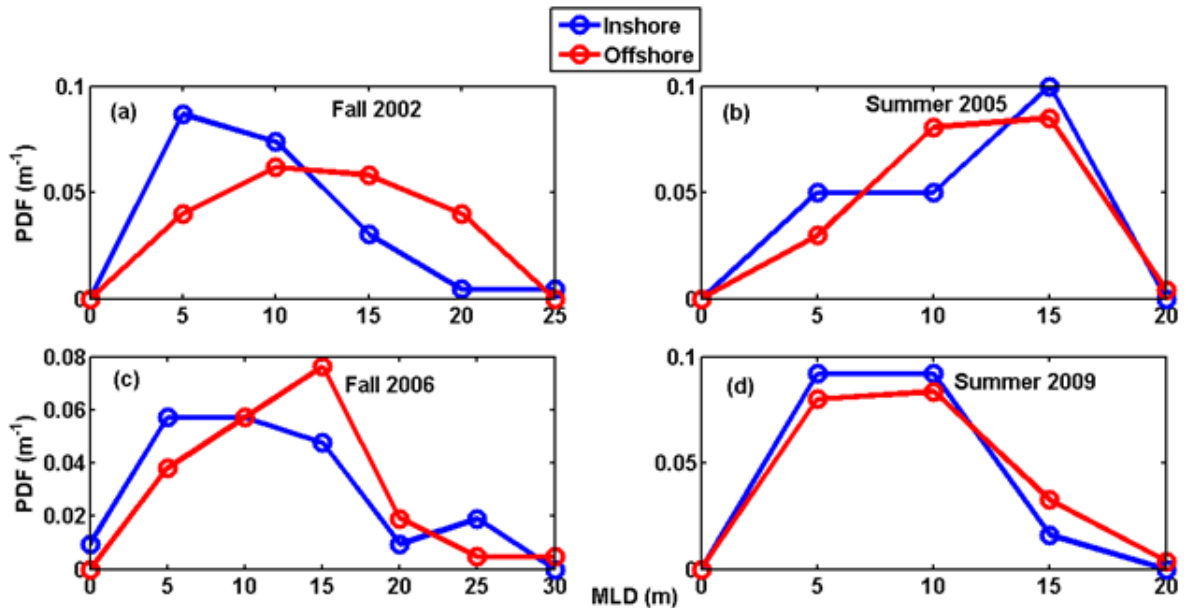


Figure 4.11: Probability density functions of MLD inshore and offshore areas during (a) Fall 2002 (CASES), (b) Summer 2005 (ArcticNet), (c) Fall 2006 (ArcticNet) and (d) Summer 2009 (Malina).

4.3.1.2 Regarding the subregions

In an attempt to assess the potential spatial effects on the inshore and offshore *MLDs*, we will compare the mean *MLDs* within the same subregions. The results are presented in Table 4.6. As shown in the table the C-*t* is larger than T-*t* in falls (with one exception) and spring while C-*t* is smaller than T-*t* in the summer. The mean *MLDs* overlap only in summer as shown in Figure 4.12f, g and h. This indicates that the mean *MLD* values in each subregion are significantly different in the fall and the spring but they are comparable in the summer. The probability density functions (PDFs) are consistent with the mean values (Figure 4.13). As shown in Figure 4.13a, b, c, d and e, the most frequent *MLDs* are larger offshore than inshore in fall and spring while Figure 4.13f, g and h shows that the most frequent *MLDs* in the summer are comparable inshore and offshore. The shallower *MLDs* inshore in fall and spring are due to the stronger stratification in this area. It should be noted that in summer the inshore and offshore *MLDs* becomes similar. Looking at Figure 4.13, we can see that some periods appear more Gaussian than others because the distribution of *MLDs* is around a specific value or there is one peak in the PDF. It can be because of different reasons such as small number of sampling which means if the number of sampling increases the distribution of the *MLDs* would be a Gaussian or ship displacement which means that the sampling were done in different locations which cause spatial effects on the *MLD*.

The reason why the deeper *MLDs* are found offshore in winter may reside in the difference between the inshore and offshore ice covers. The inshore region, Franklin Bay for example, is covered with landfast ice all winter and until June or later in most regions. Offshore, we find the Circumpolar Flaw Lead, a region where ice is drifting with the currents and the winds. These areas are either open in winter or covered with thin ice. This means that the wind can mix the surface layer, even in winter. Moreover, open area means heat loss to the atmosphere and continuous (or at least frequent) brine rejection associated with ice formation. All these processes will lead to deeper *MLDs*. In the inshore areas, as ice is formed and thickened in the fall, its growth rate decreases gradually (Smith, 1990). Therefore, the growth rate of landfast ice decreases from late fall until the spring while offshore ice forms continuously. Hence, during this period, the inshore areas are more stratified and the *MLD* is shallower.

4.3.2 Spatial variations of the *MLD* between the subregions

The goal of this section is to analyze the spatial variation of *MLD* between the subregions for the same sampling period. Table 4.7 presents all available data with sufficient

Table 4.6: Student t -test comparisons between inshore and offshore MLD s in the different sub-regions. N is the number of realizations. $T-t$ and $C-t$ are the tabulated t and calculated t values using equation 4.7. The results of the t -test are either Significant (Sig.) or Non-Significant (No Sig.).

Subregion	Season-Year	BM	N	Mean MLD (m)	$T-t$	$C-t$	Student t -test
Beaufort	Fall-2002	In	18	6.7-9.2	2.03	4.16	Sig.
		Off	19	10.8-15.1			
Beaufort	Fall-2003	In	14	5.2-7.2	2.04	5.42	Sig.
		Off	20	11.7-15.3			
Mouth	Fall-2007	In	16	12.3-19.1	2.02	0.48	No Sig.
		Off	40	14.5-18.7			
Mouth	Spring-2004	In	25	11.3-20.7	2.02	4.47	Sig.
		Off	16	27.1-40.9			
Amundsen	Spring-2008	In	76	42.2-38	1.98	7.43	Sig.
		Off	108	52.1-58.2			
Beaufort	Summer-2008	In	16	4.1-7.5	2.02	2.58	Sig.
		Off	29	6.7-9.7			
Mouth	Summer-2008	In	22	9.3-10.3	2.02	0.12	No Sig.
		Off	19	6.4-9.6			
Beaufort	Summer-2009	In	30	7.3-8.5	1.98	1.17	No Sig.
		Off	90	7.9-9.3			

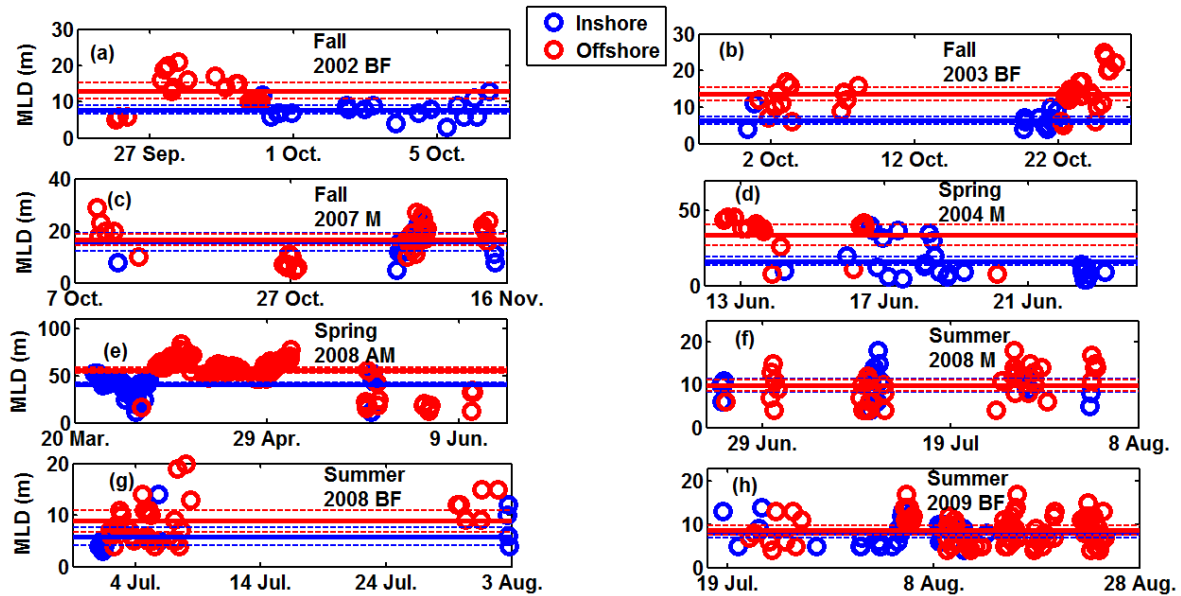


Figure 4.12: Mean values of the inshore (blue) and offshore (red) MLD s within the subregions during (a) Fall 2002 in the BF, (b) Fall 2003 in the BF, (c) Fall 2007 in the M, (d) Spring 2004 in the M, (e) Spring 2008 in the AM, (f) Summer 2008 in the M, (g) Summer 2008 in the BF and (h) Summer 2009 in the BF. The dash lines are uncertainty limits with 95% confidence intervals on the mean inshore MLD (blue solid line) and offshore (red solid line).

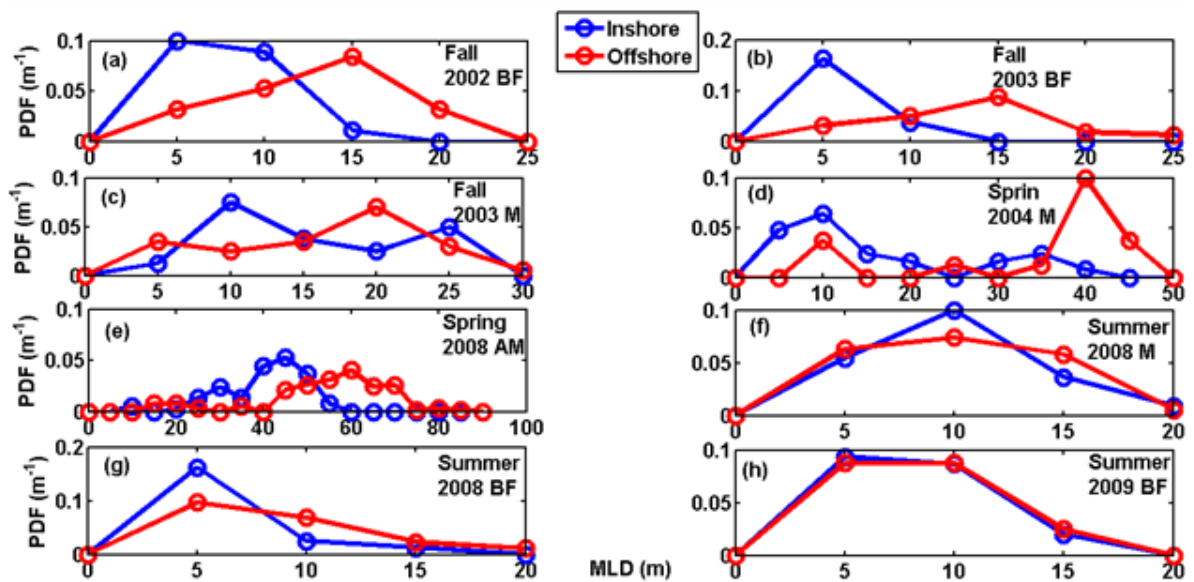


Figure 4.13: Probability density functions of MLD s inshore and offshore areas within the subregions during (a) Fall 2002 in the Beaufort subregion, (b) Fall 2003 in the Beaufort subregion, (c) Fall 2003 in the Mouth subregion, (d) Spring 2004 in the Mouth subregion, (e) Spring 2008 in the Amundsen subregion, (f) Summer 2008 in the Mouth subregion, (g) Summer 2008 in the Beaufort subregion and (h) Summer 2009 in the Beaufort subregion.

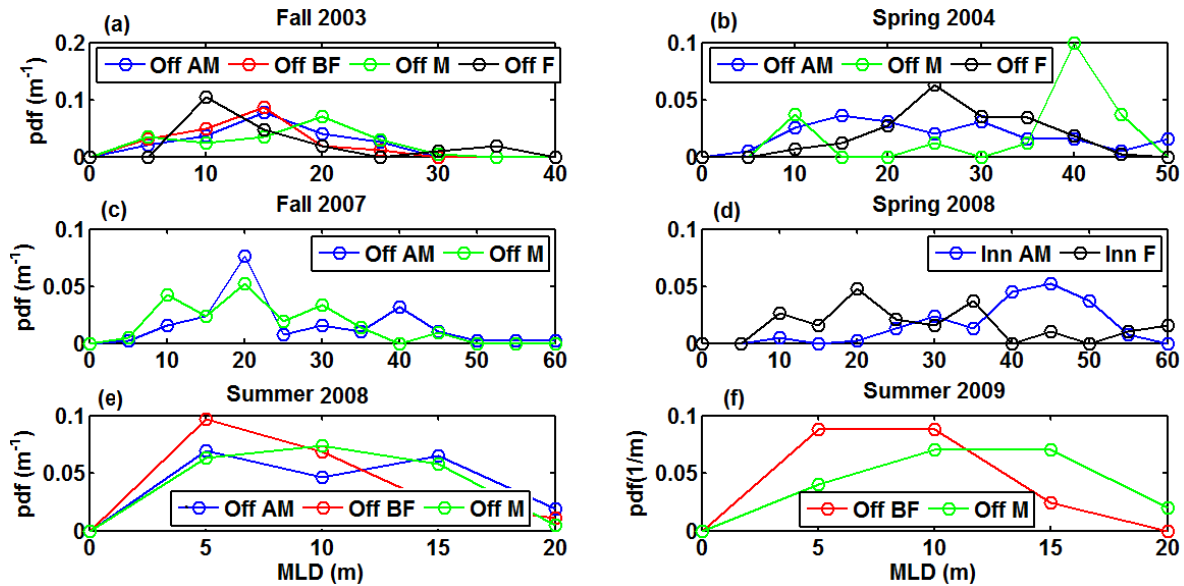


Figure 4.14: Probability density functions of offshore MLD s in different subregions in (a) Fall 2003, (b) Spring 2004, (c) Fall 2007, (d) Spring 2008, (e) Summer 2008 and (f) Summer 2009.

number of realizations (at least 14) for this analysis. Apart from spring 2008, the mean values of MLD s are reasonably comparable in all the regions for the same season. In spring 2008 (case 4), the mean value of MLD is significantly larger in the Amundsen compared to the Franklin Bay. The PDFs (Figure 4.14d) show that larger MLD s (40-50 m) are more frequent in the Amundsen Gulf while in Franklin Bay MLD s of 15-25 m are more frequent. In fall 2003 (case 1), contrary to the mean values, the probability density functions of MLD in the subregions show that the MLD s are not completely similar (see Figure 4.14a). The most frequent MLD in the Mouth region (Figure 4.14a) is the largest (20 m) while in the Franklin Bay it is the smallest (10 m). In the Beaufort and Amundsen regions the most frequent MLD s are around 15 m and comparable. Figure 4.14b shows that in spring 2004 (case 2), although the most frequent MLD s are around 15 m in the Amundsen, the PDFs in Franklin Bay and Mouth show that the most frequent MLD is around 25 m and 40 m respectively. Although the PDFs in fall 2007 and summer 2008 (Figure 4.14c and e) show that the distributions of MLD s are almost comparable in all subregions with a peak around 20 m in fall 2007 and 5 m in summer 2008, deeper MLD s are also frequent in the Amundsen and the Mouth regions (see the second peak on the right in the blue and green lines in Figure 4.14c and e). The PDFs in summer 2009 (Figure 4.14f) show that in the Beaufort subregion, the MLD s with values between 5-10 m are more frequent while in the Mouth the most frequent MLD s are around 10-15 m.

The results presented in this section based on the analysis of mean values and

Table 4.7: Comparison between offshore *MLDs* from different years and seasons. See Figure 4.2 for the definition of the regions.

Case	Year	Region	Number of casts	Mean <i>MLD</i> (m)	Uncertainty (95%)
1	Fall 2003	Amundsen	39	15.5	± 1.7
		Beaufort	20	13.5	± 1.8
		Mouth	40	16.5	± 2.1
		Franklin	21	15.5	± 3.4
2	Spring 2004	Amundsen	39	25	± 4.0
		Mouth	16	34	± 7.0
		Franklin	152	28	± 1.2
3	Fall 2007	Amundsen	100	25	± 2.3
		Mouth	42	21.5	± 2.8
4	Spring 2008	Amundsen	76	40	± 2.1
		Franklin	38	29	± 2.7
5	Summer 2008	Amundsen	29	9.4	± 1.8
		Beaufort	29	8.2	± 1.5
		Mouth	19	8	± 1.6
6	Summer 2009	Beaufort	90	8.6	± 0.7
		Mouth	20	11.5	± 1.8

their PDFs clearly prove that an analysis of only the mean values is not sufficient to compare the *MLDs* in different regions. It was shown that although the mean values are comparable, the PDFs reveal important disparities between subregions.

4.3.3 Evolution of the *MLD* in Transects

In this section the evolution of *MLD* are discussed during the same years but along different transects. The *MLDs* and physical parameters evolution are analyzed during leg 0202 in fall 2002 along two transects: Tr3 (offshore of the Mackenzie River) and TrAM (from East to West) (see Figure 4.15), and in fall 2003 during leg 0304 along four transects : Tr1 (from Cape Parry to Banks Island), Tr2 (from Cape Bathurst to Banks Island), Tr3 and TrAM (Figure 4.16).

Figure 4.15 illustrates that in fall 2002 the inshore surface water in the Beaufort Sea (Tr3) is warmer and more stratified than the offshore waters and the *MLD* is thus shallower inshore region than offshore. The sampling in the Amundsen (TrAM) during leg 0202 in fall 2002 was done starting from the middle of the Mouth subregion moving toward the East in two parts. The first part was done on 3-4 October and the second half was done on 7-8 October. The time evolution of the sampling operations is illustrated with color codes on Figure 4.15a,b. In the Amundsen Gulf the surface water is more stratified in the East and there is no mixed layer for the first 20 km but as we move westward the mixed layer appears. As it is clear in Figure 4.15c, under the mixed layer in the halocline the water is warmer compared with its upper and lower layers while we are not witnessing such layer on transect Tr3 in the Beaufort Sea.

Figure 4.16 shows the variation of the *MLD* and physical properties in fall 2003 on four transects Tr1, Tr2, Tr3 and TrAM. This figure illustrates that near the coasts the isolines of the salinity are generally closer to each other which indicates a stronger stratification and shallower *MLDs*. In transect Tr3 moving from inshore to the offshore, the surface water becomes colder and less stratified and *MLDs* become deeper. This figure also shows that Tr1 and Tr2 are generally comparable in terms of the *MLDs*, surface temperature and salinity. Right below the mixed layer a relatively warmer layer is observed in Tr1, Tr2 and TrAM while such layer is not found in Tr3.

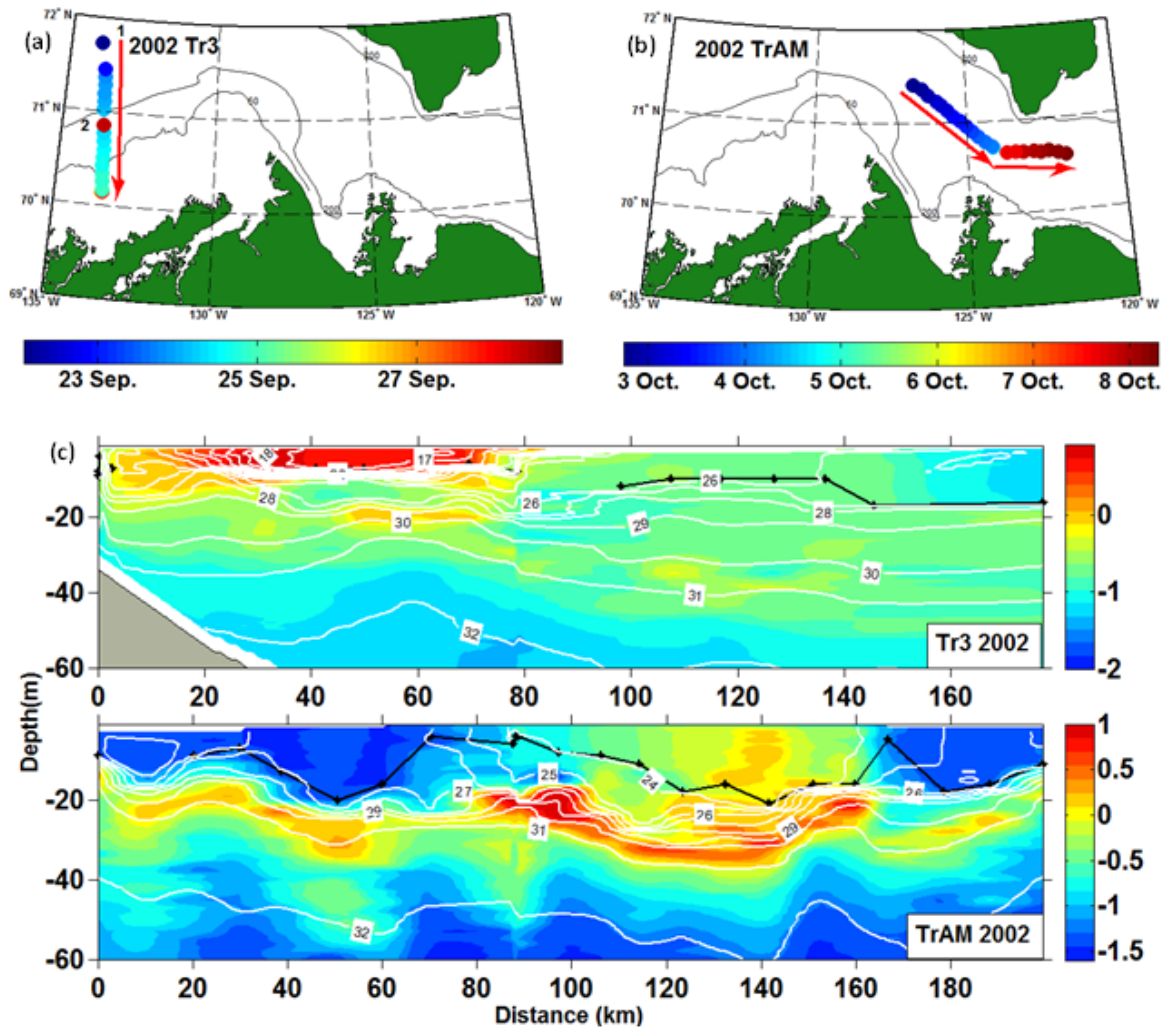


Figure 4.15: (a) and (b) Locations of the sampling stations as a function of time along transects Tr3 and TrAM during fall 2002 (leg 0202). (c) Temperature contours with salinity isolines (white lines) and the *MLD* (black lines) along Tr3 (from south to North) and along TrAM (from East to West). Distances are from the coast.

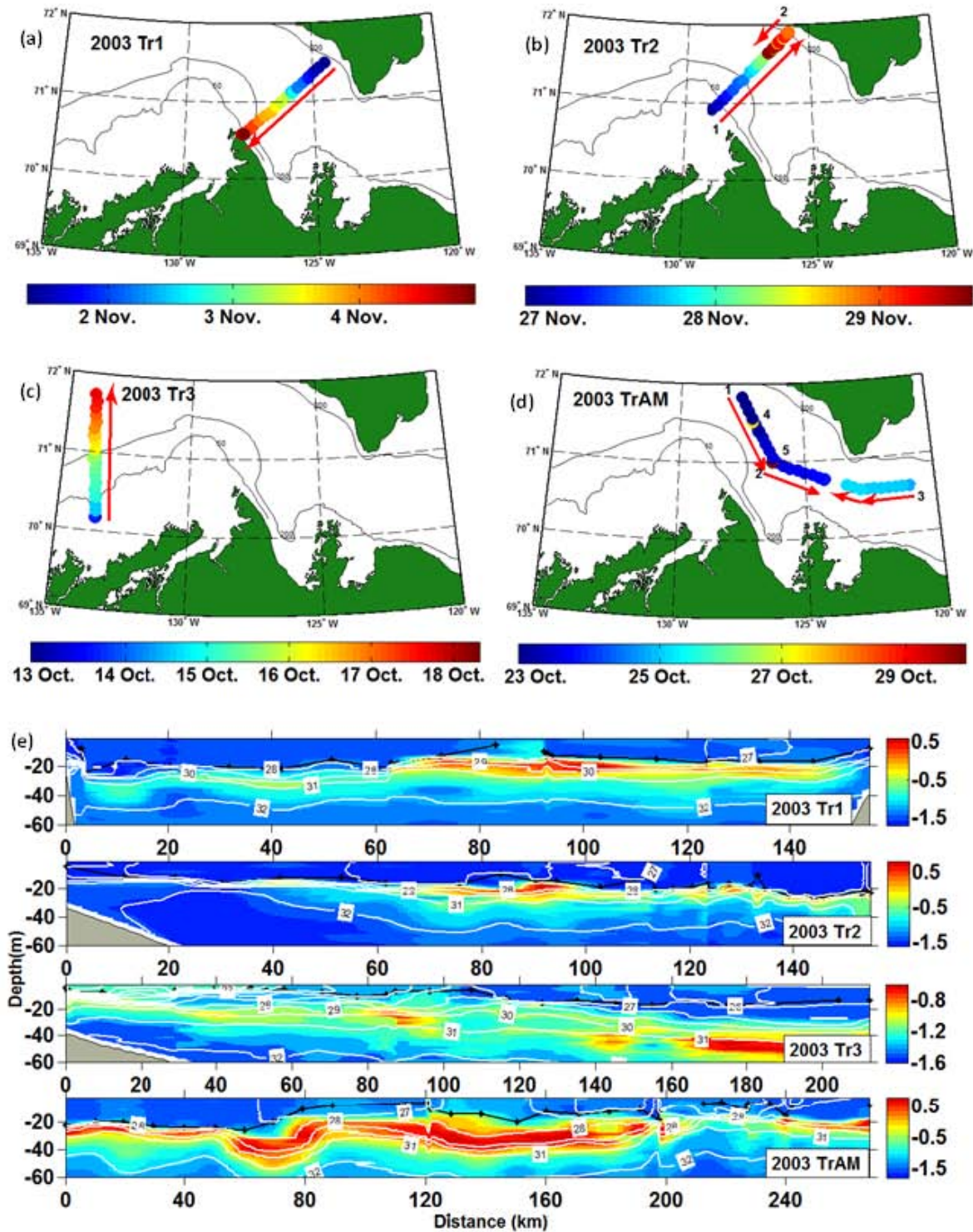


Figure 4.16: (a), (b), (c) and (d) Locations of the sampling stations as a function of time along transects Tr1, Tr2, Tr3 and TrAM during fall 2003 (leg 0304). (e) Temperature contours with salinity isolines (white lines) and the *MLD* (black lines) along Tr1 (from South to North), Tr2 (from South to North), Tr3 (from South to North) and TrAM (from East to West). The sampling is done during leg 0304 in fall 2003.

4.4 Temporal evolution of the *MLD*

In the previous section the spatial distribution of *MLD* were analyzed, in the present section the temporal (i.e. seasonal and interannual) evolution of the *MLD* is investigated. Thanks to the two year-long datasets during 2003-2004 (CASES) and 2007-2008 (CFL), we are able to investigate seasonal evolution in each year as well as interannual evolution in each subregion.

4.4.1 Seasonal evolution of the *MLD* during the CASES (2003-2004) and CFL (2007-2008)

In order to analyze the seasonal evolution of the *MLD*, we will consider five regional data sets. Three datasets were acquired during the CASES (2003-2004): in the Amundsen region (fall, spring and summer), the Mouth region (fall, spring and summer) and in Franklin Bay (fall, winter, spring and summer) and two datasets during CFL (2007-2008) in the Amundsen Gulf (fall, winter, spring and summer) and the Mouth region (fall, winter, spring and summer).

Figure 4.17 shows the seasonal *MLD* evolution in different subregions during 2003-2004. The locations of the sampling stations as functions of time in the Amundsen are shown in Figure 4.18. In the Amundsen during 2003-2004, the mean values of the *MLD* in fall, spring and summer are respectively 15.5 m, 23.5 m and 7.5 m (Figure 4.17a, left side). Considering the uncertainties, it is clear that the *MLD* is deepest in spring and shallowest in summer. Moreover, the PDFs in the Amundsen (Figure 4.17a) show a sharp peak around 5 m in summer which illustrates that in the summer the most frequent *MLD* is shallower than its mean value (7.5 m). In fall, the PDF shows a peak around 15 m and thus the most frequent *MLD* has the depth comparable with the mean value. Nonetheless, the large plateau (between 10 m and 30 m) in the PDF in spring shows that *MLDs* at that time are widely distributed, possibly because of the sparse ice distribution. In the latter case, the mean value of *MLD* per se may lead to a misinterpretation of the characteristics of *MLD* since mixed layers with depth much less or much larger than the mean value are also very frequent.

Figure 4.17b,c show that, as in the Amundsen region, the mean *MLD* is the deepest in spring and the shallowest in summer in the Mouth and Franklin subregions. Furthermore, it demonstrates that deep *MLDs* are very frequent in the spring compared to other seasons. The *MLD* in winter is deeper than that in fall but shallower than that in spring. The PDF in summer is very much similar in all subregions, i.e. a sharp peak

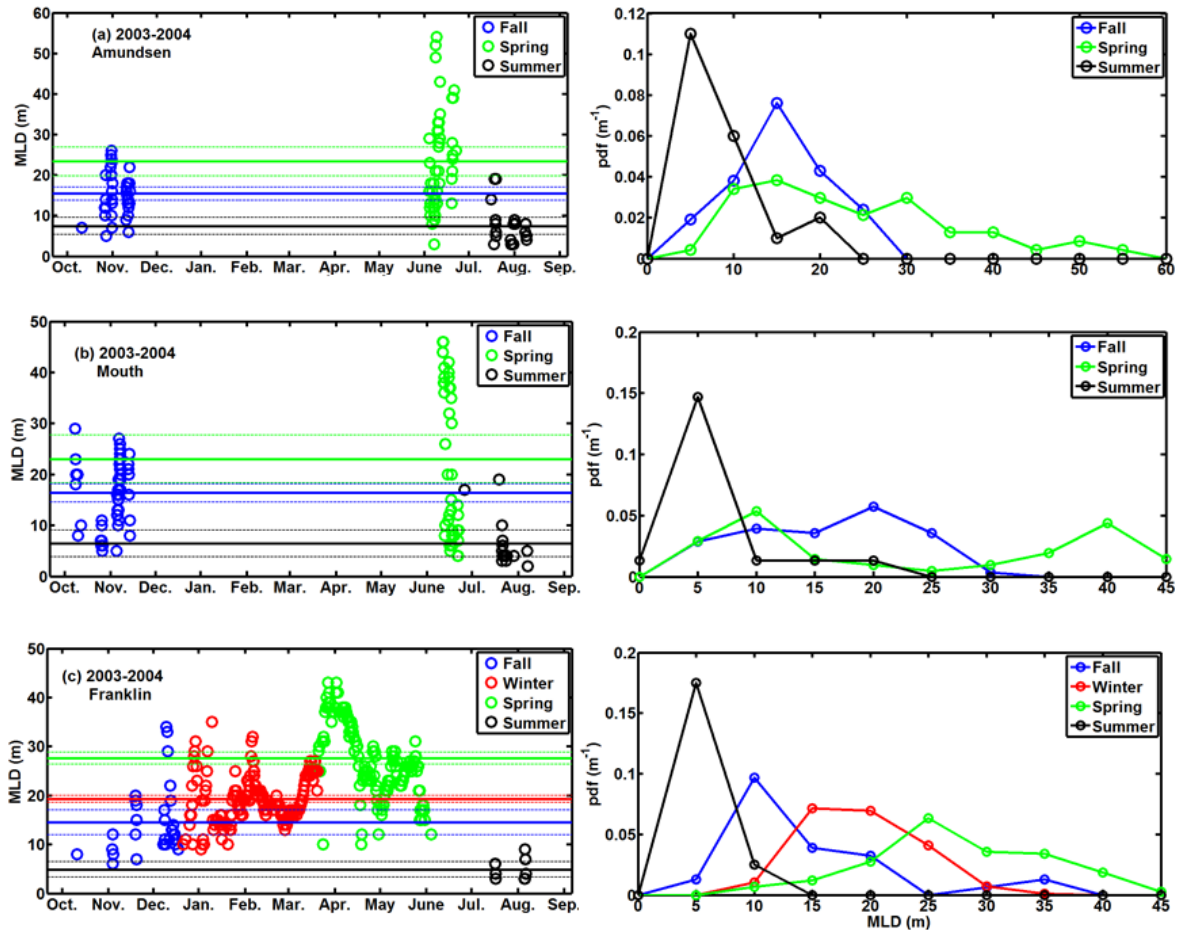


Figure 4.17: Seasonal variations of the *MLD* in different subregions during 2003-2004 (CASES); (a) Amundsen, (b) Mouth and (c) Franklin subregions. The mean values and their variability are presented on the left side and the PDF on the right side. The mean values for each season (solid lines) with their 95% confidence intervals (dashed lines) are presented with the time evolution (color coded) of the estimated *MLDs*. The right-hand figures are the PDFs for the corresponding seasons. The number of intervals in each PDF panel is selected according to the available observations. For example, in the Franklin in the summer we have the least number of intervals because the number of samples is small (13).

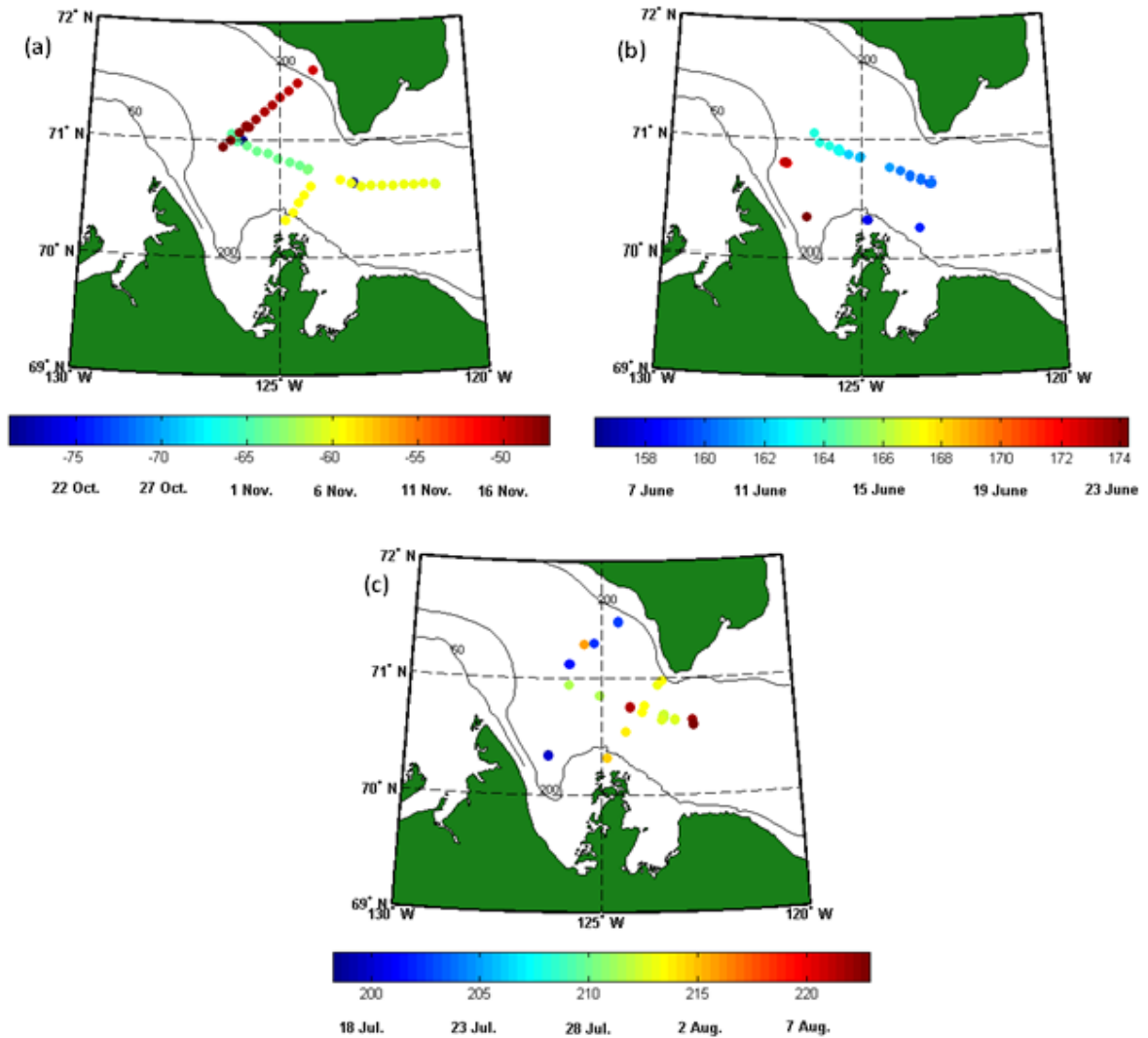


Figure 4.18: (a), (b), (c) Locations of the sampling stations as a function of time in the Amundsen region during fall, spring and summer 2003-2004, respectively. The color of the circles identifies the sampling date.

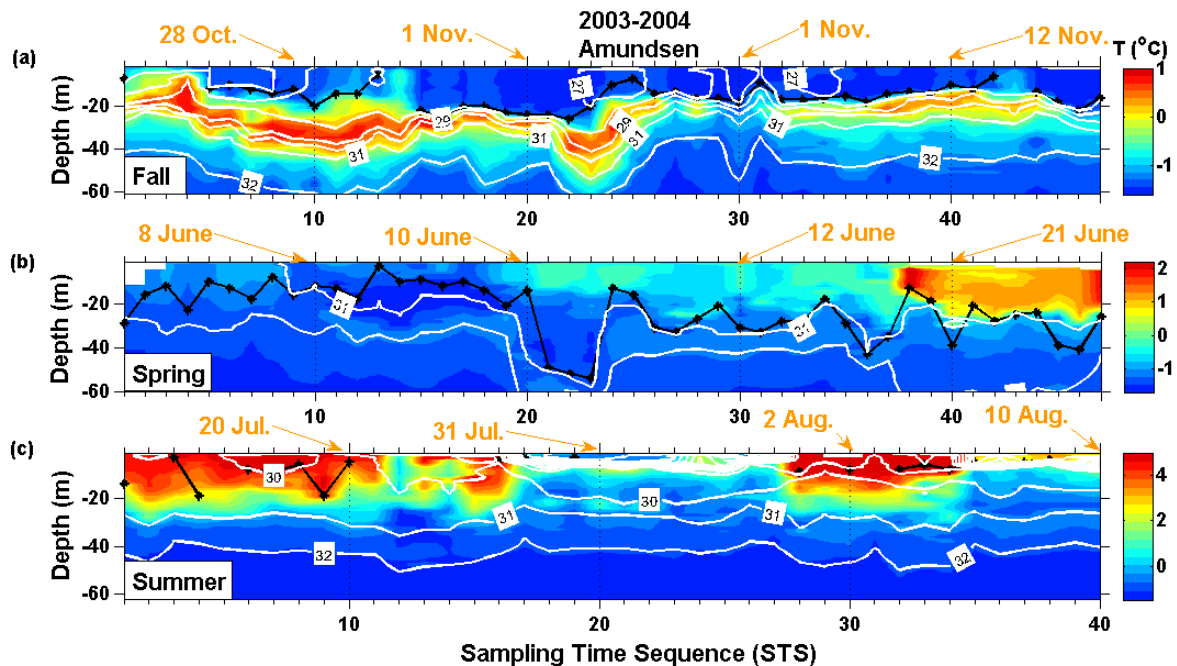


Figure 4.19: Contours of the temperature in the Amundsen subregion with salinity iso-lines (white lines) during three different seasons in 2003-2004. (a) Fall, (b) spring and (c) summer. The black broken lines are the *MLDs*. The Sampling Sequences (STS) axis (in days) start at zero in each panel. Note that density contours follow salinity contours.

at 5 m. In the Franklin region, the PDFs in fall and in winter have peaks at 10 m and 15-20 m respectively. It worth mentioning that the peak of PDF in Figure 4.17c shows that there is a clear shift toward deeper *MLDs* from summer to spring in the Franklin area.

Figure 4.19 presents the contours of the temperature and salinity and the sampling time sequence (STS) during CASES (2003-2004). As shown in this figure, during fall 2003 in the Amundsen subregion, the surface water is cold and under the *MLD* (black line) there is a large zone of high temperature which may be “Near Surface Temperature Maximum” or NSTM (Jackson et al., 2010) or sTM, i.e. sub-surface Temperature Maximum as described in Sévigny (2013). The NSTM are pools of warm water that are caught in the seasonal halocline and then pushed down by the formation of a colder mixed layer. The sTM are surface warm water that is sinking along frontal structures. NSTMs are more persistent structures.

In spring, the surface salinity is higher which generally makes the *MLD* deeper than in the fall as shown in Figure 4.19. Moreover, the surface water in spring is warmer than in fall due to the solar radiation while the surface layer is still salty because of the long period of cooling and ice freezing. This shows that in spite of the surface water warming which leads to the ice melting, the surface layer is still not stratified enough

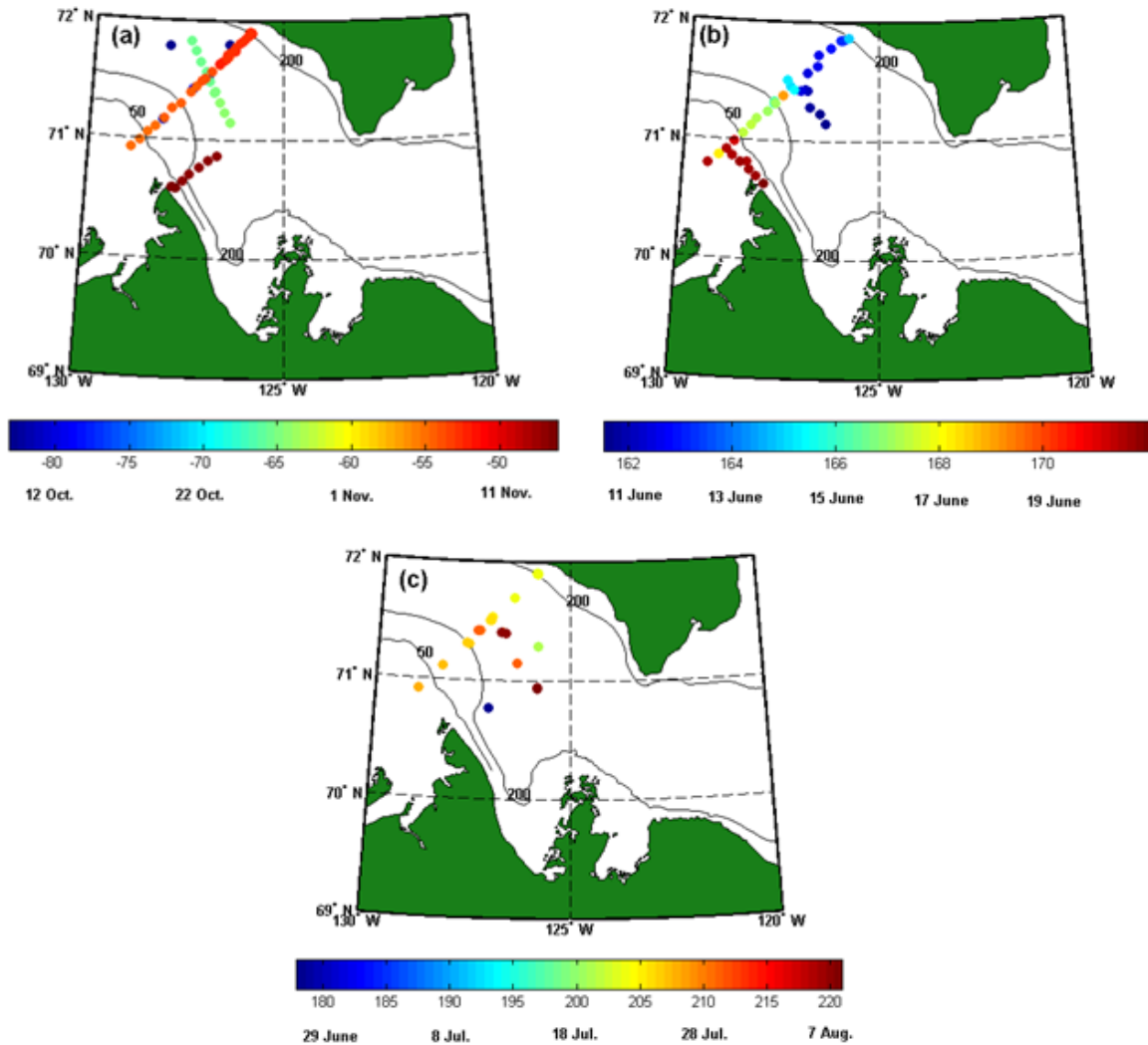


Figure 4.20: (a), (b), (c) Locations of the sampling stations as functions of time in the Mouth region during fall, spring and summer 2003-2004, respectively. The color of the circles identifies the sampling date.

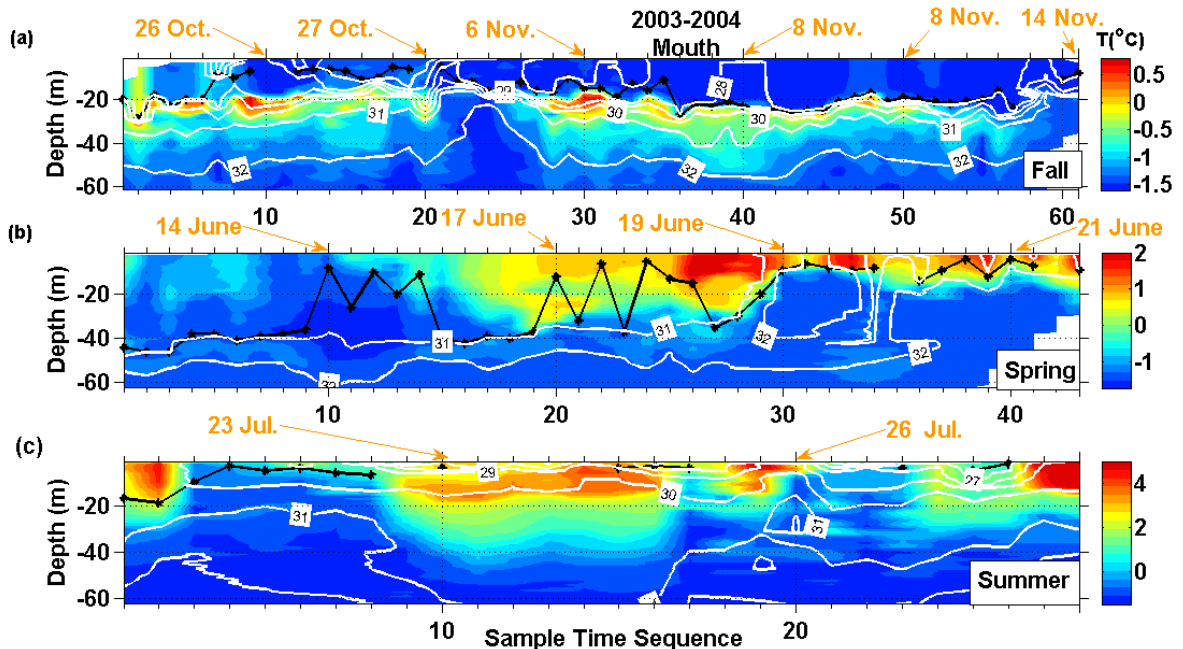


Figure 4.21: Contours of the temperature with salinity isolines (white lines) in the Mouth region during different seasons in 2003-2004. (a) Fall, (b) spring and (c) summer. The black broken lines are the *MLDs*. The Sampling Sequences (STS) axis (in days) starts at zero in each panel.

to make the *MLD* shallower. In summer the surface layer is warm and stratified due to the ice melting caused by solar radiation. This is why the peak of PDF in Figure 4.17a, is close to the summer *MLD* minimum.

The situation is similar in the Mouth region (Figure 4.20 and Figure 4.21): the ML is the thickest in spring and the thinnest in summer. Although the mean values of *MLD* are comparable in the Amundsen and Mouth, the PDFs are very different, except in summer (see Figure 4.17). In the Mouth region, the PDF in spring has two distinct peaks at two extremes of the PDF: 10 m and 40 m. It is important to mention that mixed layers with depths around the average (23 m) are not frequent at all in spring.

Figure 4.21 presents the contours of the temperature and salinity in the Mouth subregions which shows warmer and saltier surface water in the spring compared to the fall, a large zone of high temperature under the *MLD* in the fall, and warm and stratified water surface layer in the summer. As shown in Figure 4.21a, the *MLD* gradually deepens from 26 October (STS= 10) till 8 November (STS = 45) in the Mouth subregion but in 13-14 November (STS= 57 – 61) when the sampling is done near Cap Bathurst the *MLD* is found to be shallower because the surface water is more stratified. The spring sampling in the Mouth subregion is done during the last ten days of spring (11-21 June between days 163-173) as shown in Figure 4.20b. The reason

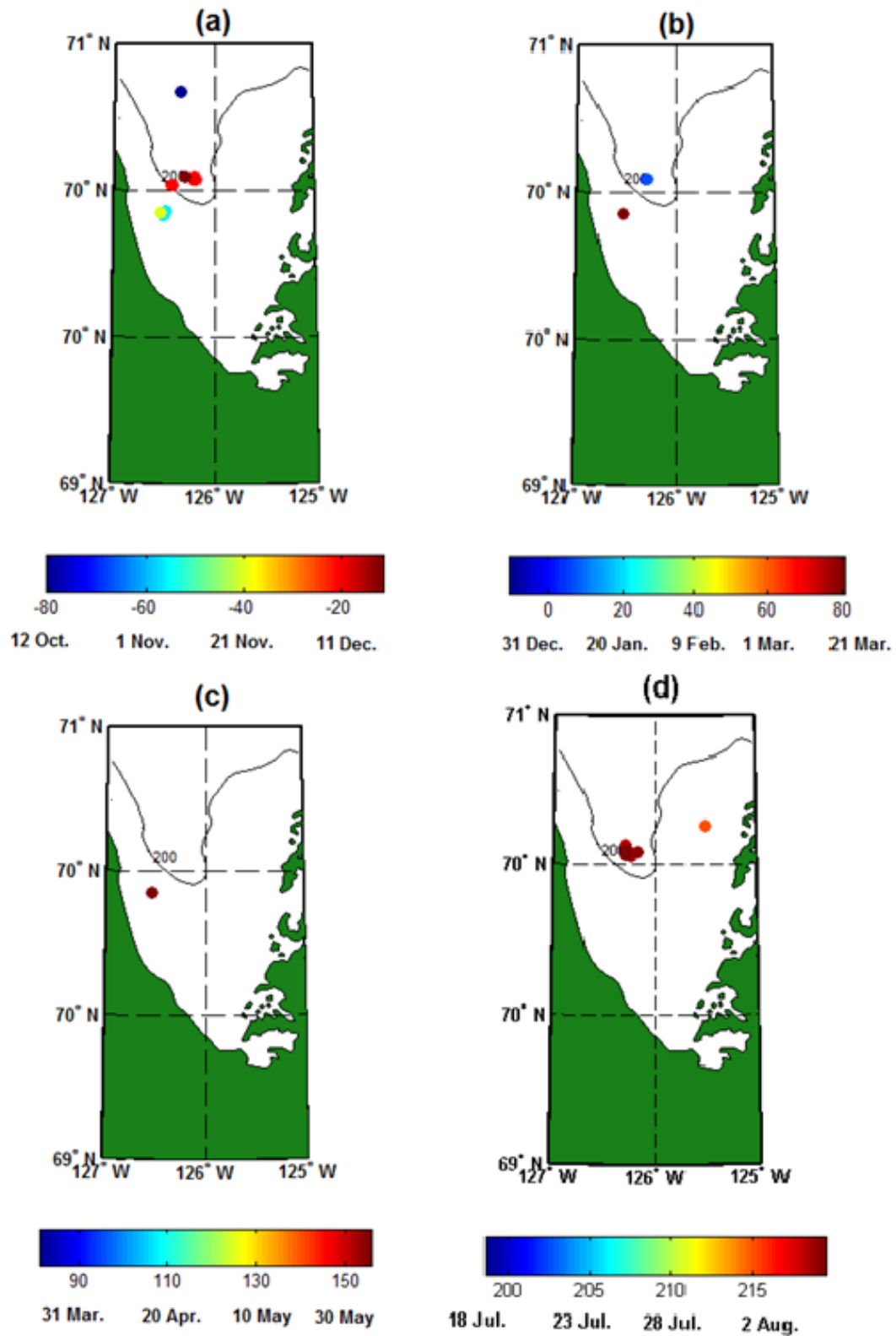


Figure 4.22: (a), (b), (c) and (d) Locations of the sampling stations as functions of time in the Franklin subregion during fall, winter, spring and summer of 2003-2004, respectively. The color of the circles identifies the sampling date.

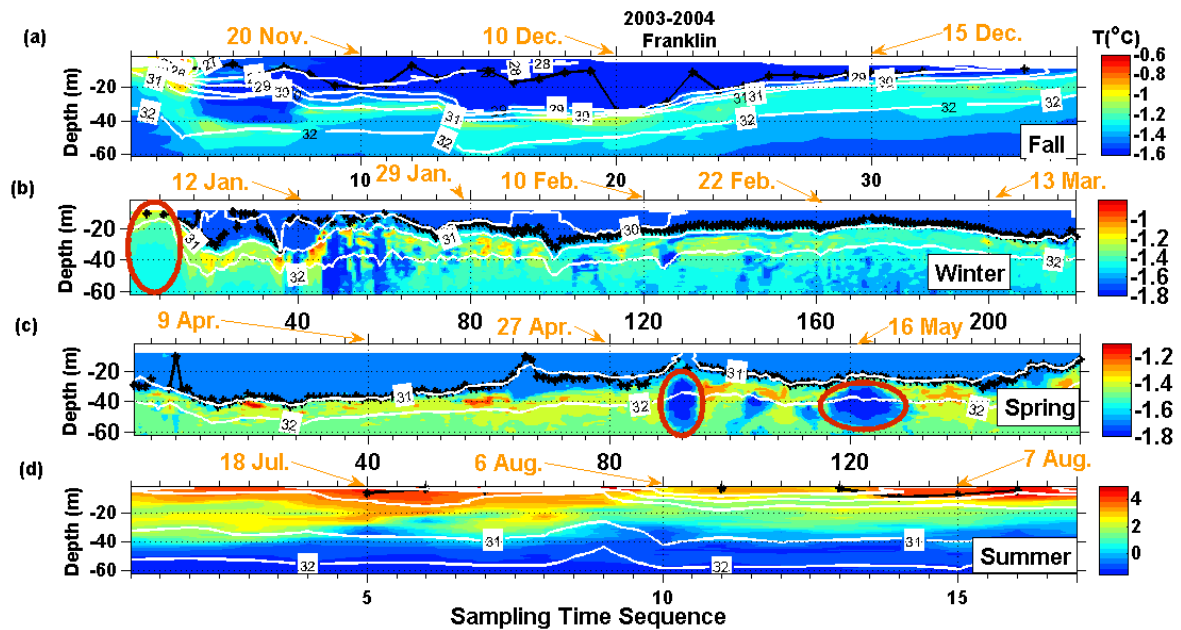


Figure 4.23: Contours of the temperature with salinity isolines (white lines) in the Franklin subregion during different seasons of 2003-2004. (a) Fall, (b) winter, (c) spring and (d) summer. The black broken lines are the *MLDs*. The Sampling Sequences (STS) axis (in days) starts at zero in each panel.

that the *MLD* fluctuates in the spring as shown in Figure 4.21b is mainly because the sampling were done during the last days of spring. This period is a transition period when in some places there is still ice while in some places there is non. On the other hand the ship displacement and sampling in different locations with different ice cover will result in variations of the *MLD*. The ML in the first period, i.e. up to STS= 9, is deep (about 45 m) at the center of the Mouth. It becomes shallower at STS = 9-14, as the ship was moving toward the coast and it deepens again in the center of the Mouth region. The *MLD* decreases as the ship moves from the center of the Mouth region towards Cape Bathurst. In the summer, as expected, the surface water temperature is high and the water column is completely stratified with shallow *MLs*.

In the Franklin subregion, a large amount of CTD data is available during four seasons in 2003-2004. The locations of the sampling stations as functions of time in the Franklin subregion during fall, winter, spring and summer 2003-2004 are shown in Figure 4.22. The available data include measurements at a fixed station between 9 December 2003 and 30 May 2004, and some measurements during the summer and fall. This large database allows us to better study the seasonal variations of the *MLD* in the same region. The measurements in the Franklin subregion during the fall was done on 11-12 October, 4-5 and 19-20 November and 8-19 December (Figure 4.22a). Figure 4.23 shows that the *MLD* is gradually increasing in the fall until it reaches its maximum value on 10 December, before gradually decreasing. The behaviour of the

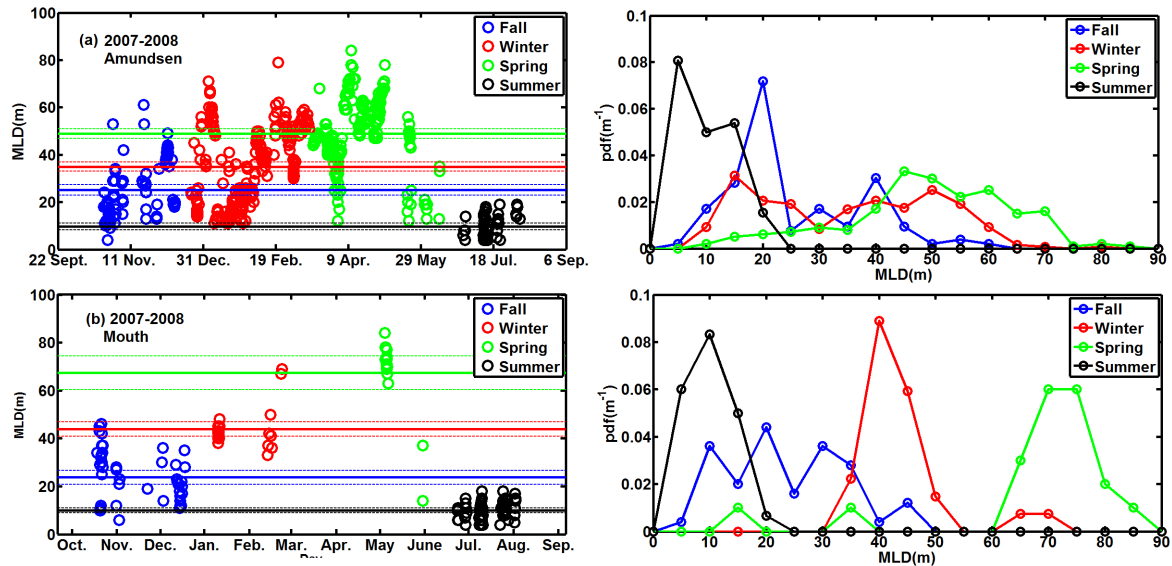


Figure 4.24: Seasonal variations of the MLD in the Amundsen and Mouth subregions during 2007-2008 (CFL). (a) Amundsen and (b) Mouth. The mean values and their variability are presented on the left side and the seasonal PDF on the right side. The mean values for each season (solid lines) with their 95% confidence intervals (dashed lines) are presented with the seasonal evolution (color coded) of the estimated $MLDs$. The number of intervals in each case is selected with respect to the available number of data.

MLD at the end of the fall and beginning of the winter may be due to ice edge upwelling caused by the favorable winds from the east near the ice edge (see Figure 4.23b and section 5.3.8). The effect of the ice edge upwelling on the water column is shown in Figure 4.23b with a red ellipse. In winter the surface layer temperature is lower and the MLD is generally deeper than in fall. After the ice edge upwelling the MLD generally increases and reaches 34 m on STS 99 (7 February) afterward it decreases to 14 m at the end of February. The MLD then increases until the end of March. Although the surface layer temperature in the spring is slightly higher than that in the winter, the salinity is also higher because of the salt rejection due to the ice formation. The MLD starts to decrease at the end of May as the surface layer temperature increases due to the solar radiation which leads to ice melting. The anticyclonic eddies on 30 April and 16 May, as suggested by Barrette (2012), make the MLD shallower as shown in Figure 4.23c with red ellipses. All over the spring and over most of the winter, the mixed layer is associated with the 31 salinity isoline. In the summer even with a small number of observations, we are witnessing that the surface layer is warm and stratified which makes the MLD shallow.

Figure 4.24 clearly shows that the mean value of MLD varies significantly from one season to another in the Amundsen and Mouth subregions during 2007-2008. The

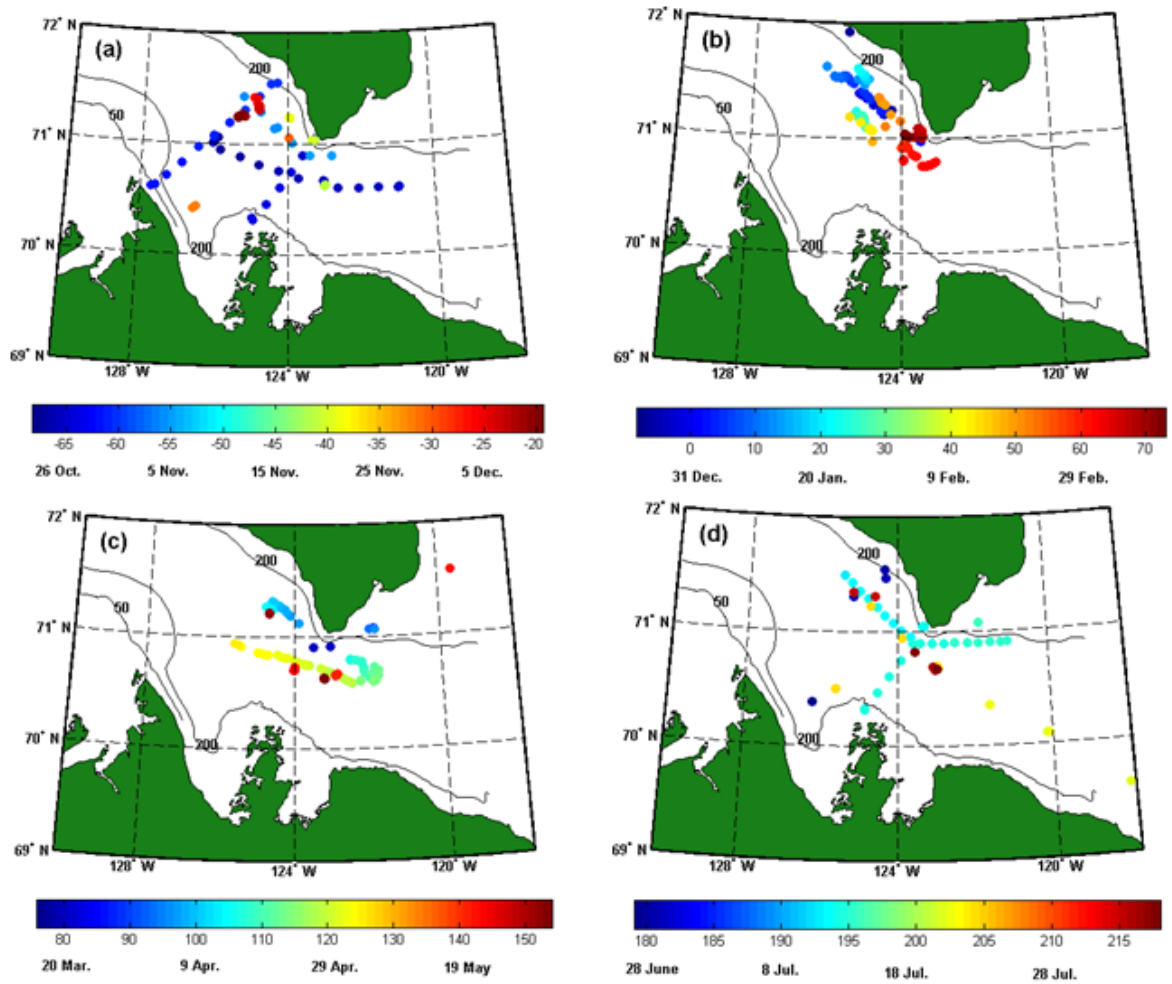


Figure 4.25: (a), (b), (c) and (d) Locations of the sampling stations as a function of time in the Amundsen subregion during fall, winter, spring and summer 2007-2008, respectively. The color of circles represents the sampling dates.

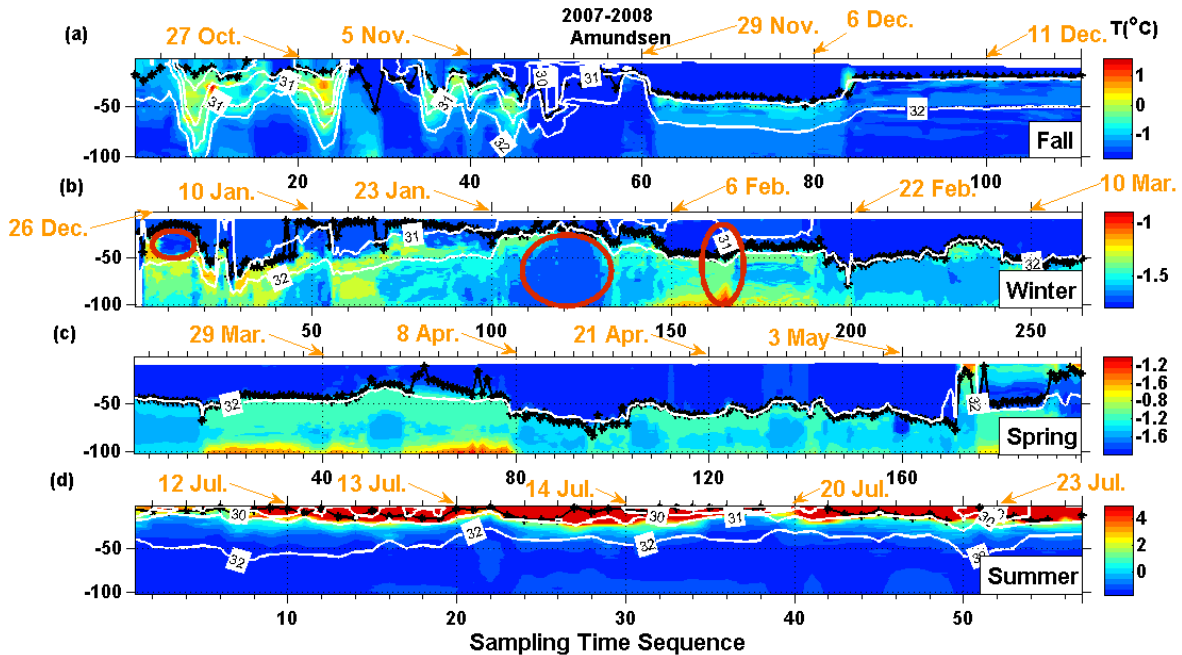


Figure 4.26: Contours of the temperature with salinity isolines (white lines) in the Amundsen subregion during different seasons of 2007-2008. (a) Fall, (b) Winter, (c) Spring and (d) Summer. The black broken lines are the *MLDs*. The Sampling Sequences (STS) axis (in days) starts at zero in each panel.

seasonal variation of the mean *MLD* is completely similar to what is already observed in different subregions in 2003-2004, i.e. the mean *MLD* is the deepest in spring (about 49 m in the Amundsen and 67 m in the Mouth) and the shallowest in summer (about 10 m in both Amundsen and Mouth subregions). The mean *MLD* in winter (about 35 m in the Amundsen and 44 m in the Mouth) is deeper than that in fall (about 25 m in the Amundsen and 24 m in the Mouth) but shallower than that in spring. The PDFs are also generally comparable to those already shown in 2003-2004. However, the mean *MLD* is much deeper in 2007-2008 compared to 2003-2004. This important increase in the depth of the ML can be clearly observed in the PDFs.

Thanks to the large number of observations in the Amundsen subregion during 2007-2008, we can analyze the seasonal evolution of the *MLD* in this region. Figure 4.25 presents the locations of the sampling stations as functions of time in this region during fall, winter, spring and summer. Also the contours of temperature with salinity isolines and the *MLD* variations in the Amundsen subregion during different seasons are presented in Figure 4.26.

As shown in Figure 4.26, the surface water becomes colder and saltier from fall 2007 until spring 2008 and consequently the *MLD* increases from the fall to the spring. The surface layer is the coldest and saltiest in the spring except for the last samplings (STS

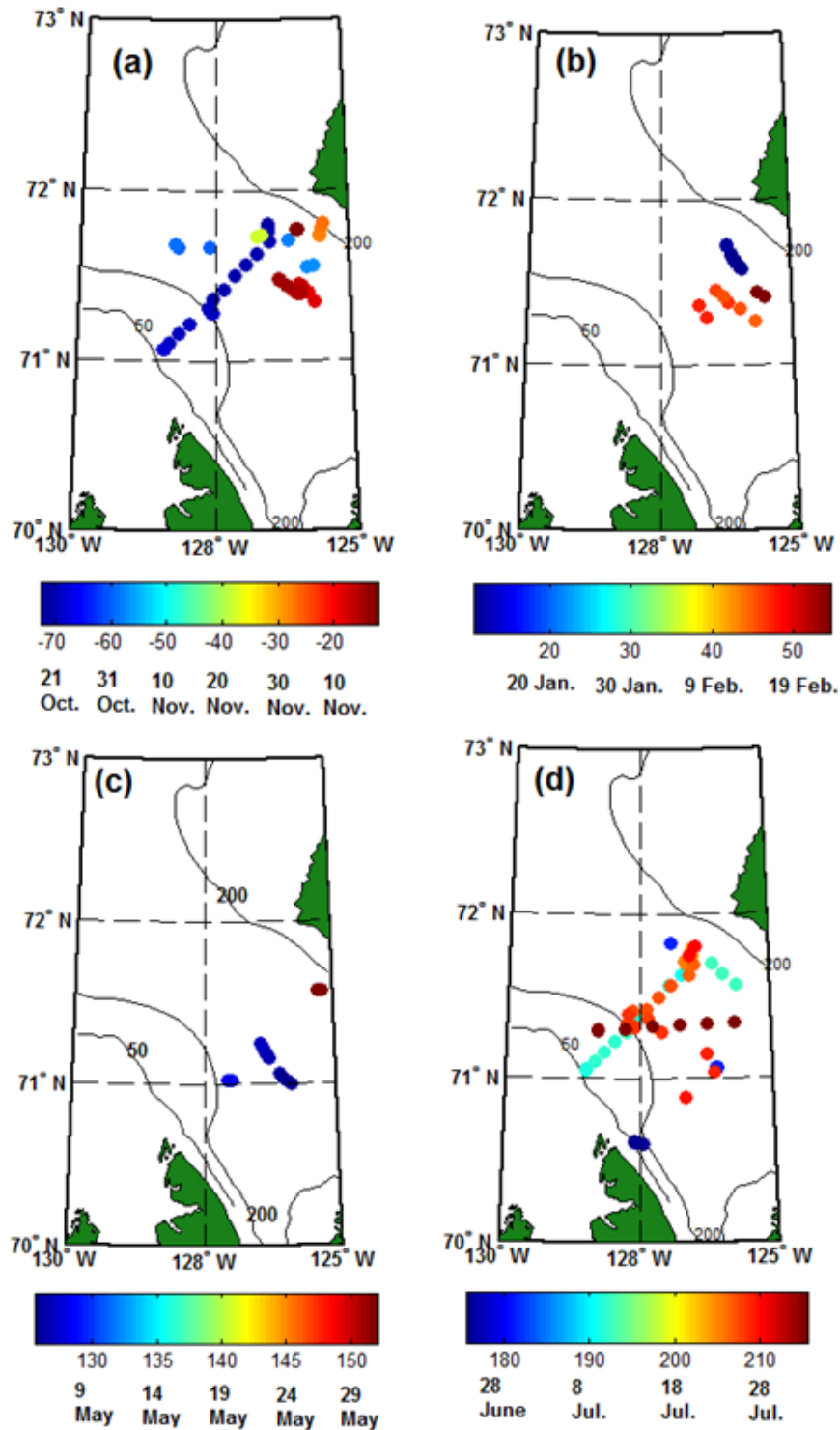


Figure 4.27: (a), (b), (c) and (d) Locations of the sampling stations as functions of time in the Mouth subregion during fall, winter, spring and summer 2007-2008, respectively. The color of the circles identify the sampling dates.

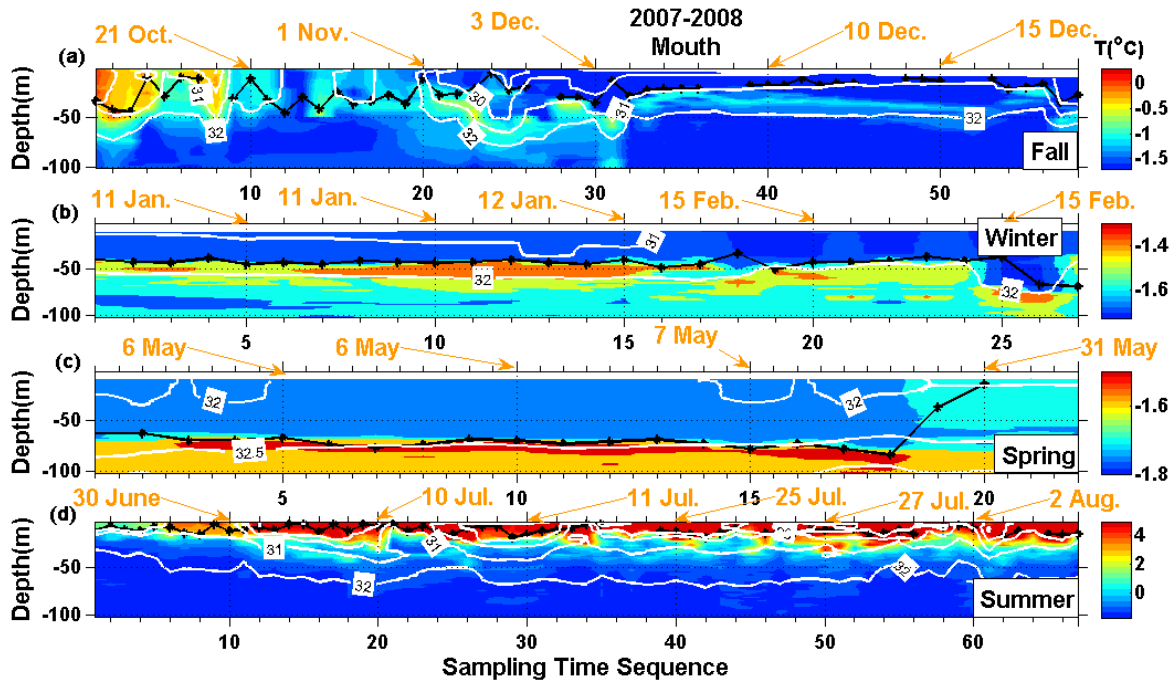


Figure 4.28: Contours of the temperature with salinity isolines (white lines) for the Mouth subregion, during different seasons of 2007-2008. (a) Fall, (b) winter, (c) spring and (d) summer. The black broken lines are the *MLDs*. The Sampling Sequences (STS) axis starts at zero in each panel.

> 176). The increasing salinity and *MLD* and decreasing surface temperature from fall to spring is due the ice formation process. The ice formation causes salt rejection which makes the *MLDs* deeper from the fall to the spring until they reach their maximum values in the spring. The sudden decrease of the salinity and increase of the surface temperature in the last days of sampling in spring 2008 (STS > 176) may be related to the ship displacement and/or the atmospheric warming which starts in the second half of the spring. As the air temperature is gradually becoming warmer, the ice is starting to melt during the summer which makes the surface layer less salty and results in shallower *MLDs*.

It is worth mentioning that eddies may have an important role in *MLD* variations in this region. As an example it seems that around 26 December an anticyclonic eddy drifts in the region which leads decreasing the *MLD* (see Figure 4.26). Another anticyclonic eddy on 26 January Barrette (2012) also makes the *MLD* shallower (see red ellipse between $110 < \text{STS} < 130$ in Figure 4.26b). The red ellipse around 7 February in Figure 4.26b highlights another possible eddy, a cyclonic eddy which makes the *MLD* deeper. Our observations show that an anticyclonic eddy in which the isolines of salinity and temperature get away from each other with a clockwise rotation, leads the *MLD* shallower. While a cyclonic eddy in which the isolines of salinity and temperature

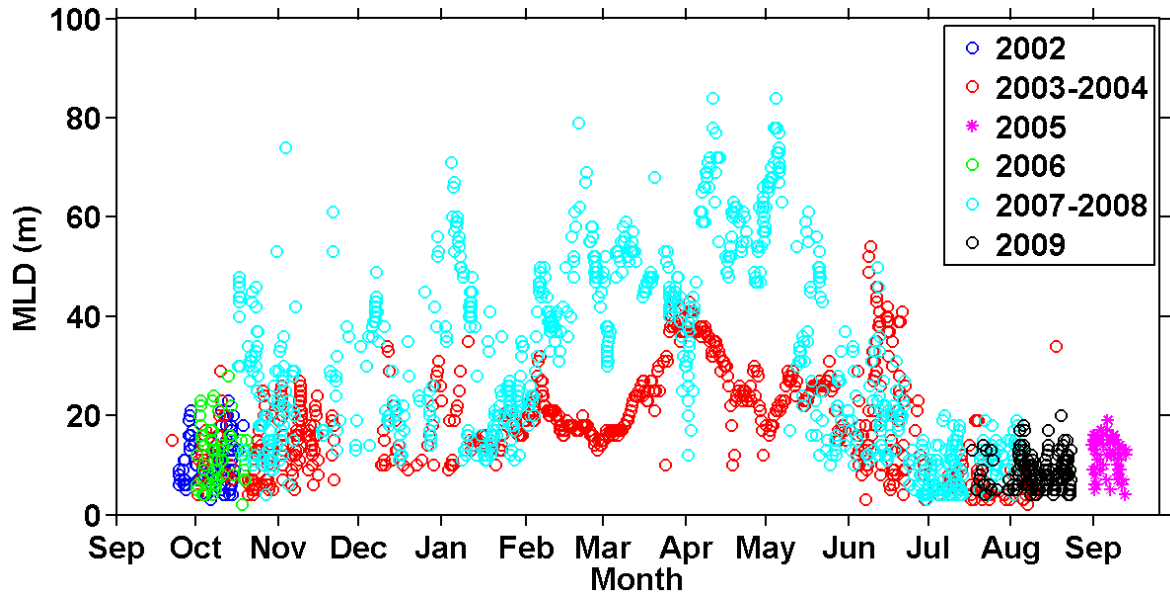


Figure 4.29: *MLDs* during fall 2002, all of 2003-2004 and 2007-2008, summer 2005, fall 2006 and summer 2009.

pinches with a counter-clockwise rotation leads deeper *MLDs*.

As shown in Figure 4.27a, in the Mouth subregion the sampling in the fall started in the Mouth near Banks Island moved towards Cape Bathurst during day -73 to -69 (19-23 October). As shown in Figure 4.28a, b and c, the surface water gradually gets colder from the fall to the spring, the surface salinity increases and the *MLD* deepens. In summer the surface layer is the warmest, least salty and more stratified, which leads the shallowest *MLD* compared with the other seasons (see Figure 4.28d). The *MLD* during winter is almost constant and follows the 31.5 and 32 salinity isolines. However, the 32 salinity isoline deepens at the end of the winter, and subsequently the *MLD* gets deeper too (see Figure 4.28d). In the spring the *MLD* is almost constant and follows the 32.5 salinity isoline, except for the last days of May in which the surface layer gets warmer and more stratified due to the start of ice melting season.

4.4.2 Interannual evolution of the *MLD*

The interannual comparison of the *MLDs* is performed using data from 2002, 2003-2004, 2005, 2006, 2007-2008 and 2009. Two complete years of CTD profiles are available: 2003-2004 (CASES) and 2007-2008 (CFL). The profiles during fall 2002 and 2006, and during summer 2005 and 2009 are also available. The interannual differences are first examined regardless of the sampling location in section 4.4.2.1.

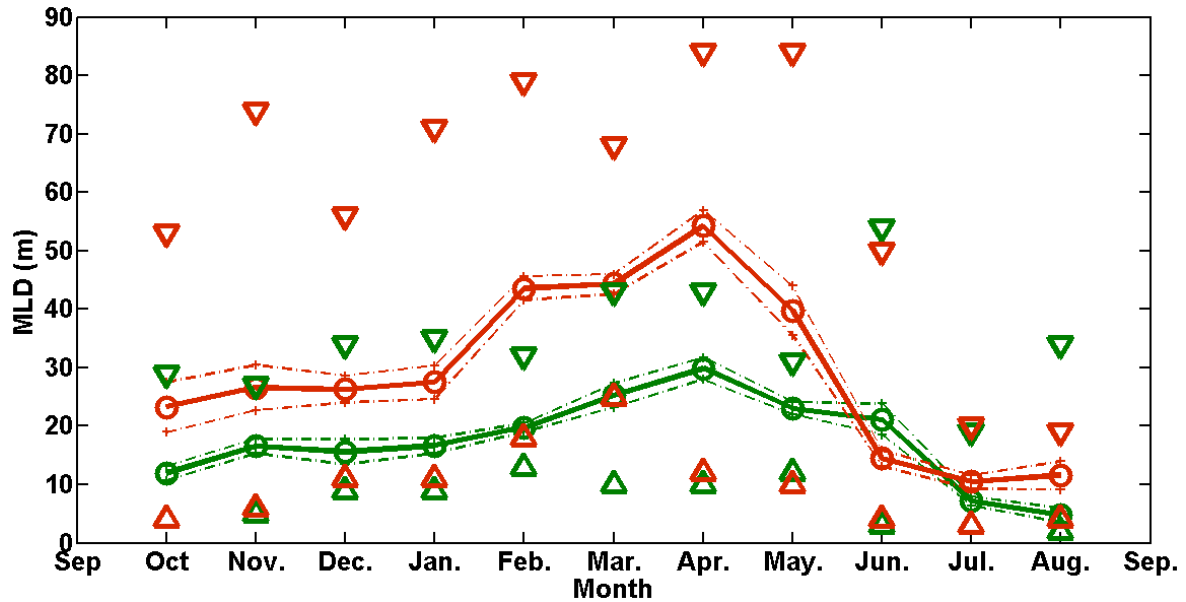


Figure 4.30: Monthly mean values of the MLD during 2003-2004 (green) and 2007-2008 (red). The dashed lines are the 95% confidence interval on the mean value of the MLD . Upward triangles in green and red are the monthly minimum $MLDs$ and downward triangles in green and red are the monthly maximum $MLDs$.

4.4.2.1 Interannual evolution of the MLD regardless of the sampling location

Figure 4.29 shows the MLD monthly variability in the Amundsen Gulf and Beaufort Sea during different years. The values are colour-coded to show the yearly variability. This figure clearly shows, again, that the MLD is generally larger in 2007-2008 especially during winter and spring. In the beginning of the fall and in the summer, the MLD is comparable in all years. This is consistent with our results in the previous section.

In order to analyze the interannual variability of the MLD during two complete years 2003-2004 and 2007-2008, we performed a set of monthly Student t -test comparisons between these two years. Table 4.8 shows that the monthly averages of the two series are significantly different. The small differences in summer means that MLD mean values are very similar during the summer. The mean values are much more different during the other seasons.

The monthly average values of MLD regardless of the region are compared graphically for the two years in Figure 4.30. Minimum and maximum values of MLD in each month are shown with triangles for CASES and CFL data. As is obvious in this figure, MLD deepens in winter and reaches its largest value in spring and the shallowest in

Table 4.8: Student t -tests comparisons between monthly averaged MLD s during 2003-2004 (CASES) and 2007-2008 (CFL). N_1 and N_2 are the number of monthly CTDs during CASES and CFL, respectively. $T-t$ and $C-t$ are the tabulated t and calculated t values. The results of the t -test are either Significant (Sig.) or Non-Significant (No Sig.). Mean CASES and Mean CFL are the 95% confidence intervals on the monthly mean value of the MLD .

Month	Oct.	Nov.	Dec.	Jan.	Feb.	Mar.	Apr.	May	Jun.	Jul.	Aug.
N_1	80	79	34	47	90	65	67	61	98	56	20
N_2	77	40	97	129	100	94	102	95	92	128	17
$T-t$	1.96	1.96	1.96	1.96	1.96	1.96	1.96	1.96	1.96	1.96	2.03
$C-t$	7.94	5.80	4.16	5.03	20.35	15.07	12.55	7.67	2.78	2.30	2.79
Student t -test	Sig.	Sig.	Sig.	Sig.	Sig.	Sig.	Sig.	Sig.	Sig.	Sig.	Sig.
Mean CASES	10.7- 13.2	15.4- 17.8	13.4- 17.7	15.3- 17.9	19- 20.6	23.3- 27.3	28- 31.7	22- 24	18.5- 23.8	6.4- 7.9	3.5- 6
Mean CFL	19- 27.5	22.7- 30.5	24- 28.6	24.6- 30.4	41.5- 45.6	42.6- 46	51.5- 57	35.5- 44	13- 15.9	9.3- 11.6	9.2- 13.9

summer during 2003-2004 (CASES) and 2007-2008 (CFL). The mean value of the MLD is obviously deeper during CFL in comparison with CASES apart from June and July which their difference is very small. The average MLD is 70% larger during CFL than during CASES and reaches 100% in February. In both years the MLD deepens from October up to April and then becomes shallower. The maximum mean value of the MLD in both datasets is observed in April and the minimum is in July and August. The maximum value of the MLD during CFL is significantly larger than during CASES in most of the months except of June, July and August. In June and August the maximum MLD is larger during CASES than during CFL, and in July the maximum MLD s are almost the same in these two years. The minimum values are always similar except in March. As is observed in Figure 4.30, the 95% confidence intervals of the monthly means do not overlap. This means that the monthly mean values of MLD are significantly different during CASES and CFL which is consistent with monthly student t -test's results shown in Table 4.8.

Furthermore, interannual comparisons during the fall is performed between 2002, 2003, 2006 and 2007 and during the summer between 2004, 2005, 2008 and 2009 (when sufficient observations are available). As shown in Figure 4.31, the means in fall 2007 are the largest compared with the other years. The PDFs also show a significant shift in 2007 while the PDFs and the MLD mean values of other years are very similar. Again, this noticeable increase in MLD s is due to the upwelling as was discussed earlier in section 4.3, and as was reported by Tremblay et al. (2011). According to Williams and Carmack (2008) tidal motions and wind in the favorable direction in vicinity of the

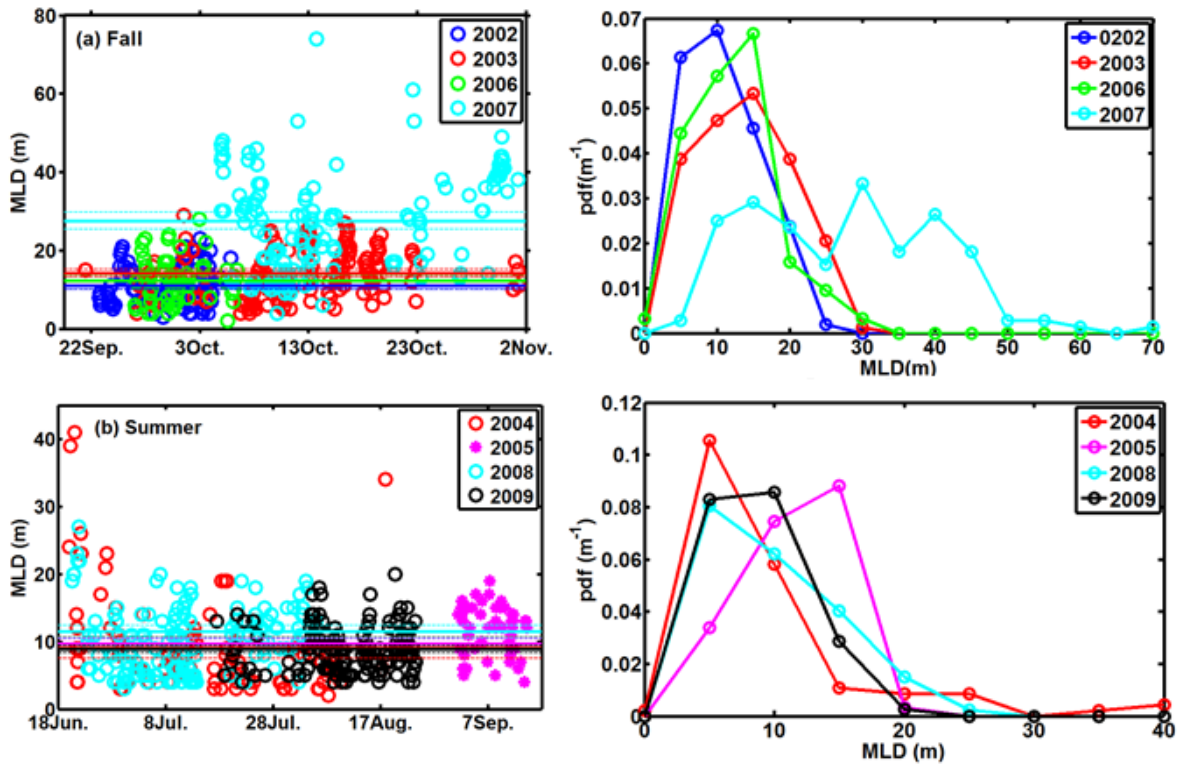


Figure 4.31: Interannual variations of the MLD s in summer and fall. The diagrams on the left-hand side present color coded, MLD seasonal distribution. The mean values for each season (solid lines) with their 95% confidence intervals (dashed lines) are also presented. The panels on the right-hand side present the corresponding PDFs. (a) Fall, (b) Summer.

Cape Bathurst can both lead to upwelling. The influence of the upwelling is generally restricted to a few kilometers from Cape Bathurst as observed on many satellite images (Gratton et al., 2012). Nevertheless, in fall 2007 as it is depicted in Figure 4.4, the upwelling effects can still be observed over 200 km north of Cape Bathurst. The upwelling signature was also observed until the next spring (Tremblay et al., 2011). The strong easterly winds blowing parallel to the coast in fall 2007 are responsible for the upwelling event as well as for delaying ice formation by as much as six weeks.

The comparison between the *MLDs* from summers of 2004, 2005, 2008 and 2009 shows that the mean values during summer 2004, 2008 and 2009 are generally comparable while the mean value of the *MLD* in 2005 is slightly larger than the other years (Figure 4.31). The PDFs in summer also show a slight shift toward larger values in 2005 while in other years the PDFs are very similar. The larger *MLDs* in summer 2005 may be because of the sampling period (i.e. between 2 September and 14 September) which is near fall. Recall that in late summer and early fall, the *MLD* often becomes deeper because of the start of the cooling period and in an increase wind speed and in the number of storms.

4.4.2.2 Interannual *MLD* evolution in the subregions

In the previous section the *MLD* seasonal variability was analyzed regardless of the sampling locations. In the present section the interannual evolution is analyzed by regions (see Figure 4.2), when a sufficient number of observations was available. The interannual comparison is discussed between fall 2002, 2003, 2006 and 2007 in three subregions, i.e. the Amundsen, Beaufort and Mouth regions; between fall 2002-2003 in the Franklin region; between summer 2004, 2005, 2008 and 2009 in the Mouth region; between spring 2004 and 2008 in the Amundsen region; between summer 2004 and 2008 in the Amundsen region and finally between summer 2008 and 2009 in the Beaufort region.

In agreement with the results of the previous section, Figure 4.32a, b and c show that the mean values in fall are significantly larger in 2007 compared to the other years in the Amundsen, Mouth and Beaufort subregions. As an example, Figure 4.33 presents contours of temperature and salinity corresponding to the Amundsen region of Figure 4.32a. Figure 4.33 shows that contours of temperature, salinity and the *MLD* variations are very different in 2007 compared to the other years. Apart from 2007, the *MLDs* are generally comparable from year to year. Figure 4.33 shows that the surface temperature is colder and saltier in fall 2003 in comparison with fall 2002. Moreover, Figure 4.33 shows that the water temperature is warmer in 2006 compared to other

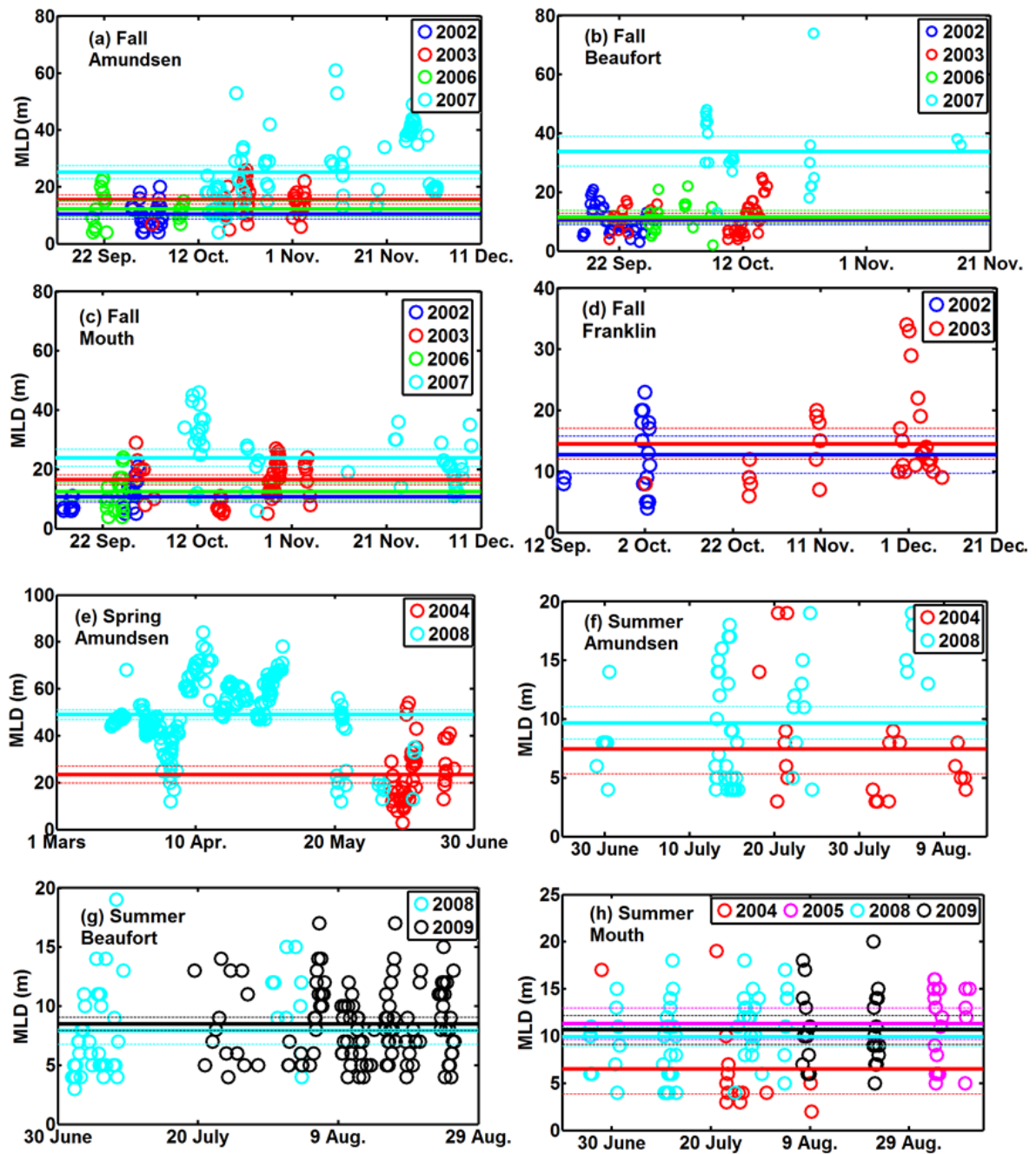


Figure 4.32: Interannual variations of the *MLD* in different subregions. The mean values for each season (solid lines) with their 95% confidence intervals (dashed lines) are also presented.

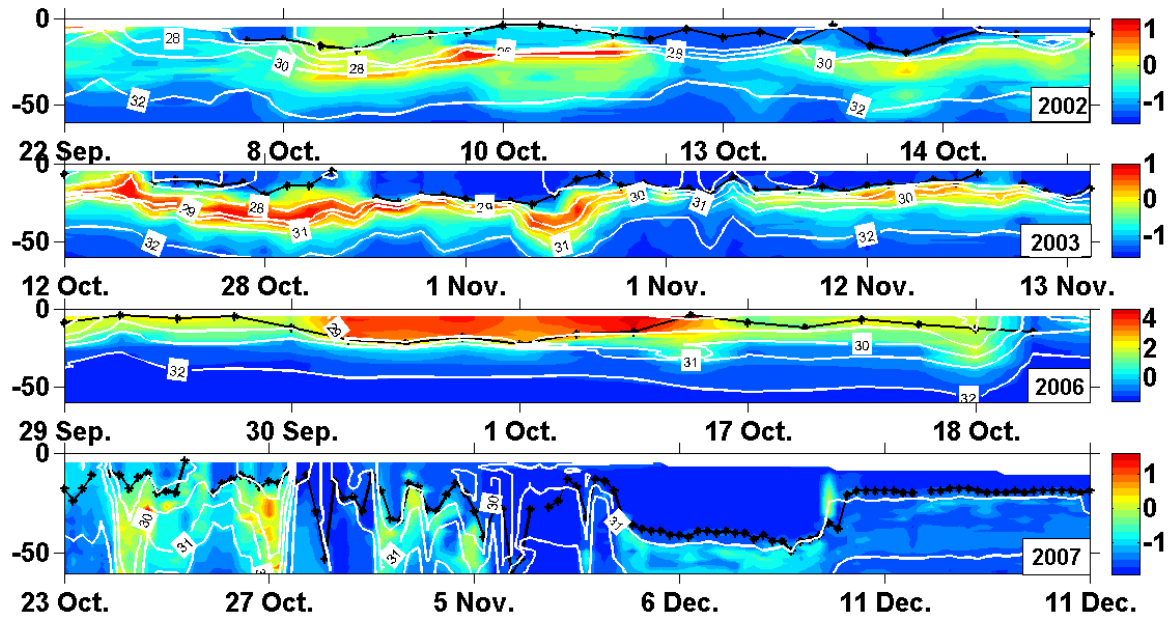


Figure 4.33: Contours of the temperature with salinity isolines (white lines) in the Amundsen subregion during different years. (a) 2002, (b) 2003, (c) 2006 and (d) 2007. The black broken lines are the *MLDs*.

years. It is also shown that the salinity is larger in 2006 than it in 2002 and 2003. It is thus of interest to verify the ice cover and atmospheric variations in the region in order to understand how these observations can be linked. Note that if surface water is warm, it is expected to have little ice and fresher water since the salty water surface in the fall is often due to the ice formation. Hence, the salty surface water observed in this example is in contradiction with an ice free surface. According to the Canadian Ice Service (<http://www.ec.gc.ca/glaces-ice/>), a very high ice concentration (9/10-10/10) was observed until mid-July in summer 2006 and which disappeared in less than one month. This may be due to the export of ice from the region rather than ice melting since the salinity is high and the surface water is not stratified. This is consistent with the results of Wang et al. (2009) who reports that, in 2006, the conditions were favorable for ice export from the Arctic, due to positive phase of both the Arctic Dipole Anomaly (DA) and Arctic Oscillation (AO). Therefore the ice free water is exposed to the direct sunlight which makes the surface water warm.

A comparison of the mean *MLDs* in the Beaufort region (Figure 4.32b) shows that *MLDs* are the deepest in fall 2007 with a mean value of 34 m while the *MLDs* during 2002, 2003 and 2006 are comparable with the mean values of about 11 m. The mean values in the Franklin region during fall 2002 and 2003 are comparable (see Figure 4.32d). It should be noted that lack of data in this region, especially in fall 2002, makes the analysis and conclusions difficult.

During the spring in the Amundsen region, as it is obvious in Figure 4.32e, the ML is deeper in 2008 compared to 2004 due to the upwelling from the previous. The surface water column is saltier in spring 2008 than spring 2004 in the Amundsen subregion because of the upwelling in fall 2007 which brings the saltier deep waters to the surface.

In all the subregions (Figure 4.32e, f and g) the surface water temperature is warmer and the surface water salinity is relatively higher in summer 2008 compared to the other years (results not shown). However, as shown in Figure 4.32e, f, g and h, the mean values of *MLD* during different years in these subregions are comparable. The warmer surface water is because the Arctic ice in summer 2008 melted about three weeks earlier than is usual and the water was thus exposed to the sunlight for a longer period. This phenomenon is possibly due to the small amount of multiyear ice remaining in the region from fall 2007 and winter 2008 after the ice export from the Arctic due to the strong rise in sea-level pressure over the northern Beaufort Sea is associated with a positive phase of the Arctic Dipole Anomaly (DA). A positive DA favors the Trans-polar Drift Stream (TDS) that pumps sea ice out of the Arctic into the Barents and Greenland seas (Wu et al., 2006).

4.5 Summary

In this chapter, the temporal variability and the spatial distribution of the Mixed Layer Depth in the southern Beaufort Sea and the Amundsen were studied. The differences between regions, seasons and years were assessed by (statistically) comparing the monthly mean *MLDs* and by interpreting their probability distribution functions. The study region was divided into four different subregions identified as Amundsen (AM), Mouth (M), Beaufort (BF) and Franklin (F), and each subregion was further divided in two: shallow (depth < 200 m) and deep (depth > 200 m). The objective was to determine the effect of the bathymetry on the *MLD* distribution.

Inshore and offshore The shallow regions were called inshore while the deep regions were called offshore. The statistical analysis showed that, except for the summer, *MLDs* were larger offshore than inshore. During the summer, we found that the inshore and offshore *MLDs* were comparable. A possible reason for shallower *MLDs* inshore in fall, winter and spring could be the stronger stratification near shore because the ice cover remains longer inshore regions. In summer, as ice is melting, the inshore and offshore *MLDs* become more similar.

Subregions The comparison between *MLDs* in the subregions showed that the *MLDs* were generally comparable in each subregion, for the same season. However, large *MLDs* were more often observed in AM and M subregions. Most of the probability distribution functions were of the one “hump” type showing a single, preferred *MLD* depth range for each region.

Transect The water temperature and salinity as well as the *MLD* variations, were compared along four different transects: Tr1 (from Cape Parry to Banks Island), Tr2 (from Cape Bathurst to Banks Island), Tr3 (offshore from the Mackenzie River) and TrAM (from eastern to western of the Amundsen Gulf). For instance, *MLD* variations and physical properties were compared in fall 2003 between the four sections. The results demonstrated that along all transects, the water was more stratified with shallower *MLDs* near the coasts, compared to offshore. A relatively warm layer (the Near Surface Temperature Minimum) was observed on Tr1, Tr2 and TrAM but not along transect Tr3 in the Beaufort Sea. This was also observed by Lanos (2009).

Seasonal The analyses showed that mean *MLDs* vary significantly from one season to another in all the subregions. The mixed layer becomes gradually deeper and deeper from late summer to its maximum depth in spring. The results also show that the range of variation of the *MLD* is the largest in the spring.

Interannual Finally, my studies established that the mean monthly *MLDs* during 2003-2004 and 2007-2008 were significantly different in fall, winter and spring, while they were comparable in summer. The monthly comparison showed that all *MLDs* were significantly deeper during 2007-2008 than during 2003-2004, with the exception of June and July where they were similar. The deepest mean *MLDs* of those two years were observed in April. The analysis for the falls of 2002, 2003, 2006 and 2007, regardless of the subregions, revealed that the mean *MLDs* were significantly larger in the fall of 2007 than in the other years. The interannual comparison between *MLDs* in summer 2004, 2005, 2008 and 2009 showed that the *MLDs* were comparable regardless of the subregions. The deep *MLDs* from fall 2007 to spring 2008 are related to a strong upwelling event that occurred in fall 2007. Its effects remained observable until the next spring. The sampling during CFL was performed from drifting ice floes and in the lead area where the ice is forming continuously, leading to frequent convection and larger *MLDs*. The differences in landfast ice versus mobile ice, and locations may also contribute to some of the interannual differences.

Processes impacting the *MLD* As was mentioned in the previous paragraph, coastal upwelling is the process that influenced the most the *MLD* in our study region between 2002 and 2009. Ice-edge upwelling was also shown to have modified the mixed layer on at least two occasions: in December 2003 and in June 2008 (as discussed in [Mundy et al. \(2009\)](#)). It was also found that smaller scale processes, namely frontal regions, can produce smaller or larger local ML ([Sévigny, 2013](#)). Finally, drifting eddies ([Barrette, 2012](#)) will carry their own smaller (in cyclonic eddies) or larger (in anticyclonic eddies) mixed layers with them.

CHAPTER 5

UNDER ICE OCEANIC FLUXES AND THEIR IMPACTS ON THE MIXED LAYER DEPTH

5.1 Introduction

The Arctic mixed layer is affected by dynamical and thermodynamical processes between the atmosphere, sea ice and surface water as well as the vertical motions under the surface layer. In this chapter the relationship between the under ice oceanic fluxes and the variations of the *MLD* are examined in our region of study. A method developed by [Prieur et al. \(2010\)](#) (hereafter referred to as LP) is employed to calculate the oceanic fluxes (i.e. mass and buoyancy) using the mass balance in the mixed layer. [Emery \(1976\)](#) examined the relationship between the heat content of the surface layer in mid-latitudes and the vertical motion deduced from temperature fluctuations under this surface layer. He developed a so-called “divergent heat budget equation” (equation 8 in [Emery 1976](#)). [Gaspar et al. \(1990\)](#) and [Caniaux and Planton \(1998\)](#) used the heat balance equation to predict the variation of the mixed layer temperature, with a variable thickness, under the influence of net surface heat flux. Finally, [Stevenson and Niiler \(1983\)](#) studied the heat balance in the upper layers of the Pacific with depth of a chosen isotherm in the thermocline. [Prieur et al. \(2010\)](#) developed a approach similar to [Emery \(1976\)](#) for the Mediterranean Sea to calculated the oceanic mass flux in a layer between the surface and a chosen reference depth ($-hc$). The difference between LP method and Emery’s is that the density is used instead of the temperature. In other words, the LP method is used for a layer between the surface and a chosen reference depth ($-hc$) to estimate the ice-ocean fluxes and the ice growth velocity. Our approach is mainly based on the mass content (density) of the surface layer because salt controls the ocean density in the Arctic. The same approach is also used for heat and salinity such that the flux of salt and heat is calculated based on LP method. The advantage of this simple method is that it can be used to characterize the evolution of the mixed layer using both drifting and fixed profiler data under the ice. Since in

the LP method the horizontal non-divergent advection is neglected, the data used to calculate the ocean fluxes are from fixed stations or quasi-fixed stations. In summary the objective of this chapter is: 1) to study the temporal variations of the oceanic fluxes in a predefined surface layer (between the surface and a chosen reference depth ($-hc$)); 2) to investigate how the *MLD* assimilates mass, salinity, heat fluxes; 3) to estimate the impact of the vertical advection at the bottom of the surface layer on the *MLD*; 4) to compare the atmospheric and under ice oceanic fluxes; 5) to calculate the evolution of the ice thickness with profiling data only.

5.2 Methodology

5.2.1 Oceanic and atmospheric flux estimations

The ocean mass (density), salt and heat contents are calculated in a vertical column between the surface and a depth $z = -hc$ ($hc > 0$, vertical z axis directed upwards). The main goal for calculating these oceanic fluxes is to investigate their temporal variations in a surface layer with a fixed thickness (hc m) and their relationship with different parameters such as *MLD*, atmospheric flux and biological parameter. The depth hc is chosen based on two following conditions: (1) hc must always be deeper than the maximum value of the *MLD*(t) during the sampling period at the station (see Figure 5.1). (2) The maximum value of the density in the mixed layer $\rho(MLD(t))$ must always be smaller than the initial density at $z = -hc$ (i.e. $\rho = \rho_{-hc}^{t=1}$). The oceanic contents are computed using the following equation:

$$C_V = \int_{-hc}^0 V dz = hc \langle V \rangle \quad (5.1)$$

where hc is the thickness of the surface layer and V is a relevant variable such as density, salinity, or temperature. $\langle \rangle$ represents the average value of the considered variable i.e. its vertical integral between $z = -hc$ and surface ($z = 0$) divided by hc . For example, the average density can be obtained from:

$$\langle \rho \rangle = \frac{1}{hc} \int_{-hc}^0 \rho dz \quad (5.2)$$

The ocean content (i.e. heat, freshwater, mass) variation in the surface layer is not equal to the surface exchanges meaning that there are other sources aside from the surface sources that affect the ocean fluxes (Emery, 1976).

5.2.1.1 Mass fluxes

In this section, I use the same approach as [Emery \(1976\)](#), but the density is used instead of the temperature. Assuming a control volume with horizontal surface A and depth hc fixed in time, the bottom of the control volume is always located in the pycnocline. The direction of the z axis is upward thus z values are negative ($-hc \leq z \leq 0$), $\rho(x, y, z)$ is the potential density and (u, v, w) is the three dimensional velocity of the flow through this volume. Neglecting molecular diffusion, radiative heat flux in the volume and turbulent exchange, we can write the mass balance in the volume as follows ([Emery, 1976](#)):

$$-\frac{\partial}{\partial t} \iiint_{-hc}^0 \rho dz da = \oint_A \rho \vec{V} \cdot \vec{n} da - J_m A \quad (5.3)$$

Here, da is the element of surface A which is the surface area of water, \vec{n} is the normal unit to the surface directed outward and J_m is the mass flux entering the ocean from the atmosphere. The term on the left hand side of equation 5.3 represents the variation in the mass of the volume with time and the term is negative because the direction of \vec{n} is outward. Therefore, if the first term on the right side of the equation, representing the outgoing mass flow from the volume, is negative ($J_m < 0$) the mass content of the volume decreases (term on left hand side). Similarly, if J_m is positive the mass of the volume increases, therefore a minus sign is placed in front to maintain the same sign as the change in mass. The mass flux (J_m) is related to the buoyancy flux (J_b) as shown by equation 5.4 and is affected by the net heat flux Q_{net} and mass loss by evaporation as shown in equation 5.5.

$$J_m = -(\rho_s/g) J_b \quad (5.4)$$

$$J_b = \frac{g}{\rho_s c_p} \alpha Q_{net} + \beta \frac{g}{\rho_s L_v} S Q_{evap} = \underbrace{\frac{g \alpha Q}{c_p \rho_s}}_{J_{bT}} + \underbrace{g \beta (E - P_r) S}_{J_{bS}} \quad (5.5)$$

The buoyancy flux (J_b) can be calculated using equation 5.5 where c_p represents the specific heat of water ($\text{J kg}^{-1} \text{ }^\circ\text{C}^{-1}$), S is the surface salinity, ρ_0 denotes the reference density, $\alpha = -\rho^{-1} \partial \rho / \partial T$ (> 0) is the thermal expansion coefficient of water at the sea surface ($^\circ\text{C}^{-1}$), $\beta = \rho^{-1} \partial \rho / \partial S$ (> 0) is the salinity contraction coefficient. α represents the ocean water tendency to change in volume at constant pressure in response to a change in temperature. β shows the contraction of a volume of water at constant pressure in response to an increase in salinity. In equation 5.5, Q_{net} (net heat flux) is

positive if the surface layer of the ocean is heating and the buoyancy of the ocean per unit of time increases ($J_b > 0$). Q_{evap} is Q_{latent} in our study which is the heat gained or lost due to the freezing and melting of the ice.

The second equation of 5.5 (bottom) is the equation of Gill (1982) for the rate of evaporation/freezing and precipitation. $E < 0$ and $Pr > 0$ are respectively the evaporation rate and precipitation rate (m s^{-1}). In other words, $E - P$ is the rate of decrease/increase of water thickness due to the freezing/melting of ice. For ice formation, $E = -\delta h/dt$, $Pr = 0$ and in the case of ice melting $E = 0$, $Pr = \delta h/dt$ where $\delta h/dt$ is the rate of increase in ice thickness. The relation between equation 5.5 and MLD variations is that during heating (cooling) periods the buoyancy flux increases (decreases). When it is cold and the ice is freezing, convection occurs due to salt rejection thus the MLD deepens in the freezing season as a result of increasing mixing. In contrast the convection ceases during heating periods, when the buoyancy flux is positive which leads to increasing stratification and decreasing MLD . However, it should be noted that the MLD does not only depend on heating and cooling. When there is no ice, the estimated buoyancy flux is almost equal to the atmospheric flux.

Equation 5.3 is transformed to the following equation using the theorem of Gauss.

$$-\frac{\partial}{\partial t} \iiint_{-hc}^0 \rho dz da = \iiint_{-hc}^0 \nabla \bullet (\rho \vec{V}) da dz - J_m A \quad (5.6)$$

If we assume that horizontal changes of ρ and J_m are small or if A is sufficiently small then we obtain:

$$-\frac{\partial}{\partial t} \int_{-hc}^0 \rho dz = \int_{-hc}^0 \nabla \bullet (\rho \vec{V}) dz - J_m \quad (5.7)$$

Using the definition of C_ρ in equation 5.8, equation 5.9 is obtained by substituting C_ρ in equation 5.7. C_ρ represents the mass content (kg m^{-2}) in a layer of water between the surface and depth $-hc$. C_ρ can be calculated for any density profile $\rho(z)$ between the surface and the reference depth ($-hc$).

$$C_\rho = hc \langle \rho \rangle = \int_{-hc}^0 \rho dz \quad (5.8)$$

Equations 5.7 and 5.8 lead to:

$$-\frac{\partial C_\rho}{\partial t} = \int_{-hc}^0 \nabla \bullet (\rho \vec{V}) dz - J_m \quad (5.9)$$

By splitting the divergence term into horizontal and vertical terms:

$$\vec{V}(x, y, z) = \vec{V}_H(x, y, z) + w(x, y, z) \vec{k} \quad (5.10)$$

$$\nabla \bullet (\rho \vec{V}) = \nabla_H \bullet (\rho \vec{V}_H) + \frac{\partial(\rho w)}{\partial z} \quad (5.11)$$

Equation 5.9 becomes:

$$-\frac{\partial C_\rho}{\partial t} = \int_{-hc}^0 \nabla_H \bullet (\rho \vec{V}_H) dz + \int_{-hc}^0 \frac{\partial(w\rho)}{\partial z} dz - J_m \quad (5.12)$$

The second term on the right hand side of equation 5.12 can be calculated by assuming that $w = 0$ at $z = 0$ and $w = w_{-hc}$ at $z = -hc$.

$$\int_{-hc}^0 \frac{\partial(w\rho)}{\partial z} dz = w_{-hc} \rho_{-hc} \quad (5.13)$$

By splitting total quantities into averaged and fluctuating parts as: $\rho = \langle \rho \rangle + \rho'$ with $\langle \rho' \rangle = 0$, the integrand of the first term on the right hand of equation 5.12 can be develop as follows:

$$\begin{aligned} \nabla_H \bullet (\rho \vec{V}_H) &= \nabla_H \bullet (\langle \rho \rangle + \rho') \vec{V}_H \\ &= \underbrace{\langle \rho \rangle \nabla_H \bullet \vec{V}_H}_I + \underbrace{\vec{V}_H \bullet \nabla_H \langle \rho \rangle}_{II} + \underbrace{\nabla_H \bullet (\rho' \vec{V}_H)}_{III} \end{aligned} \quad (5.14)$$

Each term in equation 5.14 can be analyzed separately. In term *I*, the horizontal divergence of \vec{V}_H : $\nabla_H \bullet \vec{V}_H = \left[\frac{\partial u}{\partial x} + \frac{\partial v}{\partial y} \right]$ equals $-\frac{\partial w}{\partial z}$ (equation 5.24), because the ocean water is incompressible (Boussinesq assumption). Thus, by integrating term *I* between the surface and $-hc$, 5.15 is obtained since $\langle \rho \rangle$ does not depend on the integration variable.

$$\int_{-hc}^0 \langle \rho \rangle \nabla_H \bullet \vec{V}_H dz = \langle \rho \rangle w_{-hc} \quad (5.15)$$

Term *II* in equation 5.14 can be calculated by dividing \vec{V}_H into a sum of an average value and a fluctuating parts ($\langle \vec{V}_H \rangle, \vec{V}_H'$) in the same manner as ρ .

$$\int_{-hc}^0 \vec{V}_H \bullet \nabla_H \langle \rho \rangle dz = \int_{-hc}^0 \langle \vec{V}_H \rangle \bullet \nabla_H \langle \rho \rangle dz + \int_{-hc}^0 \vec{V}_H' \bullet \nabla_H \langle \rho \rangle dz \quad (5.16)$$

Using the facts that the horizontal gradient of $\langle \rho \rangle$ and $\langle \vec{V}_H \rangle$ in the water column is independent of z , that hc is constant and that the integral of the deviation of the velocity (\vec{V}_H') is null, taking into account the definition of $\langle \rho \rangle$ and C_ρ , the average part of the velocity becomes:

$$\int_{-hc}^0 \langle \vec{V}_H \rangle \bullet \nabla_H \langle \rho \rangle dz = \langle \vec{V}_H \rangle \bullet \nabla_H C_\rho \quad (5.17)$$

Term *III* in equation 5.14 is considered to be a residual term which was neglected by Emery (1976). This is justified when it is applied to the mixed layer because the density fluctuation can be negligible in this layer. However, this term should be considered when a layer is thicker than the mixed layer. In this case ρ' remains small compared with ρ , but its horizontal gradient is not necessarily small. Therefore, the term *RES* can be interpreted as a small scale divergence if the fluctuations of the density (ρ') are correlated with the fluctuations of the velocity (\vec{V}_H') inside the surface layer. Finally substituting equations 5.13, 5.15 and 5.17 in equation 5.12 the following equation is obtained:

$$-\frac{\partial C_\rho}{\partial t} = -w_{-hc} \rho_{-hc} + \langle \rho \rangle w_{-hc} + \langle \vec{V}_H \rangle \bullet \nabla_H C_\rho - J_m + \underbrace{RES}_{\int_{-hc}^0 \nabla_H \bullet (\rho' \vec{V}_H) dz} \quad (5.18)$$

Assuming $RES \cong 0$ an equation similar to equation 8 in Emery (1976) but using density instead of temperature is obtained:

$$\underbrace{\frac{\partial C_\rho}{\partial t}}_I + \underbrace{w_{-hc}(\langle \rho \rangle - \rho_{-hc})}_{II} + \underbrace{\langle \vec{V}_H \rangle \bullet \nabla_H C_\rho}_{III} = J_m \quad (5.19)$$

This equation is also equivalent with equation 17 for temperature in Caniaux and Planton (1998), if the reference depth is constant in time and space. It is assumed that all the mass flux imposed at the surface is absorbed in the surface layer, neglecting the turbulent terms. It should be noted that the difference between the sign of the divergence term in equation 5.19 and Emery's equation (8) is due to the z axis orientation. The z axis was orientated positive-downward in Emery (1976) while we consider it orientated positive-upward as in Caniaux and Planton (1998). The physical significance of the terms in equation 5.19 deserves an explanation. Term *I* represents the temporal variation of the mass content. Term *II* shows the influence of the vertical advection at the base of the surface layer (divergent term) and term *III* represents the effect of non-divergent horizontal advection. The term on the right hand side represents the mass flux imposed by the atmosphere at the surface. Neglecting the horizontal advection (term *III* 5.19) and replacing J_m with J_b using equation 5.4 in equation 5.19 the following equation is obtained.

$$\frac{\partial C_\rho}{\partial t} = -J_b(\rho_s/g) + w_{-hc}(\rho_{-hc} - \langle \rho \rangle) \quad (5.20)$$

We define C_{pres} as the residual mass content (kg m^{-2}) by using the following equation:

$$C_{pres} = hc \times \rho_{-hc} - C_\rho = hc(\rho_{-hc} - \langle \rho \rangle) \quad (5.21)$$

and substituting equation 5.21 in the equation 5.20 we get the following equation.

$$dC_{pres}/dt = \underbrace{+J_b(\rho_s/g)}_I + \underbrace{w_{-hc}(\rho_{-hc} - \langle \rho \rangle)}_{II} + \underbrace{hc \times d\rho_{-hc}/dt}_{III} \quad (5.22)$$

It should be noted that equation 5.22 is equivalent to 5.20. The vertical velocity in the previous equations (w_{-hc}) comes from the conservation of mass law (equation 5.23) and Boussinesq assumption as shown in the following equations. The conservation of mass requires:

$$\frac{\partial \rho}{\partial t} + \frac{\partial(\rho u)}{\partial x} + \frac{\partial(\rho v)}{\partial y} + \frac{\partial(\rho w)}{\partial z} = 0 \quad (5.23)$$

Since the ocean water is incompressible (Boussinesq assumption), then:

$$\frac{\partial u}{\partial x} + \frac{\partial v}{\partial y} + \frac{\partial w}{\partial z} = 0 \quad (5.24)$$

Replacing equation 5.24 in equation 5.23 we obtain:

$$\frac{\partial \rho}{\partial t} + u \frac{\partial \rho}{\partial x} + v \frac{\partial \rho}{\partial y} + w \frac{\partial \rho}{\partial z} = 0 \quad (5.25)$$

Thus:

$$\frac{D\rho}{Dt} = \frac{\partial \rho}{\partial t} + u \frac{\partial \rho}{\partial x} + v \frac{\partial \rho}{\partial y} + w \frac{\partial \rho}{\partial z} = 0 \quad (5.26)$$

This equation expresses the fact that the temporal variation of ρ at the fixed station must be compensated for by an advection. Since it is assumed that the horizontal advection of density is negligible, we are left with equation 5.27. By putting equation 5.27 in equation 5.26, the vertical velocity at the reference depth is obtained as shown in equation 5.28.

$$u \frac{\partial \rho}{\partial x} + v \frac{\partial \rho}{\partial y} = 0 \quad (5.27)$$

$$w_{-hc} = - \left(\frac{\partial \rho}{\partial t} \right)_{-hc} / \left(\frac{\partial \rho}{\partial z} \right)_{-hc} \quad (5.28)$$

Returning to equation 5.22, the vertical advection at the bottom of the water column (term II) decreases or increases the mass content of the water column according to the sign of the term $\left(\frac{d\rho_{-hc}}{dt} \right)$ in equation 5.28. If in equation 5.20 $J_b = 0$, the mass content (C_ρ) increases or decreases according to the sign of the temporal variation of the density at the bottom of the column (note that $(\rho_{-hc} - \langle \rho \rangle) > 0$). Thus, the density at the bottom of the water column increases (decreases) if w_{-hc} is positive (negative).

As shown in equation 5.22, C_{pres} represents residual mass content which corresponds to the deficit mass of the mass content in the surface layer (see Figure 5.1). In this

figure C_{pres} is the mass loss affected by the cumulative buoyancy flux imposed by the atmosphere between the time t_1 and t_2 while the advection and diffusion are neglected (Figure 5.1b). Terms *II* and *III* in equation 5.22 are not shown in this figure and only the effect of the atmospheric forcing on the variation of C_{pres} is shown. Note that C_{pres} represents mass loss affected by vertical advection under the surface layer and also the imposed surface buoyancy flux which leads to stratification or mixing. Also shown in the figure, the positive cumulative value of the buoyancy flux (J_b) leads to a decrease in the *MLD* and an increase in C_{pres} .

To avoid an infinite velocity in equation 5.28, the average value of $\frac{\partial \rho}{\partial z}$ between two layers shallower than hc and two layers deeper than hc is used. It should be noted that the calculation of the vertical velocity (w_{-hc}) was carried out for different numbers of layers such as four layers, six layers, eight layers and ten layers. Since the results were not significantly different, two layers were chosen to calculate the vertical velocity (two layers below hc and two layers above hc).

Lets consider some special cases of equations 5.19:

1. $w_{-hc} = 0; \langle \vec{V}_H \rangle = 0$

There is neither divergent flow in the surface layer nor horizontal advection of mass. The water column is only affected by the mass flux imposed from the atmosphere which means the temporal variation of the mass content $\frac{\partial C_\rho}{\partial t}$ increases (decreases) if J_m is positive (negative).

2. $w_{-hc} = 0; \langle \vec{V}_H \rangle \neq 0$

The flow is not divergent but the horizontal advection is not zero meaning some amount of water passes horizontally somewhere through the control column. The temporal variation of the mass content $\frac{\partial C_\rho}{\partial t}$ is affected by the surface mass flux without the horizontal advection considering its sign (see equation 5.19). It should be noted that in this case contrary to the Eulerian mass content (mooring), the Lagrangian mass content (drifters) is only affected by the surface fluxes.

3. $J_m = 0; \text{horizontal advection low}$

Only the first two terms in equation 5.19 remain if $w_{-hc} \neq 0$. The value in parentheses in equation 5.19 ($\langle \rho \rangle - \rho_{-hc}$) is always negative in a hydrostatically stable water column. If the vertical velocity at the base of the column is upwards ($w_{-hc} > 0$), the dense portion of the water column becomes thicker due to the vertical advection and replaces a less dense portion of the column (as in the case of Ekman suction) which leads to divergent horizontal advection and an increase in the mass content (C_ρ).

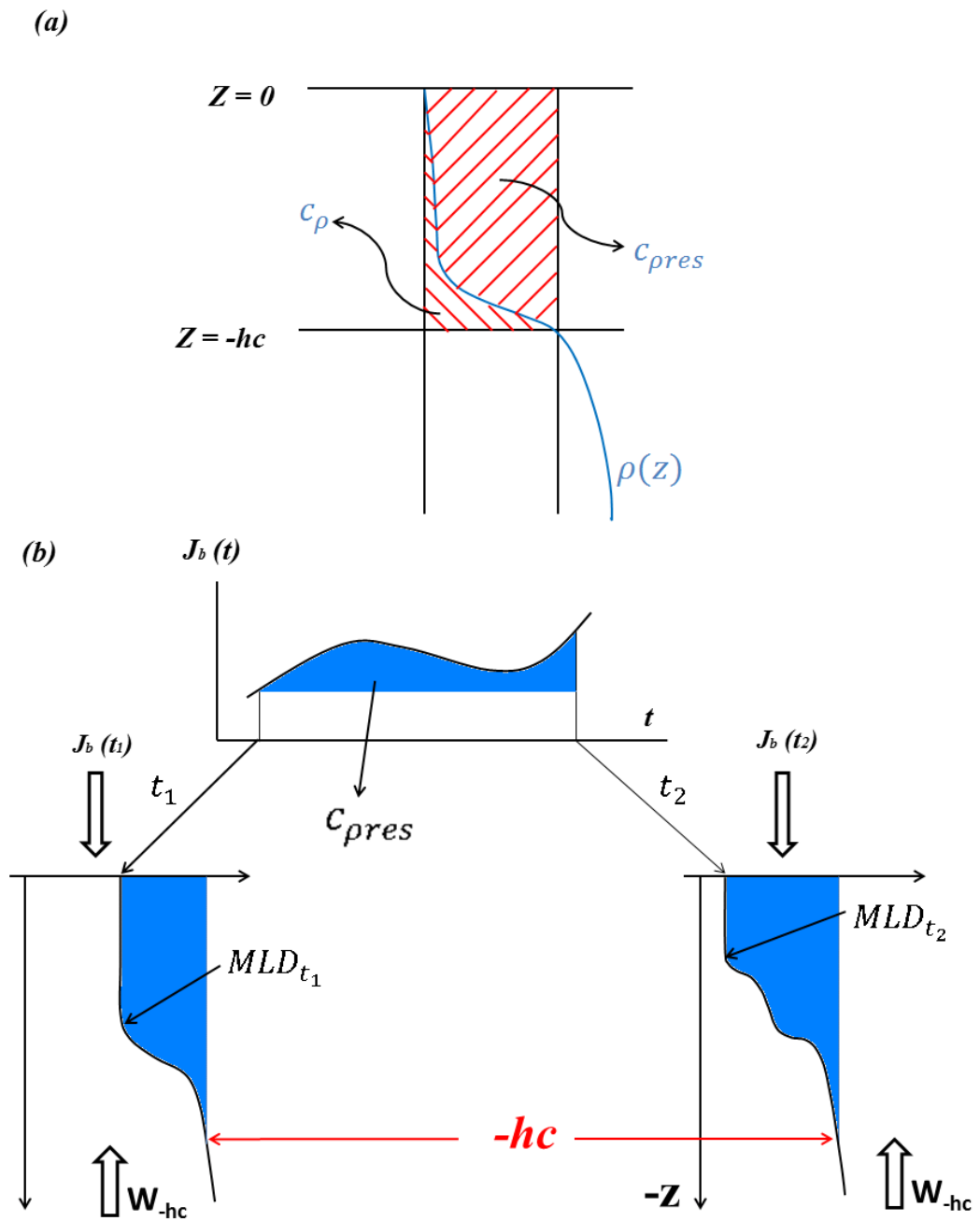


Figure 5.1: Visual presentation of the method showing how the reference depth ($-hc$) is chosen. C_{pres} is the residual mass content in a density profile; $J_b(t_1)$ and $J_b(t_2)$ are the temporal variation of the buoyancy in the time interval between t_1 and t_2 . At the bottom, the density profiles at time t_1 , $(\rho(z, t_1))$ and t_2 , $(\rho(z, t_2))$ are shown. Modified after [Prieur et al. \(2010\)](#).

It should be noted that unfavorable cases such as Ekman pumping or suction exist in many instances due to strong winds. But working on a fixed station or drifting profilers, horizontal advection effects can be reduced to some extent. In the absence of ice, the buoyancy flux (J_b) in equation 5.22, is an indicator of the atmospheric flux which is calculated from measured atmospheric data using the surface heat net flux (Q_{net}) and latent heat (Q_{evap}) in equation 5.5. When the sea surface is ice covered, J_b becomes an estimation of the atmospheric flux under the ice. Equations 5.20 or 5.22 show that if any pumping ($w > 0$) or suction ($w < 0$) occurs, the mass content (C_ρ) or residual mass content ($C_{\rho res}$) are directly affected by these processes.

In summary, the mass content variations in a water column between the surface and reference depth (hc) are affected by the imposed surface effects (buoyancy or mass flux (J_b, J_m)) and the vertical exchanges at the bottom of the surface layer.

The accumulation of buoyancy fluxes at the surface under the ice ($CumJ_b$) between the beginning of the study period ($t1$) and a subsequent time ($t2$), is related to the influence of the atmospheric flux through the ice. The following equations show how to calculate the cumulative value of the different parameters.

$$J_b \cdot \Delta t_i = (g/\rho_s) [\Delta C_{\rho res_i} - w_{-hc}(\rho_{-hc} - \langle \rho \rangle) \Delta t_i - hc \times \Delta \rho_{-hc_i}] \quad (5.29)$$

$$\begin{aligned} CumJ_b &= \sum_{i=1}^N J_b \cdot \Delta t_i \\ &= (g/\rho_s) \left[C_{\rho res}(t) - C_{\rho res}(0) \right. \\ &\quad \left. - \sum_{i=1}^N w_{-hc}(\rho_{-hc} - \langle \rho \rangle) \Delta t_i - hc \rho_{-hc}(t) + hc \rho_{-hc}(0) \right] \end{aligned} \quad (5.30)$$

5.2.1.2 Salt fluxes

In the Arctic, salinity is the most important physical property which controls the density as explained in section 3.2. Several processes control the evolution of the salinity such as evaporation, precipitation, river runoff, ice melting or freezing and mixing of water masses. Salinity variations in the Arctic are more affected by melting or freezing of the ice, river runoff and water circulations. The influence of salinity on the evolution of the *MLD* in the Arctic region is significant (Rao and Sivakumar, 2003).

The salt fluxes in the surface layer are calculated between the surface and a reference depth in the same manner as described in the previous section for density. It should be

noted that the salinity equations are similar to those of the potential density presented in the last section: Ice melting or freezing are taken into account by the salt content (C_s) and salt loss (C_{sres}).

$$C_s = hc \langle S \rangle = \int_{-hc}^0 S dz \quad (5.31)$$

$$C_{sres} = hcS_{-hc} - C_s = hc(S_{-hc} - \langle S \rangle) \quad (5.32)$$

$$dC_s/dt = hc.d \langle S \rangle /dt = +J_s - w_s(S_{-hc} - \langle S \rangle) \quad (5.33)$$

$$dC_{sres}/dt = - \overbrace{J_s}^{(1)} + \underbrace{w_s}_{=w_\rho} (S_{-hc} - \langle S \rangle) + \overbrace{hc \times dS_{-hc}/dt}^{(3)} \quad (5.34)$$

$$FWC = -J_s/S_{ref} \quad (5.35)$$

where C_s , C_{sres} , J_s , FWC , S_{ref} and S_{-hc} are respectively salt content, deficit salt content (salt loss), salt flux imposed by the atmosphere, freshwater content, reference salt which is to be taken as the maximum value of the salinity during the period and salinity at the reference depth ($-hc$). It should be noted that w_s is replaced by w_ρ as explained in section 5.3.1.

5.2.1.3 Heat fluxes

Stevenson and Niiler (1983) studied the upper surface heat content from Hawaii to Tahiti in the central Pacific Ocean in order to understand the seasonal variations in the SST. Moisan and Niiler (1998) calculated the temporal variations of the heat content integrated between the surface and a reference isotherm. As mentioned before, the variation of heat content in the surface water column is not only affected by the ocean's surface fluxes but also by the changes in heat content due to the horizontal and vertical advection (Emery, 1976). Emery (1976) calculated heat content in a layer between the surface and 250 m (H_{250}) and showed that the vertical motions due to vertical advection and horizontal convergence or divergence play important roles in the surface layer's heat content.

The equations of heat are similar to those of the potential density and salinity as presented in previous sections. Upper ocean heat fluxes calculated between the surface and reference depth (hc) are defined in equations 5.36 and 5.37. In which C_θ , $C_{\theta_{res}}$ and Q are respectively temperature content, deficit temperature (temperature loss) and under ice surface heat flux imposed by the atmosphere. Upper ocean heat storage (H_{strg}) is obtained by calculating the mean temperature between the surface and hc (equations 5.38, 5.39 and 5.40).

$$C_\theta = hc \langle \theta \rangle = \int_{-hc}^0 \theta dz \quad (5.36)$$

$$C_{\theta_{res}} = hc \langle \theta \rangle - C_\theta = hc(\theta_{-hc} - \langle \theta \rangle) \quad (5.37)$$

$$H_{strg} = \int_{-hc}^0 \rho c_p \theta dz \quad (5.38)$$

$$\frac{dH_{strg}}{dt} = Q - \overbrace{\frac{w_\theta}{hc} H_{strg}}^{Hdiv1} + \overbrace{w_\theta \rho c_p \theta_{-hc}}^{Hdiv2} \quad (5.39)$$

$$\frac{dH_{res}}{dt} = - \overbrace{Q}^{(1)} + \overbrace{\frac{w_\theta}{hc} (H_{strg} - hc \rho c_p \theta_{-hc})}^{(2)} + \overbrace{hc \rho c_p \times d\theta_{-hc}/dt}^{(3)} \quad (5.40)$$

It should be noted that w_θ is replaced by w_ρ as explained in section 5.3.1.

5.2.1.4 Buoyancy fluxes using the NS formulation

In this section the buoyancy flux originally based on the method presented in Gill (1982) (equation 5.5) is calculated. In this method the buoyancy flux is calculated by taking into account the contribution of heat and freshwater input. The equations used in this section were adapted by Nerheim and Stigebrandt (2006) (NS formulation) to calculate the buoyancy flux between the surface and MLD . In the NS formulation vertical advection is not considered. In this commonly used method the buoyancy flux in the surface layer is only affected by the atmosphere at the sea surface. The main purpose of this calculation is to compare the buoyancy flux obtained with the LP

method in which the vertical advection is considered. The buoyancy flux calculated in this method depends on the heat flux (q_{in}) and freshwater (F_{in}), both of which come through the sea surface (Gill, 1982). The buoyancy flux (J_b) is given by the following equation.

$$J_b = g \overbrace{\frac{\alpha}{\langle \rho \rangle} q_{in}}^{J_b T} + g \overbrace{\beta F_{in} \langle S \rangle}^{J_b S} \quad (5.41)$$

where g is the gravitational constant and α and β are respectively the water thermal expansion and salinity contraction coefficients. $\langle S \rangle$ and $\langle \rho \rangle$ are the mean values of salinity and density in the layer between the surface and the reference depth (hc). c_p is the specific heat of water. The heat content (HC) and freshwater content (FWC) are calculated using heat and freshwater content changes inside the surface layer using following equations.

$$HC = \int_0^{hc} \rho(z) c_p (T(z) - T_{ref}) dz \quad (5.42)$$

$$FWC = \int_0^{hc} \frac{S_{-hc} - S(z)}{S_{ref}} dz \quad (5.43)$$

$T(z)$ and T_{ref} are respectively the water temperature at depth of z and the reference temperature which has been chosen as the minimum value of the temperature in the layer (between the surface and $-hc$) during the sampling period. The freshwater content is calculated using 5.43. $S(z)$ and S_{ref} represent respectively the water salinity as a function of depth and the reference salinity which has been chosen as the maximum value of the salinity in the surface layer during the sampling period.

$$q_{in} \Delta t = HC(t + \Delta t) - HC(t) \quad (5.44)$$

$$F_{in} \Delta t = FWC(t + \Delta t) - FWC(t) \quad (5.45)$$

q_{in} and F_{in} are heat and freshwater content variations in the layer between the surface and reference depth (hc).

5.2.1.5 Atmospheric fluxes

The total atmospheric heat flux calculation is based on the Parkinson and Washington (1979) formulation, and has been carried out using the in situ atmospheric data in the

Amundsen Gulf during the CASES program. The atmospheric fluxes are incoming and outgoing long and short wavelength radiation fluxes, the sensible heat and latent heat fluxes which correspond to the total flux coming from the atmosphere.

According to [Parkinson and Washington \(1979\)](#) total heat fluxes at the surface are obtained using following equation:

$$\overbrace{H \downarrow + LE \downarrow + \varepsilon_I LW \downarrow + (1 - 0.4I_0)(1 - \alpha_I)SW \downarrow - LW \uparrow}^{\text{Total heat flux}} + \frac{k_I}{h_I}(T_B - T_{sfc}) = 0 \quad (5.46)$$

where $H \downarrow$, $LE \downarrow$, $SW \downarrow$ are sensible heat, latent heat and ingoing short wave length radiation respectively. $LW \downarrow$ and $LW \uparrow$ are respectively ingoing and outgoing long wave radiation. $\varepsilon_I = 0.97$ is the longwave emissivity of ice, $\alpha_I = 0.5$ the albedo of ice, $I_0 = 0.6$ is the incident radiation penetration in the ice, $k_I = 2.04 \text{ W m}^{-1} \text{ K}^{-1}$ is the thermal conductivity of the ice, $T_B = -1.78^\circ\text{C}$ and h_I is ice thickness.

5.2.2 Ice thickness estimation using the fluxes

In the present thesis the method for the estimation of the ice growth rate introduced by [Cox and Weeks \(1988\)](#) is used. This method is applied to oceanic measurements using CTD data collected during CASES (at the fixed station). The method is briefly described below.

Method of Cox and Weeks (1988) Brine rejection due to ice formation occurs in two phases. The first phase occurs when the ocean water reaches the freezing temperature and ice forms. The second phase occurs due to the drainage of brine from the ice into the mixed layer ([Smith, 1990](#)). The brine rejection is especially evident beneath the leads where ice growth is very fast since the open water is exposed to extremely cold temperatures. This fast ice growth may lead to large amounts of salt being released into the ocean resulting in intense convection. Since most of the salt is rejected during the ice growth phase, it is very important to find a relationship between ice growth velocity and salinity flux within the mixed layer. The method of [Cox and Weeks \(1988\)](#) is based on a simulation which estimates the salinity profiles as a function of ice growth velocity during the ice freezing period for first-year sea ice. In this model it is assumed that the temperature within the ice varies linearly. According to [Maykut \(1982\)](#) the salt flux due to salt rejection from ice growth is given by the following equation:

$$SMC = \int_{-hc}^0 \rho_z S_z / 1000 dz \quad (5.47)$$

$$F_{salt}(h) = \frac{d}{dt} SMC \quad (5.48)$$

$$F_{salt}(h) = \rho_i V(h) [1 - k_{eff}(h)] S_w \quad (5.49)$$

where SMC is the salt mass content (kg m^{-2}) and $F_{salt}(h)$ is the mass flux of salinity with units of ($\text{kg m}^{-2} \text{s}^{-1}$) which is calculated using equation 5.49 in this model. The salinity in the ocean is calculated as kilogram of salt per kilogram of water and the mass of salinity at different depths is obtained by integration ($\rho_z S_z/1000$). It should be noted that in this study the salinity flux is calculated using CTD data then the ice growth velocity is estimated using equation 5.49. Cox and Weeks (1988) calculated the salinity flux due to brine rejection using equation 5.49 using ice thickness measurements and ice growth velocity.

In equation 5.49, S_w is the salinity of the water in the mixed layer and $k_{eff}(h) = S_i/S_w$ is the effective distribution coefficient as a function of ice thickness (h) which expresses the amount of salt retained by the ice compared with the water salinity. This parameter was determined by Cox and Weeks (1988) using radioactive tracers. ρ_i is the sea ice density, assumed as 915 kg m^{-3} and $V(h)$ is the growth rate of ice thickness. Cox and Weeks (1988) proposed two equations for high and low growth velocities for calculation k_{eff} . Equation 5.50 is used for velocities greater than $3.6 \times 10^{-5} \text{ cm s}^{-1}$.

$$k_{eff} = \left[\frac{0.26}{-0.26 + 0.74 \exp(-7243V)} \right] \quad (5.50)$$

where V is the velocity of ice growth in centimeters per second. For velocities between $3.6 \times 10^{-5} \text{ cm s}^{-1}$ and $2 \times 10^{-6} \text{ cm s}^{-1}$, equation 5.51 is proposed:

$$k_{eff} = 0.8925 + 0.0568 \ln V \quad (5.51)$$

k_{eff} is assumed to be constant and equals 0.12 for velocity of ice growth less than $2 \times 10^{-6} \text{ cm s}^{-1}$. In this study the salinity fluxes related to the ice growth velocities of $3.6 \times 10^{-5} \text{ cm s}^{-1}$ and $2 \times 10^{-6} \text{ cm s}^{-1}$ are, respectively, 6.9021×10^{-4} and $4.7615 \times 10^{-5} \text{ kg m}^{-2} \text{ s}^{-1}$. If the salinity flux is larger than $6.9021 \times 10^{-4} \text{ kg m}^{-2} \text{ s}^{-1}$, k_{eff} is calculated with equation 5.50, if it is between 6.9021×10^{-4} and $4.7615 \times 10^{-5} \text{ kg m}^{-2} \text{ s}^{-1}$ equation 5.51 is used. Otherwise k_{eff} is assumed to be equal to 0.12. Using this method the ice thickness variation is obtained by adding the ice thickness at the beginning of the period to the ice thickness variation the ice thickness can be calculated for a given time.

5.2.3 Cross-correlations function

In order to better understand the effects of atmospheric and oceanic fluxes on *MLD* variations, the cross correlation function between different parameters and the *MLD* have been calculated. The cross correlation is a measure of the correlation between two parameters as a function of time lags as calculated using equation 5.52. In this equation $C_{xy}(k)$ is the cross covariance which is obtained by equation 5.53 (Bendat and Piersol, 2011).

$$R_{xy}(k) = \frac{C_{xy}(k)}{\sqrt{C_{xx}(0)C_{yy}(0)}} \quad (5.52)$$

$$C_{xy}(k) = \begin{cases} \frac{1}{N} \sum_{n=1}^{N-k} (x_n - \bar{x})(y_{n+k} - \bar{y}), & k = 0, 1, 2, \dots, N-1 \\ \frac{1}{N} \sum_{n=1-k}^N (x_n - \bar{x})(y_{n+k} - \bar{y}), & k = -1, -2, \dots, -(N-1) \end{cases} \quad (5.53)$$

The cross correlation determines the correlation between Y_t and X_t as a function of the time-lags. The original data were sampled twice a day, but at irregular intervals. Therefore, the observations time series were linearly interpolated every 0.5 day.

5.2.4 Data

The data used in this chapter were sampled at (1) a fixed station during the CASES program, (2) a drift station, (3) fast ice stations during the CFL program and (4) a fixed station during the Malina program in the summer of 2009 as explained in sections 2.2.1, 2.2.3 and 2.2.4. The different types of stations with their names, number of CTD profiles, locations, sampling time, *MLD* ranges and reference depths are presented in Table 5.1 and Figure 5.2.

The atmospheric data used in this study were measured at a meteorological station in Franklin Bay near the ship during the CASES program. The station, also on the ice was approximately 1.4 km away from the ship (red star in Figure 5.2). The data were obtained from the ‘‘Center for Earth Observation Science’’ of the University of Manitoba (Prof. Tim Papakyriakou) and allowed us to determine the atmospheric fluxes at the atmosphere/ice interface and compare them with estimated atmospheric fluxes under the ice using oceanic data. PAR (photosynthetically active radiation) data,

Table 5.1: Characteristics of the stations where the ocean fluxes are calculated. Ship's drift is the distance covered by the ship during a sampling period.

Station	Station type	No. of profiles	Date	Day of the year	MLD (m)	hc (m)	Ship's drift (km)
CASES	Fixed	394	13 Dec. 2003-30 May 2004	-22.35-174.25	3-43	50	0.00
5D	Drift ice	22	05-07 Dec. 2007	339-341.5	35-49	56	12.46
7D	Drift ice	51	10-16 Dec. 2007	344-350.6	11-29	36	19.26
12D	Drift ice	20	26-30 Dec. 2007	360-364.07	14-56	63	31.17
14D	Drift ice	45	03-11 Jan. 2008	3.86-11.73	12-86	93	61.51
17D	Drift ice	43	15-22 Jan. 2008	15.08-11.73	11-47	54	12.99
19D	Drift ice	97	24 Jan.-14 Feb. 2008	24.63-45.83	11-50	57	50.68
26D	Drift ice	28	25 Feb.-01 Mar. 2008	55.58-61.57	42-58	65	18.12
27D	Drift ice	15	02-03 Mar. 2008	62.045-63.58	30-38	45	16.99
29D	Drift ice	36	05-19 Mar. 2008	65.58-79.54	44-59	66	12.56
33D	Drift ice	60	25 Mar.-04 Apr. 2008	85.133-95.54	12-50	57	0.01
41D	Drift ice	25	16-22 Apr. 2008	107.57-114.55	48-63	70	27.80
43D	Drift ice	55	26 Apr.-06 May 2008	117.55-127.12	47-84	91	162.41
F2	Landfast ice	21	13-18 May 2008	134.055-139.04	22-37	44	0.00
F3	Landfast ice	14	20-21 May 2008	141.75-142.29	50-58	65	0.00
F7	Landfast ice	41	04-24 Jun. 2008	159.55-176.89	11-50	57	2.23
235	Summer station	28	22-24 Aug. 2009	234.35-236.6	4-15	22	5.95

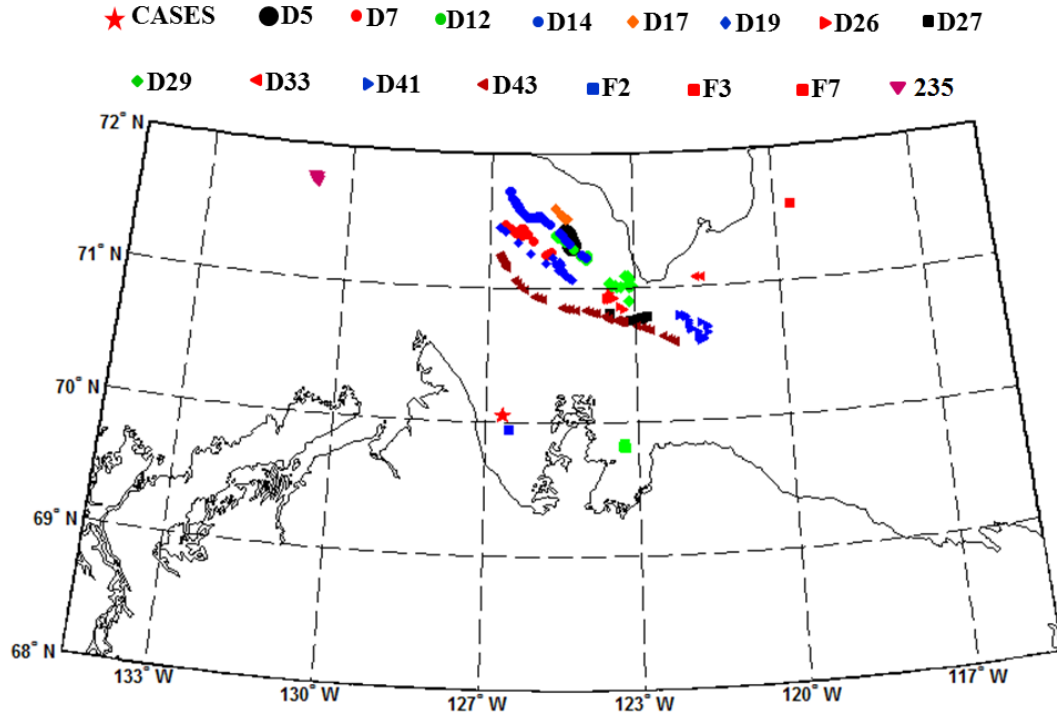


Figure 5.2: Locations and names of the stations where the ocean fluxes are calculated.

air temperature, surface salinity, ice thickness and chlorophyll a (*Chl a*) concentrations under the sea ice during the CASES (2003-2004; 27 samples) program were obtained from the “Institut des sciences de la mer de Rimouski” (Prof. Michel Gosselin). The *Chl a* sampling during CASES was conducted at a fixed station in Franklin Bay (70°04' N, 126°26' W) (Rozanska et al., 2009). The biological station was located 1.5 km northeast of the ship. The ice sampling was conducted at two different sites: high snow (> 10 cm) and low snow (< 10 cm), but in this study we use the mean values of ice thickness and *Chl a* from these two sites. The *Chl a* concentration in the sea ice and ice thickness were measured on the drift and landfast ice stations during the CFL program. The analysis of this data is presented in section 5.3.7.

5.3 Results and discussion

5.3.1 Ocean fluxes during CASES (2003-2004) and *MLD* variations

Our study was based heavily on the data gathered at the fixed station during the CASES program. This was due to the large number of data sampled during CASES, especially the measured atmospheric fluxes and ice thickness which was used to validate

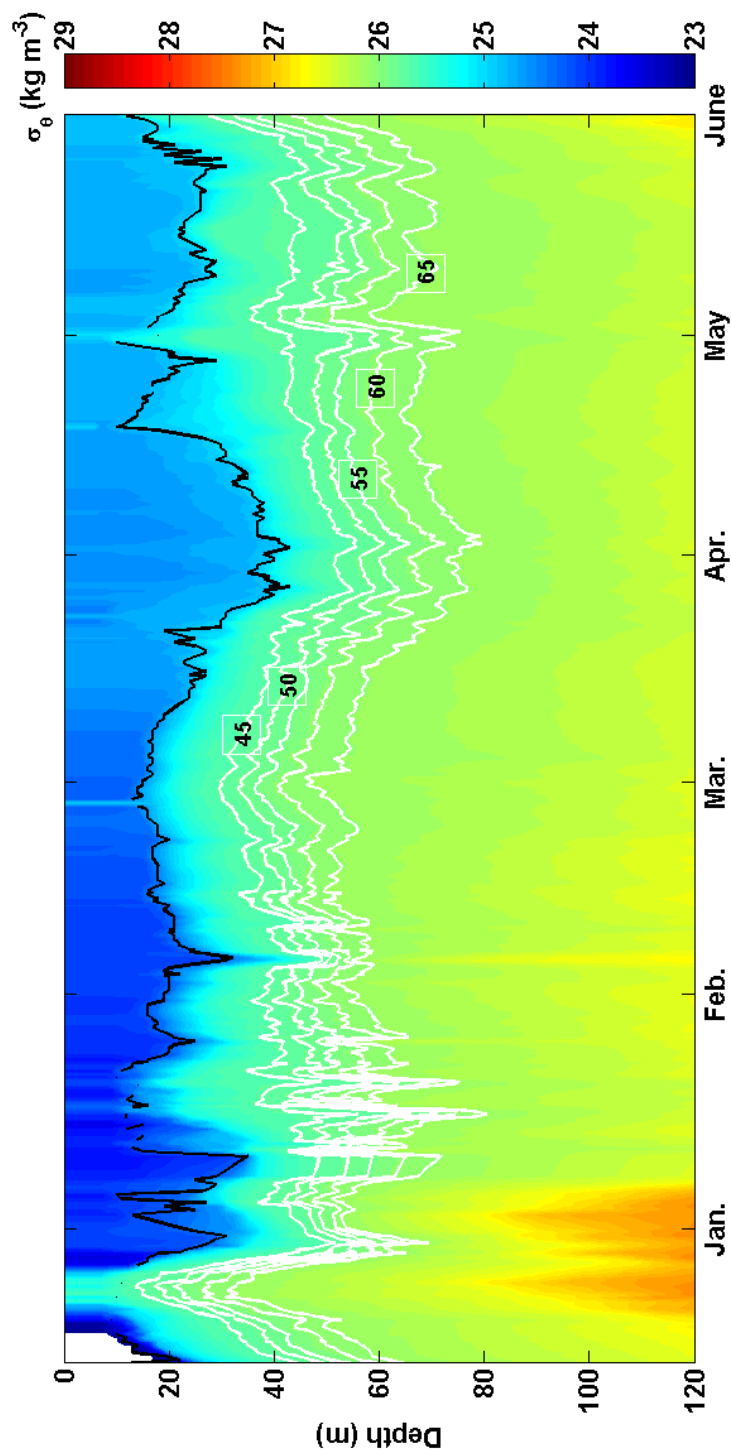


Figure 5.3: Contours of density at the fixed station. The white lines are the vertical positions with time of the density of the different reference depths $\sigma_{\theta_{hc}}^{l=1}$. The black numbers are the depths of each reference at the beginning of the sampling period. The black line is the *MLD*.

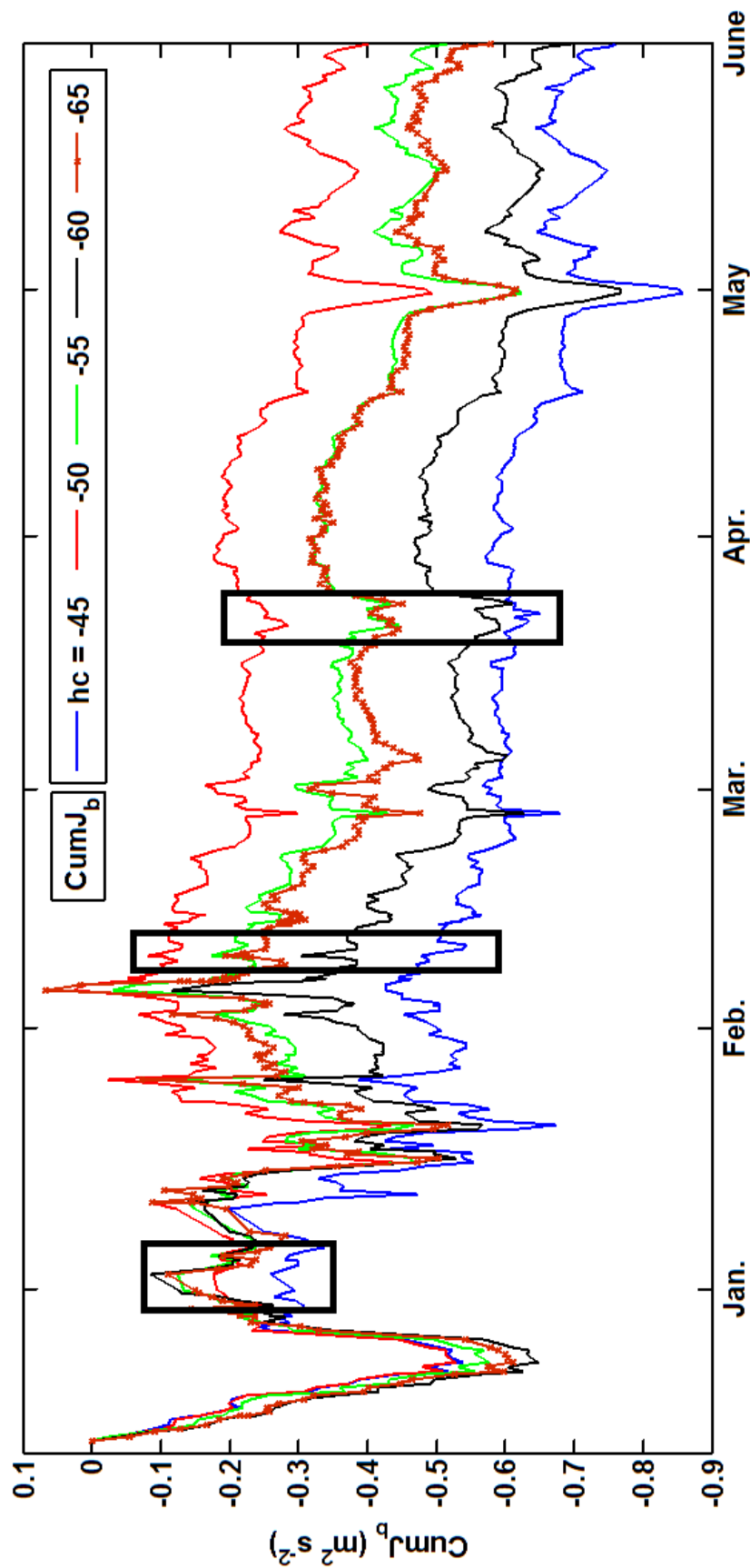


Figure 5.4: Temporal variation of the cumulative buoyancy flux ($CumJ_b$) for different reference depths: $hc = -45$ m (blue), $hc = -50$ m (red), $hc = -55$ m (green), $hc = -60$ m (black) and $hc = -65$ m (brown stars). The black rectangles highlight the events discussed in the text.

our results.

To choose the reference depth to calculate the ocean fluxes in the surface layer, different reference depths (hc) were examined for the CASES data. The chosen reference depths were 45 m, 50 m, 55 m, 60 m because the deepest MLD during the CASES program was 43 m and the reference depth should be larger than the maximum value of the MLD during the sampling at the fixed station. Figure 5.3 shows density contours of the CASES data with the density isolines at each reference depth for the first sampling period. As shown in the figure all the density isolines for the different reference depths were always larger than the densities of the $MLDs$, which means all of the chosen reference depths were appropriate as explained in section 5.2.1.

The cumulative value of the buoyancy flux ($CumJ_b$) in the surface layer was calculated using equation 5.30 for different reference depths (see Figure 5.4). As shown in Figure 5.4 the fluctuations of $CumJ_b$ and tendency values calculated for the different reference depths were very similar especially for $hc = -50$ m, -55 m, -60 m and -65 m. Looking at Figure 5.4, we may expect that $CumJ_b$ increases with an increase in the reference level but it is not the case here because of the role of vertical advection (term II in equation 5.22). In particular, the eddy at the first of the sampling period (at the end of December) has a direct impact on the vertical advection. The black rectangles in Figure 5.4 show some cases in which the fluctuations of $CumJ_b$ were similar for all of the reference depths except for $hc = -45$ m. This difference is probably because $hc = -45$ m is very close to the maximum value of the MLD at the fixed station (43 m). As previously explained in section 5.2.1 the molecular diffusion is neglected in the LP method and the reference depth should be located in the pycnocline region below the mixed layer. Therefore the reference depth at $hc = -45$ m was probably near the base of the mixed layer and was not always in the pycnocline region. To make sure that the reference depth is not being affected by the mixed layer and is located in the pycnocline region, we chose the reference depth $hc = -50$ m for the CASES fixed station (7 m deeper than the MLD_{max} during the sampling period). For consistency, in other stations shown in Table 5.1 the reference depth was also chosen 7 m deeper than the maximum value of the MLD at the station.

As it is shown in Figure 5.6, there are clear distinctions between the salinity (and density) at different depths. On the other hand, the vertical velocity based on temperature is occasionally very large due to the large fluctuations in the temperature profile. Figure 5.7c also shows that these large fluctuations (especially below the mixed layer) produce multiple isolines of temperature ($\theta_{hc}^{t=1}$). In contrast, Figure 5.7a and b show a single isoline of salinity and density ($S_{hc}^{t=1}$ and $\rho_{hc}^{t=1}$) since there is no such fluctuations in the salinity and density profiles. Since the density plays a vital role in ocean dynamics

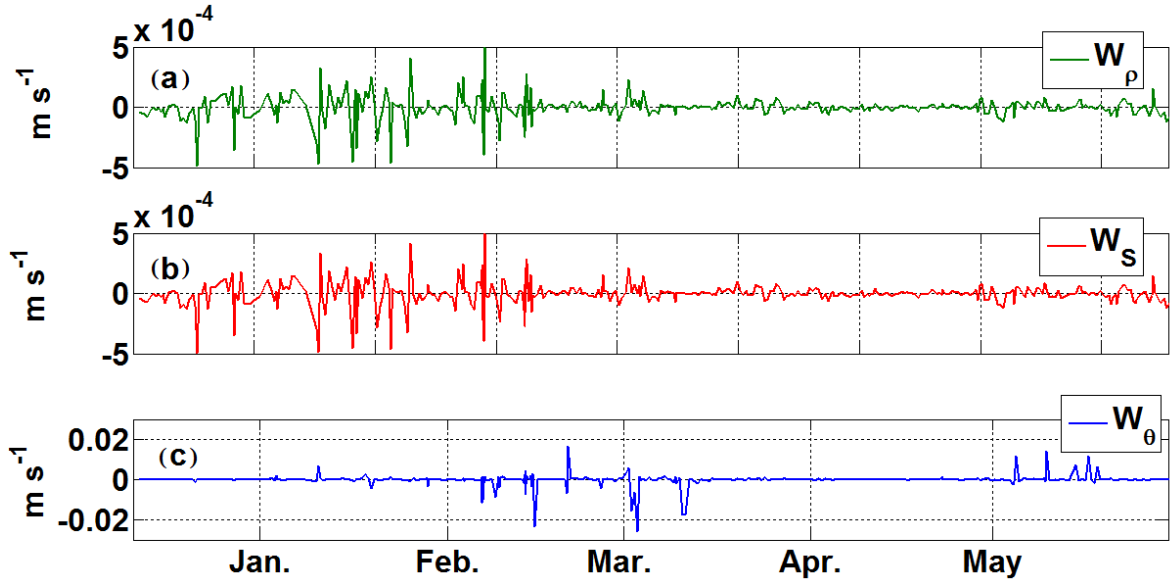


Figure 5.5: Temporal variation of (a) the vertical velocity based on density $w_\rho = -\left(\frac{\partial \rho}{\partial t}\right)_{-hc} / \left(\frac{\partial \rho}{\partial z}\right)_{-hc}$ (b) the vertical velocity based on salinity $w_s = -\left(\frac{\partial S}{\partial t}\right)_{-hc} / \left(\frac{\partial S}{\partial z}\right)_{-hc}$ and (c) the vertical velocity based on temperature $w_\theta = -\left(\frac{\partial \theta}{\partial t}\right)_{-hc} / \left(\frac{\partial \theta}{\partial z}\right)_{-hc}$ at the fixed station in the Franklin Bay. The reference depth, hc , is -50 m. Note the change of scale for the temperature-based vertical velocities. These velocities vary from zero (often) to values two orders of magnitude larger than the velocities calculated from the density or the salinity fields.

and heat transfer, for the rest of the calculations the density based vertical velocity (w_ρ) is used.

The behaviour of $CumJ_b$ (equation 5.30), C_ρ (equation 5.8) and C_{pres} (equation 5.21) during the CASES program between 9 December 2003 and 30 May 2004 at the fixed station are presented in Figure 5.8. The reference depth was chosen as $hc = -50$ m because as explained previously, it should be deeper than the maximum value of the MLD during the study period which was -43 m. Moreover, the maximum value of the density in the mixed layer $\rho(MLD(t))$ must always be smaller than the initial density at $z = -hc$ (in our case, $\rho_{hc}^{t=1} = 25.87 \text{ kg m}^{-3}$ see Figure 5.7). The location of $\rho = 25.87 \text{ kg m}^{-3}$ is highlighted in Figure 5.7a. The corresponding reference salinity and temperature are shown in Figures 5.7b and c, respectively. Regarding Figure 5.8, the cumulative buoyancy flux values ($CumJ_b$) generally decrease as well C_{pres} , while C_ρ increases with time. C_ρ increases with time as the density increases with the salinity in the surface water layer (see Figure 5.7a, b).

As shown in Figure 5.6 and Figure 5.8a, when the $CumJ_b$ increases (decreases), C_{pres} increases (decreases) and the density difference between the surface and reference depth

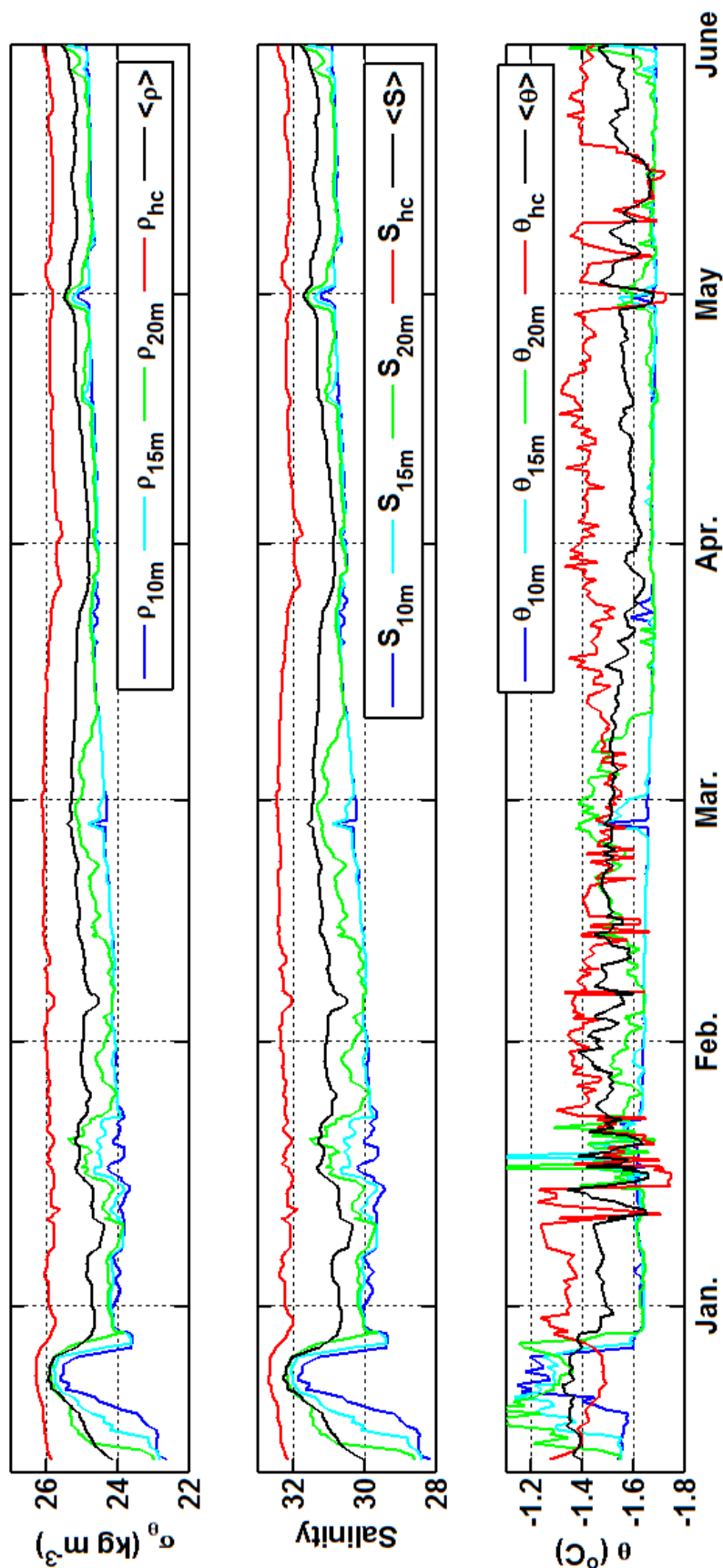


Figure 5.6: Upper panel: water density at different depths (10, 15, 20 m and h_c) and mean value of the density between the water surface and $h_c = -50$ m. The two other panels present the salinity and temperature corresponding to the density in the first panel.

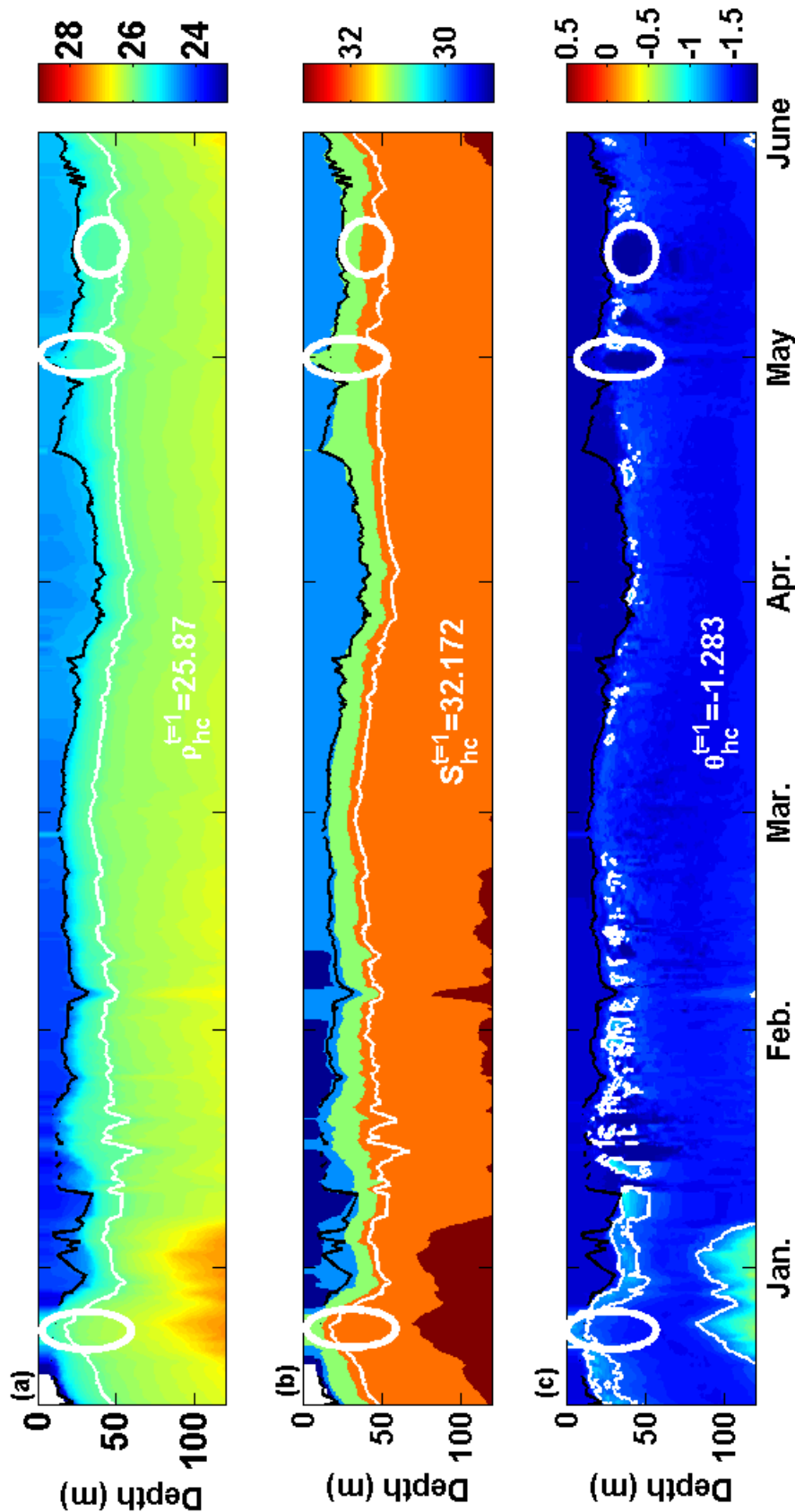


Figure 5.7: (a), (b) and (c) are the contours of density, salinity and temperature at the fixed station. The white lines are the density, salinity and temperature isolines at the reference depth ($hc = -50$ m) at the beginning of the period. The black line is the *MLD*. White ellipses are the special cases that will be discussed in the text.

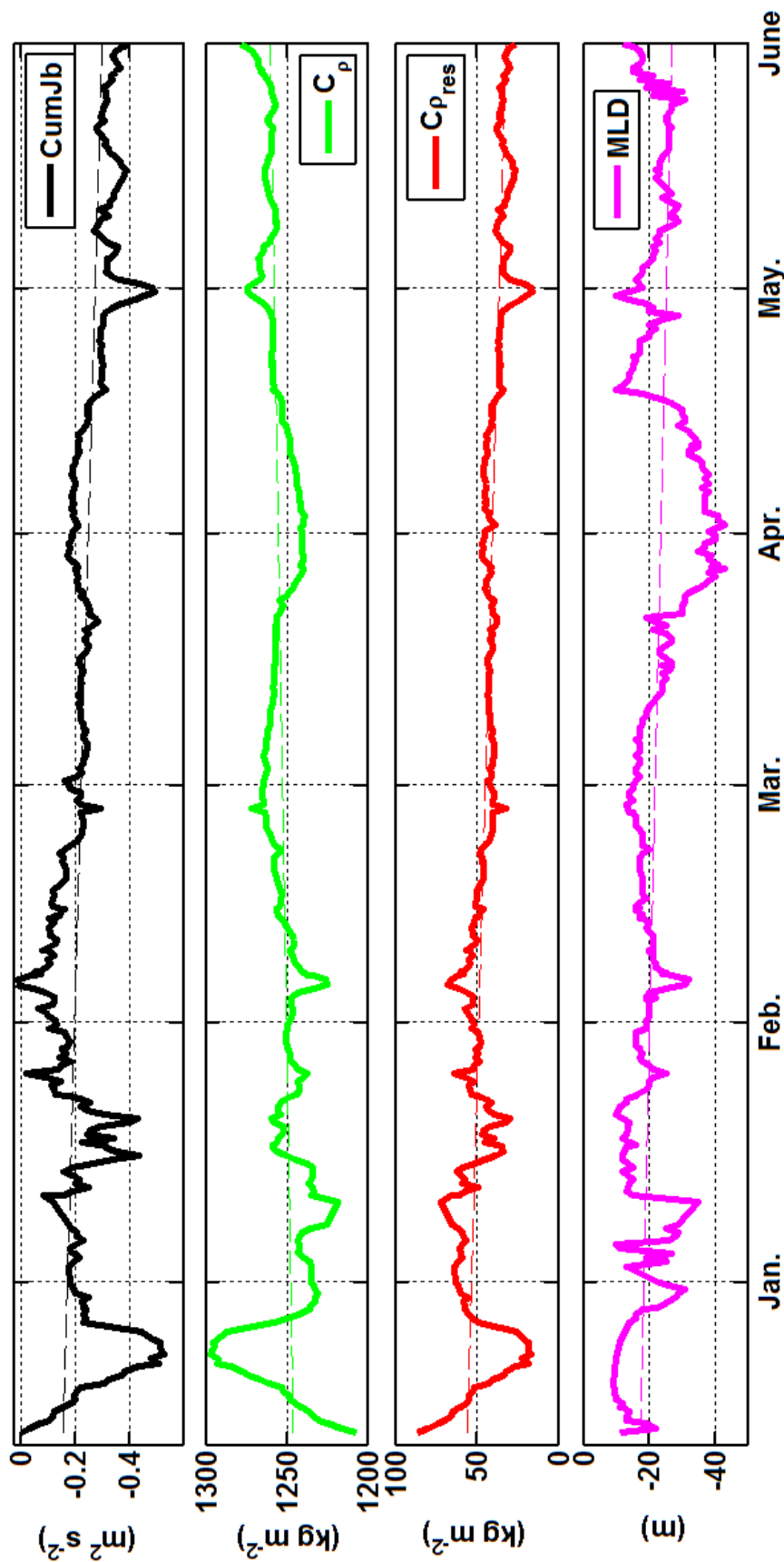


Figure 5.8: The first three panels present the temporal variations of $CumJ_b$, C_p , $C_{p_{res}}$, between the surface and $-hc$. The lower panel presents the temporal variation of the MLD at the fixed station in the Franklin Bay. The dashed lines show the trends of each curve.

increases (decreases). As mentioned earlier, the cumulative value of the buoyancy flux or mass flux ($CumJ_b$ or $CumJ_m$) can be an indicator of atmospheric influence regardless of the ice presence. The buoyancy flux is affected by heat and salinity exchanges (equation 5.5), meaning that when the water warms or the salinity decreases due to ice melting the buoyancy becomes positive, while water cooling and increased salinity lead to negative buoyancy. Hence, the buoyancy flux evolution can be used to estimate atmospheric flux variations. The *MLD* generally deepens during the sampling period (between January and March), although it does not exactly follow the $CumJ_b$. The *MLD* deepens until 2 April and then becomes shallower between 2-19 April. However, $CumJ_b$ generally shows a decreasing trend until the end of the sampling period.

Different terms of mass, salinity and heat fluxes calculated using equations 5.22, 5.34 and 5.40 are shown in Figure 5.9a,b and c. The cumulative value of the mass flux ($CumJ_m$) and the salinity flux ($CumJ_s$) increase while the cumulative value of the total heat ($CumQ$) decreases. The increasing tendency of $CumJ_m$ and $CumJ_s$ show that the salinity and density fluxes increase during the period (see Figure 5.9a,b). In both the density and salinity figures, the cumulative values of (dC_{pres}/dt using equations 5.22) and (dC_{Sres}/dt using equation 5.34) tend to decrease as does (dH_{res}/dt), the residual heat flux (equation 5.40) except for two periods of time (25-30 December and 12-29 April) in which an abrupt increase can be seen, as shown in Figure 5.9c.

The temporal variations of the cumulative vertical advection values $w_V(\langle V \rangle - V_{-hc})$ and $hc \frac{dV_{-hc}}{dt}$, for which V is any variable (density, salinity, or heat), are shown by red and green lines in Figure 5.9. Here, $Cum(Adv_{\rho hc})$ has the same increasing trends (-21.6 – 0.6 kg m⁻²) as $Cum(Adv_{S hc})$ (-26 – 1.8 m) and $Cum(hc d\rho/dt)$ has the same decreasing trend (11.9 – -0.7 kg m⁻²) as $Cum(hc dS/dt)$ (14.5 – -1 m). The cumulative surface heat flux value of ($Cum(Q)$) decreases similarly to $Cum(hc \rho C_p \frac{d\theta_{-hc}}{dt})$. Moreover, the advection part $Cum(Adv_{H hc})$ decreases very slowly.

The increase in the cumulative mass and salinity flux values ($CumJ_m$ and $CumJ_s$) in Figure 5.9a,b is because of the gain in density due to increased salinity from ice formation which leads to salt rejection (see Figure 5.9a). $CumJ_m$ (equation 5.19) increases while $CumJ_b$ (equation 5.30) decreases in Figure 5.9a. Additionally, the surface heat flux ($CumQ$) values are negative, demonstrating a cooling in the surface layer as the air temperature declines and causes a decrease in the surface water temperature. As shown in Figure 5.7, the physical properties of the *MLD* varied during CASES between 9 December 2003 and 30 May 2004. These variations could be due to ice formation or melt, advection such as eddy transition or horizontal advection, upwelling, etc. As mentioned before, the *MLD* deepens gradually between December and the end of March or the beginning of April, then it shoals until the beginning of May. As shown in Fig-

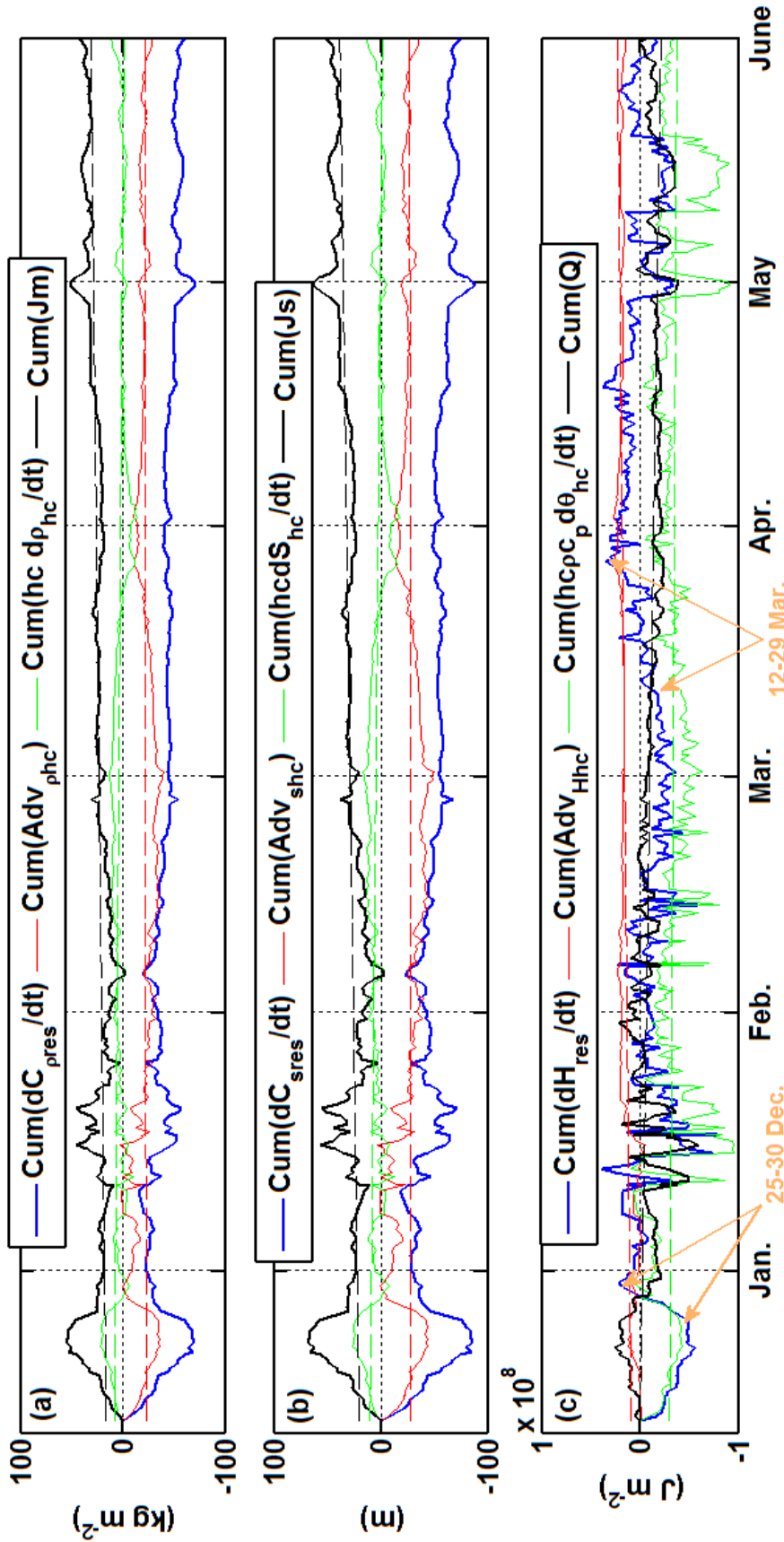


Figure 5.9: Temporal variation of (a) the cumulative values of the different terms contributing to the density flux. The blue line shows the cumulative value of dC_{pres}/dt , the red line the cumulative value of the vertical advection term $w_{\rho}((\rho) - \rho_{-hc})$, the green line the cumulative value of $(hc \frac{d\rho_{-hc}}{dt})$ and the black line is cumulative value of the mass flux at the surface. (b) The cumulative values of the salinity flux components. The blue line shows the cumulative value of (dC_{sres}/dt) , the red line the cumulative value of the vertical advection $w_s((S) - S_{-hc})$, the green line the cumulative value of $(hc \frac{dS_{-hc}}{dt})$ and the black line the cumulative value of the salinity flux at the water surface (J_s). (c) The cumulative values of the different heat flux terms. The blue line shows the cumulative value of dH_{res}/dt , the red line cumulative value of the vertical advection term $\frac{w_{\theta}}{hc}(H_{\text{strg}} - hc \rho C_p \theta_{-hc})$, the green line the cumulative value of $(hc \rho C_p \frac{d\theta_{-hc}}{dt})$ and the black line cumulative value of the heat flux at the water surface. The dashed lines represent the tendency of each variable.

Table 5.2: The trend of the *MLD* and of the different terms in equation 5.22, $CumJ_b$, $Cum(dC_{pres}/dt)$, $Cum(Adv_{\rho_{hc}})$ and $Cum(hc d\rho_{hc}/dt)$, at each station. D, A and NS are used to qualify the trends and mean “Descending”, “Ascending” and “Not Significant”, respectively. A “Not Significant” trend means that the variation of the parameter during the sampling period is less than 5%.

Station	<i>MLD</i>	$CumJ_b$	$Cum(dC_{pres}/dt)$	$Cum(Adv_{\rho_{hc}})$	$Cum(hc d\rho_{hc}/dt)$
CASES	D	D	D	A	D
5D	NS	NS	NS	NS	NS
7D	NS	NS	NS	NS	NS
12D	D	A	D	A	D
14D	A	D	NS	D	A
17D	D	D	D	D	A
19D	D	A	A	A	D
26D	A	D	D	NS	A
27D	D	A	A	D	A
29D	NS	A	A	D	A
33D	A	A	A	D	A
41D	NS	NS	NS	NS	NS
43D	D	D	D	A	D
F2	NS	NS	D	NS	D
F3	NS	NS	NS	NS	NS
F7	A	A	A	A	D
235	A	D	D	A	D

ure 5.6, $CumJ_b$ decreases until approximately 20 March then it slightly increases until mid-April which coincides with the period of shoaling the *MLD*. Afterward, $CumJ_b$ decreases toward a larger negative value (descending trend) which virtually coincides with the *MLD* deepening period in May. As shown in Figure 5.7, anticyclonic eddies, which are present at the end of April and mid May (white ellipse and circles) (Barrette, 2012), cause shoaling the *MLD* while $CumJ_b$ increases toward a larger negative (decending trend).

Table 5.2 shows the trends of the *MLD*, $CumJ_b$, $Cum(dC_{pres}/dt)$, $Cum(Adv_{\rho_{hc}})$ and $Cum(hc d\rho_{hc}/dt)$ for the studied stations. As shown in this table, 70% of the *MLDs* and $CumJ_b$ have similar trends. Similarly, 77% of the *MLDs* have similar trends to $Cum(dC_{pres}/dt)$, as was expected. The *MLD* and $Cum(Adv_{\rho_{hc}})$ displayed different trends 70% of the time, while the *MLD* and $Cum(hc d\rho_{hc}/dt)$ were similar 67% of the time. Similar trends between the *MLD* and $CumJ_b$, as previously mentioned, confirms that during cooling (heating) periods $CumJ_b$ decreases (increases) and the *MLD* deepens (shoals). Inverse trends between the *MLD* and $Cum(Adv_{\rho_{hc}})$ indicate that

when $Cum(Adv_{\rho_{hc}})$ increases the MLD deepens. When $Cum(hc d\rho_{-hc}/dt)$ increases (decreases) the MLD shoals (deepens). Figures showing the temporal variation of the MLD , $Cum(dC_{pres}/dt)$, $Cum(Adv_{\rho_{hc}})$ and $Cum(hc d\rho_{-hc}/dt)$ at the different stations listed in Table 5.2 are shown in Appendix A. Their temperature, salinity and density contours are presented in Appendix B.

5.3.2 Comparison between buoyancy flux calculated with the NS and the LP methods

As previously discussed in section 5.2.1.4 and in equation 5.41, temperature and salinity contribute to the buoyancy flux (Gill, 1982, Nerheim and Stigebrandt, 2006). In this section the total buoyancy flux through the surface, the heat and freshwater (salinity) contributions are calculated for data collected during the CASES program. Then, the results of these two approaches are compared. Heat ($CumJ_{bT}$) and salt ($CumJ_{bS}$) contributions and the buoyancy flux in NS method are calculated using equation 5.41. The same terms are calculated using the LP approach. The results of NS formulation and LP method are shown in Figure 5.10. This figure shows that in both method the contribution of the salinity $CumJ_{bS}$ (freshwater content) in the buoyancy flux is dominant. The dash-dotted black line ($CumJ_b$) comes from the direct calculation of the buoyancy flux using the density profile (equation 5.20 or 5.22), while the dash-dotted green line is obtained by summing heat and salinity contributions to the buoyancy flux (J_{bT} , J_{bS}). The comparison between $CumJ_b$ calculated based on density profile (using LP method, dash-dotted black line in Figure 5.10) and $CumJ_b$ calculated based on salinity and temperature contributions (using LP method, dash-dotted green line in Figure 5.10) shows very good agreement which confirms the contribution role of heat and salinity to buoyancy flux. Additionally, the buoyancy flux calculated directly using the density profile is very similar to the salinity contribution ($CumJ_{bS}$) which also confirms the minor role of heat in buoyancy flux in the study region.

On the other hand, while the heat contributions to the buoyancy fluxes ($CumJ_{bT}$) obtained from the NS formulation and LP method are more comparable, the salinity contributions ($CumJ_{bS}$) are significantly different. The difference between the buoyancy flux obtained by the NS formulation and LP method is due to the vertical advection. That result shows the important effect of vertical advection on the oceanic flux in the surface layer which is taken into account in the LP method, but is not considered in the NS formulation. A strange minimum in the cumulative value of the buoyancy, between 20-25 December as shown in Figure 5.10a,b, is due to what appears to be ice-edge upwelling (this will be discussed in details in section 5.3.8). Furthermore, as can be seen in Figure 5.10b, the MLD displays a descending tendency (deepens) until the end

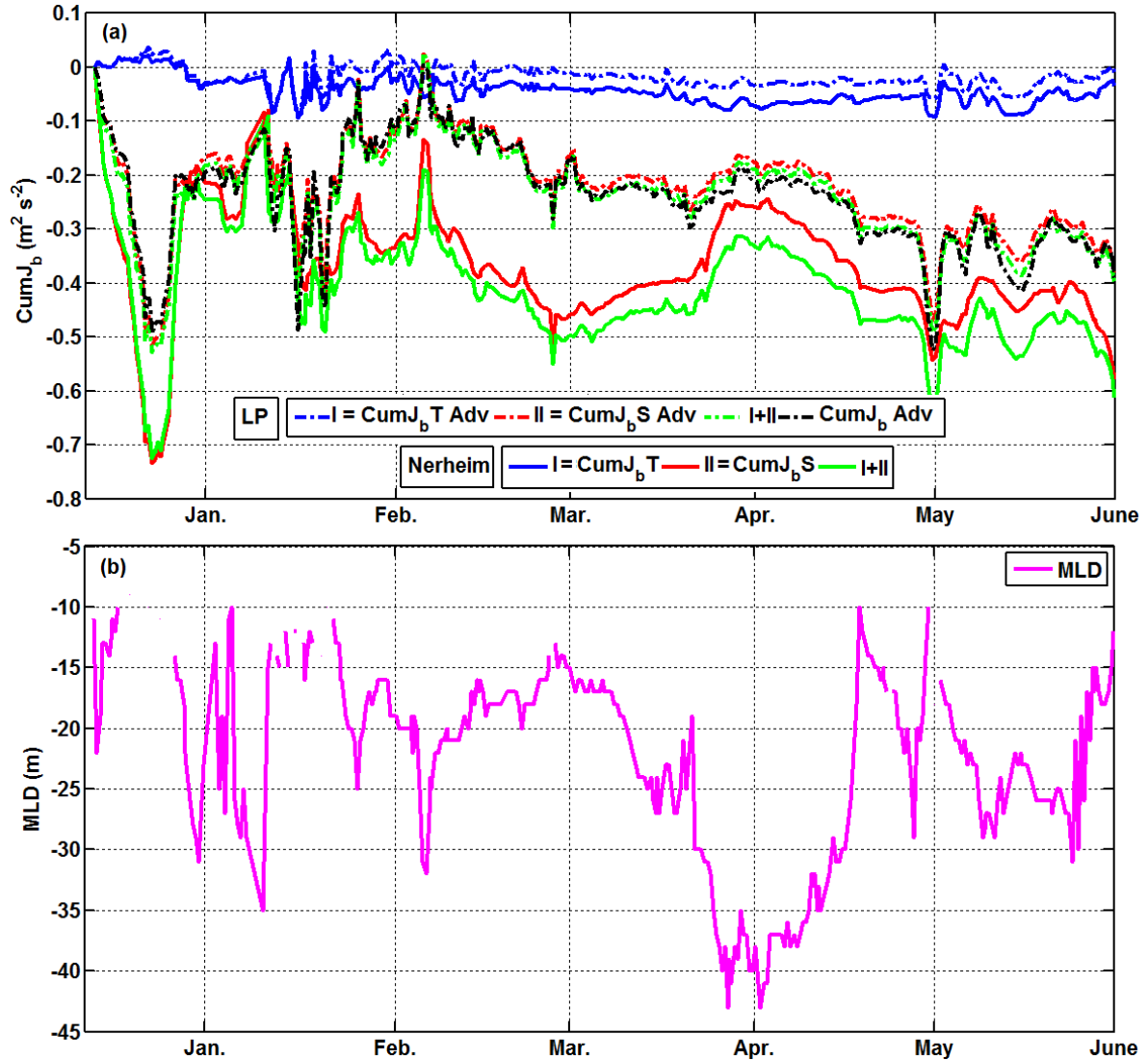


Figure 5.10: (a) Cumulative value of the heat and salinity flux contributions to the surface buoyancy flux based on the NS formulation and the LP method. The blue line is $CumJ_{bT}$, the red line $CumJ_{bS}$ and the green line ($CumJ_{bT} + CumJ_{bS}$) for the NS formulation. For the LP method, the dash-dotted blue line is $CumJ_{bT}$, the dash-dotted red line is $CumJ_{bS}$, the dash-dotted green line is $CumJ_{bT} + CumJ_{bS}$ and the dash-dotted black line is $CumJ_b$. The lower panel presents the temporal evolution of the MLD .

of March - beginning of April, after which it ascends (shallows; see below).

5.3.3 Atmospheric flux, oceanic flux and the *MLD*

Figure 5.11 and Figure 5.12 show the comparison between the estimated atmospheric flux (Q in equation 5.39 or 5.40) and the in-situ atmospheric flux (total heat flux in equation 5.46). As was mentioned before, under ice heat flux estimated using LP method ($CumQ$) is an indicator of the atmospheric flux. As shown in Figure 5.11, $CumQ$ generally has a descending tendency which shows a cooling period during the winter and spring. More precise examination of the figure reveals that $CumQ$ decreases until the beginning of April and thereafter it increases. The in-situ total atmospheric flux (blue line in top plot in Figure 5.12) is negative until the beginning of April (as it is more evident in Figure 5.12), after that it starts to become positive over time. Figure 5.12 shows different components of the atmospheric heat fluxes in equations 5.46 with their linear trends before and after the end of March. The bottom plot in Figure 5.12 also shows the cumulative value of under ice surface flux given in equation 5.40 with its tendency before and after the end of March.

As seen in Figure 5.12, the mean value of the atmospheric total flux (*Total*) is negative between 22 January and the end of March-early April, which indicates a cooling period during the winter until the beginning of April when the *MLD* begins shoaling. Latent heat (LE), long wave ingoing (LW_{in}) and sensible heat (H) decrease from 22 January until the end of March and early April and then they increase. Outgoing long wave (LW_{out}) remains almost constant between the beginning of the sampling period and the end of March when it starts decreasing. The sensible heat, which affects the ice surface temperature, decreases before the end of March and increases slowly afterwards. This suggests that the ice surface cools before the end of March and early April and starts to warm afterward. The ingoing long wave radiation decreases during the winter between 22 January and the end of March-early April and after this time it begins to increase. The increase of ingoing long wave after the end of March is because the sun is more present and strong at this time. The absolute value of outgoing long wave radiation, which is reflected by the earth decreases before the end of March and then increases with the increase in sunlight. The short wave ingoing, SW_{in} , is about 20-30 $W\ m^{-2}$ in January then increases afterwards with the appearance of the sun.

The $CumQ$, calculated using equation 5.40 is shown at the bottom of Figure 5.12 with its trends before and after the end of March-beginning of April in order to compare it with the atmospheric fluxes and *MLD* variations. As shown in Figure 5.10b, the *MLD* deepens until the end of March-April, after which it shoals with some fluctuations.

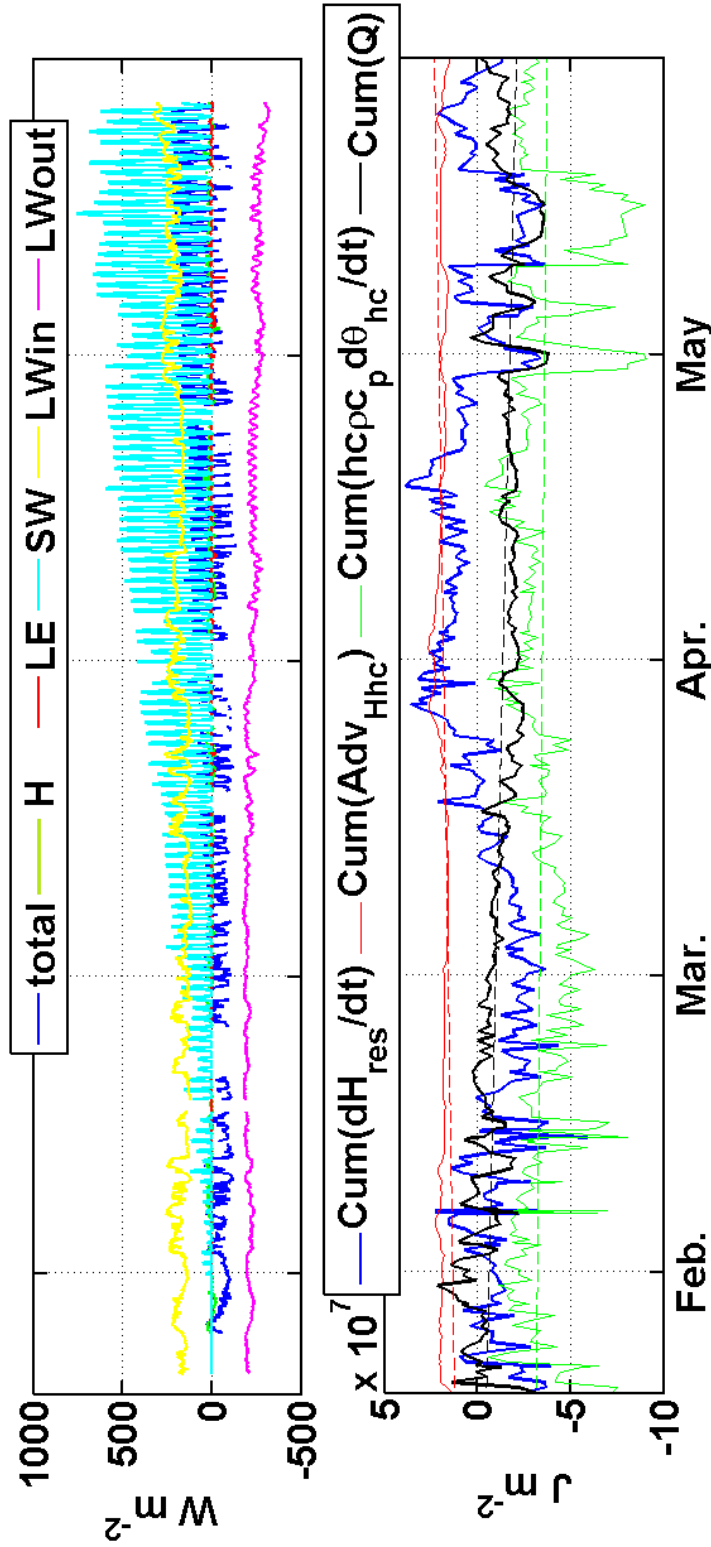


Figure 5.11: In the upper panel, the blue line shows the in-situ total atmospheric flux calculated using sensible the heat flux in green, the latent heat flux in red, the short wave radiation in cyan, the incoming and outgoing long wave radiation in yellow and magenta, respectively. In the lower panel, the blue line is the cumulative value of dH_{res}/dt , the red line is the cumulative value of the vertical advection term $Cum(Adv_{Hhc}) = \frac{w_0}{hc}(H_{strg} - hc\rho C_p \theta_{-hc})$, the green line is the cumulative value of $(hc\rho C_p d\theta_{-hc}/dt)$ and the black line is cumulative value of the heat flux under the ice ($CumQ$) between the surface water and depth of $-hc$ (hear $hc = 50$ m). Black dashed lines represent the tendency of each variable.

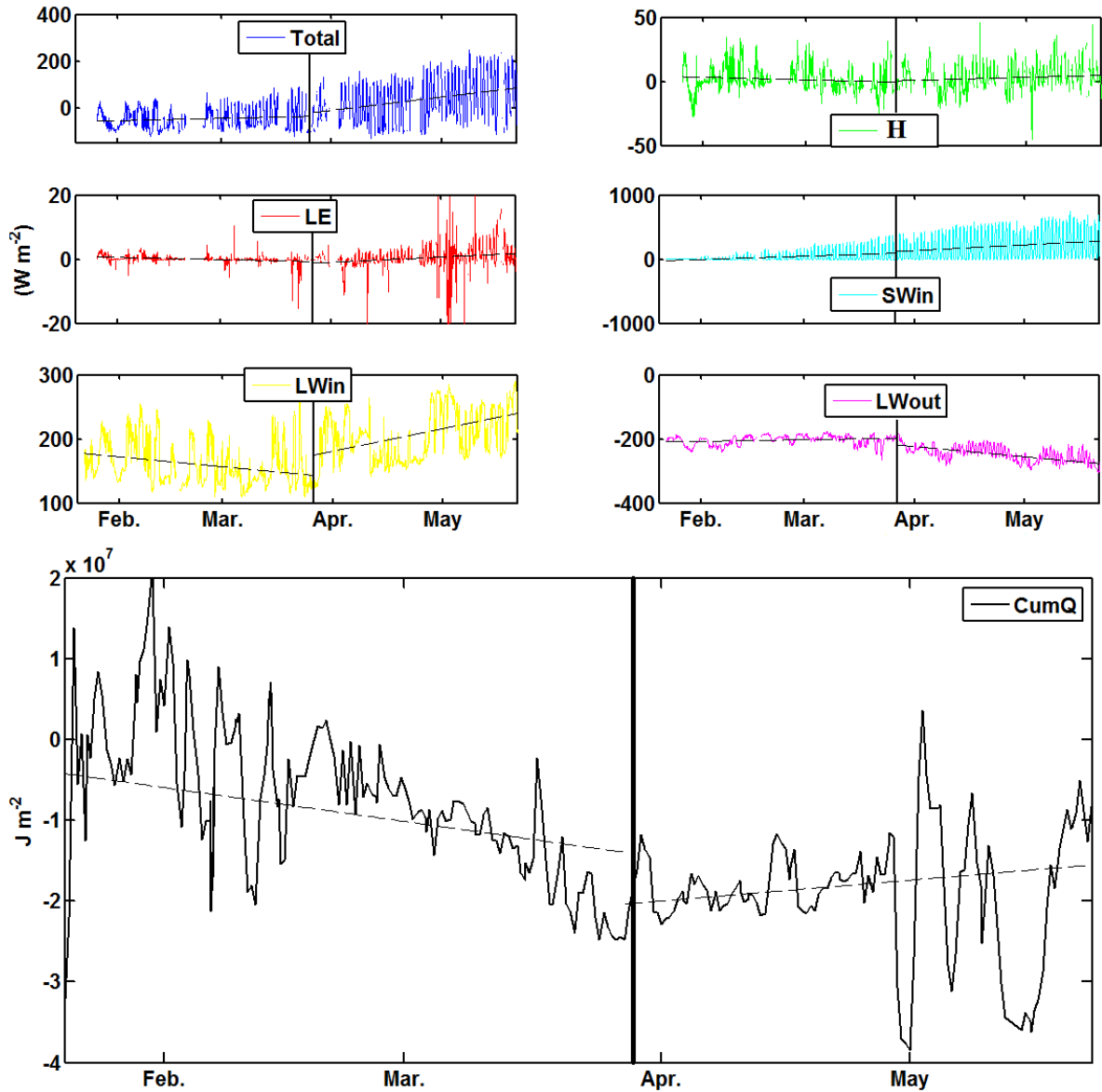


Figure 5.12: Atmospheric fluxes with their tendency before and after 26 March (day 87, shown by vertical black line), blue line shows atmospheric in-situ total flux calculated using the sensible heat flux (in green), the latent heat flux (in red) and the short wave radiation (in cyan). Long wave heat ingoing and outgoing are respectively in yellow and magenta.

Figure 5.12, shows that $CumQ$, which can be an indicator of the total atmospheric flux, is generally similar to the total atmospheric flux. The difference between the in-situ surface atmospheric flux and the estimated flux is due to the limitations of the model and because $CumQ$ is the surface flux under the ice cover, whereas the atmospheric fluxes are measured over the ice. According to Figure 5.12, between 20 January and the end of March-April, the total atmospheric flux (blue line in Figure 5.12) is negative, $CumQ$ decreases and the MLD (Figure 5.10b) deepens. After the first of April, the total atmospheric flux begins to increase, $CumQ$ increases and the MLD shoals.

Figure 5.13a, b and c shows the surface air temperature as well as snow and ice temperatures at different depths between 22 January and 23 May. The descending and ascending trends of the temperature in ice and snow are similar to those of surface air temperature. Diurnal fluctuations of the surface air temperature increase after late March which is due to the growing presence of the sun in the second half of the spring. As shown in Figure 5.13, from the beginning of the sampling until 8 March, the MLD deepens as surface air, snow and ice temperatures decrease. However, the temperatures start to increase gradually after that time while the MLD continues to deepen until 2 April. Therefore, it seems that these temperatures impact the MLD in a delayed manner and not immediately. This is probably related to the insulation effects of the snow and ice, which may lead to the delayed transfer of atmospheric variations to the ocean.

5.3.4 Cross-correlation between ocean fluxes and the MLD at different stations

The cross-correlation function calculated between the MLD and each term in equation 5.22 for the first 60 lags (30 days), is shown in Figure 5.14. The blue line with the circles, red line with squares, green line with diamonds and the line with star markers shows respectively the cumulative value of temporal variation of mass deficit ($Cum(dC_{pres}/dt) = C_{pres}(t) - C_{pres}(t_0)$), surface added buoyancy flux ($CumJ_b$), term II in equation 5.22 which is vertical advection ($Cum(w_{-hc}(\rho_{-hc} - \langle\rho\rangle))$) and term III ($Cum(hc d\rho_{-hc}/dt)$) in equation 5.22. Confidence intervals are calculated at the 95% ($\alpha = 0.05$) level, using the equation of $1.96/\sqrt{n}$ (black dashed lines in Figure 5.14). The cross correlation between the MLD and $Cum(dC_{pres}/dt)$ and $CumJ_b$ show similar trends which are confirmed in Figure 5.6 in which $CumJ_b$ follows the C_{pres} variations. The maximum values of cross-correlation coefficients between the MLD and $Cum(dC_{pres}/dt)$ and $CumJ_b$ (cumulative values of dC_{pres}/dt and MLD) are respectively 0.36 and 0.4 for a lag of approximately 21 days, meaning that the MLD is correlated with $Cum(dC_{pres}/dt)$ and $CumJ_b$ with a temporal delay of 21 days. The delayed cor-

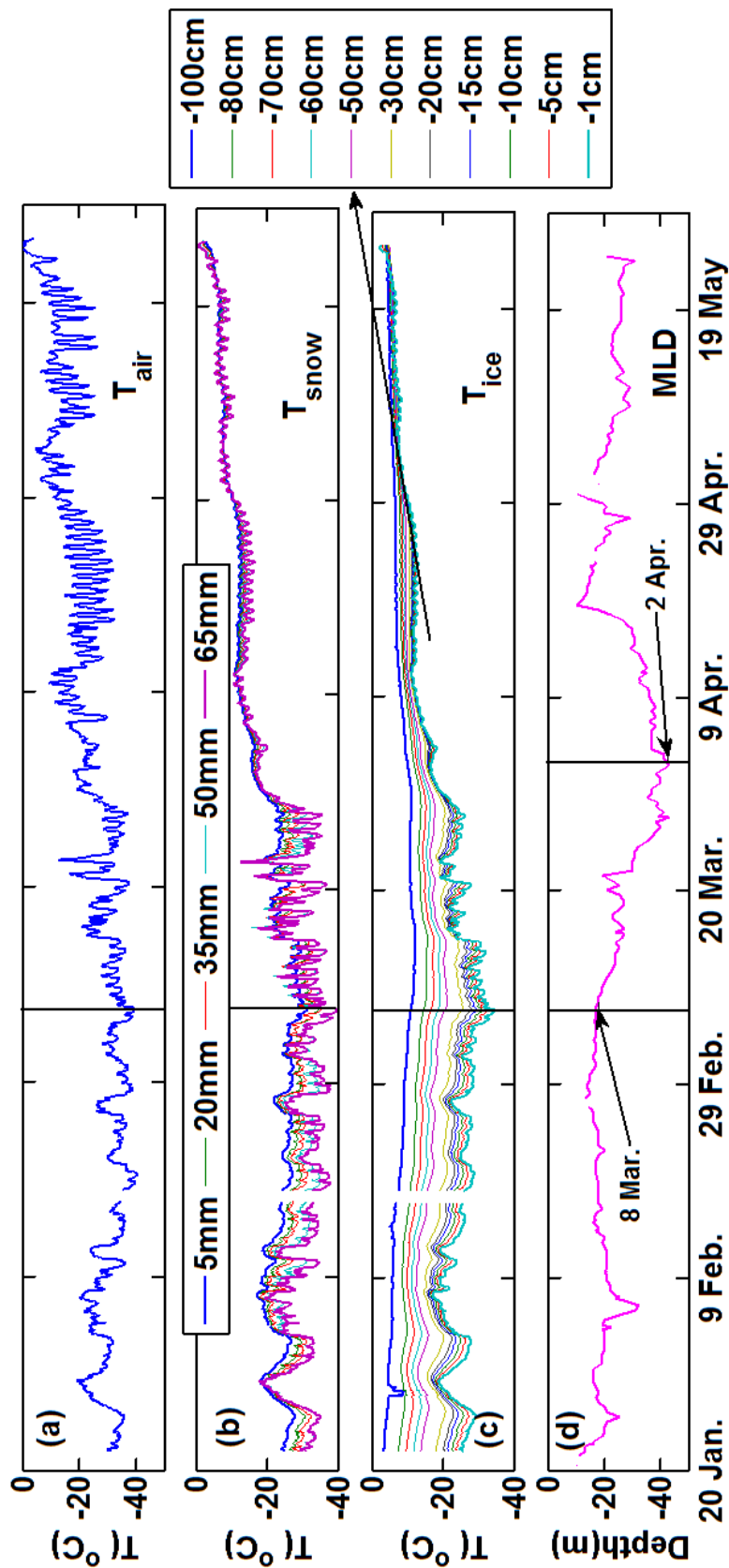


Figure 5.13: (a) Surface air temperature. (b) Snow temperature at different depths (5, 20, 35, 50 and 60 mm). (c) Ice temperature at different depths (100, 80, 70, 60, 50, 30, 20, 15, 10, 5 and 1 cm). (d) The Mixed Layer Depth. The vertical black line identifies the position of 26 March 2004 (day 87).

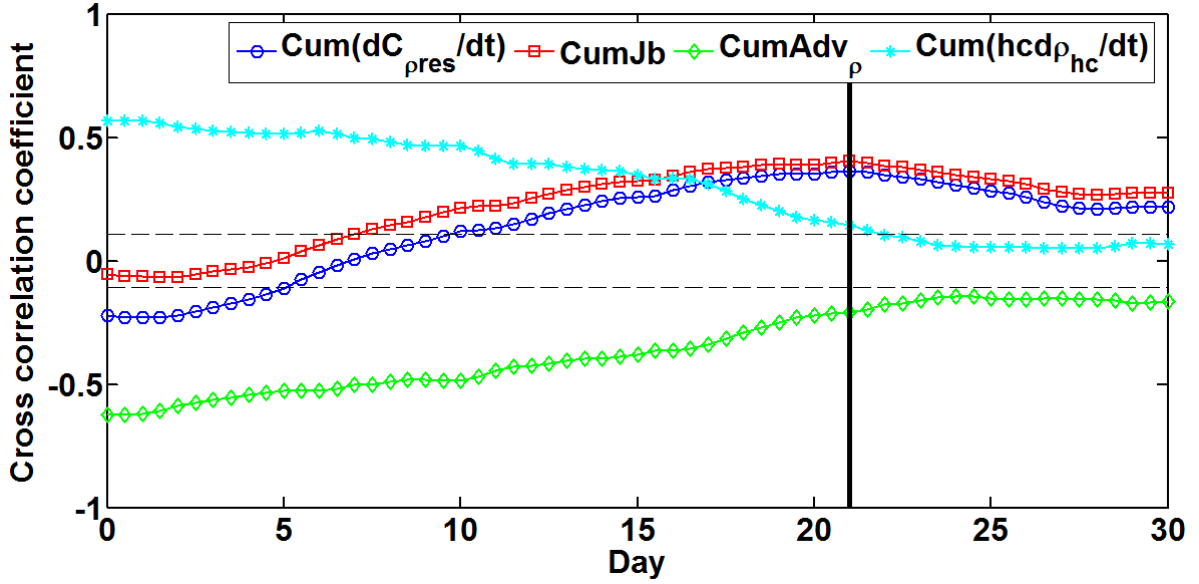


Figure 5.14: Cross-correlation between the *MLD* and different terms: $Cum(dC_{\rho_{pres}}/dt)$ in blue, $CumJ_b$ in red, $Cum(Adv_{\rho_{hc}})$ in green and $Cum(hcd\rho_{hc}/dt)$ in cyan. The number of lags is 60 and the cross-correlations for the lags are shown with circles, squares, diamonds and stars for $Cum(dC_{\rho_{pres}}/dt)$, $CumJ_b$, $Cum(Adv_{\rho_{hc}})$ and $Cum(hcd\rho_{hc}/dt)$, respectively. The dashed black lines are the confidence limits. Vertical black line shows maximum cross-correlation values of cross-correlation coefficients between the *MLD* and $Cum(dC_{\rho_{pres}}/dt)$ and $CumJ_b$ (around 21th day).

relation between the *MLD* and $CumJ_b$ and $Cum(dC_{\rho_{pres}}/dt)$ shows that these factors impact the *MLD* in a delayed manner and not immediately. As shown in Figure 5.14, $Cum(Adv_{\rho_{hc}})$ and $Cum(hcd\rho_{hc}/dt)$ are correlated with the *MLD* without any delay with maximum values of correlation coefficients of -0.63 and 0.57 respectively in the same day. The negative correlation between the *MLD* and $Cum(Adv_{\rho_{hc}})$ (term II in equation 5.22), shows that this term has an inverse effect on the *MLD*. In other words, when $Cum(Adv_{\rho_{hc}})$ decreases (increases) or is downwards (upwards) the *MLD* increases (decreases).

Table 5.3 shows the cross correlation between the *MLD* and each term of equation 5.22, $CumJ_b$, $Cum(dC_{\rho_{pres}}/dt)$, $Cum(Adv_{\rho_{hc}})$ and $Cum(hcd\rho_{hc}/dt)$, at the studied stations. The results of the cross-correlation coefficient calculations between the *MLD* and the different terms in equation 5.22 at different stations, show that in 72% of the cases, the *MLD* and $Cum(dC_{\rho_{pres}}/dt)$ are positively related (+ in Table 5.3) and 50% of the positive relationships are simultaneous (S+ in Table 5.3). Since the mass deficit (Figure 5.1) changes with *MLD* variations, it can be said that $Cum(dC_{\rho_{pres}}/dt) = C_{\rho_{pres}}(t) - C_{\rho_{pres}}(0)$ is an indicator of *MLD* evolution, thus the correlations between the *MLD* and this term are expected. Positive correlations between the *MLD* and $Cum(dC_{\rho_{pres}}/dt)$ show the same relation between the *MLD* and $C_{\rho_{pres}}$ in

Table 5.3: Cross correlation between the *MLD* and the terms in equation 5.22, $CumJ_b$, $Cum(dC_{pres}/dt)$, $Cum(Adv_{\rho_{hc}})$ and $Cum(hcd\rho_{hc}/dt)$, at each station. The blue and red boxes indicate respectively that the parameter is positively (negatively) correlated with the *MLD* with delay (D+ and D-). The green and yellow boxes highlight respectively that the parameter is positively (negatively) correlated with the *MLD* simultaneously (S+ and S-). NS means that correlation is not significant.

Station	$CumJ_b$	$Cum(dC_{pres})/dt$	$Cum(Adv_{\rho_{hc}})$	$Cum(hcd\rho_{hc}/dt)$
CASES	D+	D+	S-	S+
5D	S+	D+	S-	S+
7D	S-	S-	D+	D-
12D	S+	S-	S-	S+
14D	NS	D-	S-	S+
17D	S+	S+	S+	S-
19D	S-	S-	S-	S+
26D	D-	D-	S-	S+
27D	S-	S-	NS	D+
29D	D+	D+	NS	NS
33D	S+	D+	S-	S+
41D	S+	D-	S-	S+
43D	D+	D+	S-	S+
F2	S+	D+	NS	S+
F3	NS	NS	S-	S+
F7	S+	S-	S+	S-
235	S-	S-	S+	S-

Figure 5.6. As the C_{pres} or $Cum(hc d\rho_{hc}/dt)$ decreases the MLD deepens. It should be noted that since the z axis coordinate is upwards the MLD values are negative.

In most cases (58%) the MLD and $CumJ_b$ are positively correlated and in 64% of the positive correlations there is a delay which shows that $CumJ_b$ often does not affect the MLD immediately, but rather takes time for the surface flux to affect the surface layer and MLD . In other words, the surface flux affects the surface layer and its properties after a certain time. Furthermore, between $Cum(Adv_{\rho_{hc}})$ and the MLD , in 73% of the cases there is an immediate negative correlation which shows that vertical advection has negative and simultaneous impact on the MLD . In other words, when $Cum(Adv_{\rho_{hc}})$ decreases (increases) the MLD increases (decreases). The relation between $Cum(hc d\rho_{hc}/dt)$ and the MLD is very similar to the $Cum(Adv_{\rho_{hc}})$ but in an opposite direction. The study of 11 stations (Table 5.1) shows that in 73% of the cases, there were positive correlations between $Cum(hc d\rho_{hc}/dt)$ and the MLD . This term can be seen as an indicator of advection (both horizontal and vertical), because it is related to the temporal variations of the density at the reference depth which can be directly affected by vertical and horizontal advection. It should be noted that in order to calculate a meaningful cross correlation function, a large number of data over a long period is needed. That is why the CASES data are the most reliable station data to perform this test and the difference between the results from other stations could be due to the lack of data or other unknown processes. Additional results for other stations are presented in Appendix C.

5.3.5 Modeling the MLD using a linear and multiple regression method

As mentioned in the previous section, the MLD has considerable correlations with the terms in equation 5.22 such as mass deficit, added surface buoyancy flux, vertical advection and temporal variation of density in the reference depth. We have also shown that the correlation between the MLD and $CumJ_b$ is often with a delay. In the present section, simple and multiple linear regression approaches are employed in order to determine if the MLD can be modeled properly based on the four aforementioned parameters.

For this purpose, a simple linear regression is first considered between the value of the MLD as a scalar dependent variable and the cumulative value of each of the terms (i.e. $CumJ_b$, $Cum(dC_{pres}/dt)$, $Cum(Adv_{\rho_{hc}})$, $Cum(hc d\rho_{hc}/dt)$) in equation 5.22 as an explanatory variable for the CASES fixed station data. The results show that comparing with other terms, $CumJ_b$ fails to model the MLD because as it is shown in Figure 5.15 the value of R^2 between the modeled MLD and observed MLD is the

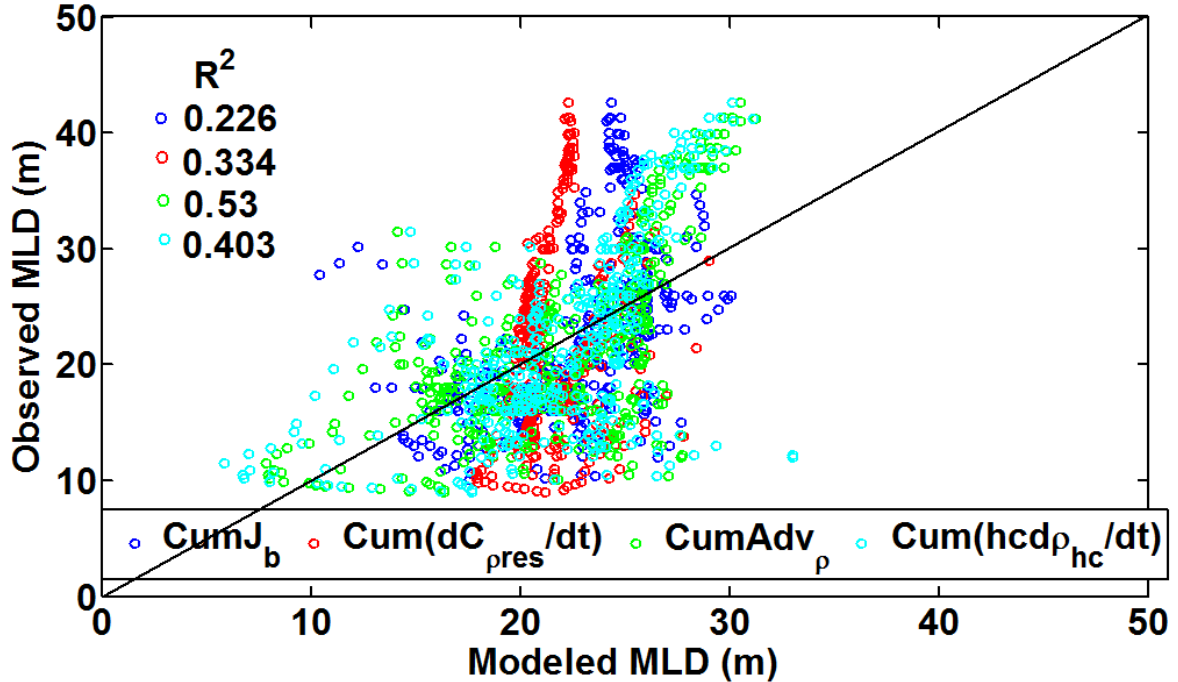


Figure 5.15: Observed MLD s vs. Modeled (linear regression) MLD s using the cumulative value of each term. The blue circles are the MLD s modeled using the value of $CumJ_b$ 21 days prior to MLD s observation as an explanatory variable. The red circles are the modeled MLD s using $Cum(dC_{pres}/dt)$; the green circles are the modeled MLD s using $Cum(Adv_{\rho_{hc}})$; the cyan circles are the modeled MLD s using $Cum(hcd\rho_{hc}/dt)$.

lowest value. In addition to a simple linear regression, a multiple linear regression is done between the MLD and the different terms of equation 5.22. The results of multiple linear regression is shown in Figure 5.16. In agreement with the results of the cross-correlations study (section 5.3.4), Figure 5.16 (red circles) shows that if we consider the delayed-characteristic of the $CumJ_b$ term then this term can model the MLD . It should be noted that in Figure 5.15 (red circles) $CumJ_b$ is considered as the only independent variable to model the MLD . In this figure, the $CumJ_b$ data acquired with a 21 day delay are used to model the MLD . The regression equation for this model is $MLD = -10.439 + 25.747 CumJ_b|_{prior}$ where $CumJ_b|_{prior}$ are $CumJ_b$ data with a 21 day delay. The independent variable (here $CumJ_b$) is said to be useful in predicting the dependent variable (MLD) when the level of significance (labeled with Sig. in the figure) is below 0.05, which here is of the order 10^{-3} .

The same test has been done for each of the terms successively of equation 5.22 to model the MLD . Based on the values of the R^2 illustrated in Figure 5.15, it can be seen that $Cum(Adv_{\rho_{hc}})$ (green circles) and $Cum(hcd\rho_{hc}/dt)$ (cyan circles) can better model the MLD compared to the other terms.

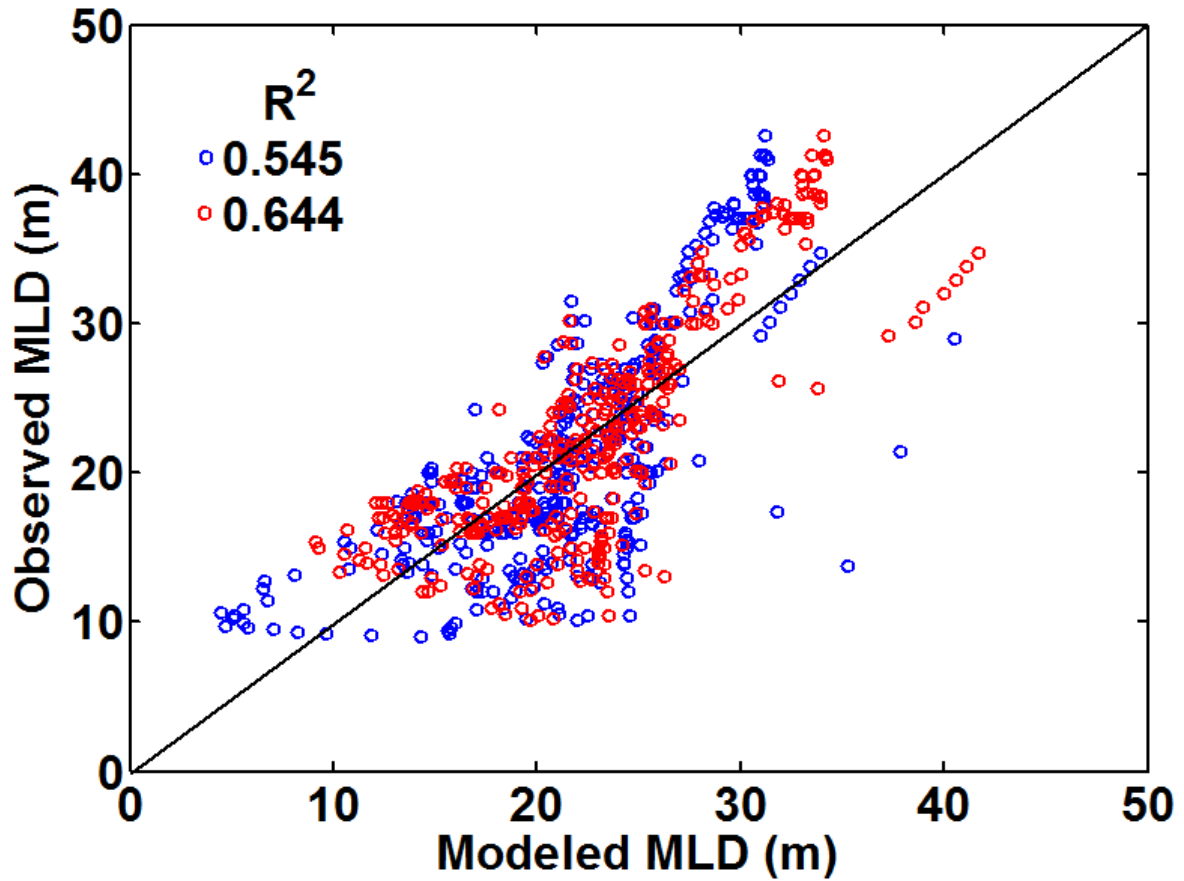


Figure 5.16: Observed $MLDs$ vs. Modeled (multiple linear regression) $MLDs$. Blue circles are the modeled $MLDs$ using the sum of $Cum(dC_{pres}/dt)$, $Cum(Adv_{\rho_{hc}})$ and $Cum(hc d\rho_{-hc}/dt)$; the red circles are the modeled $MLDs$ using the sum of $Cum J_b$ (with a delay of minus 21 days), $Cum(dC_{pres}/dt)$, $Cum(Adv_{\rho_{hc}})$ and $Cum(hc d\rho_{-hc}/dt)$.

In addition to the simple linear regressions, backward multiple linear regression analyses are also performed. The idea here is to find if a combination of the four terms that can properly model the MLD . The results show that by keeping the $CumJ_b$ in any combination of the terms, the multiple regressions will fail. Figure 5.16 shows that a combination of $Cum(Adv_{\rho_{hc}})$, $Cum(hc d\rho_{-hc}/dt)$ and $Cum(dC_{pres}/dt)$, can better model the MLD . The regression is accomplished by a backward selection method, which means the model starts with a full model and then in each step eliminates the variables which do not significantly enter the regression equation.

By employing the same approach as in the simple regression, we can consider the earlier-characteristic of the $CumJ_b$ term. Figure 5.16 (blue circles), shows the MLD modeled with a combination of modified $Cum(Adv_{\rho_{hc}})$, $Cum(hc d\rho_{-hc}/dt)$ and $Cum(dC_{pres}/dt)$ versus original MLD values. Comparing R^2 values in Figure 5.15 and Figure 5.16, it is obvious that the three term combination regression can model the MLD better than the unaccompanied regression models. Figure 5.16 (red circles), suggests that the combination of modified $Cum(Adv_{\rho_{hc}})$, $Cum(hc d\rho_{-hc}/dt)$ and $Cum(dC_{pres}/dt)$ and the earlier values of $CumJ_b$ (prior the 20th day) gives the best estimation of the MLD compared with any other combination of parameters (considering $R^2 = 0.644$ which is the highest between all the models). The equation of the multiple linear regression for the Figure 5.16 (red circles) is $-0.53Cum(hc d\rho_{-hc}/dt) - 0.37Cum(dC_{pres}/dt) + 0.97Cum(Adv_{\rho_{hc}}) + 11.7CumJ_b|_{prior} - 43.53 = MLD_{model}$. It should be noted that these results are in agreement with those emerging from the cross-correlations study confirming the connection between the MLD and the surface buoyancy flux and the motions at the bottom of the surface layer.

5.3.6 Ice thickness estimation and the MLD

As it is already explained in section 5.2.2, the ice thickness is estimated using salt fluxes computed from CTD data sampled during the CASES program from the fixed station in Franklin Bay. The salt mass content (equation 5.47) is shown in Figure 5.17a. As shown in this figure, the salt mass content gradually increases between 24 February and 27 March and is almost constant with small fluctuations between 27 March and 22 April. It then decreases suddenly between 22 April and 28 April, after which it generally increases. Figure 5.17b also shows the salt flux which is the temporal differential of the salt mass content and is calculated using equation 5.48. Figure 5.17c shows the ice growth velocity calculated using k_{eff} as is explained in section 5.2.2.

The first measured ice thickness is placed at the beginning of period. Therefore the ice thickness at each time is obtained using the cumulative sum of the ice growth

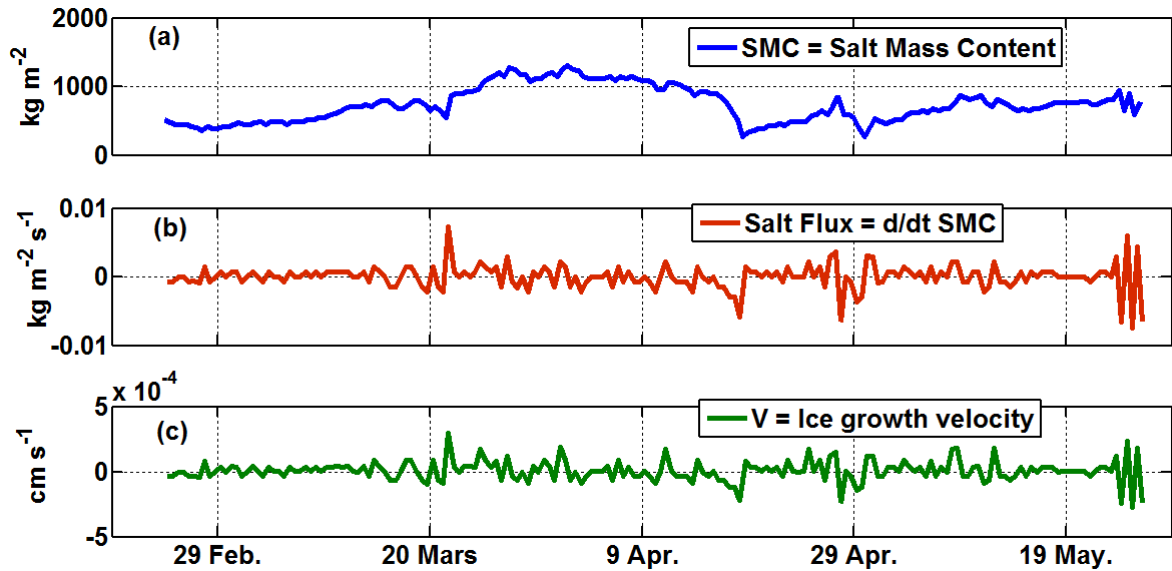


Figure 5.17: Upper panel: salt mass content; middle panel: salt flux using the time variation of the salt mass content; lower panel: ice growth velocity calculated by the [Cox and Weeks \(1988\)](#) method.

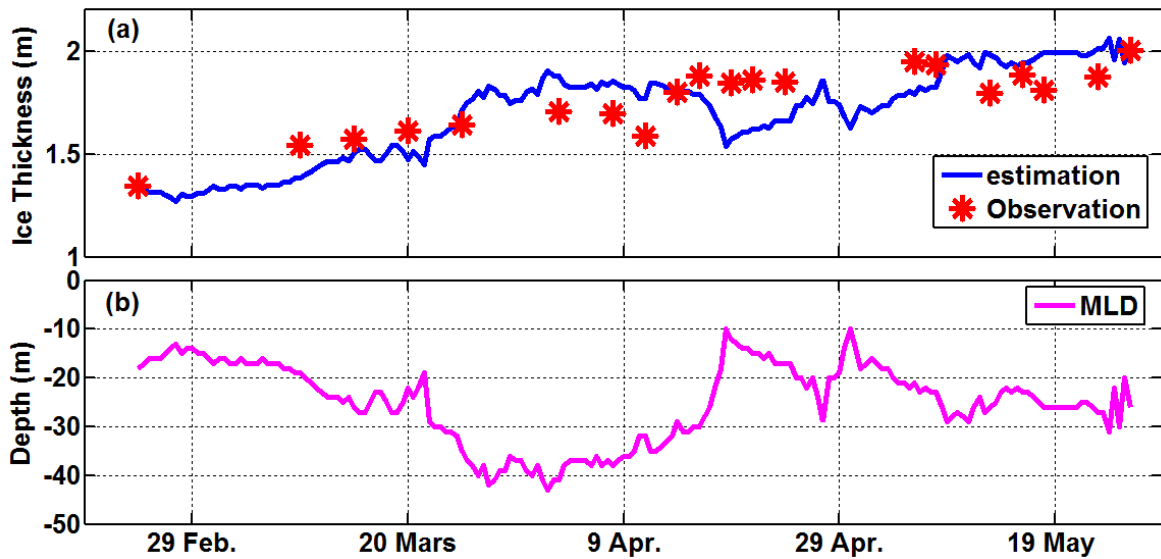


Figure 5.18: Upper panel: comparison between the estimated ice thickness using the [Cox and Weeks \(1988\)](#) method and observed values from the literature. Lower panel: corresponding *MLD*.

velocity. Figure 5.17 and Figure 5.18 show that with increasing *SMC* (Figure 5.17a) the estimated ice thickness and the *MLD* also increase and vice versa. Figure 5.18a shows the estimated and observed ice thickness: the estimated ice thickness values computed using Cox and Weeks (1988) method are very close to the measured ice thickness values. The mean absolute error between estimated and measured ice thickness is 0.16 m. Since the ice thickness measurement is complicated these results show that it is possible to estimate the ice thickness based on oceanic CTD profiles only.

5.3.7 Blooming and the *MLD*

In this section the temporal variation of the *Chl a* concentration in sea ice and its relation with ice thickness and the *MLD* during 2003-2004 is investigated. The photosynthetically active radiation (PAR) showed in Figure 5.19a increased gradually from the beginning of the sampling following the sunlight period which increased from 8.3 h on 24 February to 24 h after 3 May for the rest of the sampling. Following the sunlight period the air temperature increased from -35 to 1.3°C during the same period. The surface water salinity remained between 28.6 and 31.2 from the beginning of the sampling till 28 May. After 28 May the salinity decreased to 3.4 on 20 June (see Figure 5.19c). As shown in Figure 5.19d, the ice thickness increases from 1.34 m on 24 February to 2 m on 26 May then it decreases and reaches to 1.55 m on 20 June which confirms the salinity variations in Figure 5.19c. At the beginning of March, the increased irradiance (PAR at Figure 5.19a) allows phytoplankton to grow, which is evident by the increase in *Chl a* concentration at the bottom of the sea ice. At the beginning of the sampling (late February) the *Chl a* concentration in the sea ice at the fixed station during the CASES program (2003-2004) was very low (0.015 mg m⁻²) while before the bloom period which is defined by a fast increase in *Chl a* concentration (from 3 April to 23 May) the concentration was lower than 2.035 mg m⁻² as shown in Figure 5.19e. The ice bottom *Chl a* concentration began to increase at the beginning of April with the seasonal increase in air temperature (Figure 5.19b). Then it reached its maximum of 27.82 mg m⁻² on 23 May. After this date, the *Chl a* concentration decreased until it reached near zero (1.44 mg m⁻²) on 21 June which coincides with the start of the ice melt (Figure 5.19d and e). As shown in Figure 5.19f, the *MLD* deepens from the beginning of the sampling period till it reaches its maximum (43 m) on 2 April, after which it decreases with some minor fluctuations. It should be noted that there was no CTD sampling at the fixed station in June. As shown in Figure 5.19d and f the first local maximum of bottom ice *Chl a* concentration on 3 May occurs about 1 month after the maximum value of the *MLD* on 2 April and 20 days later we witnessed the maximum value of *Chl a* on 23 May. As shown in Figure 5.19d and e, the *Chl a* concentration decreases rapidly after this date when the ice thickness declined during the melt period

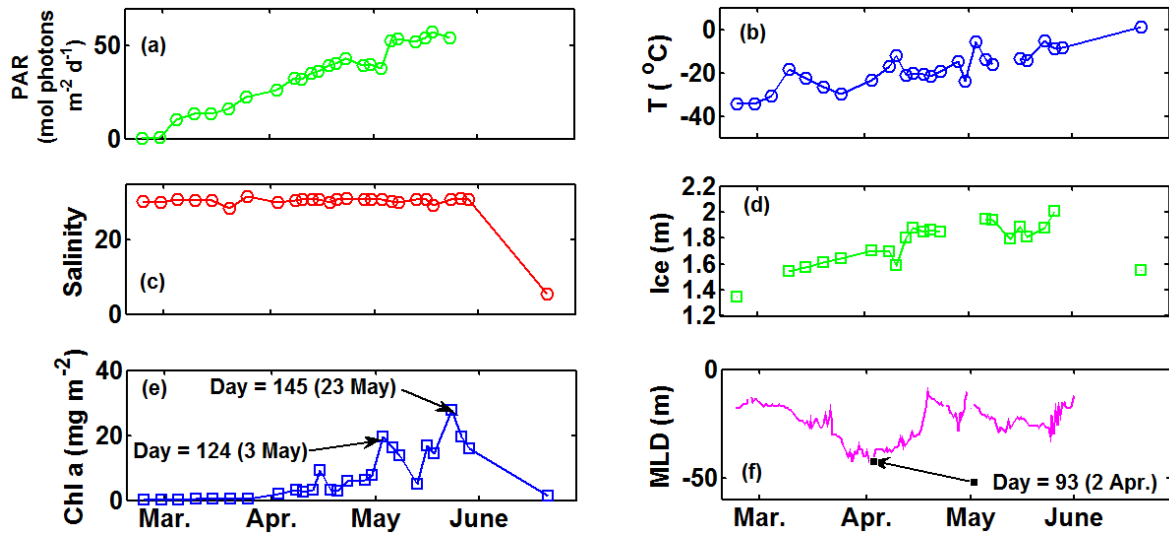


Figure 5.19: Temporal variation of (a) the PAR, (b) the air temperature, (c) the surface water salinity, (d) the ice thickness, (e) the chlorophyll a (*Chl a*) concentration and (f) the *MLD* at the CASES fixed station.

following an increase in air temperature. The results show that the increase of *Chl a* is followed by *MLD* deepening and about one month after MLD_{max} , the *Chl a* reaches its maximum value. The ice thickness increased until the end of May despite an increase in air temperature because the water temperature was still sufficiently cold for ice freezing. On the other hand, the increase of *Chl a* (bloom period) indicates that light passes through the ice, increasing the heat absorbed by the surface layer. The *MLD* decreases after reaching its maximum at the beginning of the blooming period.

Figure 5.20 shows the subsurface *Chl a* concentration, ice thickness and the *MLD* at the stations listed in Table 5.1 during the CFL program (2007-2008). Blooming starts in early April when the ice *Chl a* concentration starts increasing and reaches its maximum on 13 May as shown in the figure. The *MLD* deepened until it reached its local maximum on 11 April and its second maximum occurred on 4 May. Similar to what was noted for the CASES data, Figure 5.20 shows that the $Chl a_{max}$ occurs about a month after the first MLD_{max} and about 9 days after second MLD_{max} . This confirms the previous results from the CASES study that there is a delay between MLD_{max} and $Chl a_{max}$. The difference between the CASES and CFL results is because the CFL sampling was not in the same location and was performed from different station types (drift and landfast ice stations).

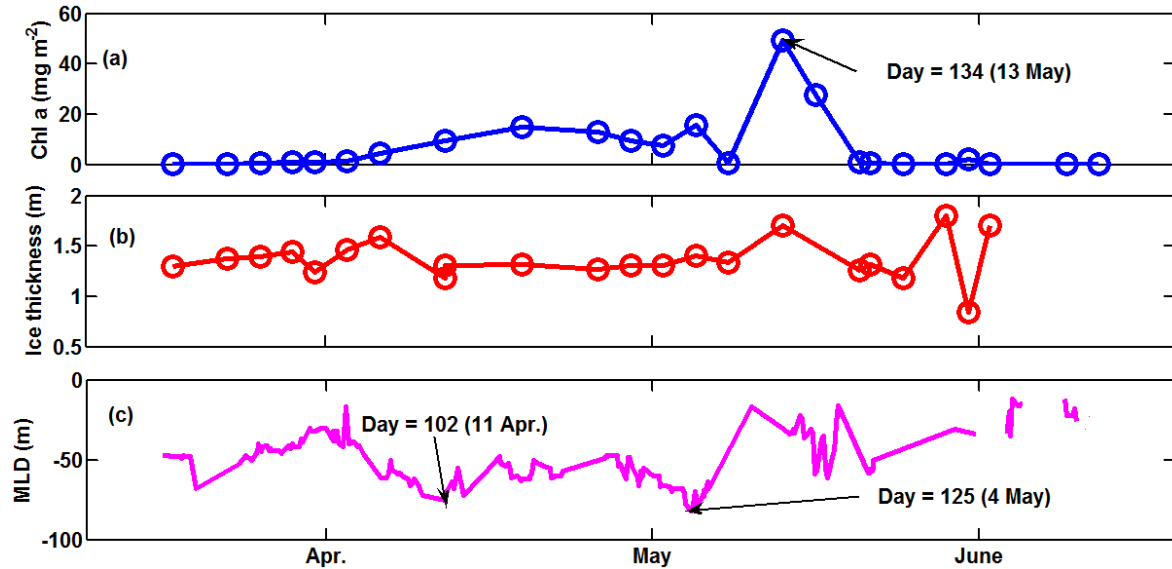


Figure 5.20: Temporal variation of the (a) chlorophyll a (*Chl a*) concentrations, (b) ice thickness and (c) *MLD* at the CFL stations listed in Table 5.1.

5.3.8 Two unusual cases

In this section we analyze two cases (a period of CASES 2003-2004 and station 19D of CFL) in which the relationship between the *MLD* and fluxes deviates from what we already reported in the previous sections. Figure 5.6 shows that between 11 and 24 December 2003, the values of $CumJ_b$ decrease towards a larger negative value while the *MLD* shoals, which is not consistent with the previous results, i.e. when $CumJ_b$ or estimated buoyancy flux under the ice cover decreases then the *MLD* deepens.

Tremblay et al. (2008) suggested that a cyclonic eddy occurred during December 2003, during the CASES program. This suggestion is associated with the rise of isohalines near the surface as can normally be observed during the passage of a cyclonic eddy surface (see Figure 5.21). However, this type of observation can also be related to an ice edge upwelling due to the surface winds (Mundy et al., 2009). As shown in Figure 5.21, the rise of isohalines to the surface is associated with the presence of upwelling favorable winds from the east along the ice edge. After December 24, the winds are reversed and, at the same time, a sinking of the isohalines can be observed within the water column. There is an horizontal transport towards the ship, under the ice, associated with upwelling. As previously mentioned, in our model horizontal advection is neglected but upwelling or downwelling completely change the water mass. If the model assumptions are not verified, this can lead to unexpected or inconsistent results.

Another example in which the model results are not as expected comes from sta-

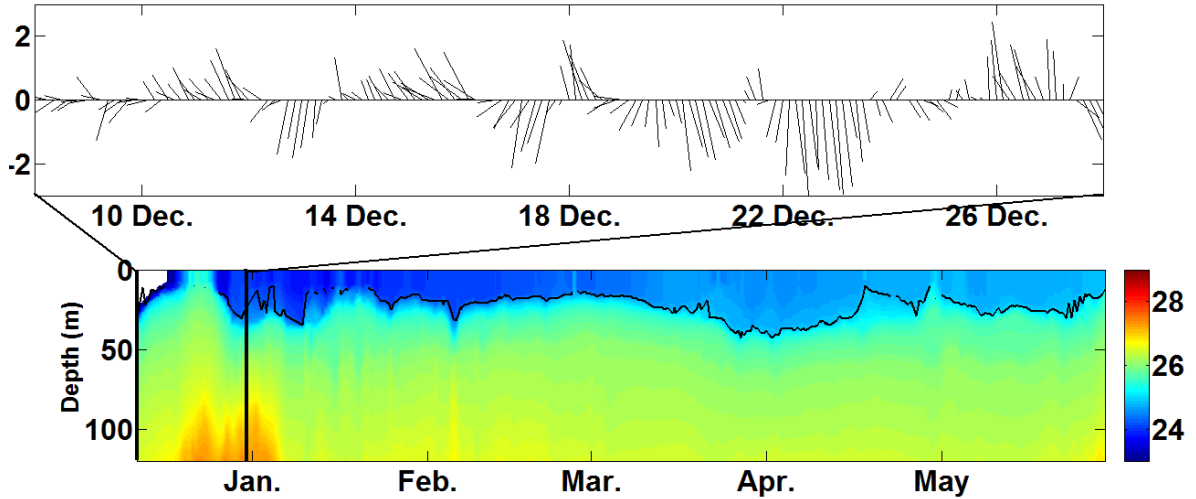


Figure 5.21: Upper panel: wind speed (m s^{-1}) and direction in southern Amundsen Gulf; north is upwards. The wind data are from the NARR reanalysis. Bottom panel: density contours at the CASES fixed station.

tion 19D which was the longest CFL drift station visited between 24 January and 14 February 2008 (97 CTD profiles). As shown in Figure 5.22, $CumJ_b$ has an ascending trend while $CumJ_m$ and the MLD have descending trends, however $Cum(hc d\rho_{-hc}/dt)$ and $Cum(Adv_{\rho_{hc}})$ are directly and inversely related with the MLD respectively. Since $CumJ_b$ is the under ice surface flux which can be an indicator of the atmospheric flux, it is assumed that when it has an ascending trend the MLD also has an ascending trend (shallow) however, in the figure the opposite trend is observed and the MLD deepens (descending trend).

To understand the occasional incompatibility between oceanic fluxes, such as under ice surface flux and the MLD evolution it is useful to verify the vertical evolution of physical properties. According to Barrette (2012) and as it is obvious in Figure 5.23, two eddies were observed during the sampling at station 19D. An anticyclonic eddy passed on 26 January and a cyclonic eddy on 7 February which both resulting in to horizontal advection. Due to these two eddies, the hypothesis of the LP method is not respected. But what is interesting in the results of this station is the relation between the vertical advection $Cum(Adv_{\rho_{hc}})$ and $Cum(hc d\rho_{-hc}/dt)$ and the MLD variations. According to Figure 5.24 (which shows cross-correlation coefficient between MLD and cumulative value of different terms in equation 5.22) and also Figure 5.24, the cumulative values of term II $Cum(Adv_{\rho_{hc}})$ and III $Cum(hc d\rho_{-hc}/dt)$ have respectively negative and positive correlations with the MLD . This means that terms II and III affect the MLD instantly, which confirms what has been mentioned in section 5.3.4. The negative correlation between $CumJ_b$ and the MLD is not expected and is likely related to the passing of two eddies during our sampling period.

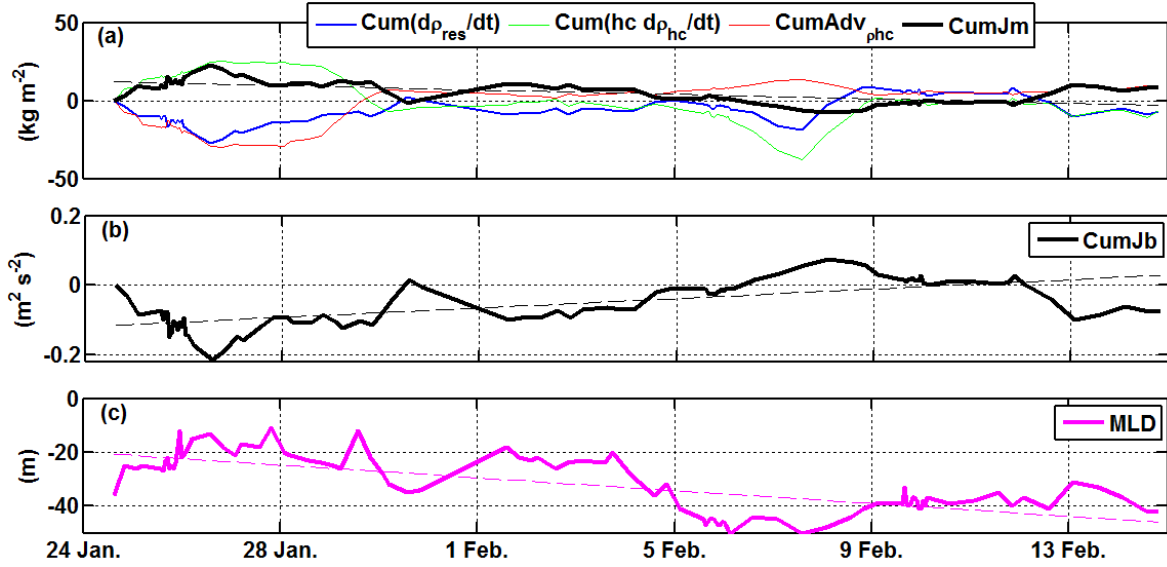


Figure 5.22: Temporal variation of (a) the cumulative value of $Cum(dC_{pres}/dt)$, $Cum(hc d\rho_{hc}/dt)$, $Cum(Adv_{phc})$ and $CumJ_m$. (b) Temporal variation of $CumJ_b$ and (c) of the MLD at the drift station 2008-19D during CFL. The dashed line in each panel is the linear tendency of each curve.

As mentioned in this section some phenomena such as upwelling or eddies which cause horizontal advectons do not respect the assumptions of the LP method in which the horizontal advection is assumed to be negligible. When there is a know horizontal advection, as in upwelling and eddies, it is possible to modify the LP model to take this advection into account. This can only be done a posteriori.

5.4 Summary

In this chapter, I analyzed the time evolution of the mass, salinity and oceanic heat budgets in the layer between the surface and a chosen reference depth hc . I used the layer approach of Emery (1976), modified by Prieur et al. (2010) for the mass budget. The cumulative buoyancy flux or $CumJ_b$ calculated with this method was compared with the one obtained by the method of Gill (1982) (detailed in Nerheim and Stigebrandt 2006). Note that in the latter method, they don't consider the vertical advection. The difference between these two approaches is found to be important, revealing that the vertical advection has important effects on the mixed layer mass budget.

The relationship between the oceanic fluxes and the MLD was analyzed. The results show that the surface buoyancy fluxes under the ice, which can be regarded as an indicator of the atmospheric flux in ice-free regions, are directly related to the MLD , but

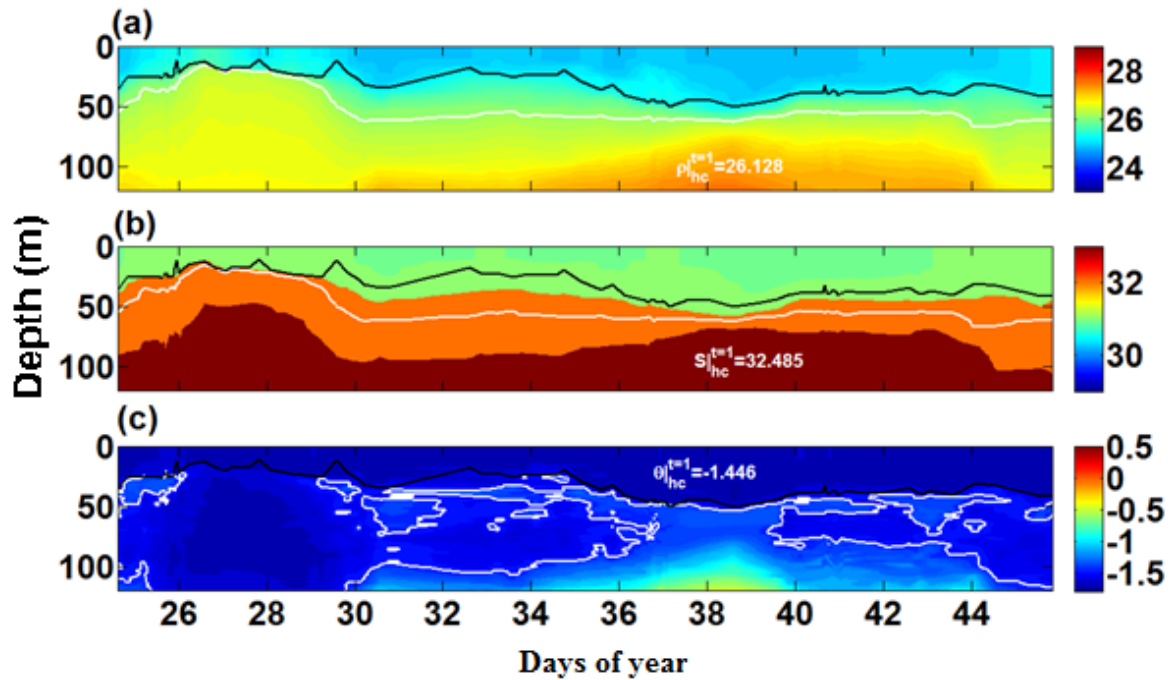


Figure 5.23: (a), (b) and (c) are the contours of density, salinity and temperature, respectively, at the drift station 2008-19D during CFL. The white lines are the density, salinity and temperature of the reference depth ($hc = -57$ m) and the black line in each panel is the *MLD* for the same period.

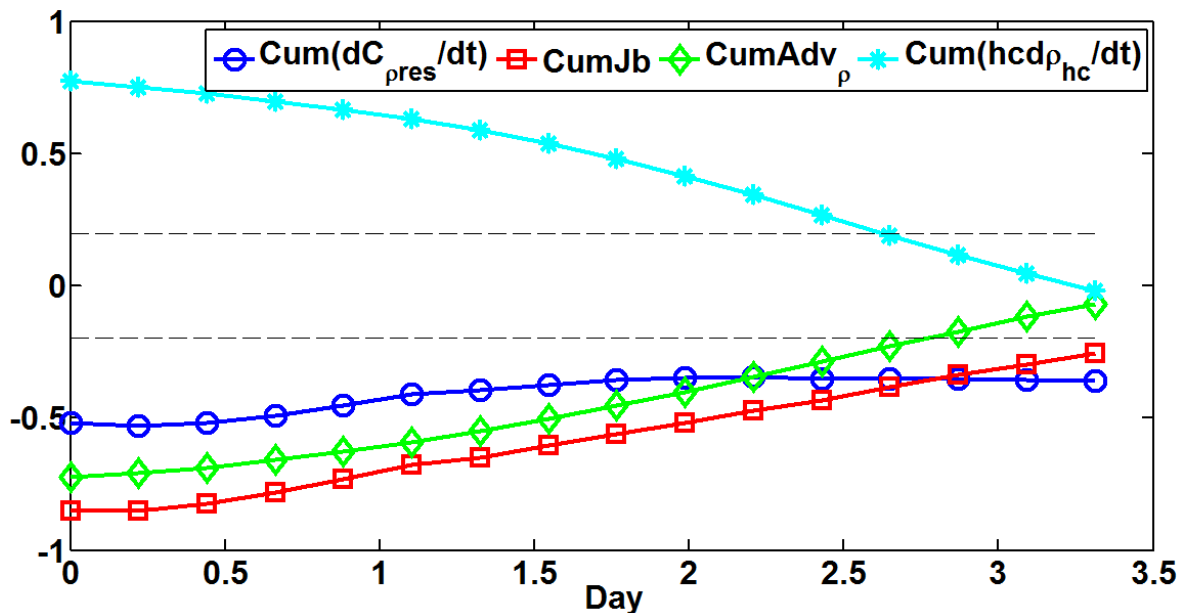


Figure 5.24: Cross-correlation at drift station 2008-19D between the *MLD* and $Cum(dC_{pres}/dt)$ in blue, $CumJ_b$ in red, $Cum(Adv_{\rho_{hc}})$ in green and $Cum(hc d\rho_{hc}/dt)$ in cyan. The number of lags is 15 and the cross-correlations for the lags are shown with circles, squares, diamonds and stars respectively for $Cum(dC_{pres}/dt)$, $CumJ_b$, $Cum(Adv_{\rho_{hc}})$ and $Cum(hc d\rho_{hc}/dt)$. The dashed black lines are the confidence limits.

with a delay of approximately 21 days for the Franklin Bay region. This delay is the time it takes for the surface buoyancy fluxes to be redistributed over the mixed layer. This means that a decreasing (increasing) trend in the ice-ocean fluxes leads to deepening (shoaling) of the *MLD* but with a delay. The ice thickness is also estimated based on the approach of [Cox and Weeks \(1988\)](#), using CTD profiles. The calculated ice thickness and the thickness estimated with our method are then compared with observations during CASES. The results show a very good agreement between the estimated and measured ones. Moreover, the analysis of the under ice *Chla* concentration reveals that blooming began just after the *MLD* reached its maximum value. The maximum concentration of *Chla* occurred approximately one month after the *MLD_{max}*. The starting date of the bloom was used as an indicator revealing when the light started to penetrate through the ice, suggesting that heat also began to reach the surface oceanic layer. This explained why both the *MLD* and the ice thickness kept increasing after the atmospheric warming had begun.

CHAPTER 6

SUMMARY AND CONCLUSIONS

The mixed layer is the oceanic surface layer where the density is almost uniform due to the high mixing initiated by air-sea exchanges of momentum, heat and freshwater. The mixed layer depth (*MLD*) is a particularly important parameter because it affects biological productivity and controls the CO₂ exchange with the atmosphere. The present thesis is an attempt to improve our understanding of the temporal evolution and spatial distribution of the mixed layer depth in the southern Beaufort Sea and the Amundsen Gulf. Despite the fact that this study region plays an important role in the Arctic dynamics, circulation and ecology, very little is known about the physical processes in the region. The importance of this study lies in the fact that it benefited from the recent and unique winter data sets collected during the CASES (winter of 2003-2004) and CFL (winter of 2007-2008) programs, as well as the seasonal observations from eight ArcticNet cruises (2002 to 2009) and the Malina early summer cruise in 2009. In the course of this study, a number of statistical techniques were employed to define the mixed layer depth in a set of subregions and to compare their spatial distributions and temporal evolutions. These analyses present, for the first time, a comprehensive picture of the seasonal and interannual evolution of the mixed layer in the southern Beaufort Sea.

The thesis was organized around three objectives: (1) to choose an appropriate method to estimate the *MLD* in the study region, (2) to study the spatial distribution and temporal evolution of the *MLD* in different subregions of the southern Beaufort Sea and Amundsen Gulf, and (3) to identify the major contributors to the mixed layer mass budget in Amundsen Gulf by calculating the under-ice surface fluxes and the vertical advection at the bottom of the mixed layer. This led me to propose a new method to estimate ice thickness using only vertical density profiles.

MLD estimation methods The Arctic Ocean is strongly stratified and the salinity controls the density distribution. This is why I needed a *MLD* estimation method adapted to the Canadian Arctic Ocean. The potential density profile was used to calculate the *MLDs* and the most widely used methods were tested. I found that a modified version of Holte and Talley (2009) method is the most appropriate method for this region, with a modified Thomson and Fine (2003) method a close second. However, my analysis suggests that, as elsewhere in the world oceans, no universal method and no single threshold can be used to estimate the *MLD* without errors.

Spatial distribution and temporal evolution of the MLD In order to investigate the spatial distribution of the *MLD*, the study region was divided into four subregions: Amundsen, Mouth, Beaufort and Franklin. Each subregion was further divided into *inshore* (depths < 200 m) and *offshore* (depth > 200 m). The comparison between inshore and offshore *MLDs* revealed that offshore *MLDs* were deeper than inshore *MLDs* in fall, winter and spring. During summer the inshore and offshore *MLDs* were comparable. The result of the seasonal comparisons between regions showed that the *MLDs* were generally comparable if the comparisons were restricted to the same subregion and to the same season, but the largest *MLDs* were observed in the Amundsen and Mouth subregions. The seasonal analyses demonstrated that in all the subregions the mean *MLDs* and the most frequent *MLDs* start deepening in late summer and continue to deepen until they reach their maximum in spring. Interannual *MLD* comparisons between CASES (2003-2004) and CFL (2007-2008) showed that they are significantly different in fall, winter and spring while they were comparable in summer. The monthly comparison between these two yearly series demonstrated that all *MLDs* were significantly deeper during the CFL, except for the months of June and July. The deepest mean value of the *MLD* was observed in April in both time series. The interannual comparison, all subregions combined, between the falls of 2002, 2003, 2006 and 2007 showed that the mean *MLDs* were significantly larger in fall 2007 than in all the other years, and that the most frequent *MLDs* were also consistently larger. The deep *MLDs* in 2007-2008 were due to the coastal upwelling that occurred in the fall of 2007 and its effects remained observable until the next spring. The use of probability density functions enabled me to establish two very important results. Firstly, the majority the probability density functions are of the unimodal type, showing a single, preferred *MLD* depth range for each region and for each season. The most interesting result of this chapter was the systematic differences between the mean *MLD* and the most probable *MLD*. In fact, the mean *MLD* in each region or season was rarely observed, showing the importance of always calculating the probability density function. This difference is related to the patchiness of the surface ice distribution as alternating ice-covered and ice-free regions, polynyas in winter and ice patches in summer, are found all year round.

Oceanic and atmospheric fluxes and their effects on the *MLD* We analyzed the mass budget of the mixed layer in Franklin Bay between December 2003 and June 2004, using a method developed by Prieur et al. (2010). This method is a modified version of the heat budget approach of Emery (1976). The only assumption needed was that there was no non-divergent lateral advection. It was found that the vertical advection at the base of the mixed layer immediately affects the *MLD* by continuity. On the other hand, the mixed layer needs time to integrate the surface fluxes. I showed that it takes approximately 21 days, in Franklin Bay, for the mixed layer to assimilate the surface fluxes. Moreover, a multiple linear regression suggest that the combination of $Cum(Adv_{\rho_{hc}})$, $Cum(hc d\rho_{hc}/dt)$, $Cum(dC_{pres}/dt)$ and $CumJ_b$ (with a delay of 21 days) gives a better estimation of the *MLD* ($R^2 = 0.644$) than any other combination of parameters.

One of the most interesting results of this chapter is that this method can be used to estimate the ice growth rate and it only needs an initial ice thickness value to calculate the absolute ice thickness. The beauty of the LP method is that it is possible to follow the time evolution of the mixed layer mass budget and to estimate the ice thickness using only vertical density profiles from moored instruments. The time evolution of the *MLD* of a water mass can also be estimated by the same method using Lagrangian profilers. Finally, the analysis of the under ice *Chl a* concentrations demonstrated that the starting date of the bloom can be used as an indicator of when the light starts to penetrate through the ice and begins to warm the surface layer. Since there was no CTD data available for the first 10 m of the water column, this event enabled me to explain why both the *MLD* and the ice thickness kept increasing after the atmospheric warming had begun: the near-surface water will remain cold enough ($< 0^\circ C$) to support ice growth and salt rejection until heat reaches through the ice to begin the water warm-up process.

Outlook A next obvious step would be to modify the LP method to include, a posteriori, the horizontal advection produced by eddies and upwellings, coastal or ice-edge, as these processes are well known. However, the most important application of our method is that it is now possible to develop a year-long mixed layer model for the Amundsen Gulf (or nearby regions). The mixed layer evolution can be modeled (and analyzed) using the original LP approach during the ice-free season and using my approach during the ice-covered season. My approach also enables us to produce an inexpensive estimate of the ice thickness during all winter.

I showed that the most probable mixed layer depth produced the probability density function approach was a much better estimator of the mixed layer depth than the simple

arithmetic mean. A further analysis is needed to determine if a single known probability density function could be used to describe the mixed layer in this region or in the oceans general. A better estimate of the seasonal mixed layer depth would also improve greatly the biological production models.

REFERENCES

- Aagaard, K. (1981). On the deep circulation in the Arctic Ocean. *Deep-Sea Research*, 28(3):251–268.
- Aagaard, K. and Carmack, E. C. (1994). The Arctic Ocean and climate: A Perspective. In Johannessen, O. M., Muench, R. D., and Overland, J. E., editors, *The Polar oceans and their role in shaping the global environment*, The Nansen Centennial Volume, Geophysical Monograph Series 85, pages 5–20, Washington, D.C. American Geophysical Union.
- Aagaard, K., Coachman, L. K., and Carmack, E. C. (1981). On the halocline of the Arctic Ocean. *Deep-Sea Research*, 28(6):529–545.
- Alexander, M. A., Timlin, M. S., and Scott, J. D. (2001). Winter-to-winter recurrence of sea surface temperature, salinity and mixed layer depth anomalies. *Progress in Oceanography*, 49(1):41–61.
- Arrigo, K. R. and VanDijken, G. L. (2004). Annual cycles of sea ice and phytoplankton in Cape Bathurst polynya, southeastern Beaufort Sea, Canadian Arctic. *Geophysical Research Letters*, 31(8):L08304.
- Barber, D. G. and Hanesiak, J. M. (2004). Meteorological forcing of sea Ice concentration in the southern Beaufort Sea over the period 1979 to 2000. *Journal of Geophysical Research*, 109:1–16, doi:10.1029/2003JC002027.
- Barrette, J. (2012). Inventaire et caractérisation des tourbillons marins observés dans le golfe d’Amundsen au cours des programmes CASES et CFL. Master’s thesis, Institut National de la Recherche Scientifique, Centre eau, terre et environnement, Québec (Qc).
- Bendat, J. S. and Piersol, A. G. (2011). *Random data: analysis and measurement procedures*. John Wiley & Sons, New York, 604 p.
- Caniaux, G. and Planton, S. (1998). A three-dimensional ocean mesoscale simulation using data from the SEMAPHORE experiment: Mixed layer heat budget. *Journal of Geophysical Research*, 103(C11):25081–25099.

- Carmack, E. C. and Kulikov, E. A. (1998). Wind-forced upwelling and internal Kelvin wave generation in Mackenzie Canyon, Beaufort Sea. *Journal of Geophysical Research-Oceans*, 103(C9):18447–18458.
- Carmack, E. C. and Macdonald, R. W. (2002). Oceanography of the Canadian Shelf of the Beaufort Sea: A setting for marine life. *Arctic*, 55(supp 1):29–45.
- Carmack, E. C., Macdonald, R. W., and Papadakis, J. E. (1989). Water mass structure and boundaries in the Mackenzie shelf estuary. *Journal of Geophysical Research*, 94(C12):18043–18055.
- Chaigneau, A., Morrow, R. A., and Rintoul, S. R. (2004). Seasonal and interannual evolution of the mixed layer in the Antarctic Zone south of Tasmania. *Deep-Sea Research Part I*, 51(12):2047–2072.
- Christensen, M. K. and Pringle, J. M. (2012). The frequency and cause of shallow winter mixed layers in the Gulf of Maine. *Journal of Geophysical Research-Oceans*, 117.
- Coachman, L. K., Aagaard, K., and Tripp, R. B. (1975). *Bering Strait: the regional physical oceanography*. University of Washington Press, 172 p.
- Coleman, H. W. and Steele, W. G. (1999). *Experimentation and uncertainty analysis for engineers*. Wiley, New York, 336 p.
- Comiso, J. C. (2006). Arctic warming signals from satellite observations. *Weather*, 61(3):70–76.
- Comiso, J. C., Parkinson, C. L., Gersten, R., and Stock, L. (2008). Accelerated decline in the Arctic sea ice cover. *Geophysical Research Letters*, 35(1):L01703, doi:10.1029/2007GL031972.
- Cox, G. F. N. and Weeks, W. F. (1988). Numerical simulations of the profile properties of undeformed first-year sea ice during the growth season. *Journal of Geophysical Research-Oceans*, 93(C10):12449–12460.
- Cummins, P. F. and Lagerloef, G. S. E. (2002). Low-frequency pycnocline depth variability at Ocean Weather Station P in the northeast Pacific. *Journal of Physical Oceanography*, 32(11):3207–3215.
- Dawson, C. W., Abraham, R. J., and See, L. M. (2007). HydroTest: a web-based toolbox of evaluation metrics for the standardised assessment of hydrological forecasts. *Environmental Modelling & Software*, 22(7):1034–1052.

- de Boyer Montégut, C., Madec, G., Fischer, A. S., Lazar, A., and Iudicone, D. (2004). Mixed layer depth over the global ocean: An examination of profile data and a profile-based climatology. *Journal of Geophysical Research-Oceans*, 109(C12):C12003.
- Denman, K. L. and Freeland, H. J. (1985). Correlation scales, objective mapping and a statistical test of geostrophy over the continental shelf. *Journal of Marine Research*, 43(3):517–539.
- Deutsch, C. V. and Journel, A. G. (1992). *Geostatistical software library and user's guide*. Oxford University Press, New York, 340 p.
- Ekwurzel, B., Schlosser, P., Mortlock, R. A., Fairbanks, R., and Swift, J. H. (2001). River runoff, sea ice meltwater, and Pacific water distribution and mean residence times in the Arctic Ocean. *Journal of Geophysical Research*, 106(C5):9075–9092.
- Emery, W. J. (1976). The role of vertical motion in the heat budget of the upper northeastern Pacific Ocean. *Journal of Physical Oceanography*, 6(3):299–305.
- Fett, R. W., Burk, S. D., Thompson, W. T., and Kozo, T. L. (1994). Environmental phenomena of the Beaufort Sea observed during the leads experiment. *Bulletin of the American Meteorological Society*, 75(11):2131–2168.
- Freeland, H., Denman, K., Wong, C. S., Whitney, F., and Jacques, R. (1997). Evidence of change in the winter mixed layer in the Northeast Pacific Ocean. *Deep Sea Research Part I: Oceanographic Research Papers*, 44(12):2117–2129.
- Galley, R. J. (2009). *Sea ice Thermodynamic and Dynamic Processes in the Ocean-sea ice-Atmosphere System of the Canadian Arctic*. Ph.D. thesis, University of Manitoba, Department of Environment and Geography, Winnipeg (MA), 249 p.
- Garneau, M. E., Vincent, W. F., Alonso-Sáez, L., Gratton, Y., and Lovejoy, C. (2006). Prokaryotic community structure and heterotrophic production in a river-influenced coastal arctic ecosystem. *Aquatic Microbial Ecology*, 42:27–40.
- Gaspar, P. (1988). Modeling the seasonal cycle of the upper ocean. *Journal of Physical Oceanography*, 18:161–180.
- Gaspar, P., André, J. C., and Lefevre, J. M. (1990). The determination of the latent and sensible heat fluxes at the sea surface viewed as an inverse problem. *Journal of Geophysical Research-Oceans*, 95(C9):16169–16178.
- Gill, A. E. (1982). *Atmosphere-ocean dynamics*. International Geophysics Series, volume 30. Academic Press, San Diego, 662 p.

- Gratton, Y., Bourgault, D., Galbraith, P., Prieur, L., Tsarev, V., Barette, J., Salcedo-Castro, J., Nahavandian, S., Sharatunova, M., Brouard, C., Hamel, C., Sévigny, C., Rail, M. E., Lago, V., Guillot, P., Bélanger, C., and Boisvert, D. (2012). Team 1: Physical Oceanography. In Barber, D., Tjaden, T., Leitch, D., Barber, L., and Chan, W., editors, *On the edge: from knowledge to action during the fourth international polar year circumpolar flaw lead system study (2007-2008)*, pages 33–50. Winnipeg (MA), 242 p.
- Holte, J. and Talley, L. (2009). A new algorithm for finding mixed layer depths with applications to Argo data and subantarctic mode water formation. *Journal of Atmospheric and Oceanic Technology*, 26(9):1920–1939.
- Ingram, R. G., Bacle, J., Barber, D. G., Gratton, Y., and Melling, H. (2002). An overview of physical processes in the North Water. *Deep-Sea Research II*, 49(22):4893–4906.
- Jackson, J. M. (2006). An Examination of horizontal advection and causes of mixed layer variability in the northeast Pacific Ocean from 2001-05 using Argo data and the General Ocean Turbulence Model. Master’s thesis, University of Alberta.
- Jackson, J. M., Carmack, E. C., McLaughlin, F. A., Allen, S. E., and Ingram, R. G. (2010). Identification, characterization, and change of the near-surface temperature maximum in the Canada Basin, 1993–2008. *Journal of Geophysical Research-Oceans*, 115(C5):C05021.
- Jackson, J. M., Myers, P. G., and Ianson, D. (2006). An examination of advection in the northeast Pacific Ocean, 2001-2005. *Geophysical Research Letters*, 33(15):L15601.
- Jones, E. P., Anderson, L. G., and Swift, J. H. (1998). Distribution of Atlantic and Pacific waters in the upper Arctic Ocean: Implications for circulation. *Geophysical Research Letters*, 25(6):765–768.
- Journel, A. G. and Huijbregts, C. J. (1978). *Mining geostatistics*. Academic Press London, 600 p.
- Kara, A. B., Rochford, P. A., and Hurlburt, H. E. (2000). An optimal definition for ocean mixed layer depth. *Journal of Geophysical Research-Oceans*, 105(C7):16803–16821.
- Kowalik, Z. and Proshutinsky, A. Y. (1994). The Arctic Ocean tides. In Johannessen, O. M., Muench, R. D., and Overland, J. E., editors, *The Polar oceans and their role in shaping the global environment*, The Nansen Centennial Volume, Geophysical Monograph Series 85, pages 137–158, Washington, D.C., 525 p. American Geophysical Union.

- Kraus, E. B. and Turner, J. S. (1967). A one-dimensional model of the seasonal thermocline II. the general theory and its consequences. *Tellus*, 19(1):98–106.
- Lagerloef, G. S. E. (1995). Interdecadal variations in the Alaska Gyre. *Journal of Physical Oceanography*, 25(10):2242–2258.
- Lanos, R. (2009). *Circulation régionale, masses d'eau, cycles d'évolution et transports entre la mer de Beaufort et le Golfe d'Amundsen*. Ph.D. thesis, Institut national de la recherche scientifique, Centre eau, terre et environnement, Québec (Qc), 245 p.
- Large, W. G. and Crawford, G. B. (1995). Observations and simulations of upper-ocean response to wind events during the Ocean Storms Experiment. *Journal of Physical Oceanography*, 25(11):2831–2852.
- Lavigne, H., D'Ortenzio, F., Migon, C., Claustre, H., Testor, P., d'Alcalà, M. R., Lavezza, R., Houpert, L., and Prieur, L. (2013). Enhancing the comprehension of mixed layer depth control on the mediterranean phytoplankton phenology. *Journal of Geophysical Research-Oceans*, 118(7):3416–3430.
- Levine, M. D., Gard, S. R., and Simpkins, J. (1986). Moored temperature and conductivity observations during AIWEX. Technical Report 86-9, Oregon State University, Corvallis (OR), 195 p.
- Levitus, S. (1982). *Climatological atlas of the world ocean*. NOAA Professional Paper, No. 13, U.S Gov. Printing Office, 173 p.
- Liu, H. (2009). *Global oceanic mixed layer properties*. Ph.D. thesis, University of Maryland, 111 p.
- Lukovich, J. V. and Barber, D. G. (2006). Atmospheric controls on sea ice motion in the southern Beaufort Sea. *Journal of Geophysical Research-Atmospheres*, 111:D18103, doi:10.1029/2005JD006408.
- Macdonald, R. W. (2000). Arctic estuaries and ice: A positive-negative estuarine couple. In Lewis, E. L., Jones, E. P., Lemke, P., Prowse, T. D., and Wadhams, P., editors, *The Freshwater Budget of the Arctic Ocean*, volume 70 of *NATO Science Series*, pages 383–407. Springer, Netherlands, 623 p.
- Macdonald, R. W., McLaughlin, F. A., and Carmack, E. C. (2002). Fresh water and its sources during the SHEBA drift in the Canada Basin of the Arctic Ocean. *Deep-Sea Research Part I: Oceanographic Research Papers*, 49(10):1769–1785.
- Maykut, G. A. (1982). Large-scale heat exchange and ice production in the central Arctic. *Journal of Geophysical Research-Oceans*, 87(C10):7971–7984.

- McLaughlin, F. A., Carmack, E. C., and Macdonald, R. W. (1996). Physical and geochemical properties across the Atlantic/Pacific water mass front in the southern Canadian Basin. *Journal of Geophysical Research*, 101(C1):1183–1197.
- McLaughlin, F. A., Carmack, E. C., Macdonald, R. W., Melling, H., Swift, J. H., Wheeler, P. A., Sherr, B. F., and Sherr, E. B. (2004). The joint roles of Pacific and Atlantic-origin waters in the Canada Basin, 1997-1998. *Deep-Sea Research, Part I: Oceanographic Research Papers*, 51(1):107–128.
- Melling, H. and Lewis, E. L. (1982). Shelf drainage flows in the Beaufort Sea and their effect on the Arctic Ocean pycnocline. *Deep-Sea Research*, 29(8):967–985.
- Moisan, J. R. and Niiler, P. P. (1998). The seasonal heat budget of the North Pacific: Net heat flux and heat storage rates (1950-1990). *Journal of Physical Oceanography*, 28(3):401–421.
- Mundy, C. J., Gosselin, M., Ehn, J., Gratton, Y., Rosznagel, A., Barber, D. G., Martin, J., Tremblay, J. É., Palmer, M., Arrigo, K. R., et al. (2009). Contribution of under-ice primary production to an ice-edge upwelling phytoplankton bloom in the Canadian Beaufort Sea. *Geophysical Research Letters*, 36(17):L17601.
- Nerheim, S. and Stigebrandt, A. (2006). On the influence of buoyancy fluxes on wind drift currents. *Journal of Physical Oceanography*, 36(8):1591–1604.
- Newton, B., Tremblay, L. B., Cane, M. A., and Schlosser, P. (2006). A simple model of the Arctic Ocean response to annular atmospheric modes. *Journal of Geophysical Research-Oceans*, 111(C9):9019.
- Niiler, P. P. (1977). One-dimensional models of the upper ocean. In Kraus, E. B., editor, *Modelling and Prediction of the Upper Layers of the Ocean*, pages 143–172. Pergamon Press, New York, 325 p.
- Paci, A., Caniaux, G., Gavart, M., Giordani, H., Lévy, M., Prieur, L., and Reverdin, G. (2005). A high-resolution simulation of the ocean during the POMME experiment: Simulation results and comparison with observations. *Journal of Geophysical Research*, 110(C7), doi:10.1029/2004JC002712.
- Parkinson, C. L. and Washington, W. M. (1979). A large-scale numerical model of sea ice. *Journal of Geophysical Research-Oceans*, 84(C1):311–337.
- Pavlidis, T. and Horowitz, S. L. (1974). Segmentation of plane curves. *Computer, IEEE Trans.*, 23(8):860–870.

- Peterson, I. K., Prinsenber, S. J., and Holladay, J. S. (2008). Observations of sea ice thickness, surface roughness and ice motion in Amundsen Gulf. *Journal of Geophysical Research-Oceans*, 113(C6):C06016.
- Philips, E. J., Cichra, M., Havens, K., Hanton, C., Badylak, S., Rueter, B., Randall, M., and Hansen, P. (1997). Relationships between phytoplankton dynamics and the availability of light and nutrients in a shallow sub-tropical lake. *Journal of Plankton Research*, 19(3):319–342.
- Pickart, R. S. (2004). Shelfbreak circulation in the Alaskan Beaufort Sea: Mean structure and variability. *Journal of Geophysical Research-Oceans*, 109(C4):4024.
- Pickart, R. S., Spall, M. A., Ribergaard, M. H., Moore, G. W. K., and Milliff, R. F. (2003). Deep convection in the Irminger Sea forced by the Greenland tip jet. *Nature*, 424(6945):152–156.
- Pickart, R. S., Torres, D. J., and Clarke, R. A. (2002). Hydrography of the Labrador Sea during active convection. *Journal of Physical Oceanography*, 32(2):428–457.
- Polovina, J. J., Mitchum, G. T., and Evans, G. T. (1995). Decadal and basin-scale variation in mixed layer depth and the impact on biological production in the Central and North Pacific. *Deep Sea Research*, 42(10):1701–1716.
- Polyakov, I. V., Walsh, J. E., and Kwok, R. (2012). Recent changes of Arctic multiyear sea ice coverage and the likely causes. *Bulletin of the American Meteorological Society*, 93(2):145–151.
- Pond, S. and Pickard, G. L. (1983). *Introductory dynamical oceanography*. Elsevier Butterworth-Heinemann, Oxford, U.K., 329 p, 2 edition.
- Price, J. F., Weller, R. A., and Pinkel, R. (1986). Diurnal cycling: Observations and models of the upper ocean response to diurnal heating, cooling, and wind mixing. *Journal of Geophysical Research*, 91(C7):8411–8427.
- Prieur, L., Caniaux, G., D’Ortenzio, F., Lavigne, H., and Giordani, H. (2010). Etude de faisabilité de l’application de méthodes d’exploitation conjointe des séries de profils in situ (CTD au point fixe, profils ARGO) et des séries d’image satellitaire (SST, Schla) aux fins de l’Océanographie Opérationnelle. Technical report, PROSAT Project, GMMC MERCATOR, contrat no Ifremer 08/ 2 210 118, 55 p.
- Rao, R. R. and Sivakumar, R. (2003). Seasonal variability of sea surface salinity and salt budget of the mixed layer of the north Indian Ocean. *Journal of Geophysical Research*, 108(C1):3009.

- Rozanska, M., Gosselin, M., Poulin, M., Wiktor, J. M., and Michel, C. (2009). Influence of environmental factors on the development of bottom ice protist communities during the winter-spring transition. *Marine Ecology Progress Series*, 386:43–59.
- Rudels, B., Anderson, L. G., and Jones, E. P. (1996). Formation and evolution of the surface mixed layer and halocline of the Arctic Ocean. *Journal of Geophysical Research-Oceans*, 101(C4):8807–8821.
- Rudels, B., Jones, E. P., Anderson, L. G., and Kattner, G. (1994). On the intermediate depth waters of the Arctic Ocean. In *The Polar Oceans and Their Role in Shaping the Global Environment*, pages 33–46. American Geophysical Union.
- Rudels, B., Muench, R. D., Gunn, J., Schauer, U., and Friedrich, H. J. (2000). Evolution of the Arctic Ocean boundary current north of the Siberian shelves. *Journal of Marine Systems*, 25(1):77–99.
- Sarkar, N. (2007). Mixed Layer dynamics along the Seward Line in the northern Gulf of Alaska. Master’s thesis, Old Dominion University, Norfolk, 71 p.
- Sarkar, N., Royer, T. C., and Grosch, C. E. (2005). Hydrographic and mixed layer depth variability on the shelf in the northern Gulf of Alaska, 1974-1998. *Continental Shelf Research*, 25(18):2147–2162.
- Schneider, N. and Müller, P. (1990). The meridional and seasonal structure of the mixed-layer depth and its diurnal amplitude observed during the Hawaii-to-Tahiti Shuttle experiment. *Journal of Physical Oceanography*, 20(9):1395–1404.
- Serreze, M. C., Walsh, J. E., Chapin, F. S., Osterkamp, T., Dyrugerov, M., Romanovsky, V., Oechel, W. C., Morison, J., Zhang, T., and Barry, R. G. (2000). Observational evidence of recent change in the northern high-latitude environment. *Climatic Change*, 46(1):159–207.
- Sévigny, C. (2013). *Mélange et fronts océaniques dans la couche de surface du Golfe d’Amundsen et de l’Arctique Canadien*. Ph.D. thesis, Institut national de la recherche scientifique, Centre eau, terre et environnement, Québec (Qc), 247 p.
- Shimada, K., Carmack, E. C., Hatakeyama, K., and Takizawa, T. (2001). Varieties of shallow temperatures maximum waters in the western Canadian Basin of the Arctic Ocean. *Geophysical Research Letters*, 28(18):3441–3444.
- Smith, S. D., Muench, R. D., and Pease, C. H. (1990). Polynyas and leads: An overview of physical processes and environment. *Journal of Geophysical Research*, 95(C6):9461–9479.

- Smith, W. O. (1990). *Polar Oceanography. Part A: Physical Science*. Academic Press, San Diego, CA, USA, 406 p.
- Stevenson, J. W. and Niiler, P. P. (1983). Upper ocean heat budget during the Hawaii-to-Tahiti shuttle experiment. *Journal of Physical Oceanography*, 13(10):1894–1907.
- Thomson, R. E. and Fine, I. V. (2003). A Diagnostic Model for Mixed Layer Depth Estimation with Application to Ocean Station P in the Northeast Pacific. *Journal of Atmospheric and Oceanic Technology*, 20(2):319–329.
- Thomson, R. E. and Fine, I. V. (2009). Estimating mixed layer depth from oceanic profile data. *American Meteorological Society*, 39:1399–1415.
- Toole, J. M., Timmermans, M. L., Perovich, D. K., Krishfield, R. A., Proshutinsky, A., and Richter-Menge, J. A. (2010). Influences of the ocean surface mixed layer and thermohaline stratification on Arctic Sea ice in the central Canada Basin. *Journal of Geophysical Research-Oceans*, 115:C10018.
- Tremblay, J. É., Bélanger, S., Barber, D. G., Asplin, M., Martin, J., Darnis, G., Fortier, L., Gratton, Y., Link, H., Archambault, P., et al. (2011). Climate forcing multiplies biological productivity in the coastal Arctic Ocean. *Geophysical Research Letters*, 38(18):L18604.
- Tremblay, J. É., Simpson, K., Martin, J., Miller, L., Gratton, Y., Barber, D., and Price, N. M. (2008). Vertical stability and the annual dynamics of nutrients and chlorophyll fluorescence in the coastal, southeast Beaufort Sea. *Journal of Geophysical Research-Oceans*, 113(C7):C07S90.
- Våge, K., Pickart, R. S., Moore, G. W. K., and Ribergaard, M. H. (2008). Winter mixed layer development in the central Irminger Sea: The effect of strong, intermittent wind events. *Journal of Physical Oceanography*, 38(3):541–565.
- Wadhams, P. (2000). *Ice in the ocean*. CRC Press, London, 364 p.
- Wang, J., Zhang, J., Watanabe, E., Ikeda, M., Mizobata, K., Walsh, J. E., Bai, X., and Wu, B. (2009). Is the Dipole Anomaly a major driver to record lows in Arctic summer sea ice extent? *Geophysical Research Letters*, 36(5):L05706.
- Wang, M. and Overland, J. E. (2009). A sea ice free summer Arctic within 30 years? *Geophysical Research Letters*, 36(7):L07502.
- Whitney, F. A. and Welch, D. W. (2002). Impact of the 1997-1998 El Niño and 1999 La Niña on nutrient supply in the Gulf of Alaska. *Progress in Oceanography*, 54(1):405–421.

- Williams, W. J. and Carmack, E. C. (2008). Combined effect of wind-forcing and isobath divergence on upwelling at Cape Bathurst, Beaufort Sea. *Journal of Marine Research*, 66(5):645–663.
- Wu, B., Wang, J., and Walsh, J. E. (2006). Dipole anomaly in the winter Arctic atmosphere and its association with sea ice motion. *Journal of Climate*, 19(2):210–225.
- Yunker, M. B. and Macdonald, R. W. (1995). Composition and origins of polycyclic aromatic hydrocarbons in the Mackenzie River and on the Beaufort Sea shelf. *Arctic*, pages 118–129.

APPENDIX A

Temporal variations of $CumJ_b$, $Cum(dC_{pres}/dt)$, $Cum(Adv_{\rho_{hc}})$ and $Cum(hc d\rho_{hc}/dt)$ (equation 5.22) and the MLD, at different stations during CFL (2007-2008) and Malina (2009) are presented. The meta-information about the different stations whose data were used here are given in Table 5.1.

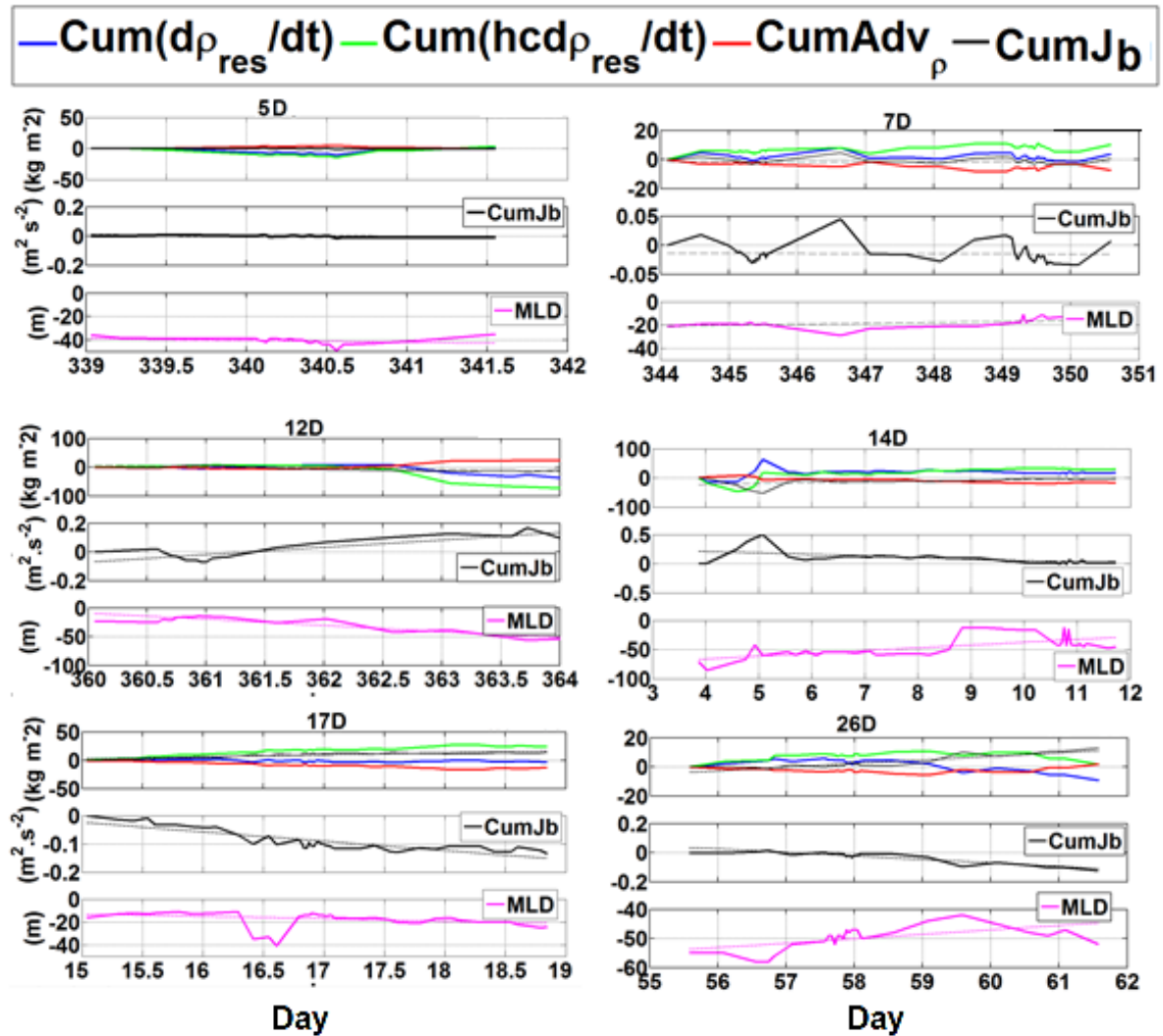


Figure A.1: Temporal variation of $CumJ_b$, $Cum(dC_{pres}/dt)$, $Cum(Adv_{\rho_{hc}})$ and $Cum(hc d\rho_{hc}/dt)$ and the MLD at stations 5D, 7D, 12D, 14D, 17D and 26D during CFL (2007-2008). The dashed line in each subplot shows the linear tendency of each curve.

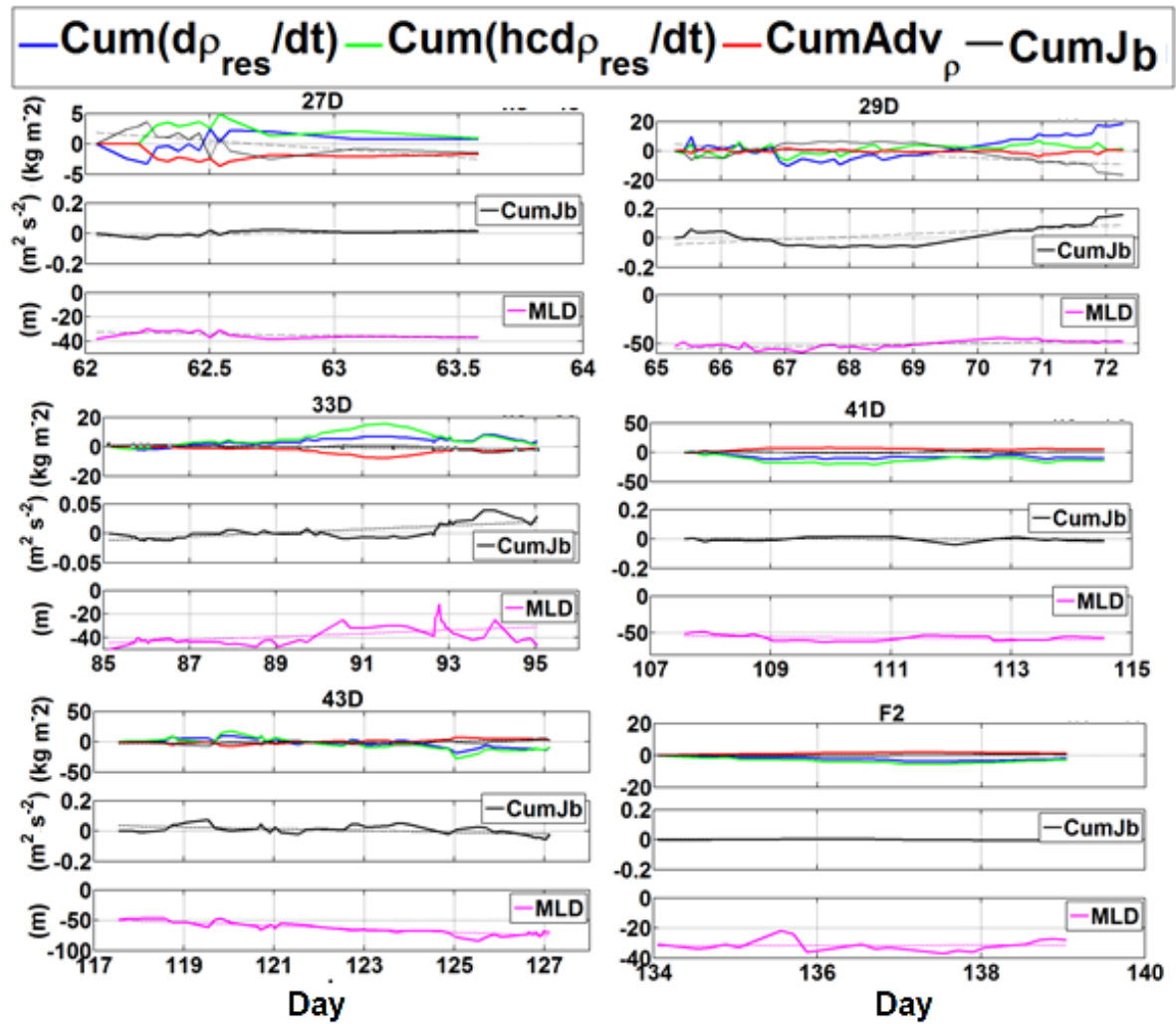


Figure A.2: Temporal variation of $CumJ_b$, $Cum(dC_{pres}/dt)$, $Cum(Adv_{\rho_{hc}})$ and $Cum(hcd\rho_{hc}/dt)$ and the MLD at stations 27D, 29D, 33D, 41D, 43D and F2 during CFL (2007-2008). The dashed line in each subplot shows the linear tendency of each curve.

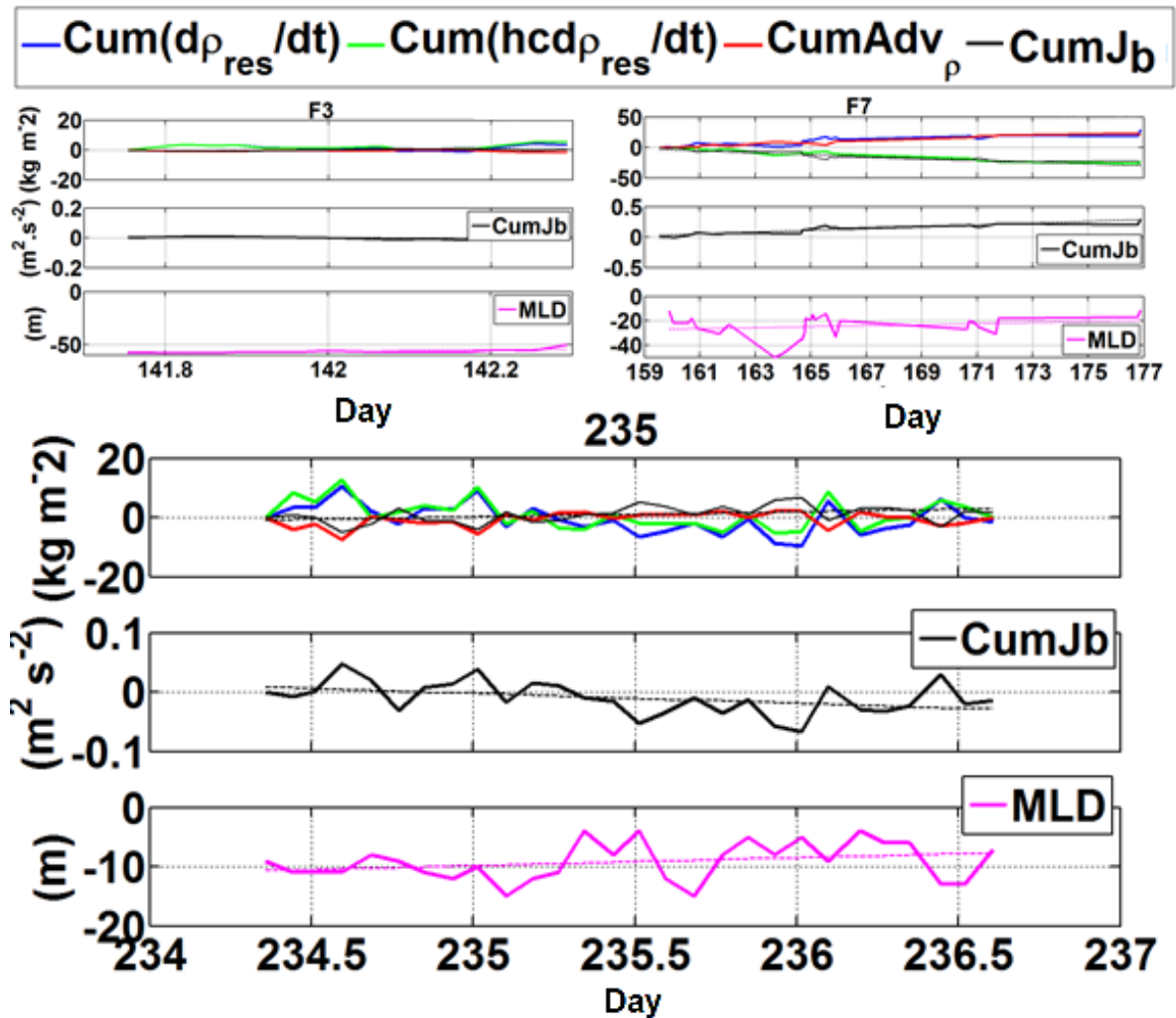


Figure A.3: Temporal variation of $CumJ_b$, $Cum(dC_{pres}/dt)$, $Cum(Adv_{\rho_{hc}})$ and $Cum(hcd\rho_{hc}/dt)$ and the MLD at stations F3, F7 and 235 during CFL (2007-2008) and Malina (2009). The dashed line in each subplot shows the linear tendency of each curve.

APPENDIX B

Contours of density, salinity and temperature for the different stations of Appendix I. The meta-information about the different stations are given in Table 5.1. More complete results for the CASES and 19D data are presented and discussed in section 5.3.

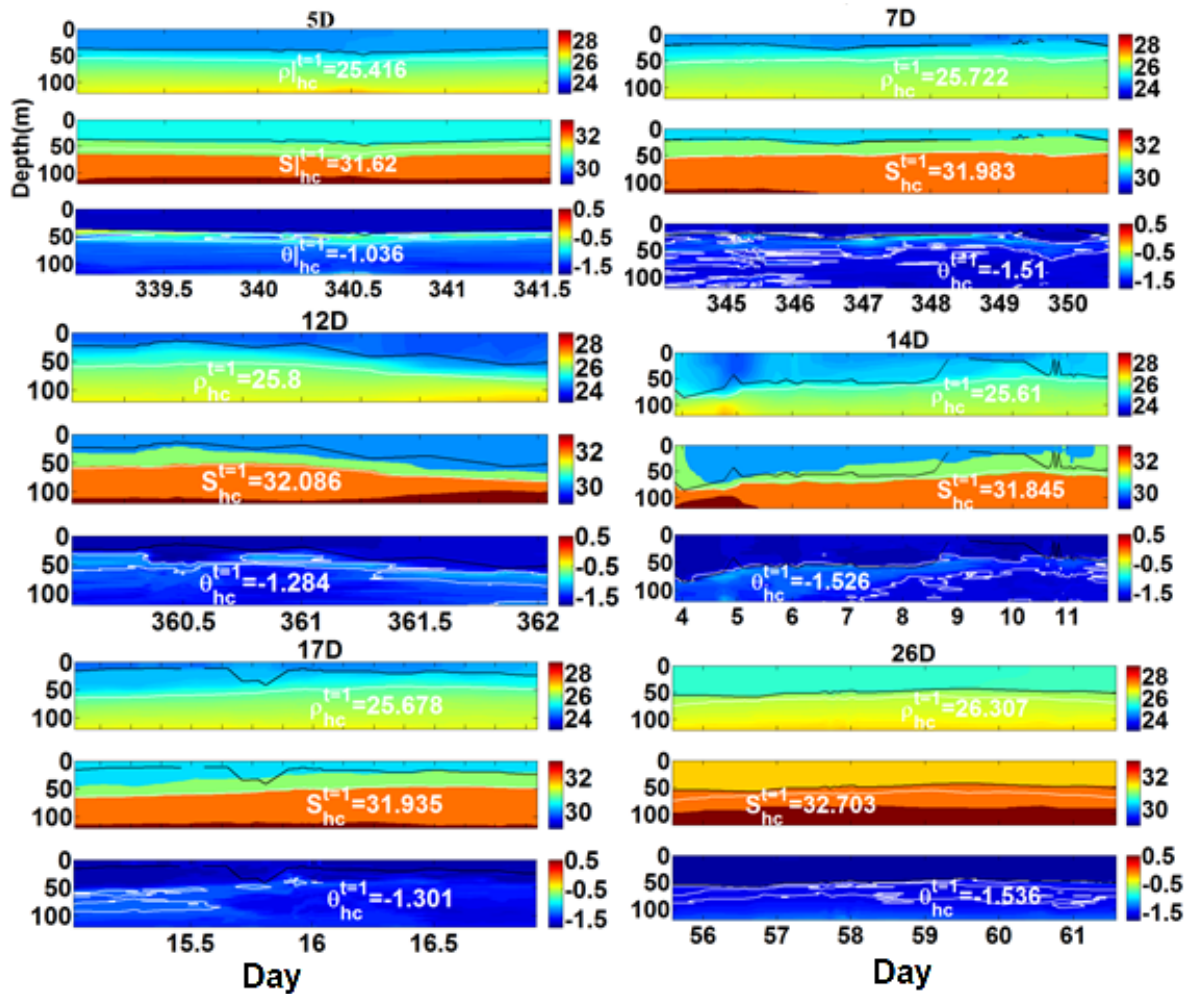


Figure B.1: Contours of density, salinity and temperature at stations 5D, 7D, 12D, 14D, 17D and 26D. The white lines are the density, salinity and temperature isolines at the reference depth. The black lines are the MLD.

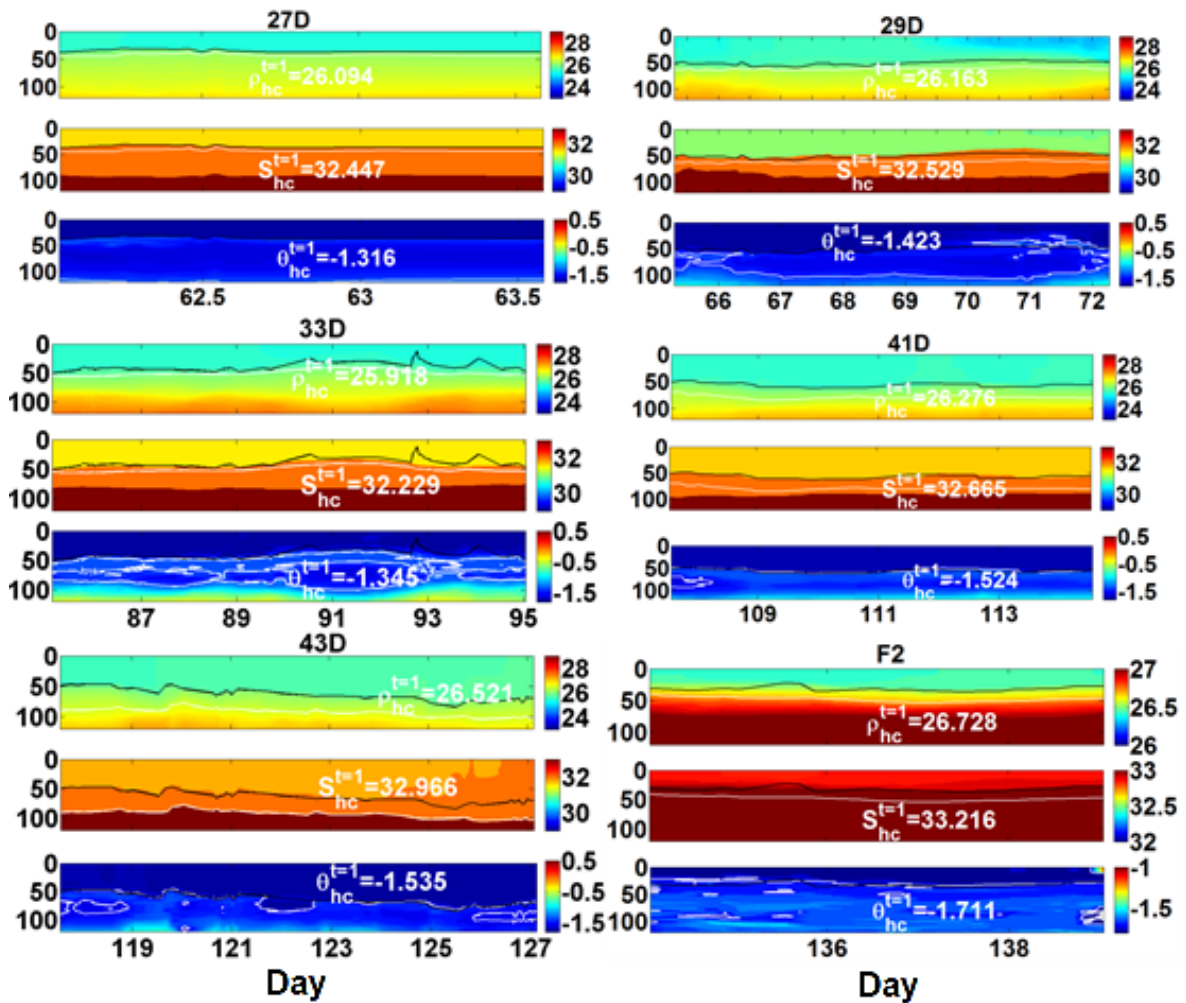


Figure B.2: Contours of density, salinity and temperature at stations 27D, 29D, 33D, 41D, 43D and F2. The white lines are the density, salinity and temperature isolines at the reference depth. The black lines are the MLD.

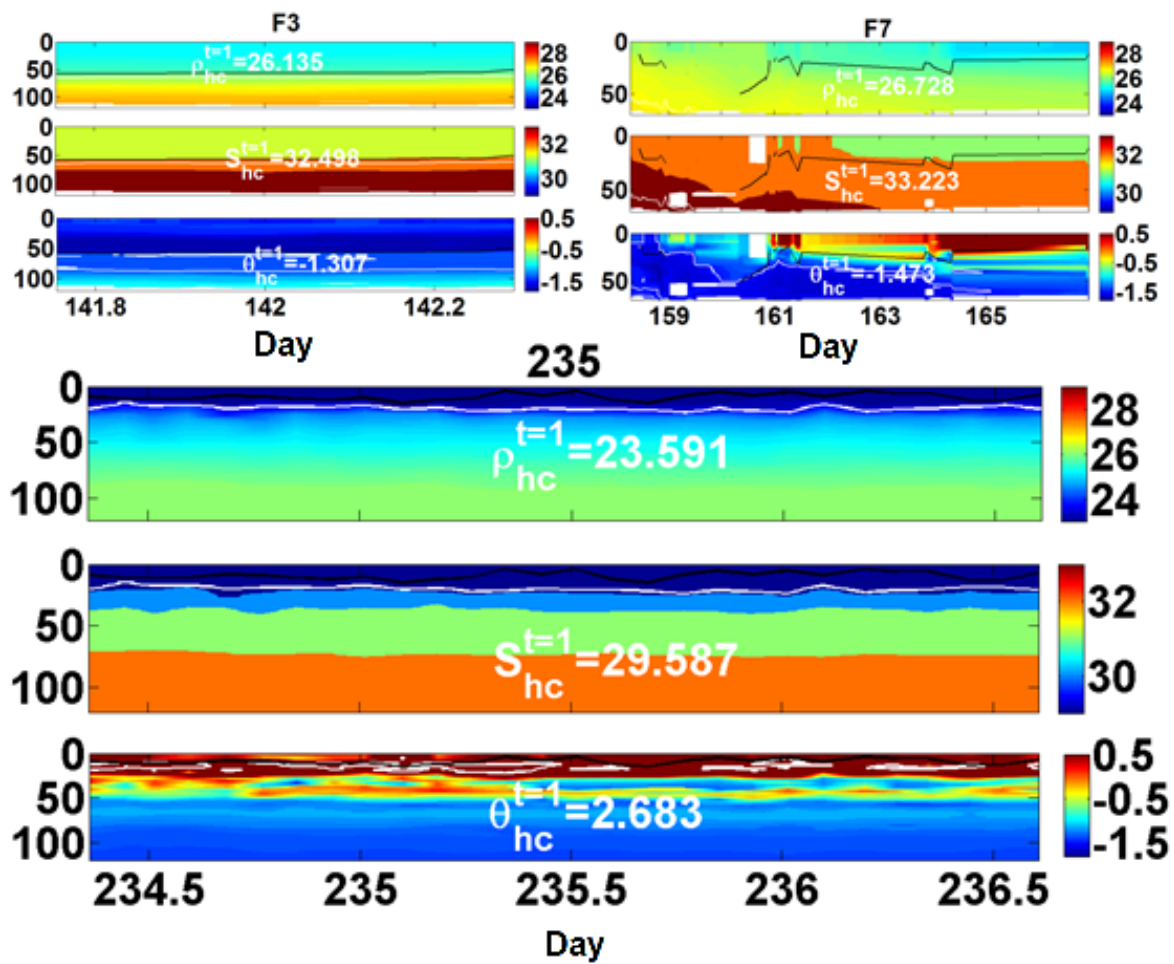


Figure B.3: Contours of density, salinity and temperature at stations F3, F7 and 235. The white lines are the density, salinity and temperature isolines at the reference depth. The black lines are the MLD.

APPENDIX C

Cross-correlations between the MLD and the terms in equation 5.22, $CumJ_b$, $Cum(dC_{pres}/dt)$, $Cum(Adv_{\rho_{hc}})$ and $Cum(hc d\rho_{hc}/dt)$, are shown for the different stations of Appendix I. The meta-information about the different stations are given in Table 5.1. More information about the relationship between the MLD and these terms is shown in Table 5.2 and 5.3.

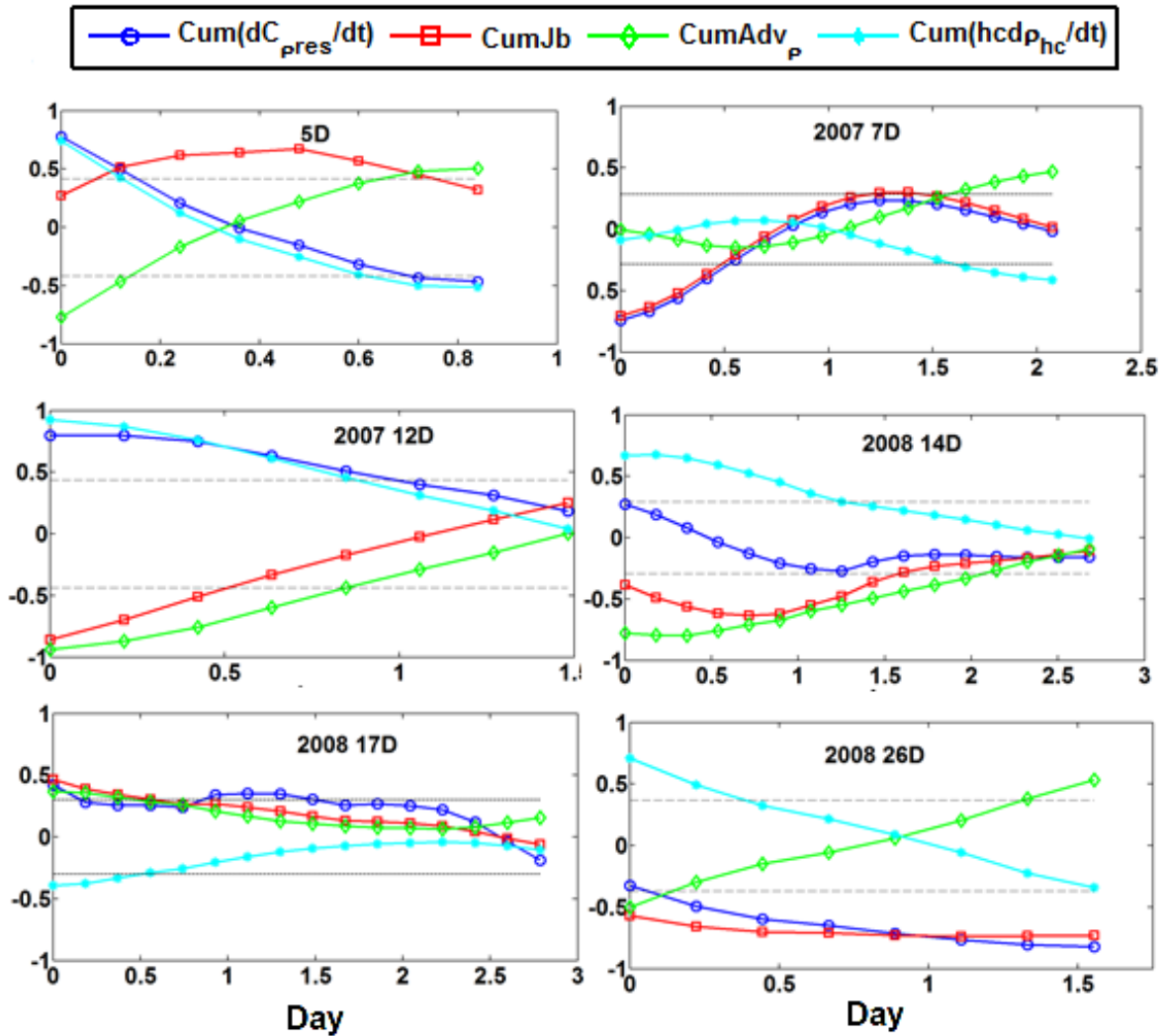


Figure C.1: Cross-correlation, at stations 5D, 7D, 12D, 14D, 17D and 26D, between MLD and $Cum(dC_{pres}/dt)$ in blue, $CumJ_b$ in red, $Cum(Adv_{\rho_{hc}})$ in green and $Cum(hcd\rho_{hc}/dt)$ in cyan. The cross correlations for the lags are shown with circles, squares, diamonds and stars respectively for $Cum(dC_{pres}/dt)$, $CumJ_b$, $Cum(Adv_{\rho_{hc}})$ and $Cum(hcd\rho_{hc}/dt)$. The dashed black lines are confidence limit.

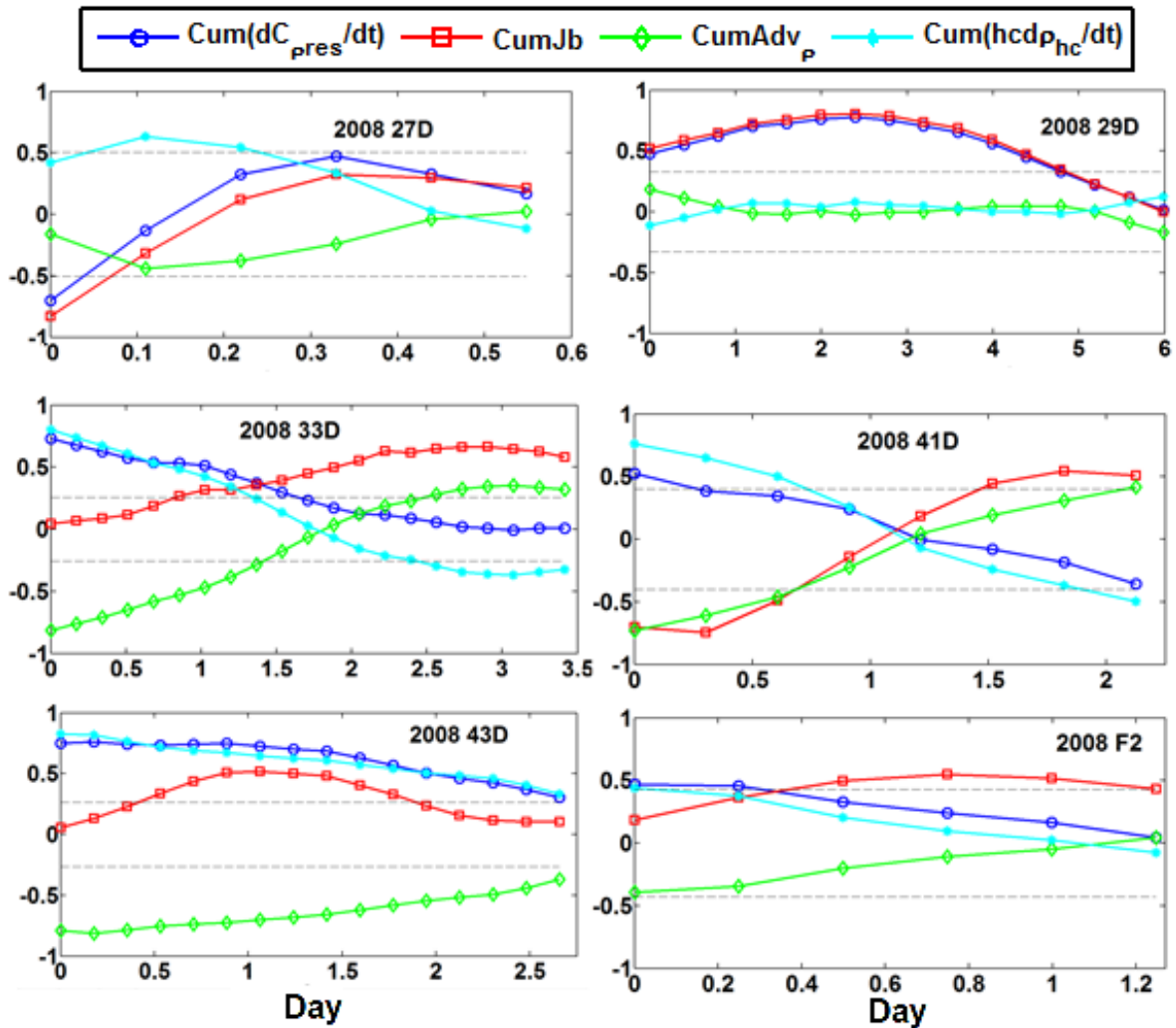


Figure C.2: Cross-correlation, at stations 27D, 29D, 33D, 41D, 43D and F2, between MLD and $Cum(dC_{pres}/dt)$ in blue, $CumJ_b$ in red, $Cum(Adv_{\rho_{hc}})$ in green and $Cum(hcd\rho_{hc}/dt)$ in cyan. The cross correlations for the lags are shown with circles, squares, diamonds and stars respectively for $Cum(dC_{pres}/dt)$, $CumJ_b$, $Cum(Adv_{\rho_{hc}})$ and $Cum(hcd\rho_{hc}/dt)$. The dashed black lines are confidence limit.

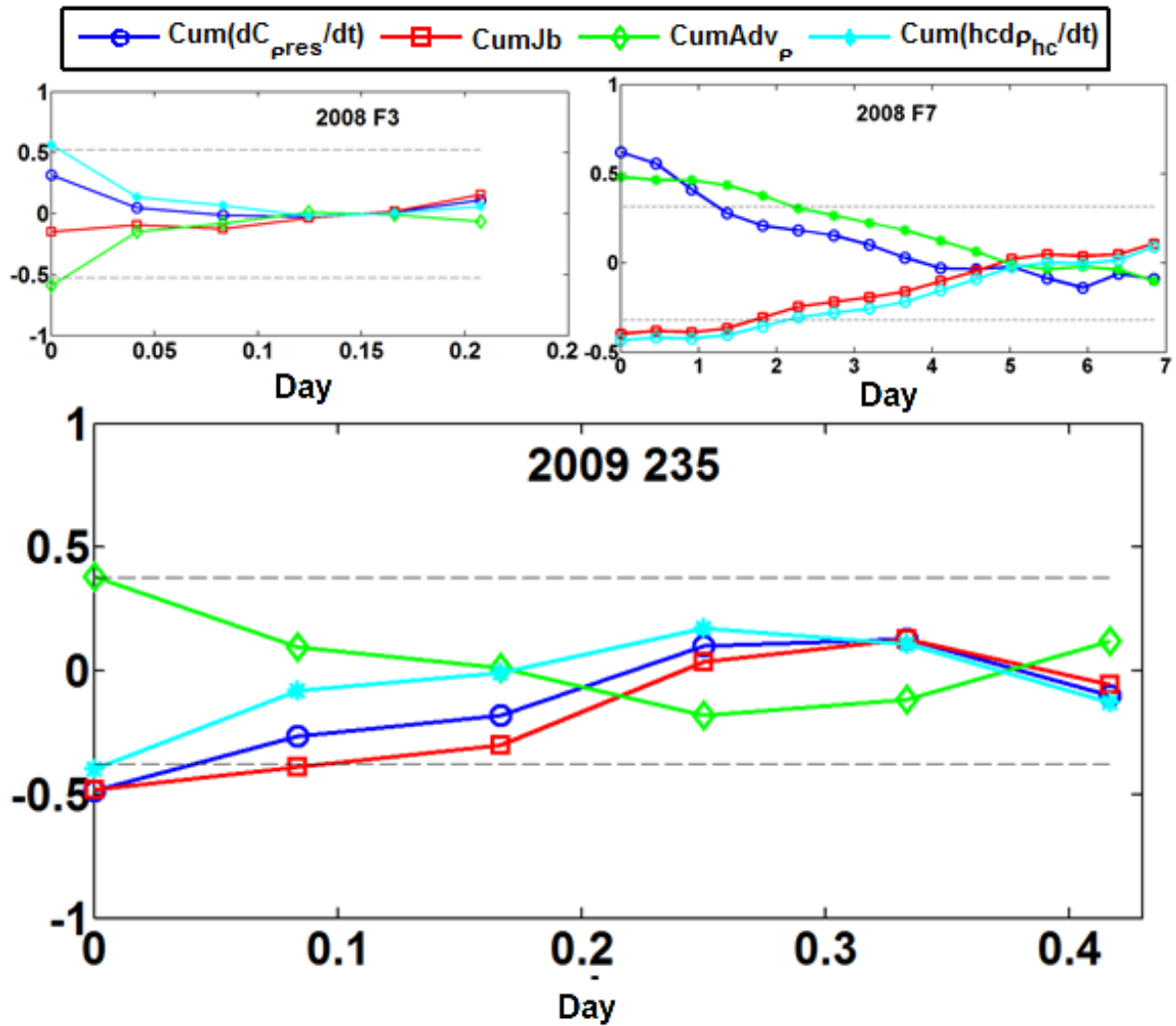


Figure C.3: Cross-correlation, at stations F3, F7 and 235, between MLD and $Cum(dC_{pres}/dt)$ in blue, $Cum(J_b)$ in red, $Cum(Adv_{\rho_{hc}})$ in green and $Cum(hcd_{\rho_{hc}}/dt)$ in cyan. The cross correlations for the lags are shown with circles, squares, diamonds and stars respectively for $Cum(dC_{pres}/dt)$, $Cum(J_b)$, $Cum(Adv_{\rho_{hc}})$ and $Cum(hcd_{\rho_{hc}}/dt)$. The dashed black lines are confidence limit.